Springer Theses
Recognizing Outstanding Ph.D. Research

Boon-Kok Tan

Development of Coherent Detector Technologies for Sub-Millimetre Wave Astronomy Observations

Springer

Springer Theses

Recognizing Outstanding Ph.D. Research

Aims and Scope

The series "Springer Theses" brings together a selection of the very best Ph.D. theses from around the world and across the physical sciences. Nominated and endorsed by two recognized specialists, each published volume has been selected for its scientific excellence and the high impact of its contents for the pertinent field of research. For greater accessibility to non-specialists, the published versions include an extended introduction, as well as a foreword by the student's supervisor explaining the special relevance of the work for the field. As a whole, the series will provide a valuable resource both for newcomers to the research fields described, and for other scientists seeking detailed background information on special questions. Finally, it provides an accredited documentation of the valuable contributions made by today's younger generation of scientists.

Theses are accepted into the series by invited nomination only and must fulfill all of the following criteria

- They must be written in good English.
- The topic should fall within the confines of Chemistry, Physics, Earth Sciences, Engineering and related interdisciplinary fields such as Materials, Nanoscience, Chemical Engineering, Complex Systems and Biophysics.
- The work reported in the thesis must represent a significant scientific advance.
- If the thesis includes previously published material, permission to reproduce this must be gained from the respective copyright holder.
- They must have been examined and passed during the 12 months prior to nomination.
- Each thesis should include a foreword by the supervisor outlining the significance of its content.
- The theses should have a clearly defined structure including an introduction accessible to scientists not expert in that particular field.

More information about this series at http://www.springer.com/series/8790

Boon-Kok Tan

Development of Coherent Detector Technologies for Sub-Millimetre Wave Astronomy Observations

Doctoral Thesis accepted by
University of Oxford, Oxford, UK

Springer

Author
Dr. Boon-Kok Tan
Department of Physics (Astrophysics)
University of Oxford
Oxford
UK

Supervisor
Prof. Ghassan Yassin
Department of Physics (Astrophysics)
University of Oxford
Oxford
UK

ISSN 2190-5053 ISSN 2190-5061 (electronic)
Springer Theses
ISBN 978-3-319-19362-5 ISBN 978-3-319-19363-2 (eBook)
DOI 10.1007/978-3-319-19363-2

Library of Congress Control Number: 2015948770

Springer Cham Heidelberg New York Dordrecht London

Printed on acid-free paper

Springer International Publishing AG Switzerland is part of Springer Science+Business Media (www.springer.com)

Supervisor's Foreword

Sub-millimetre astronomy is the branch of astronomy that makes observations at wavelengths between microwave frequencies and the far infrared. Most existing sub-millimetre telescopes, however, observe at wavelengths between 1 mm and 200 μm. An important area of science that sub-millimetre astronomy seeks to investigate is the complex process of formation of stars from dense molecular clouds. One way of carrying out this investigation is by the coherent detection of the intensity of spectral lines emitted by the chemical elements in the star forming areas. Measurements of the spectrum at various redshifts (hence at different frequencies) allow us to study the evolution of galaxies, or in other words, the history of the universe. For many years, these observations have been extremely difficult for two reasons. The first is that the development of sensitive receivers at those wavelengths is extremely hard. For example, the small size of wavelength requires very precise machining of receiver components such as feeds and optical windows. Also, the relatively high frequency requires a detector with extremely sharp non-linearity, which cannot be provided by conventional solid-state devices. The second difficulty in sub-millimetre observations is the existence of water vapour in the atmosphere that has absorption lines at these wavelengths. This restricts ground-based sub-millimetre telescopes to be installed on high and dry sites, and even then, observations are only possible within frequency bands known as the atmospheric windows. For example, the largest sub-millimetre telescope ever built ALMA (Atacama Large Millimetre/sub-millimetre Array) observes in 10 frequency bands between 30–950 GHz.

The single most important technological development in sub-millimetre receivers in recent years is undoubtedly the employment of the superconducting tunnel junctions as coherent detectors in sub-millimetres receivers. The SIS (Superconductor-Insulator-Superconductor) consists of two small area ($\sim 1 \mu m^2$) superconducting films (~ 400 nm thickness) sandwiching a very thin insulator (~ 20 Å). When this device is biased appropriately, an incident photon may have enough energy to break a cooper pair into normal electrons that can tunnel to the opposite superconductor through the thin insulator. By measuring the tunnelling

current, the intensity of the incident beam is obtained. In most cases, however, the tunnel junction is used as a heterodyne receiver or an SIS mixer. Here, the device is illuminated by two signals: The signal from the sky at a frequency ν_s and a Local Oscillator (LO) signal ν_{LO} generated by the receiver. At the output of the mixer, we obtain a signal whose frequency is equal to the difference $|\nu_s - \nu_{LO}|$. In other words, the frequency of the signal is down-converted by the mixer to a value that can be handled by the electronics. The performance of a mixer is determined by its conversion loss and its noise temperature which is a measure of the noise added to the signal by the mixing process. Modern mixers operating at frequencies below the superconducting gap frequency (defined as $\nu_g = E_g/h$ where E_g is the superconductor energy gap and h is the Planck's constant) achieve noise temperatures that approach the limit imposed by Heisenberg uncertainty principle. All modern sub-millimetre telescopes employ heterodyne receiver based on SIS mixer including ALMA and the space telescope Herschel.

The design of SIS mixers is by no means straightforward, particularly at frequencies approaching 700 GHz or above. First, the high energy of the photon requires quantum treatment of mixing process as the classical mixer model is no longer valid and the analysis becomes even more complicated at frequencies comparable to the superconducting gap. Also, the power incident on the receiver will need to be coupled very efficiently to a device of tiny dimension which is fabricated in a planar circuit. The work described in this thesis aims to contribute to the design and the analysis of SIS mixers fabricated near the superconducting gap of Niobium which is approximately 680 GHz at 4 K. It will address the issues of how to create a high performance mixer design that is reliable as a result of rigorous modelling, fully integrated for ease and repeatable fabrication and doesn't require a complicated mixer block.

A very important achievement of this work is the ability to accurately model the full mixer chip, including the SIS device and the superconducting transmission lines deposited on the mixer chip to couple power from the waveguide to the tunnel junction and to tune out the capacitance of the device. This requires simulations that combine quantum mixing software based on Tucker's theory of quantum detection with commercial electromagnetic software, while rigorously including the effect of superconductivity on the wave propagation. This design procedure was extensively tested experimentally and the results were truly impressive. Not only that the simulations generated by the author were able to predict the behaviour of a well fabricated mixer but perhaps more importantly it was able to predict the performance when fabrication errors were made such as an offset in the tunnel junction location. This is an extremely important feature considering the complexity of SIS mixer chip fabrication. Using these simulations the author was able to design mixers with wide RF and IF ranges. An IF bandwidth of more than 10 GHz was demonstrated and up to 20 GHz was shown possible. This is a very promising result considering that the sensitivity of the receiver is proportional to the IF bandwidth.

The SIS mixer chip employed in this work employs a finline taper that couples the power from the waveguide to a slotline. The finline transition has several

advantages including wide RF bandwidth, large substrate area for planar circuits and results in a simple mixer block design that does not need an accurately machined backshort.

Conventionally, SIS mixer chips were fabricated on quartz substrates of approximately 60 micron thickness at 700 GHz. The mixer chips described in this thesis use the newly developed SOI (Silicon-on-Insulator) technology where the mixer circuits are deposited on a 15 micron silicon substrate and the planar circuits terminated by gold beam lead electrodes. This fabrication technology developed at KOSMA, University of Cologne has several crucial advantages such as light loading of the waveguide, easy grounding of the chip and removing parasitic inductance from the IF circuit. Also, fabricating SIS mixers using beam leads on an ultra-thin SOI substrate reduces the handling process significantly, and thus makes producing a large number of detector chips that are identical in a single fabrication run feasible. Since all the mixer circuits and the finline taper used to feed the mixer chip are fabricated on-chip, do not rely on complicated mechanical waveguide designs to support the operation of the mixer.

The mixer chip described above is mounted at the E-plane of a rectangular waveguide which is fed by an electromagnetic horn. Modern high quality SIS mixers employ corrugated horn for high beam circularity, low cross polarisation and low sidelobes. The mixer described in this work pioneers the use of multiple flare-angled horn at these frequencies, avoiding the complexity of accurately machining corrugations at the throat of the horn without compromising the performance. The integrity of the feed horn performance was verified directly by measuring the beam patterns, demonstrating excellent performance across 100 GHz which is sufficiently wide for typical astronomical window.

I believe that the work in this thesis has made important contributions to the design of SIS mixers and has developed key technologies that make the fabrication of SIS receivers substantially easier without compromising high performance. All proposed design simulations and new technologies were verified by extensive experimental testing. This will hopefully pave the way for the fabrication of large mixer arrays and extending the operation of SIS mixer above 1 THz.

Oxford, UK Ghassan Yassin
August 2015

Preface

This thesis describes the works completed in the duration of my doctorate study at the Department of Physics (Astrophysics) of the University of Oxford for the fulfilment of the D.Phil. degree requirements. Following from the general discussions about the millimetre and the sub-millimetre astronomy in Chap. 1, I describe a new type of feed horn in Chap. 2 that has high performance similar to the conventional corrugated horn, and yet is much easier to fabricate. This is followed by several chapters focusing on SIS mixers, starting with Chap. 3 which describes the fundamentals of SIS mixer theory and the experimental techniques used to assess the performance of the newly designed mixers. Chapter 4 presents the details of new SIS mixer designs, which is a central theme in this thesis, while Chap. 5 reports the measured performance of these mixers together with performance analysis. Chapter 6 describes the design and measured performances of the single-chip balanced SIS mixers at 700 GHz integrated onto an SOI (Silicon-on-Insulator) substrate, and Chap. 7 describes the design of integrated single sideband mixers such as sideband separating and balanced with sideband separating SIS mixers. In Chap. 8, I present two interesting features of the SIS mixers, namely the effect of heating in SIS tunnel junctions by the tunnelling currents, and the effect of Josephson currents on the sensitivity of SIS mixers near 700 GHz. In Chap. 9, I discuss an alternative method of generating LO power using infrared lasers, and finally in Chap. 10, I present our work on astronomical observations of ^{12}CO $J = 3 \rightarrow 2$ emission line from two nearby galaxies, NGC 2976 and NGC 3351.

After the completion of the thesis, I have continued some of the work presented in this thesis and run several more experiments and analysis. Hence, several chapters in the current version of the thesis have been updated to reflect the progress of the subjects. The main body of the thesis however remains largely similar to the version submitted to the University of Oxford for the D.Phil. degree, except for these additional materials. It is therefore no longer fully compliant to the length requirement of the University.

During this post-doctoral period, I have also been engaged in several other new topics such as the development of high frequency supra-THz mixers, the construction of superconducting phase switches and the development of multi-pixel SIS mixer arrays. Therefore, I would like to take this opportunity to update the reader with some recent developments, especially in the area of millimetre and sub-millimetre detector technologies.

Recent Developments

Since the submission of the thesis, the field of millimetre and sub-millimetre astronomical instrumentations has moved on considerably. Atacama Large Millimetre/sub-millimetre Array (ALMA) is now fully operational and is performing routine observations for the ALMA Early Science Cycle Two science cases. It has since then produced impressive results with unprecedented sensitivity, albeit with only four receiver bands fully deployed to its 34 (out of the planned 54) 12-m antennas and 9 (out of the planned 12) 7-m compact array antenna currently installed on the Chajnantor site. Further development works are still ongoing to install the remaining antennas, and to commission new receiver bands. There is strong interest within the ALMA scientific community to extend the capability of ALMA beyond 1 THz limit as well. Apart from the ALMA observatory, several other millimetre and sub-millimetre instruments have also entered their routine observation phase now, such as the airborne Stratospheric Observatory for Infrared Astronomy (SOFIA) observatory, the Balloon-borne Large Aperture Sub-millimeter Telescope (BLAST) and the Atacama Pathfinder EXperiment (APEX). A new millimetre and sub-millimetre observatory, the Green Land Telescope (GLT), has also been undertaken by the Academia Sinica Institute of Astronomy and Astrophysics (ASIAA), the Smithsonian Astrophysical Observatory (SAO), the MIT Haystack Observatory and the National Radio Astronomy Observatory (NRAO), to perform state-of-the-art THz observation at the peak of the Greenland ice sheet, complementing the scientific capability of the ALMA array in the southern hemisphere.

Apart from the ground-based and airborne experiments, the Herschel Space Telescope has now completed its mission and produced vast amount of state-of-the-art data and results. The millimetre and sub-millimetre instrumentation community has recently been focusing their effort on constructing new space telescopes such as SPICA (Space Infra-Red Telescope for Cosmology and Astrophysics telescope) and the Millimetron. FIRSPEX (Far-Infrared Spectroscopic Explorer), a small satellite mission has also been proposed jointly by the European Space Agency (ESA) and the Chinese Academy of Sciences (CAS) to perform an unbiased all sky spectroscopic survey between 0.69–1.9 THz with high spectral resolution. It consists of four heterodyne detection bands, targeting at the key molecular and atomic transitions near the 1 THz frequency range, and will be stationed along the Low Earth Orbit (LEO) when launched in 2021.

The extensive works on the detection of B-polarisation mode of the Cosmic Microwave Background (CMB) by the BICEP2 (Background Imaging of Cosmic Extragalactic Polarization 2) and the Keck Array, along with the impressive observational results from the Planck satellite mission have drawn attention from the worldwide scientific community to push for even more sensitive experiments to be performed. Most of these B-mode CMB experiments, including the POLARBEAR experiment mounted on the Huan Tran Telescope (HTT) and SPIDER (a balloon-borne polarimeter), incorporate a number of Transition Edge Sensor (TES) bolometer array in the focal plane to achieve ultra-sensitive polarisation signal detection. In order to achieve the unprecedented sensitivity required to successfully detect the B-mode CMB, the TES community have since then been focusing their effort on improving the optical coupling efficiency and increasing the transition temperature of the TES, along with the even more compact bolometer array design. It is well known, however, that TES detectors require complicated SQUID (Superconducting QUantum Interference Device) readout and suffer from low saturation power. Therefore, in the past few years, the development of the Kinetic Inductance Detectors (KIDs) that needs only a very simple readout system based on the frequency multiplexing superconducting resonant circuits at microwave frequencies has begun to gain traction. It has been piloted on several currently planned CMB experiments such as BLAST-TNG (The Next Generation) and there are programmes initiated recently to investigate their suitability to be deployed on balloon-borne and space-based instruments.

Another exciting new development in the millimetre and sub-millimetre detector area recently is the fast growing interest in the development of parametric amplifiers as ultra low noise detectors, especially the travelling wave kinetic inductance based parametric amplifiers developed at the California Institute of Technology (CalTech). Theoretically, a superconducting parametric amplifier can be configured to only half a quantum of noise to the incoming signal via a technique called noise squeezing. These sub-quantum limited amplifiers can be configured, if developed successfully, to be used as the first stage low noise amplifier for high frequency heterodyne receivers and readout for quantum computing experiment, or potentially as the front end detectors of a radiometer at sub-millimetre wavelength.

For heterodyne receivers at high THz region (2–5 THz), considerable research efforts have been invested in enhancing the intermediate frequency (IF) bandwidth of the hot electron bolometers (HEBs). Recent results from several groups in the Europe and United States of America have shown encouraging improvements in the IF bandwidth performance of the HEB detectors, with the indication that HEB detectors with several GHz (3–4 GHz) of IF bandwidth is possible. Nevertheless, this is still much narrower compared to the IF bandwidth achievable by the SIS receivers. Although the performance of SIS mixers is superior below and near the superconducting gap of niobium ($\sim$680 GHz), there is still much room for improvement. Two major areas currently pursued in the SIS mixer community are the development of SIS mixers near and above 1 THz, and construction of multi-pixel SIS mixer array at 200–900 GHz regime.

Supra-THz SIS Mixer

The sub-millimetre wave spectrum is rich in spectral lines which hold the key to understanding the chemical and kinematical structure of the cold interstellar medium (ISM). Two of the most important calling lines in our own and external galaxies above 1 THz are the [CII] (158 μm) and [NII] (205 μm) fine-structure lines. High resolution observations of these lines in the frequency range 1.0–1.5 THz, corresponding to the intermediate redshift range $0.5 < z < 1$ (approximately 6–9 Gyr after the Big Bang), will reveal vital information about the way in which galaxies form and evolve. This part of the THz spectrum is also rich in high-*J* transitions of the carbon monoxide (CO) ladder, that could provide valuable information about the temperature, density and other properties of interstellar gas. Combining these observations with the low-*J* transitions at sub-THz regime will allow the astronomers to probe the dust opacity of the surrounding ISM.

Many of the sub-millimetre observatories discussed earlier will be suited for observations above 1 THz, as they generally have superior main reflector specifications with surface profile sufficient for supra-THz operation and are either sited at high and dry environment or are stationed above the Earth's atmosphere. For example, the CO N+ Deuterium Observations Receiver (CONDOR) on the APEX 12 m telescope at the ALMA site in Chile with an elevation of 5050 m, was design to perform observations at these supra-THz frequencies. Even higher at 5525 m elevation on Sairecabur, the Smithsonian 80 cm Receiver Lab Telescope (RLT) has receivers for frequencies up to 1.5 THz, and the planned 25 m Cerro Chajnantor Atacama Telescope (CCAT) telescope at 5600 m on Cerro Chajnantor should have the dish that is able to operate at these frequencies as well.

Apart from the large single-dish telescope, ALMA as an interferometer can also be configured to operate above 1 THz. A new receiver cartridge covering the frequency range from 1.0–1.6 THz for ALMA, known as Band 11, has been proposed and has generated considerable interest from the sub-millimetre astronomy community. Interferometry with ALMA offers two distinct advantages over single-dish telescopes: First, even ALMA's most compact configuration would yield a resolution better than 0.4 arcsec at 1.3 THz; second, interferometric observations allow deep integration to faint flux levels even in the presence of atmospheric fluctuations. The combination of a wide-field THz focal-plane array on large single-dish telescope, and a narrow-field high-angular resolution THz receiver system on ALMA would therefore create a powerful observing capability.

The technological development for constructing a supra-THz receiver, however, is challenging. The key receiver components needed are high-gap SIS tunnel junctions, complete low-noise SIS mixer chips with low-loss transmission line, high performance feed horns and THz local oscillator (LO) sources. Nevertheless, the prospects are realistic as a consequence of some recent technical advances in new superconducting materials for SIS junction fabrication, such as niobium titanium nitride (NbTiN) and niobium nitride (NbN), and great improvements in mechanical and lithographic micro-machining techniques.

One of the main challenge in this aspect is to fabricate high quality SIS tunnel junctions using a high-gap superconductor. The quantum-limited performance of SIS mixers is restricted to frequencies below the superconducting energy gap of the superconductor. For niobium (Nb), the material used routinely for most of SIS receivers to date, this restriction implies an effective upper frequency limit of about 0.68 THz. Above this frequency, the superconductor starts to become lossy due to the breaking of Cooper pairs and the RF loss in the superconducting planar transmission lines increases substantially. This results in a rapid rise in the mixer noise temperature. Therefore, to operate at frequencies in the supra-THz region, higher gap superconductors are needed. Two of the most studied materials are the niobium titanium nitride and niobium nitride which have gap energies of about 5.0 mV and 5.8 mV ($\sim$1.2 THz and $\sim$1.4 THz), respectively. The development of these materials for use as SIS mixers, although progressing, is very challenging and critical fabrication steps still need to be overcame. For example, it is difficult to fabricate high current density NbN junctions. However, complex thin film deposition processes associated with the fabrication of high-gap SIS devices are becoming better understood and are more effectively controlled now, and therefore show considerable promise for use as supra-THz detectors. The use of a combination of superconducting materials to alleviate the fabrication difficulties has shown to be a promising step towards pushing the SIS technology into the supra-THz region, but much more work is needed to explore this option.

Receiver performance does not, however, depend solely on the tunnel junction. For instance, a substantial improvement in sensitivity can be obtained by employing on-chip balanced and single-sideband mixers, which reduce noise from the LO and atmosphere respectively, and promote system stability. In addition, above 1 THz the noise contribution from waveguide and optical losses increases due to the skin effect. Care must be taken with regard to the design of the mixer embedding structure, including the coupling antenna, or feed horn, and beam-forming optics. Nevertheless, development techniques are improving and the use of high-precision electron-beam lithography in the fabrication of the SIS mixer circuits, state-of-the-art mechanical fabrication facilities, and most importantly the fabrication of planar transmission lines from low-loss superconducting materials, could provide enhanced performance. For example, fabricating thin-film transmission lines from NbN whilst maintaining the use of Nb tunnel junctions has shown to produce a substantial improvement in mixer noise temperature. Above 1 THz, it also becomes more pressing to have sufficient LO power. Hence it is critical that appropriate LO technology is available. An SIS mixer cannot operate without an LO source, and it is desirable that close integration of the LO source with the mixer is undertaken in order to minimise LO signal-power loss, maximise LO tuning range and ensure good overall system stability.

Sub-Millimetre Heterodyne Focal-Plane Array Receivers

Although ALMA has a near quantum-limited sensitivity with the use of niobium-based SIS mixer as front-end detector, a heterodyne focal-plane array with significant number of elements will undoubtedly increase ALMA's current mapping speed at these frequencies. For example, replacing the current single-pixel Band 9 or 10 receiver with a 2 × 2 compact mixer array will immediately quadruple the output of Band 9 and 10 science. The deployment of tens or even hundreds of pixel on to a compact focal-plane array will certainly be beneficial to large single-dish telescope such as APEX and the upcoming CCAT as well. This would provide the ability to map large scale structures and deliver the essential survey science needed in the era of ALMA, and induce a transformational change in the sub-millimetre astronomy similar to the revolution experienced in the infrared and radio astronomy many years ago. Considerable research efforts have thereforebeen invested in the recent years aiming at developing the underpinning technologies that would enable the construction of such high frequency large format focal-plane array.

There are a variety of technical challenges that are unique to heterodyne multi-pixel systems. In a generic single-pixel heterodyne receiver, the RF signal and the LO power are fed to the mixer chip through the cryostat window via the mixer feed horn and the Intermediate Frequency (IF) signal is extracted from the output of a high performance cryogenics amplifier following the mixer. In principle, a heterodyne array is an *N* channel of these signal chains packed in a tight configuration, but a practical array receiver will need to have an easy-to-fabricate large array of high performance feeds and mixer block with wide RF bandwidth, reproducible, easy to fabricate and easy to mount mixer chip, simple mechanism for suppression of Josephson tunnelling in a large number of detector chips, and a compact LO injection scheme that would fully harness all the available LO power.

There exist a variety of methods pursued by different groups in the community to address these challenges. One such scheme proposed based on the works here at the University of Oxford is to utilise the highly array-able multiple flare-angle smooth-walled horn and planar on-chip circuit integration technology to construct such focal-plane array. As shown in this thesis, the multiple flare-angle smooth-walled horn's performance is similar to that of a corrugated horn and yet much easier and cheaper to fabricate. They can be fabricated rapidly by milling directly into a block of aluminium plate using a profiled-tool. Utilising these horns will reduce significantly the cost and time required to construct a heterodyne array.

The back-to-back planar on-chip balanced SIS mixer architecture presented in this thesis will also be highly viable for construction of such medium/large format array. These balanced mixers were fabricated on a 15 μm SOI substrate with fully integrated circuits fabricated on-chip using minimum photo-lithography steps. The mixer chip is so light that it can be supported by gold beam leads, avoiding the need of dicing and bonding with thin wires when the chip is mounted in the waveguide, thus simplifying the handling process significantly. Since all the required

superconducting circuits are integrated on-chip, it only requires a very simple mixer block structure, which is crucial for making large format SIS mixer arrays feasible.

The major advantage of a back-to-back balanced SIS mixer over single-ended mixer is its ability to improve the instrument stability, reject the LO sideband noise and make full use of the available LO power. This is especially important for high frequency mixers where the available LO power is often limited, and the need to feed an array of mixers with a minimal number of LO sources. The back-to-back architecture allows the RF and LO signal to be injected into the mixer chip from either side of the mixer chip, eliminating the use of a beam splitter. This further reduces the losses in the RF path, simplifies the RF/LO feeding mechanism, hence reduces significantly the physical size of the array and ensures a compact mixer array design.

Final Remarks

The work presented in this thesis describes the design and fabrication of various components required for constructing a heterodyne SIS mixers at the high sub-millimetre frequency range. These precursor works would hopefully pave the way to develop high density compact SIS mixer array and extend their applications above 1 THz. These high frequency SIS mixers, both single- and double-ended mixer chip designs, were fabricated using the recently developed silicon-on-insulator technology with beam lead electrodes. This SOI technology uses an inverted-etch process, resulting in very thin, as thin as 5 μm silicon substrates, simplifies the waveguide embedding structure and the mechanical arrangement. We believe that the SOI technology will be crucial to supra-THz mixer development, as all the mixer circuit components required can be fabricated onto a single mixer chip, avoiding the use of complicated mechanical machining. This does not only reduce the size of the mixer block and ancillary mechanical components needed to construct a complete heterodyne receiver, but it also relaxes the tolerance requirement on the machining blocks, which become critically difficult above 1 THz. The design and fabrication of a novel smooth-walled horn above 1 THz has also been demonstrated successfully, and recently, they have been employed to construct focal-plane array for many heterodyne and bolometric receivers even up to 1.5 THz. This and the single-chip SIS mixer technology will ensure repeatability in producing high quality heterodyne system, and promote their operations in the supra-THz frequency regime.

Abstract

Superconductor-Insulator-Superconductor (SIS) mixers are now used regularly in sub-millimetre astronomical receivers. They have already achieved sensitivity approaching the quantum limit at frequencies below the superconducting gap of niobium ($\sim$680 GHz). Above that, the mixer performance is compromised by losses, unless materials with higher superconducting gap are employed in conjunction with the niobium tunnel junction. In this thesis, we present the development of 700 GHz niobium SIS mixers, employing a unilateral finline taper on a thin Silicon-On-Insulator (SOI) substrate. These mixers are broadband with full on-chip planar circuit integration, and require only a very simple mixer block. They were designed using rigorous 3-D electromagnetic simulator (HFSS), in conjunction with a quantum mixing software package (SuperMix), and have demonstrated good performance with the best noise temperature measured at 143 K. Our mixer devices were fed by multiple flare angle smooth-walled horns, which are easy to fabricate, yet retain the high performance of corrugated horns. The radiation patterns measured from 600–740 GHz have shown good beam circularity, low sidelobe and cross-polarisation levels.

In this thesis, we also present SIS mixer designs with balanced and sideband separating capability. These mixers employ back-to-back finline tapers, so that the RF and local oscillator (LO) signals can be injected separately without a beam splitter. We have fabricated and tested the performance of the balanced mixers, and analysed their performance thoroughly. We have also investigated a new method of generating LO signals by beating the tones of two infrared lasers.

Using the current 16-pixel 350 GHz SIS receiver, HARP-B, we have observed the ^{12}CO $J = 3 \rightarrow 2$ emission lines from two nearby galaxies. An important result we found is that the ^{12}CO $J = 3 \rightarrow 2$ correlates strongly with the 8 μm Polycyclic Aromatic Hydrocarbon emission.

Acknowledgments

This thesis would not be possible to reach fruition without help from so many remarkable people. First and foremost, I owe my deepest gratitude to my sifu, Ghassan Yassin, who as a mentor and a friend, spent so much time and effort guiding me. I am especially grateful for his academic advices, financial support and teachings from which I have been benefited greatly. It has been an enjoyable time working with Ghassan, who is kind, determined and has strong opinions on just about everything but still allowed me to explore freely new ideas and topics (except rigorous grammars). I am also enormously grateful to Dimitra Rigoupoulou, Peter Huggard and Brian Ellison and for their patience and guidances on the astronomy and photonic LO chapters. I am indebted to Rakyat Malaysia, particularly to the Royal Family of Malaysia for the award of King's Scholarship, without which I would not be here at Oxford pursuing a doctorate degree. I would also like to convey my personal gratitude towards Tham Choy Yoong, who had always been supportive and inspired me to pursue a greater dream that was almost out of reach.

Now I must thank all my colleagues here in Oxford Astrophysics: Jamie Leech, a great friend, for unstintingly sharing his great knowledge on just about everything (and alcohol); Paul Grimes, who has taught me a lot about the mixer works; Rik Elliot, who deserves a special thanks for all his helps in setting up the test system; Paul Pattingson, Mike Tacon and his team in the mechanical workshop; Martin Bureau, my college adviser; Stafford Withington for lending us one of the system setup; Chris Groppi for manufacturing the mixer blocks; Karl Jacobs for mixer fabrications; NGLS team; a special thanks to Ashling Morris and Vanessa Ferraro-Wood for all their fantastic supports; and all my friends here whom I have had a great time with.

Finally, my brothers and above all, my lovely Mom, for her unconditional loves, supports, trusts and understandings, and to my Dad, "I've made it, Dad!".

Contents

Chapter 1
Introduction

One of the most exciting developments in science after the War is the emergence of radio astronomy. Radio astronomers exploited the newly developed high-speed computers, radar and radio communication technologies, to invent new techniques such as radio interferometry, to achieve high angular resolution observations. These developments have resulted in many key discoveries, including the Cosmic Microwave Background (CMB), quasar and interstellar gas, setting the scene for understanding astrophysical and cosmological problems.

The advancement of techniques developed for radio astronomy to work at higher and higher frequencies, enhanced the interest in studying astronomy in the millimetre (mm) and sub-millimetre (sub-mm) wavebands. Although impressive observations at centimetre and radio wavelengths have made progress and important discoveries over an extended period, the arrival of sub-mm astronomy needed to await for the development of new types of heterodyne detectors. A major breakthrough was made when the quantum mixing based on Superconductor-Insulator-Superconductor (SIS) detectors was invented during the 1980s, giving a substantial improvement in the sensitivity of receivers at these frequencies. This, together with the ever improving technology in cryogenics, fabrication, machining and electronics, have made possible the construction of a new generation of millimetre and sub-mm heterodyne receivers with unprecedented sensitivity. New millimetre and sub-mm telescopes were built at high and dry sites enabling, for the first time, astronomical observations from about 100 GHz to 1 THz.

A high performance sub-mm telescope relies on a number of key components, in particular highly sensitive detectors, since the astronomical signals from the sky are extremely weak. In this thesis, we describe our contributions to develop technologies for sub-mm instrumentation. These include the development of coherent detectors, and also work on front end feeds and local oscillators, which form an integral part of a coherent receiver system. In the last part of the thesis, we present astronomical observations of nearby galaxies that we have made at sub-mm wavelengths and the resulting scientific achievements. These observations were undertaken using the existing sub-mm receiver HARP-B (Heterodyne Array Receiver Project) on the

B.-K. Tan, *Development of Coherent Detector Technologies for Sub-Millimetre Wave Astronomy Observations*, Springer Theses, DOI 10.1007/978-3-319-19363-2_1

world's largest single-dish sub-mm telescope, the JCMT (James Clerk Maxwell Telescope).

In what follows, we shall briefly review the background of sub-mm astronomy, followed by a brief description of selected sub-mm telescopes, with emphasis on the concept of the heterodyne receiver and the use of SIS tunnel junctions as coherent detectors.

1.1 Sub-Millimetre Astronomy

Almost half of the energy generated by the visible stars and galaxies is absorbed by the surrounding dust and re-emitted at far-infrared and sub-mm frequencies. A unique feature of sub-mm observation is that the interstellar dust that obscuring many interesting sites becomes transparent in this range (at certain frequencies), especially around the dense molecular clouds which are the birth chambers of protostars. Direct observation into these dense cores offers valuable information of how these giant molecular clouds (GMCs), typically having masses about $10^6 M_\odot$, form stars and planetary systems (e.g., Shu et al. 1987). These local universe objects are normally composed of cool matters at around 10–100 K, with their blackbody radiation peaking in the sub-mm and far-infrared regions. The background in Fig. 1.1 is an example of the composite sub-mm images taken by the Herschel Space Telescope of the Orion

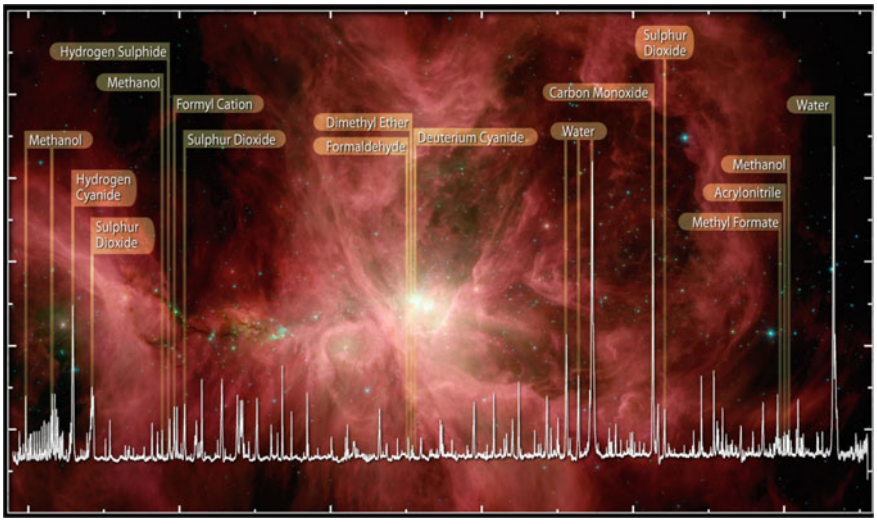

Fig. 1.1 Example of image taken in sub-mm region, and the wealth of spectral lines available in this region (480 GHz–2 THz). This European Space Agency (ESA) public released image was downloaded from `http://herschel.cf.ac.uk` (hosted by Cardiff University), in courtesy of UK Herschel team

Nebula showing clusters of hot, bright young stars warming up the surrounding gas and dust.

The main constituent of these molecular clouds and the surrounding interstellar medium (ISM) is molecular hydrogen (H_2), which fuels star formation but does not emit strongly due to a lack of a permanent dipole moment. However, mm and sub-mm wavebands contain more than a thousand spectral lines from different interstellar and circumstellar molecule species (see for example Fig. 1.1) that allow us to trace physical conditions such as density, temperature and dynamics of these clouds. The most important of these are the strong rotational ladder lines from carbon monoxide (CO) molecules, first observed by Wilson et al. (1970). CO being the second most abundant molecules in ISM after H_2, posses electric dipole transitions between neighbouring rotational states, which emit strongly in the millimetre and sub-mm region, for example ^{12}CO $J = 3 \rightarrow 2$ at 350 GHz and ^{12}CO $J = 6 \rightarrow 5$ at 690 GHz. Therefore, CO has always been used as a tracer for understanding the distribution and physical states of molecular hydrogen clouds, allowing us to study even violent processes such as inflow and outflow of gas (e.g., Parker et al. 1991; Richer et al. 1992) and bipolar outflows of matter during star formation (e.g., Richer et al. 2000). As shall be seen in Chap. 10, correlating these ^{12}CO emission lines with observations at other wavelengths also helps to construct star formation models and provides information to further understand the galaxy formation process at a larger scale.

Interstellar molecules undergo a series of complex chemical phases, from collapse of dense cloud forming young star to ejection of materials after star formation. High resolution spectroscopic mappings of CO and other atomic/molecular species therefore allow us to explore the physical and chemical properties of the interstellar gas, which is essential for understanding how the initial conditions of the gas incorporated into the GMCs that form stars. Following these composition changes and the chemistry taking place in the ISM and GMCs as they cycle through different phases, provide us with a valuable diagnostic tool to understand the chemical evolution and further constrains the physical models of the ISM and GMCs. As well as this spectroscopic information, broadband continuum observations of cold interstellar dust (<100 K) also provide clues as to the cooling mechanisms which promote condensation of these gaseous molecules to form protostars.

In recent years, astronomical interest has shifted towards the terahertz (THz) regime, which is relatively unexplored. This region is of particular importance for extra-galactic observations and a large population of highly redshifted (high-z) sub-mm galaxies have been uncovered by SCUBA (Sub-millimetre Common User Bolometer Array) of the JCMT and the Herschel Space Telescope. Studies of these high-z objects, such as ultra luminous galaxies (e.g., Solomon et al. 1992), and the highly redshifted spectra of atomic species like CII and NII, allow us to understand star and galaxy formation at these early epochs. Emissions from the CO transition ladders would also be compressed in frequency for high-z sources, by a ratio of $1+z$, allowing simultaneous observation of several CO lines within one spectral band. All these observations could provide important links between the local universe and the very early universe ($z > 10$), to construct an overview of the evolution of the entire universe.

1.2 Sub-Millimetre Telescopes

There are two main categories of sub-mm telescopes, ground based large sub-mm facilities and space or air-borne sub-mm telescopesair-borne sub-mm telescopes. Ground based sub-mm observations are restricted by poor atmospheric transmission. Large amounts of water vapour and other constituents in the atmosphere absorb strongly at certain sub-mm frequencies, rendering the atmosphere opaque and virtually unusable for any meaningful science at these frequencies. Consequently, only high sites with extremely dry and stable conditions are suitable for sub-mm observations, and even then, high transmission is only possible at certain frequency bands. The most recent, is the Llano de Chajnantor plateau at the Atacama desert in Chile, whose atmospheric transmission windows are shown in Fig. 1.2. It can be seen that even at one of the best sites in the world, only certain frequency bands have good transmission. Above 1 THz, the transmission becomes poor, hence observations of spectral lines above 1 THz from ground is very challenging (Marrone et al. 2005; Wiedner et al. 2006). Ground based sub-mm telescopes can be constructed as a large single dish telescope or an interferometer that combines several antennas to achieve higher spatial resolutions and reduce the impact of atmospheric fluctuations. Table 1.1 shows examples of some of the existing and future sub-mm telescopes.

The major advantage of space and air-borne sub-mm telescopes is that they can access the frequency ranges that are blocked by the Earth's atmosphere. However, space telescope are costly, inflexible and has a limited lifetime and collecting area. Telescopes on board of high altitude flying aircrafts or balloons offer another alternative for sub-mm observations, free from atmospheric contamination. They also allow rapid replacement of new instruments, but they are normally limited to short term observations and have relatively small collecting area too. These difficulties in observing imposed by the atmosphere imply that observation time on both

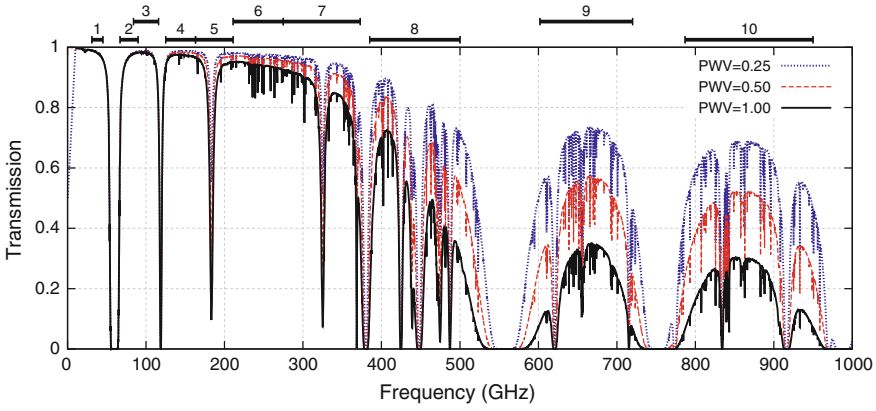

Fig. 1.2 Atmospheric transmission window at Llano de Chajnantor, Chile, at the altitude of 5040 m. Downloaded from http://almascience.eso.org

Table 1.1 Examples of existing and currently built/planned large sub-mm telescopes

Ground based telescope	
Single dish	Interferometer
15 m JCMT (James Clerk Maxwell Telescope)	SMA (Sub-Millimetre Array)
10 m CSO (Caltech Submillimetre Observatory)	ALMA (Atacama Large Millimetre/Sub-millimetre Array)
15 m SMT (SubMillimetre Telescope)	
25 m CCAT (Cerro Chajnantor Atacama Telescope)	
Space borne telescope	
Space telescope	High altitude aircraft/balloons
Herschel Space Telescope	Kuiper Airborne Observatory
SPICA (Space Infra-Red Telescope for Cosmology and Astrophysics telescope)	BLAST (Balloon-borne Large Aperture Sub-millimeter Telescope)
	SOFIA (Stratospheric Observatory for Infrared Astronomy)

Earth-based and space/air-borne telescopes is precious and restricted, highlighting the need for the quantum limited sensitivity of sub-mm detectors.

1.2.1 ALMA

The current generation of millimetre and sub-mm astronomers will see the arrival of ALMA (Atacama Large Millimetre/submillimetre Array), which upon completion, will almost certainly dominate millimetre and sub-mm astronomy for the next 20–30 years. It is one of the largest ground based astronomical facilities ever built, comprising 66 antennas (54 of 12 m and 12 of 7 m diameter dish) with baselines up to 15 km and a total collecting area of approximately 7,000 m^2. It is located on top of the 5000 m altitude Llano de Atacama in Chile, an exceptionally dry and high site with a median precipitate water vapour content in the atmosphere of only about 1 mm. In addition, Llano de Atacama has a flat and wide topography that is very suitable for accommodating the large area required for the ALMA interferometer. The telescope itself will have an angular resolution of $0.2''$ in its most compact configuration, almost a factor of 10 times better than the Hubble Space Telescope. ALMA was designed to operate in 10 wavebands, defined by the atmospheric windows, spanning the 30–950 GHz range, as shown in Table 1.2, with dual polarization capability at all bands. Some of the channels are also capable of sideband separating operation.

The ALMA front-end receivers architecture is unique in the sense that it has adopted a modular cartridge-type receiver concept. Each cartridge itself is a self-contained receiver of a specific ALMA band, equipped with all the required components, such as the cooled optics and detector units etc. Each individual ALMA antenna will therefore have a front-end cabin that would assemble all the 10 cartridges

Table 1.2 The 10 frequency bands of ALMA

Band	Frequency range (GHz)	Target receiver noise temperature (K)		Detector technology
		80 % RF band	At any RF frequency	
1	31–45	17	26	HEMT[a]
2	67–90	30	47	HEMT
3*	84–116	37	60	SIS
4	125–163	51	82	SIS
5	162–211	65	105	SIS
6*	211–275	83	136	SIS
7*	275–373	147	219	SIS
8	385–500	196	292	SIS
9*	602–720	175	261	SIS
10	787–950	230	344	SIS

Notes
*Selected for initial phase of operations
[a]High electron mobility transistor

from all 10 bands, forming a compact independent receiver unit. Since each band cartridge has a compatible pre-designed interface with the front-end cabin, their designs and constructions could be distributed amongst different groups, allowing parallel mass production. In the initial operation phase, only four cartridge bands have been selected (see Table 1.2), where the subsequent bands will be installed progressively after an initial commissioning phase. In recent years, there has been growing interest in pushing the upper frequency limit of ALMA above the THz frequency, forming the ALMA band 11, which is expected to cover the 1.0–1.6 THz range.

1.3 Sub-Millimetre Wave Detection

There are two modes of detection in the sub-mm waveband: coherent (heterodyne) and incoherent (direct) detection. Direct detection in the sub-mm regime often makes use of the change in the detector's resistance due to the thermometric effect caused by the incident photons, hence they are normally called bolometers. They are sensitive to total incident power and are used mainly for broadband continuum observation, but they lack the ability to preserve phase information. Sub-mm coherent detectors are used for their ability to preserve both phase and amplitude information. One such coherent detector is the SIS mixer which utilises a highly nonlinear device to down-convert sub-mm astronomical signals to lower frequencies for subsequent processing. They are the main detectors in the modern high resolution sub-mm interferometers.

1.3.1 SIS Junctions as Heterodyne Mixers

The SIS tunnel junctions are by far the most popular choice for sub-mm coherent detectors due to the superior sensitivity and the stable operation they offer. Consequently, they have been routinely used in sub-mm spectroscopic astronomy below 1 THz. In fact, 8 out of the 10 operating bands of ALMA will use SIS junctions (the other two are below 100 GHz as shown in Table 1.2). The SIS tunnel junction consists of two thin superconducting films, separated by a very thin (∼10–20 Å) insulating barrier. They are capable of both direct and coherent detection, but are mainly used for the latter.

The operation of SIS mixers will be discussed in details in Chap. 3, but in principle, an SIS tunnel junction detection utilises the photon-assisted quantum tunnelling of quasiparticles across the thin insulating barrier to achieve highly nonlinear current-voltage (IV) curve. This is a mechanism where Cooper pairs in a superconductor below its transition temperature are broken to form quasiparticles through absorption of external radiation with energy $nh\upsilon + eV_b > eV_{gap}$, where n is the integer representing the number of photon absorbed, h is the Planck's constant, υ is the frequency of the photon, V_b is the bias voltage applied across the SIS junction, e is the electron charge and eV_{gap} is the binding energy of the two electrons forming the Cooper pair. Superconductors have V_{gap} of the order of several meV, and therefore are sensitive to millimetre and sub-mm wavelength radiation. The most commonly used superconductor in SIS mixer, niobium (Nb), have a transition temperature of about 9 K and an energy gap of about 2.8 meV, which translate to about 680 GHz.

Above the gap frequency, the superconductor starts to become lossy due to the breaking of Cooper pairs, although the SIS junction can still in principle be used as a mixer up to double the gap frequency (see Chap. 3). Therefore, to operate at frequencies in the supra-terahertz region, higher gap superconductors are needed. Two of the most studied materials are the niobium titanium nitride (NbTiN) and niobium nitride (NbN) which have could potentially have V_{gap} energies of about 5.0 and 5.8 mV (∼1.2 THz and ∼1.4 THz), respectively. However, the use of these materials as SIS devices is still to be achieved due to the fabrication difficulties. For example, it is difficult to fabricate high current density NbN junctions and the existence of pinholes in their barrier degrades the performance of the SIS mixer (Kawamura et al. 1999). Successful operation of SIS mixers above 1 THz has nevertheless been achieved by using tunnel junctions with electrodes comprising Nb and NbTiN (Karpov et al. 2007).

1.3.2 SIS Heterodyne Receivers

The heterodyne technique was invented by Reginald Fessenden in 1901 (Cooper 2001), where two frequency components are combined (mixed) to generate a new lower frequency component while preserving the phase information of the original frequencies. These two frequencies are normally referred to as the RF (radio

frequency) and the LO (local oscillator) frequencies, while the newly generated signal is named the IF (intermediate frequency).

The concept of heterodyne detection can be explained by considering two sinusoidal voltages $V_{RF} \sin \omega_{RF} t$ and $V_{LO} \sin \omega_{LO} t$ impinged on a nonlinear device that has an output current proportional to the square of the applied voltage. The response of the device can thus be written as

$$\begin{aligned} I(\omega) &= (V_b + V_{RF} \sin \omega_{RF} t + V_{LO} \sin \omega_{LO} t)^2 \\ &\approx \frac{V_{RF}^2}{2} + \frac{V_{LO}^2}{2} + V_b^2 + V_{RF} V_{LO} \cos(\omega_{LO} - \omega_{RF})t - V_{RF} V_{LO} \cos(\omega_{LO} + \omega_{RF})t + \cdots , \end{aligned} \tag{1.1}$$

where V_b is the DC bias point of the mixer. One can see clearly that after mixing, the signal voltage V_{RF} generates currents flowing at the IF frequency $\omega_{IF} = |\omega_{LO} - \omega_{RF}|$ and various other frequencies. The unwanted harmonics are usually filtered out using suitable filters, or naturally by the intrinsic capacitance of the SIS junction. One advantage of a heterodyne system is that a broad RF spectrum can be resolved by simply varying the LO frequency, while retaining the same back end electronics for the IF frequency processing. This method of transferring the amplitude and spectral information at the RF frequencies (several hundred GHz) to lower IF frequencies (a few GHz) is necessary at sub-mm frequency, because it enables an extremely weak signal from an astronomical source to be down-converted for further amplifications, since low noise amplifiers operating at several hundred of GHz are extremely difficult to construct and conduction losses at sub-mm frequencies are very high.

An SIS mixer is sensitive to all RF signals shifted by $\pm\omega_{IF}$ at both sides of the LO frequency ($\omega_{RF} = \omega_{LO} \pm \omega_{IF}$), as shown in Fig. 1.3a. The RF frequency band that contains the sought astronomical signals is known as the signal sideband, while the other sideband that usually contributes only to noise is known as the image sideband. These two sidebands are sometimes referred to as upper (USB) and lower sideband (LSB), depending on its position with reference to the LO frequency. A double sideband (DSB) SIS mixer converts both sidebands with equal sensitivity, hence both USB and LSB will be folded onto the same IF band. To reduce the noise contribution from the mixer, it is often desirable to reject or separate the image sideband since it may not contain useful information. These mixers are known as single sideband (SSB) SIS mixers.

Figure 1.3b illustrates the main components comprising an SIS heterodyne receiver. It consists of four main parts: the local oscillator, the input antenna (feed) coupling the astronomical and LO signal to the mixer chip, the SIS mixer itself, and the low-noise amplifier (LNA) with the associate IF electronics. Apart from the LO and the room temperature IF electronics, this entire assembly is cooled to well below the transition temperature of the tunnel junction material to make the junction operate as a highly nonlinear device. It should be noted however that the performance of a heterodyne receiver does not only depend on the quality of the mixer itself, but also relies critically on other components, especially the front end optics and the IF amplifier. These components need to be designed and optimised properly to realise a quantum limited SIS receiver.

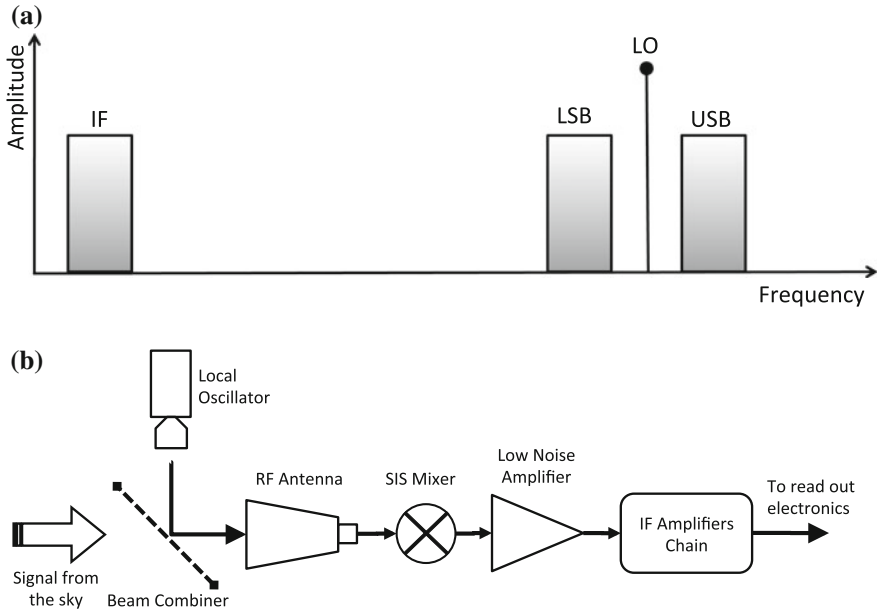

Fig. 1.3 Diagrams illustrating frequency down-conversion using a heterodyne receiver system. **a** Frequency down conversion, **b** architecture of a heterodyne receiver

1.3.3 Mixer Feeds

The main function of the front end optics of a heterodyne receiver is to couple the signal from free space into the mixer with maximum efficiency. Sub-mm mixers can be classified into two main categories based on their input antenna: quasioptical mixers or waveguide mixers. The former employs a hemispheric lens to focus the radiation onto a thin film antenna glued at the back of the lens, where the mixer is fabricated on the same substrate across the electrodes of the antenna. The mixer is easy to manufacture using planar circuit technology, but they often have high sidelobe level and can suffer from multiple beam reflections by the lens (e.g., Wengler et al. 1985; Zmuidzinas et al. 1992).

Waveguide mixers, on the other hand, employ a feed horn to provide good power coupling from free space to a guided wave (e.g., D'Addario 1984; Raisanen et al. 1985). These horns require high precision mechanical machining but they have excellent beam properties including low sidelobe, low cross-polarization, and high beam circularity. Once the incoming radiation is propagated into the waveguide mode, a thin film probe positioned across the waveguide is normally used to deliver the signal to the planar circuit where the SIS junction is fabricated. Figure 1.4 illustrates the physical layout of both quasioptical and waveguide mixers.

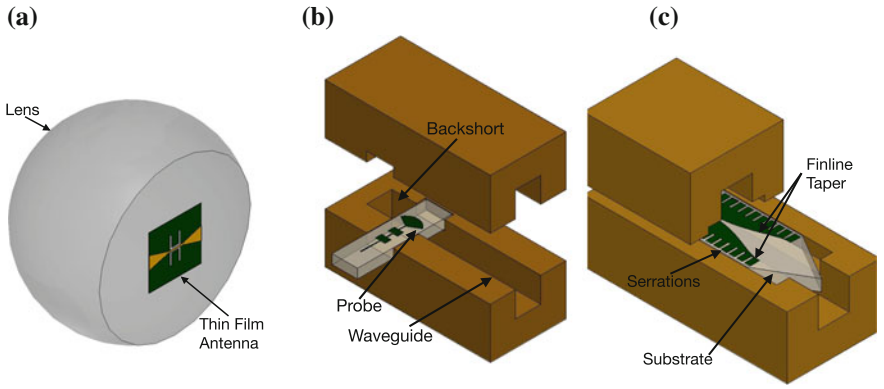

Fig. 1.4 Examples of various types of mixer, utilising different coupling mechanisms to the mixer. They were drawn only for illustration, hence are not drawn to scale. **a** Quasioptical mixer, **b** waveguide probe mixer, **c** finline mixer

1.3.3.1 Finline Mixers

A finline mixer employs a finline taper to extract the electromagnetic energy from the waveguide to the mixer chip. It is a fixed-tuned (tunerless) mixer and a major difference between the finline mixer and other waveguide mixers is that the finline chip is oriented along the propagation axis of the waveguide. This feature and the fact that the design does not require back shorts reduce the complexity of fabricating the mixer block significantly. In addition, finline tapers are known to exhibit a very large bandwidth, well above that of the waveguide mode. The back-to-back configuration provides the option of LO coupling from one side and the RF from another, avoiding the need for a beam splitter that wastes most of the power available from the source (see Chap. 6). The large substrate area also allows elegant integration of advanced mixer circuits such as power dividers and hybrids for single sideband SIS mixer designs (see Chap. 7).

Traditionally, finline mixers used antipodal fins to couple RF signal from the waveguide to a microstrip line containing the miniature SIS tunnel junction (Yassin et al. 1997, 2000). As shown in Fig. 1.5a, the metallisation for the base and the wiring layer consists of two niobium fins separated by a thin layer ($\sim$ 400 nm) of oxide. The whole arrangement is deposited onto a thick quartz substrate, which can occupy a significant fraction of the waveguide height. The resulting dielectric loading losses which increases with frequency makes this traditional finline mixer design less attractive at higher frequency bands. Nevertheless, this technology has been fabricated and tested extensively at various sub-mm bands (Grimes 2006; Kittara et al. 2007; Yassin et al. 1997, 2000), and was shown to yield state-of-the-art performance, comparable to those obtained by probe coupled waveguide mixers.

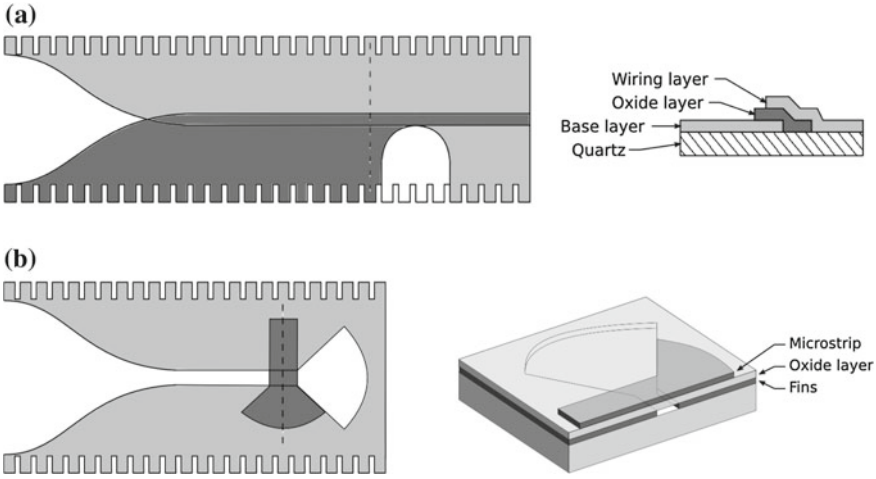

Fig. 1.5 Two different types of finline taper. The diagram is not drawn to scale. Image courtesy of Grimes (2006). **a** Antipodal finline structure, **b** unilateral finline structure

Despite the reported excellent performance of an antipodal finline mixers at 230, 350 and 700 GHz (Grimes et al. 2005; Kittara et al. 2004; Yassin et al. 1997, 2000), their structure exhibits an important fabrication difficulty. The need for overlapping fins to transform the slotline to the microstrip makes the mixer chip longer, and is susceptible to shorting during the fabrication process. The electromagnetic behaviour of the mixer is also very difficult to simulate, making it hard to design. To overcome these difficulties, we have employed a new waveguide-to-planar circuit transition that replaces the antipodal fins with a unilateral finline taper (e.g., Tan et al. 2012; Yassin et al. 2008). Unilateral finline mixers retain all the above-mentioned advantages of antipodal finline mixers, but have no overlapping taper regions. This yields a shorter mixer chip, which is much easier to fabricate and model rigorously.

As can be seen from Fig. 1.5b, the unilateral finline transforms the RF power from the waveguide mode into a slotline, that provides a natural band-pass filter to prevent the IF signal leakage. The electromagnetic behaviour of this design can be easily simulated using conventional software packages like HFSS (Ansys High Frequency Structure Simulator) or well-understood algorithms such as the Optimum Taper Method or Spectral Domain Analysis (Yassin et al. 2008). All the mixer designs reported in this thesis use unilateral finline as the main waveguide-to-planar circuit feed, and as we shall see in later chapters, the unilateral finline design works very well in conjunction with SIS mixer technology. The unilateral finline taper has also been shown to work well with Transition-Edge Sensors (TES) for the CLOVER project (Audley et al. 2006; Piccirillo et al. 2008), yielding high optical efficiency.

1.4 Current State of SIS Mixers

The sensitivity of an SIS mixer is commonly represented by its measured noise temperature (see Chap. 3 for details). The benchmark for good performance is the quantum limit given by $T_N = h\upsilon/k_B$, where k_B is the Boltzmann's constant. With current technology, SIS mixers operating below 500 GHz have routinely achieved sensitivity approaching the quantum limit. However, at higher frequencies, waveguide and superconductor's conduction losses become significant, and the machining tolerance become much harder to achieve. Consequently, it becomes very challenging to achieve quantum limited sensitivities. Nevertheless, as shown in Fig. 1.6a, remarkable performance has been achieved by SIS receivers of ALMA and Herschel Space Telescopes. This was done by using high precision electron-beam lithography in fabrication of the SIS tunnel junctions, transmission lines employing higher superconducting gap materials and state-of-the-art mechanical fabrication facilities.

The next paradigm for improving the performance of an SIS receiver is expected to come from the following three routes: increasing the number of SIS mixers per receiver (large arrays), simplifying the architecture of the receiver, and enhancing the functionality of the SIS mixer such as image rejection capability.

High sensitivity heterodyne receivers enable detection of extremely weak astronomical signals in a relatively short integration time. Hence, a clear way to improve the mapping speed of telescopes is to construct a multi-pixel focal plane arrays. However, current SIS mixer technology still employs rather complicated receiver structure owing to the employment of multiple bulky components for dual polarisation and sideband separation. Figure 1.6b shows the currently built Band 8 single

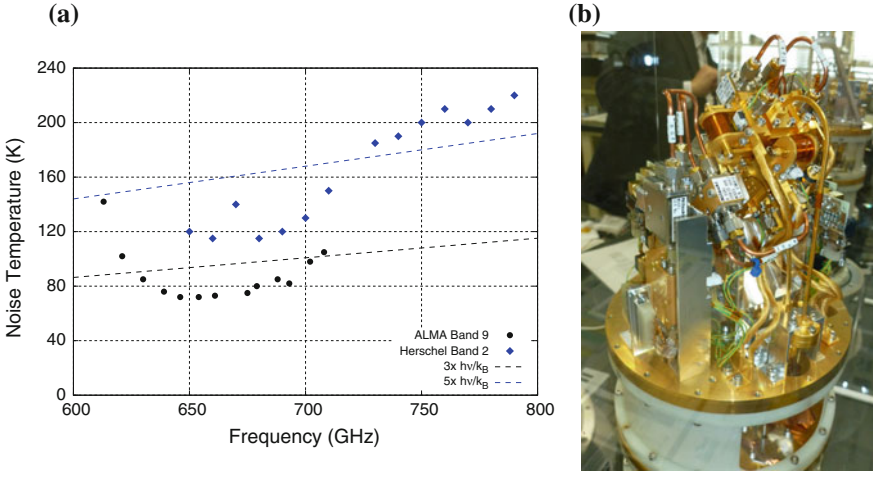

ALMA & Herschel noise temperature performance

ALMA Band 8 cartridge

Fig. 1.6 **a** The measured performance of ALMA Band 9 and Herschel Band 2 SIS receivers. **b** The examples of Band 8 cartridges build for ALMA

sideband receiver cartridge of ALMA. As can be seen, the mechanical structure is rather complex and bulky, since the single sideband operation requires more than one mixer block and additional waveguide circuit components. The same complexity would arise for other advanced SIS mixer designs, such as balanced SIS mixer which has the ability to reject the sideband noise from the LO. In summary, additional functionalities that help to reduce the noise or increase the receiver capability come at the cost of complex receiver structure that restricts the employment of focal plane array.

The work in this thesis aims to address these targets by proposing several new innovations to the current SIS mixer design, including

- the use of Silicon-On-Insulator (SOI) technology (Chaps. 4 and 5),
- single-chip integrated advanced SIS mixer designs (Chaps. 6 and 7),
- development of easy-to-machined sub-mm horns (Chap. 2) and,
- generating sub-mm signals using a photonic local oscillator (Chap. 9).

With these advancements, we hope to make arrayable SIS mixers at high frequencies feasible for future sub-mm telescopes.

References

Audley, M. D., Barker, R. W., Crane, M., Dace, R., Glowacka, D. et al. (2006). TES imaging array technology for C$_l$OVER. In *Society of Photo-Optical Instrumentation Engineers (SPIE) Conference Series*, (vol. 6275).

Cooper, C. (2001). *Physics*. Fitzroy Dearborn: Trends in Science.

D'Addario, L. R. (1984). An SIS mixer for 90–120 GHz with gain and wide bandwidth. *International Journal of Infrared and Millimeter Waves*, *5*, 1419–1442.

Grimes, P. (2006). *Design and analysis of 700 GHz Finline Mixers*. Ph.D. thesis, University of Cambridge, UK.

Grimes, P., Yassin, G., Jacobs, K. & Withington, S. (2005). A 700 GHz single chip balanced SIS mixer. In *Sixteenth International Symposium on Space Terahertz Technology*, 46–52.

Karpov, A., Miller, D., Rice, F., Stern, J. A., Bumble, B., Leduc, H. G., et al. (2007). Low noise 1–1.4 THz mixers using Nb/Al-AlN/NbTiN SIS junctions. *IEEE Transactions on Applied Superconductivity*, *17*, 343–346.

Kawamura, J., Chen, J., Miller, D., Kooi, J., Zmuidzinas, J., Bumble, B., et al. (1999). Low-noise submillimeter-wave NbTiN superconducting tunnel junction mixers. *Applied Physics Letters*, *75*, 4013.

Kittara, P., Grimes, P., Yassin, G., Withington, S., Jacobs, K., & Wulff, S. (2004). A 700-GHz SIS antipodal finline mixer fed by a pickett-potter horn-reflector antenna. *IEEE Transactions on Microwave Theory Techniques*, *52*, 2352–2360.

Kittara, P., Jiralucksanawong, A., Yassin, G., Wangsuya, S., & Leech, J. (2007). The design of Potter horns for THz applications using a genetic algorithm. *International Journal of Infrared Millimeter Waves*, *28*, 1103–1114.

Marrone, D. P., Blundell, R., Tong, E., Paine, S. N., Loudkov, D., Kawamura, J. H., Lühr, D. & Barrientos, C. (2005). Observations in the 1.3 and 1.5 THz atmospheric windows with the receiver lab telescope. In *Sixteenth International Symposium on Space Terahertz Technology*,(64–67).

Parker, N. D., White, G. J., Williams, P. G., & Hayashi, S. S. (1991). High resolution CO J = 3–2 observations of L 1551—fragmentary structure in the outflowing shell. *A&A*, *250*, 134–142.

Piccirillo, L., Ade, P., Audley, M. D., Baines, C. & et. al (2008). The ClOVER experiment. In *Society of Photo-Optical Instrumentation Engineers (SPIE) Conference Series*, (vol. 7020).

Raisanen, A., McGrath, W. R., Richards, P. L., & Lloyd, F. L. (1985). Broad-band RF match to a millimeter-wave SIS quasi-particle mixer. *IEEE Transactions on Microwave Theory Techniques*, *33*, 1495–1500.

Richer, J.S., Shepherd, D.S., Cabrit, S., Bachiller, R. & Churchwell, E. (2000). Molecular outflows from young stellar objects. *Protostars and Planets IV*, 867.

Richer, J. S., Hills, R. E., & Padman, R. (1992). A fast CO jet in Orion B. *MNRAS*, *254*, 525–538.

Shu, F. H., Adams, F. C., & Lizano, S. (1987). Star formation in molecular clouds—observation and theory. *ARA & A*, *25*, 23–81.

Solomon, P. M., Radford, S. J. E., & Downes, D. (1992). Molecular gas content of the primaeval galaxy IRAS 10214 + 4724. *Nature*, *356*, 318.

Tan, B.-K., Yassin, G., Grimes, P., Leech, J., Jacobs, K., & Groppi, C. (2012). A 650 GHz unilateral finline SIS mixer fed by a multiple flare-angle smooth-walled horn. *IEEE Transactions on Terahertz Science and Technology*, *2*(1), 40–49.

Wengler, M. J., Woody, D. P., Miller, R. E., & Phillips, T. G. (1985). A low noise receiver for millimeter and submillimeter wavelengths. *International Journal of Infrared and Millimeter Waves*, *6*, 697–706.

Wiedner, M. C., Wieching, G., Bielau, F., Rettenbacher, K., Volgenau, N. H., Emprechtinger, M., et al. (2006). First observations with CONDOR, a 1.5 THz heterodyne receiver. *A&A*, *454*, L33–L36.

Wilson, R. W., Jefferts, K. B., & Penzias, A. A. (1970). Carbon monoxide in the orion nebula. *ApJ*, *161*, L43.

Yassin, G., Padman, R., Withington, S., Jacobs, K., & Wulff, S. (1997). Broadband 230 GHz finline mixer for astronomical imaging arrays. *Electronics Letters*, *33*, 498–500.

Yassin, G., Withington, S., Buffey, M., Jacobs, K., & Wulff, S. (2000). A 350-GHz SIS antipodal finline mixer. *IEEE Transactions on Microwave Theory Techniques*, *48*, 662–669.

Yassin, G., Grimes, P. K., King, O., & North, C. E. (2008). Waveguide-to-planar circuit transition for millimetre-wave detectors. *Electronics Letters*, *44*(14), 866–867.

Zmuidzinas, J., Leduc, H. G. & Stern, J. A. (1992). Slot antenna SIS mixers for submillimeter wavelengths. In *Third International Symposium on Space Terahertz Technology*, 234.

Chapter 2
Multiple Flare-Angle Smooth-Walled Horn

Overview: In this chapter, we shall discuss the employment of multiple flare-angle smooth-walled horns optimised to operate at 700 GHz. We will first describe the design of the feed horn, then the fabrication technique we developed to machine these horns, followed by the experimental setup we built to measure the far field radiation patterns. The measured results will be analysed and compared with the theoretical predictions produced using our own software package. In addition, we shall discuss the use of Ansys HFSS for tolerance analysis.

2.1 Introduction

Feed horns with a good radiation characteristic are an essential component in the design of a sub-mm wave heterodyne receivers. They offer high beam efficiency and low sidelobes level required by sensitive astronomical observations. Most of modern sub-mm receivers use corrugated horns (Clarricoats and Olver 1984) to efficiently couple the RF signal from the sky to the detector. Corrugated horns however require azimuthal corrugations in their interior wall to create isotropic surface boundary conditions to the propagating E- and H-field wavefronts. This suppresses unwanted waveguide modes, and allows only the propagation of the hybrid HE_{11} mode (Olver et al. 1994), to produce uniform and polarized illumination at the horn aperture. The result is a far-field radiation pattern that has high directivity, low sidelobes and low cross-polarization levels across a large operational bandwidth (around 50 %).

Corrugated horns are fabricated using either direct machining or electroforming. Direct machining needs a high precision milling machine to achieve the required machining tolerances and repeatability, in particular near the horn's throat where the diameter is too small for a robust tool. Electroforming, on the other hand, requires complicated mandrel fabrication, electroplating and chemically dissolving stages, albeit the machining of the mandrel is easier. Both processes are costly (approximately $1,000–2,000 per horn) and time consuming (several weeks per horn).

B.-K. Tan, *Development of Coherent Detector Technologies for Sub-Millimetre Wave Astronomy Observations*, Springer Theses, DOI 10.1007/978-3-319-19363-2_2

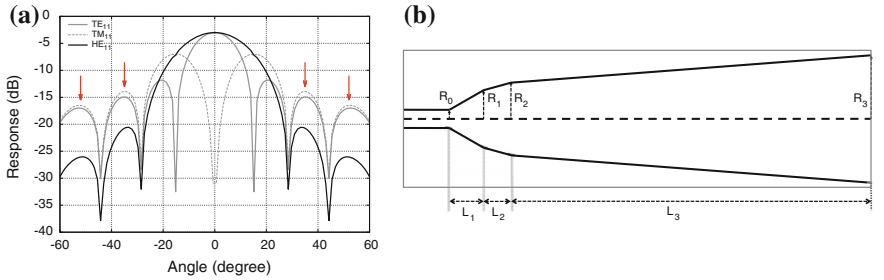

Fig. 2.1 **a** Plot illustrating how the combination of TE_{11} and TM_{11} modes resulting in sidelobes cancellation. **b** Schematic drawing of a 3-section multiple flare-angle horn. The drawing is not according to the scale

The new generation of sub-mm astronomical telescopes would require a larger number of feed horns for their large multi-pixel focal plane array receiver systems ($\sim$10$-$1000 pixels). The cost for producing these large number of horns has become considerably high and the time required for their construction has become a major concern.

In recent years therefore, there has been considerable interest to find alternatives to corrugated horns without compromising the radiation pattern quality (e.g. Granet et al. 2004; Yassin et al. 2007; Britton et al. 2010). Smooth-walled horns that have comparable radiation characteristics to a corrugated horn, but without the large number of high density corrugation grooves ($\sim$5 corrugations per wavelength) is an attractive option. The simplest form of a smooth-walled horn is a Pickett-Potter horn (Pickett et al. 1984; Potter 1963), which has only a single step discontinuity near the throat followed by a smooth conical flaring section. The step discontinuity excites the TM_{11} mode at about 16 % of the total incident power of the incoming TE_{11} mode. Both fields propagate along the conical flaring section until they arrive in phase at the horn aperture. Figure 2.1a shows the resulting far field pattern of the TE_{11} and TM_{11} modes, and it can be seen clearly that the sidelobes level and position of both modes are now coincide with each other. The combination of both modes therefore results in cancellation of sidelobes, and a main beam with high circularity. This generates a highly uniform field that give low sidelobes level, and low cross-polarization in the far-field radiation pattern.

One disadvantage of a Pickett-Potter horn is that it has a narrow operating bandwidth. The performance however can be substantially improved by increasing the number of discontinuities near the throat of the horn (Yassin et al. 2007), that generate a carefully chosen combination of the higher order modes which could widen the operating bandwidth of the horn (Kittara 2002; Kittara et al. 2000, 2004). The optimised depth of these discontinuities, the horn length and flare angles can be predicted using modal matching in conjunction with optimisation algorithms (Granet et al. 2004; Zeng et al. 2010). For designing the multiple flare-angle smooth-walled horn described in this chapter, we employed modal matching for design

analysis, and Genetic Algorithm (GA) for optimisation (Haupt and Haupt 1998; Kittara et al. 2007).

The two algorithms were incorporated into a self-contained C++ package written by Kittara et al. (2007), *HornSynth*. Using this package, they have successfully produced a variety of high performance feed horns, with two, three and four flare-angle sections, giving respectively 15, 20 and 25 % operating bandwidth (Kittara et al. 2008; Leech et al. 2012). As shall be seen later, one major advantage of the multiple flare-angle horn is that they only require a simple fabrication process due to their simple interior geometry (see Fig. 2.1b). A series of 230 GHz multiple flare-angle horns and horn arrays have been fabricated using this technique and tested extensively by Leech et al. (2009, 2010, 2011, 2012), and the results showed low level of sidelobes, good beam circularity, low cross-coupling level and low cross-polarization over a 20 % bandwidth, in agreement with the *HornSynth*'s predictions.

2.2 Feed Horn Design

As we have explained before, *HornSynth* comprises two main components, the modal matching analysis and the Genetic Algorithm. Modal matching is used to predict the fields propagating along the feed horn, and to calculate the horn aperture field by calculating the scattering matrix, whilst GA is employed for reliable optimisation.

Modal-matching is a powerful technique that had been used extensively by many authors (e.g. James 1981; Olver and Xiang 1988) to accurately predict the feed horns aperture distribution. In the discussion that follows, we shall briefly summarise the basic principles used in modal matching employing a conical horn as an example. The reader is referred to Kittara et al. (2004) and Olver et al. (1994) for a more detailed description.

In modal matching analysis, the feed horn's interior is first divided into a series of cylindrical sections, with the tangential field components propagating within each section described as the superposition of waveguide base functions (modes). Using an appropriate coordinate system (i.e., cylindrical coordinates for conical horns), these modes can be obtained by solving Helmholtz equations. Assuming the wave is propagating in the z-direction, the solutions are normally found by calculating the z components of the E- and H-field within the horn that satisfy the wave equations and the boundary condition. For a conical horn, this can be written as

$$\psi_z(\rho, \phi, z, t) = J_n(k\rho)\cos(n\phi + \phi_0)e^{-\gamma z}e^{j\omega t} \tag{2.1}$$

where ψ_z is either the E_z or H_z component, ρ and ϕ are the radial distance from the z axis and the azimuth angle respectively, J_n is Bessel function of the 1st kind of order n, and ϕ_0 is a phase constant. The wave number is defined as $k^2 = \gamma^2 + \omega^2\mu\epsilon$ where γ is the propagation constant and ω, μ and ϵ representing the radial frequency, the permeability and electric permittivity, respectively. The remaining transverse

components of the E- and H-field propagation wave can then be expressed in terms of E_z and H_z as

$$E_\rho = -\frac{1}{k^2}\left(\gamma\frac{\partial}{\partial\rho}E_z + \frac{j\omega\mu}{\rho}\frac{\partial}{\partial\phi}H_z\right), \tag{2.2a}$$

$$E_\phi = \frac{1}{k^2}\left(-\frac{\gamma}{\rho}\frac{\partial}{\partial\phi}E_z + j\omega\mu\frac{\partial}{\partial\rho}H_z\right), \tag{2.2b}$$

$$H_\rho = \frac{1}{k^2}\left(\frac{j\omega\mu}{\rho}\frac{\partial}{\partial\phi}E_z - \gamma\frac{\partial}{\partial\rho}H_z\right), \tag{2.2c}$$

$$H_\phi = -\frac{1}{k^2}\left(j\omega\mu\frac{\partial}{\partial\rho}E_z + \frac{\gamma}{\rho}\frac{\partial}{\partial\phi}H_z\right). \tag{2.2d}$$

A conical horn with a perfectly conducting wall supports two orthogonal mode sets, the *transverse magnetic* TM_{nm} modes and the *transverse electric* TE_{nm} modes, where the subscript n and m are integers representing the cyclic variation with ϕ and the mth root of the Bessel function of order n, respectively. TM modes have only the tangential magnetic fields with $H_z = 0$ while TE modes have only the tangential electric fields with $E_z = 0$. The boundary conditions imposed on the perfect conductor wall require that $E_\phi = 0$ for TM modes, and $E_\phi = E_z = 0$ for TE modes, at $\rho = a$ where a is the radius of the cylindrical section. Applying these boundary conditions to Eqs. 2.2 gives the expressions of the specific transverse modes of TE and TM fields within that particular cylindrical section. enlargethispage2pt The total modal fields at the interface between two adjacent cylindrical sections are matched with boundary conditions that are dictated by the conservation of power. As shown in Fig. 2.2, this interface junction is represented by a scattering matrix, and the power coupling across the junction is related using the scattering matrix defined by

$$\begin{pmatrix}\mathbf{B}\\ \mathbf{D}\end{pmatrix} = \begin{pmatrix}\mathbf{S}_{11} & \mathbf{S}_{12}\\ \mathbf{S}_{21} & \mathbf{S}_{22}\end{pmatrix}\begin{pmatrix}\mathbf{A}\\ \mathbf{C}\end{pmatrix}, \tag{2.3}$$

where **A** and **B** are the input and reflected mode coefficient matrices from the input side (left), while **C** and **D** are the similar matrices from the output side (right).

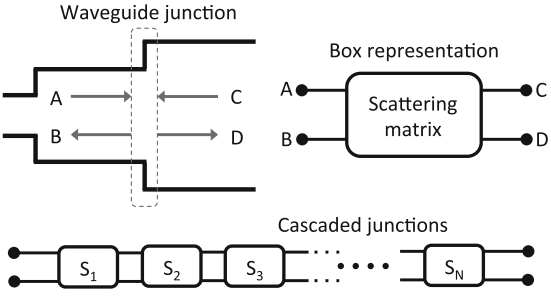

Fig. 2.2 Diagram illustrating the scattering matrices used to model a feed horn

The transverse electric fields in each uniform cylindrical section are represented as a spectrum of N nodes. From Fig. 2.2, the electric and magnetic fields on the left hand side are given as

$$\boldsymbol{E}_L = \sum_{n=1}^{N} [A_n e^{-\gamma_n z} + B_n e^{\gamma_n z}]\, \boldsymbol{e}_{nL}, \tag{2.4a}$$

$$\boldsymbol{H}_L = \sum_{n=1}^{N} [A_n e^{-\gamma_n z} - B_n e^{\gamma_n z}]\, \boldsymbol{h}_{nL}, \tag{2.4b}$$

where A_n and B_n are the forward and reflected amplitude coefficients of mode n from the input side, and $\boldsymbol{e}$ and $\boldsymbol{h}$ represent the transverse electric and magnetic modal functions respectively. On the right hand side of the junction, the fields are

$$\boldsymbol{E}_R = \sum_{m=1}^{M} [C_m e^{-\gamma_m z} + D_m e^{\gamma_m z}]\, \boldsymbol{e}_{mR}, \tag{2.5a}$$

$$\boldsymbol{H}_R = \sum_{m=1}^{M} [C_m e^{-\gamma_m z} - D_m e^{\gamma_m z}]\, \boldsymbol{h}_{mR}, \tag{2.5b}$$

where C_m and D_m are the forward and reflected amplitude coefficients of mode m at the output side. Matching these transverse fields across the junction i.e., $\boldsymbol{E}_L = \boldsymbol{E}_R$ and $\boldsymbol{H}_L = \boldsymbol{H}_R$ at boundary $z = 0$, we have

$$\sum_{n=1}^{N} (A_n + B_n)\, \boldsymbol{e}_{nL} = \sum_{m=1}^{M} (C_m + D_m)\, \boldsymbol{e}_{mR}, \tag{2.6a}$$

$$\sum_{n=1}^{N} (A_n - B_n)\, \boldsymbol{h}_{nL} = \sum_{m=1}^{M} (C_m - D_m)\, \boldsymbol{h}_{mR}. \tag{2.6b}$$

Multiplying Eqs. 2.6a and 2.6b with $\mathbf{h}_R$ and $\mathbf{e}_L$ respectively, and integrating over the cross sectional area of the junction, produce a pair of simultaneous matrix equations:

$$\mathbf{P}(\mathbf{A} + \mathbf{B}) = \mathbf{Q}(\mathbf{C} + \mathbf{D}), \tag{2.7a}$$

$$\mathbf{P}^T(\mathbf{D} - \mathbf{C}) = \mathbf{R}(\mathbf{A} - \mathbf{B}), \tag{2.7b}$$

where the matrix $\mathbf{P}$ representing the mutual coupled power between mode i on the left hand side and the mode j on the right hand side. $\mathbf{Q}$ and $\mathbf{R}$ are the self-coupled power between modes on the right hand and left hand side of the junction. These matrices are given by

$$P_{ij} = \int_{S_L} (\boldsymbol{e}_{iL} \times \boldsymbol{h}_{jR}) \cdot \mathbf{ds}, \tag{2.8a}$$

$$Q_{jj} = \int_{S_R} (\boldsymbol{e}_{jR} \times \boldsymbol{h}_{jR}) \cdot \mathbf{ds}, \tag{2.8b}$$

$$R_{ii} = \int_{S_L} (\boldsymbol{e}_{iL} \times \boldsymbol{h}_{iL}) \cdot \mathbf{ds}. \tag{2.8c}$$

Rearranging Eqs. 2.7 into the matrix form gives the elements in the scattering matrix **S** as

$$\mathbf{S}_{11} = (\mathbf{R} + \mathbf{P}^T\mathbf{Q}^{-1}\mathbf{P})^{-1} \times (\mathbf{R} - \mathbf{P}^T\mathbf{Q}^{-1}\mathbf{P}) \tag{2.9a}$$

$$\mathbf{S}_{12} = 2 \times (\mathbf{R} + \mathbf{P}^T\mathbf{Q}^{-1}\mathbf{P})^{-1}\mathbf{P}^T \tag{2.9b}$$

$$\mathbf{S}_{21} = 2 \times (\mathbf{Q} + \mathbf{P}\mathbf{R}^{-1}\mathbf{P}^T)^{-1}\mathbf{P} \tag{2.9c}$$

$$\mathbf{S}_{22} = -(\mathbf{Q} + \mathbf{P}\mathbf{R}^{-1}\mathbf{P}^T)^{-1} \times (\mathbf{Q} - \mathbf{P}\mathbf{R}^{-1}\mathbf{P}^T) \tag{2.9d}$$

All these scattering matrices describing each junction are then cascaded together to form the complete scattering matrix that represents the overall feed horn. The horn aperture field can then be directly computed from the output transmission coefficient of the complete scattering matrix, which is then Fourier-transformed to find the far-field radiation patterns of the horn (Kittara et al. 2004).

2.2.1 Genetic Algorithm

Genetic algorithm is an optimisation technique that imitates the natural selection process of biological evolution. It is based on the genetic evolution of a population of a certain size to find the *fittest individual* i.e., the optimised solution. One advantage of GA is that it is well suited for parallel computation. Another important advantage of GA is that it can simultaneously search a wide sampling parameter space and have the ability to escape local minima.

GA optimisation begins with encoding each key parameter or variable to be optimised into a binary string called a *chromosome*. These chromosomes are converted to a Gray code to ensure that the numerical value of the chromosomes do not change by a large fractional amount when bits are flipped through *mutation* and *crossover* (see below).

A set of chromosomes, containing each parameters, is an *individual*. An initial *population* of individuals is formed where the chromosomes of each individual are chosen stochastically within sensible constraints. The *fitness* of each individual is evaluated via a *cost function*evaluated via a and the higher fitness half of the population is selected to becomes *parents* that produce offspring via *mating*. The lower fitness half of the population is eliminated and replaced by the new offspring individuals. Together, they form the next generation of population.

In the mating stage, the parent's chromosomes are spliced at random length. Each ends are then swapped between the parents and recombined to produce two new offspring chromosomes. This process is called *crossover*. The Gray code makes sure that the chromosomes of the offsprings are not too numerically different from their parents, hence preserving the overall fitness quality of the population. This also prevents the algorithm from suddenly straying away from a converging solution.

After crossover, a single bit of the offspring chromosome is flipped with a small probability, mimicking the *mutation* process in the genetic evolution. A combination of crossover and mutation ensures the diversity of the offspring, and it is these processes that give the searching algorithm the ability to explore a wider parameter space. After a new population is formed, the fitness of each offspring is re-evaluated and the mating process is repeated for a few generations. In general, the average fitness of the population increases from one generation to the other. The optimisation process is stopped after it reaches a user specified limit of the generation (typically 1,000–2,000 generations). The fittest individual is then further optimised using the Simplex minimisation (Nelder and Mead 1965) in the *HornSynth* case.

2.2.2 700 GHz Multiple Flare-Angle Horn

For the operation at the 700 GHz waveband, we have chosen a multiple flare-angle smooth-walled horn with 3 flared sections. The 5 parameters to be optimised are R_1, R_2, L_1, L_2 and L_3 (see Fig. 2.1). R_0 is set by the cutoff frequency of the input circular waveguide, and the horn aperture R_3 is determined by the required beam width of the feed horn, which in this case is about 14.6° Full-Width Half-Maximum (FWHM). The initial chromosomes in each individual in the first generation are randomly assigned within a range that ensure a long phasing section, and the flare discontinuities are located nearer to the throat of the horn. The rationale behind this is that the resulting feed horn design is not too dissimilar with the Pickett-Potter horn to retain its general good features.

The cost function which measures the fitness of each individual horn is evaluated from the far-field beam pattern calculated using the modal matching technique (Yassin et al. 2007). At a specific frequency f, the cost function is given by

$$\delta_f^2 = w_X \left[\sum_{P=-1}^{P=-30} \left(\frac{\sigma_P}{\sigma_P^{\text{av}}} \right)^2 w_P \right], \tag{2.10}$$

where w_X is the peak cross-polar power relative to main beam peak power, P is the power response in dB, σ_P and σ_P^{av} are the difference between the E- and the H-plane beam widths and the average beam width of both planes at the power response P dB, and $w_P = 10^{P/15}$ is the weighting function for the beam circularity (Kittara et al. 2007). This cost function is evaluated at several frequencies across the entire bandwidth. The final cost function for a particular horn design centred at f_0 is calculated by

Table 2.1 Geometrical parameters for the 3-section multiple flare-angle horn design

Centre frequency	Parameter	R_0	R_1	R_2	R_3	L_1	L_2	L_3
700 GHz	Length (mm)	0.203	0.488	0.595	1.200	0.487	0.398	7.886

$$\delta^2 = \sum_f \delta_f^2 \exp\left(\frac{-(f - f_0)^2}{2\sigma_f^2}\right), \tag{2.11}$$

where the exponential term is the frequency dependent weighting factor, and σ_f is the bandwidth ($f_{upper} - f_{lower}$).

These cost function was chosen to specify the fitness criterion for high beam circularity and low cross-polarization level. The combination of these two criteria produced a horn that exhibits low sidelobes level and since Pickett-Potter type horns generally have low return loss (Pickett et al. 1984), this requirement was not included in the cost function. Other criteria can clearly be chosen, depending on the horn applications.

The most computationally intensive step in the entire design procedure is the beam pattern calculation via the modal matching for each individual in the population across a wide bandwidth. Since GA optimisation is well suited for parallelisation, the beam patterns and the cost function of each individual within a certain generation can be distributed to separate central processing units (CPUs) as a slave tasks for simultaneous calculations. The parallel computing technique vastly reduces the time required to optimised a multiple flare-angle horn. For example, using a 28 cores machine, we managed to optimise the 3-section horn within 1,000 generation of 27 individuals, taking only about 3 hours of computing time.

Table 2.1 shows the result from the GA optimisation for a 3-section multiple flare-angle horn centred at 700 GHz. As shown in Fig. 2.3, the predicted beam patterns have high circularity and low sidelobes levels across ~140 GHz bandwidth.

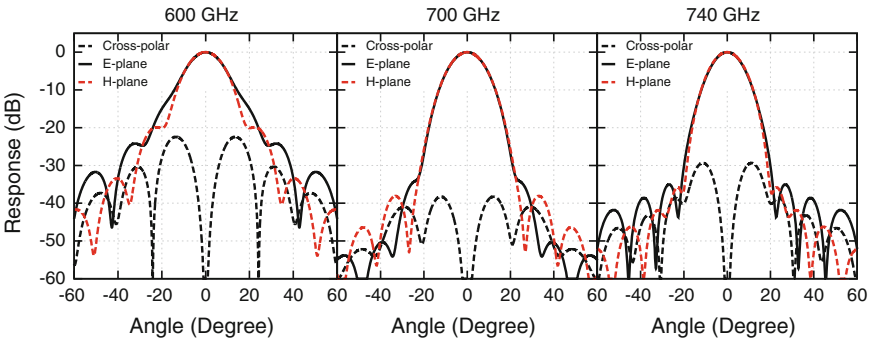

Fig. 2.3 Theoretical E-, H-plane and cross-polarization beam pattern calculated using modal matching

2.3 Horn Fabrication

The major advantage of the multiple flare-angle horn is that its simple interior profile lends itself to easy and fast fabrication process. These horns can be made via the simple direct milling technique using a standard 5-axis computer-numerical-control (CNC) machine. Figure 2.4a shows a high-speed steel machine tool manufactured (by a standard machine tool company) to have its cutting edge shaped according to the horn profile. This tool is used to mill the desired feed horn directly into a block of aluminium. The circular waveguide that feeds the horn is formed by simply milling through the apex of the feed horn profile from the other end of the aluminium plate. Figure 2.4b shows an example of the fabricated horn made using this technique.

In order to demonstrate that the direct milling method is repeatable, the sharpness of the discontinuities of the shaped cutting tool was inspected after using it to fabricate several horns. As shown in Fig. 2.5a, the discontinuities of the machine tool remained reasonably sharp. The apparent damage of the cutting edge away from the first discontinuity (enlarged in Fig. 2.5b) is mainly caused by the aluminium waste not being properly cleared out of the milling area, hence adhering to the cutting tool.

Using the direct milling method described above, a large number of horns can be fabricated very rapidly. Once the machine tool and the working metal plate are properly aligned within the 5-axis CNC machine, the feed horns can be fabricated

Fig. 2.4 **a** The high speed steel machine tool used to fabricate the multiple flare-angle horns. **b** A prototype of 700 GHz smooth-walled horn made by direct milling into an aluminium block

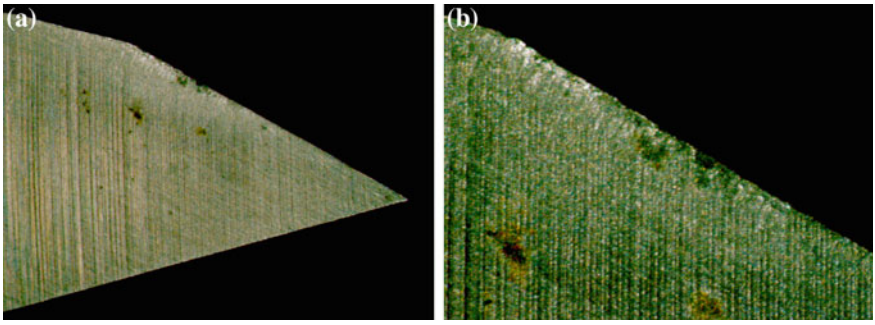

Fig. 2.5 Sharpness of the discontinuities of the machine bit examined under a microscope

simply by repeating the milling process along the programmed coordinates, forming a horn array. Leech et al. (2012) have successfully fabricated and measured high quality beam patterns across a 37 horn array operating at 230 GHz, demonstrating that this fabrication technique is feasible for constructing large format focal plane arrays.

2.4 Experimental Setup

Our far-field test facility consisted of a rotary table, a local oscillator (LO), a lock-in amplifier, a data logging system, and 4 K cryogenic bolometric detector, all housed in an anechoic chamber. The anechoic chamber walls were lined with high loss microwave absorbers (Eccosorb® AN-72 from Emersion & Cuming Microwave Products), to reduce electromagnetic interference and reflection.

Figure 2.6 shows a schematic diagram of the test range, without the surrounding Eccosorb®. The horn under test was used as a transmitter, fed by the LO via a circular-to-rectangular waveguide transition. The whole arrangement was aligned to the cooled receiver horn feeding the bolometer inside the cryostat. This assembly was affixed firmly onto a rotary table, with the aperture of the horn aligned parallel to the rotating axis of the rotary table. Extra Eccosorb® RF absorbers were placed at key positions around the experimental setup to eliminate stray power pickup and reduce the effect of standing waves.

The separation distance between the horn under test and the window of the cryogenic Dewar housing the detector is set to be further than $10\frac{D^2}{\lambda}$ to ensure that the

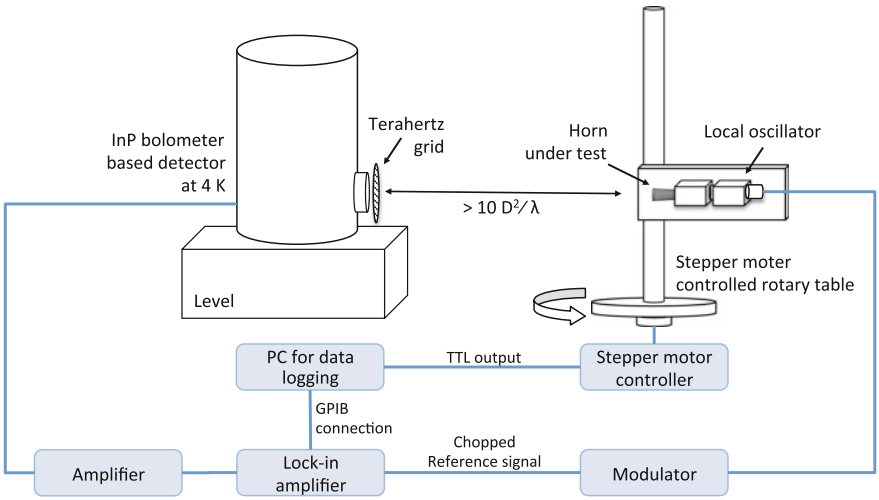

Fig. 2.6 Schematic diagram showing the setup of the far-field beam pattern test range

horn is in the far-field region. The radiation patterns were measured by logging the signal received from the lock-in amplifier while rotating the transmitter. This method gave a high dynamic range of ∼60 dB.

For measuring co-polar and cross-polarization patterns, a terahertz polarizer grid was placed in front of the detector cryostat window, with the polarization axis tilted at 45° to the plane of rotation (Ludwig 1973). The input polarization of the horn under test was then aligned parallel to the grid polarization axis for measuring a co-polar pattern, or perpendicular to the grid axis for measuring a cross-polar pattern.

2.5 Measurement Results and Analyses

We had fabricated six multiple flare-angle horns in two fabrication runs, with three prototypes at each run. At 700 GHz, the tolerance required to achieve good performance is stringent since an error similar to that of the fabrication for a 230 GHz horn would be a significant fraction of a wavelength at this higher frequency. The cutting tool at this frequency is also much smaller, with a maximum radius of 1.2 mm.

Along with the feed horns, we had also fabricated a 13° semi-flare angle conical circular-to-rectangular waveguide transition as a separate piece to fit the rectangular output waveguide of the 700 GHz LO. This transition was made by direct milling as well, with a 13° conical cutting tool milled into the aperture of the rectangular waveguide formed in a split-block beforehand. A standard UGC 387/U (modified) flanges was then machined to provide an interface for attaching the transition to the horn and the LO source.

Figure 2.7 shows the beam patterns measured for one of the best prototype horn (Horn No. 1) among the three fabricated in the first run. The results were reasonably

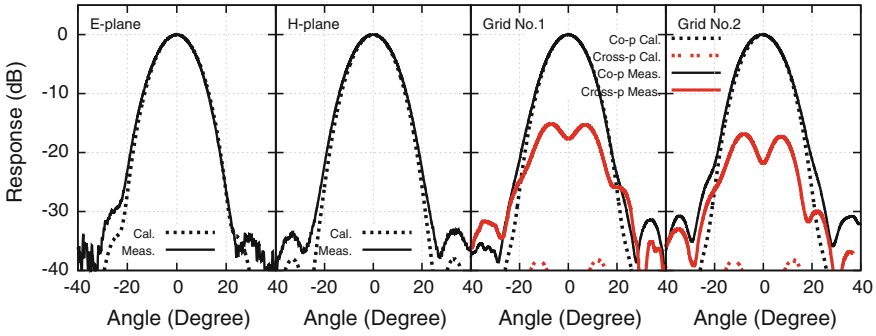

Fig. 2.7 Beam pattern measurements of the first generation smooth-walled horn No. 1 at the central frequency 700 GHz. The measured beam patterns match reasonably well with theory, given the tight tolerances required at this wavelength. Grid No. 1 and grid No. 2 represent two different polarizers used during the measurements for comparison purpose. The beam patterns measured at various other frequencies across the wavebands are presented in Appendix C

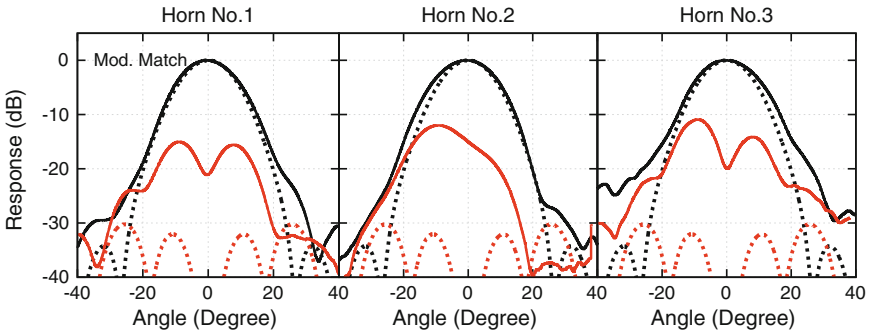

Fig. 2.8 Measurements of co-polar and cross-polar pattern for the first generation of horns at 660 GHz, compared with modal matching predictions. The *solid curves* are the measured data while the *dotted curves* are computed patterns. The *black curves* represent the co-polar patterns, while the *red curves* correspond to the cross-polar patterns

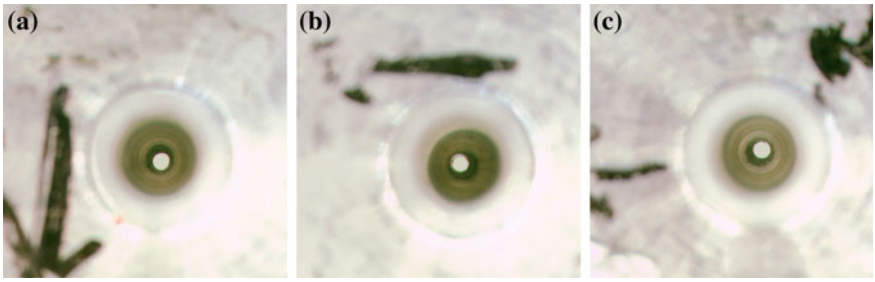

Fig. 2.9 Microscope photos show the lateral misalignment between the input circular waveguide and the horn aperture of the first generation horns. **a** Horn 1. **b** Horn 2. **c** Horn 3

good, but there were some notable differences between the calculated E- and H-plane and the measured beam patterns. The sidelobe positions were almost coincide with the theoretical predictions and the sidelobe level was only a few dB higher. The measured cross-polarization was higher than expected though, with a slight asymmetry in all the measured beam patterns. It can however be clearly seen that the pattern quality is quite acceptable at this frequency.

Figure 2.8 shows the measured co-polar and cross-polar beam pattern of the three prototypes at 660 GHz. There was a clear asymmetry in the main beam of the co-polarization patterns for 2 out of the 3 prototypes. The measured cross-polar level was significantly higher than that predicted by modal matching. We believe that these effects were caused by a lateral translational offset between the input circular waveguide and the horn section.

We have inspected the interior of the horns under microscope to look for any obvious lateral misalignment, and as shown in Fig. 2.9, there was evidence that the input circular waveguide was indeed offset with respect to the horn. This showed up as asymmetry in the circularity of the first dark rim around the first smooth-walled section of the horn profile.

With the experience gained from the first fabrication run, a new batch of the horns were fabricated to minimise the translational offset error of the input waveguide. We realised that the major contributor to this translational offset is the inability to accurately place the cylinder aluminium block back to its original position after removing it for the manufacturing of the circular waveguide. Hence, in the new batch of feed horns, we used a longer aluminium cylinder block to ensure that the CNC machine clamp can hold it firmly in place. The circular waveguide was then milled along with all the holes of the flanges to ensure that the circular waveguide was aligned to the centre of the flange with minimum offset.

Figure 2.10 shows that the asymmetry in the measured beam patterns for all three horns was substantially reduced now, except for prototype No. 1. The cross-polarization level for all three horns was also lowered by several dB compared to the first batch of prototypes. Figure 2.11 shows the top-down view into the interior of all the three new horns. As can be seen, the first dark rim is now much more circular.

Figure 2.12 shows the E-, H-, co-polar and cross-polar radiation patterns measured for Horn No. 3 at the design central frequency of 700 GHz, and at the edges of the LO

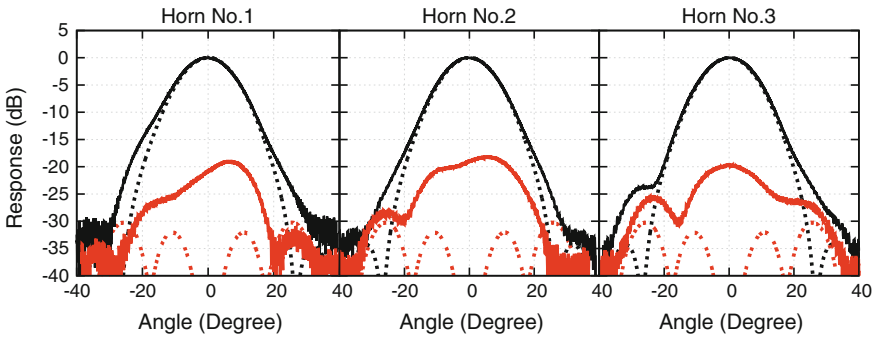

Fig. 2.10 Co- and cross-polarization measurements for all three horns from the second fabrication run at 660 GHz

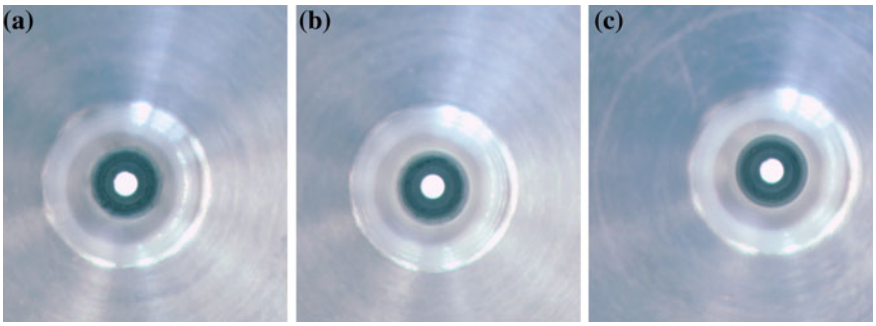

Fig. 2.11 Microscope photos showing the lateral misalignment of the horns from second fabrication run. **a** Horn 1. **b** Horn 2. **c** Horn 3

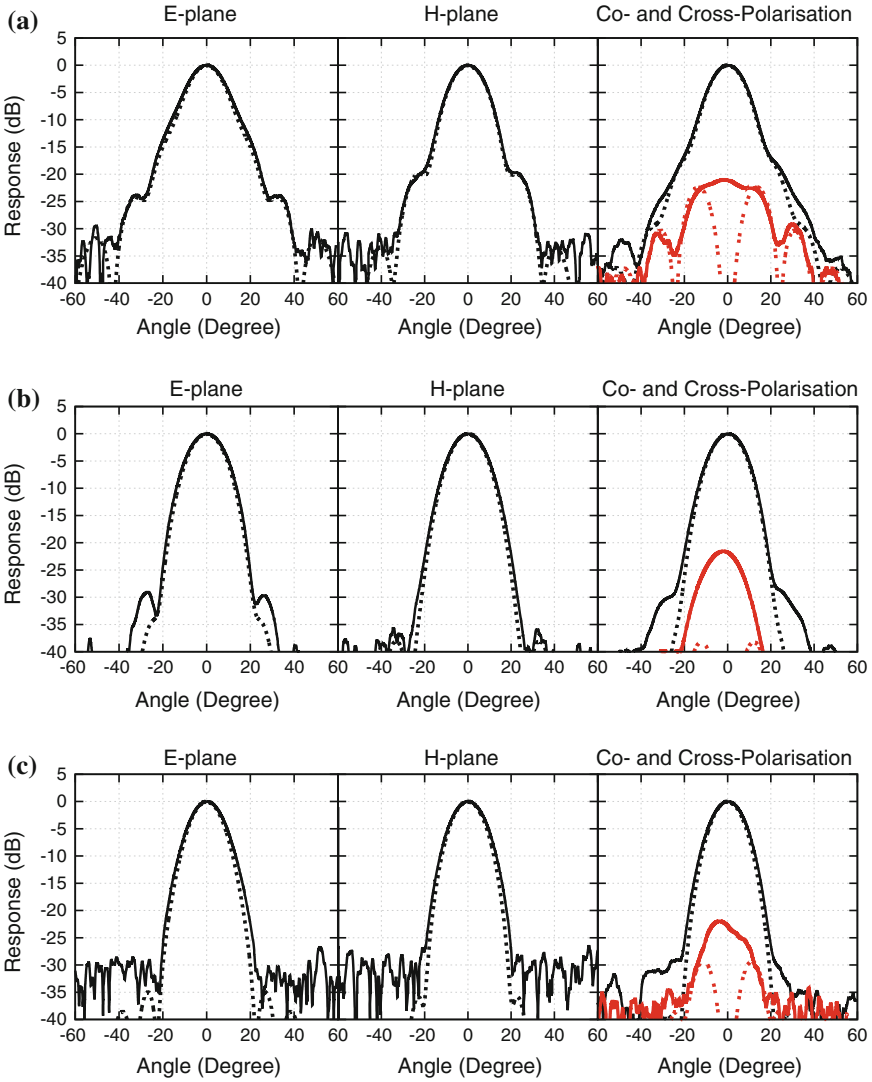

Fig. 2.12 Beam pattern measurements of horn No. 3 from the second generation smooth-walled horn in the 700 GHz frequency band. The *solid lines* are the measured beam patterns, while the *dash lines* are the calculated patterns using modal matching. In the *right column*, the *red colour lines* represent the cross-polar patterns, and the *black lines* are the co-polar patterns. **a** 600 GHz. **b** 700 GHz. **c** 740 GHz

frequency range 600–740 GHz. The measured patterns at other frequencies across the band are shown in the Appendix C.

It can clearly be seen that the measured first sidelobe level is below –30 dB at the central frequency. The main beam has excellent beam circularity down to the –30 dB

level and is symmetrical and clear of standing wave ripples. The co-polar patterns agreed very well with the computed prediction and the peak cross-polarization level was below –22 dB, limited by the polarizer's efficiency to filter out non-polarized component (typically about 99 % at high frequencies). This limitation can be seen by noting that the level of cross-polarization remains approximately fixed across a bandwidth of 140 GHz. In particular, at the 600 GHz plot, the cross-polar level remains approximately at –20 dB, showing no trend of worsening performance as predicted by theory.

2.6 Study of Multiple Flare-Angle Horn Using Ansys HFSS

Most horn design software packages, including *HornSynth*, can only model horns with axial symmetry. They are particularly useful in predicting the behaviour of a certain feed horn design with circular or rectangular symmetry, but cannot be employed to incorporate non-axisymmetric features. In this section, we describe the use of HFSS to model the feed horn in 3-D, including the non-axisymmetric errors.

3-D electromagnetic simulators are not commonly employed for predicting the performance of horns because the electrically-large dimension of the model ($\sim 20\lambda$) often presents a huge challenge for the computational memory requirement, particularly for corrugated horns with large numbers of corrugations per wavelength. Multiple flare-angle horn however, consist of only a few flare-angle discontinuities and long phasing sections, hence the volume of meshing needed to accurately describe the surface of the horn model is greatly reduced. This relaxes the heavy requirement on computer memory, and makes possible the use of HFSS to study critical features of our horn design, such as tolerances on fabrication errors and cross coupling between adjacent horns.

2.6.1 Comparing Simulation Results with Modal Matching

Constructing a 3-D model of a multiple flare-angle horn using HFSS is rather straightforward. First, the feed horn model is set to be aluminium or a perfect conductor, within a free space environment (boundary at least $\lambda/4$ away from the feed horn). This free space structure is assigned with the *Radiation Boundary Condition*, which presents an infinite boundary by presenting a perfect match to the electromagnetic field at the boundary. An E-field polarized wave port is then launched at the base of the input waveguide, shown as a small circle at the bottom of Fig. 2.13 with a coordinate triad. An infinite far-field radiation sphere is setup by assigning the origin of this *infinite sphere* at the centre of the horn aperture plane.

For generating the E- and H-plane far-field radiation patterns, we plot the *total gain* at the x-plane ($\phi = 0°$) and the y-plane ($\phi = 90°$, assuming the polarized

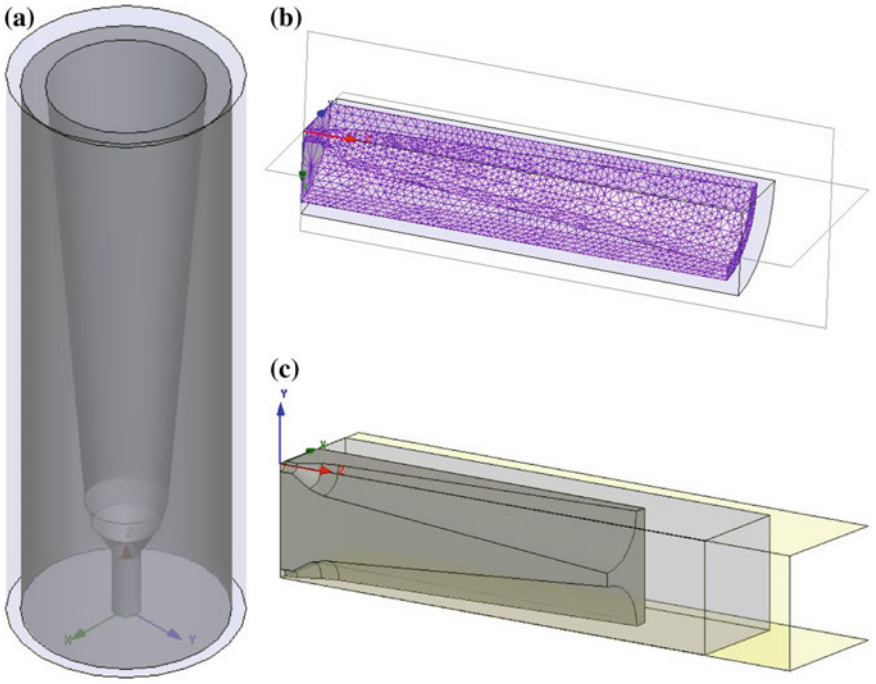

Fig. 2.13 Examples of HFSS model of multiple flare-angle smooth-walled horn with the free space boundary approximately one wavelength away from the feed horn. **a** Full HFSS model. **b** A simplified wedged model with meshing. **c** A simplified two-horn array

E-vector is aligned to the x-axis). The co-polar and cross-polar measurements are obtained from the *gain X* and *gain Y* at $\phi = 45°$, respectively.

In some cases, to further reduce the computational loading and time, we could take advantage of the symmetry of the E- and H-field configuration of the horn (hereinafter simplified model). This is done by drawing only a quarter portion of the original model, including the free space environment, and assigning a *perfect E*-boundary condition at the x-plane, and a *perfect H*-boundary condition at the y-plane, as shown in Fig. 2.13b. This virtually creates a mirror image of the model on the other side of the x- or y- symmetric plane, hence resembling a full feed horn model.

As shown in Fig. 2.14, the far-field patterns simulated by HFSS using both simplified and full model match very well the results produced using modal matching. The sidelobe positions were almost identical, but at the power level below –30 dB, results from HFSS often show slightly lower power level and slight asymmetry. This is because the HFSS finite tetrahedron meshing imitating the horn model might not necessarily be entirely axial symmetric (see Fig. 2.13b).

Note that in the cross-polarization plots, the matching with modal matching was remarkably similar at the edge of the waveband. However, there were significantly different in the central waveband where the cross-polar level is substantially lower.

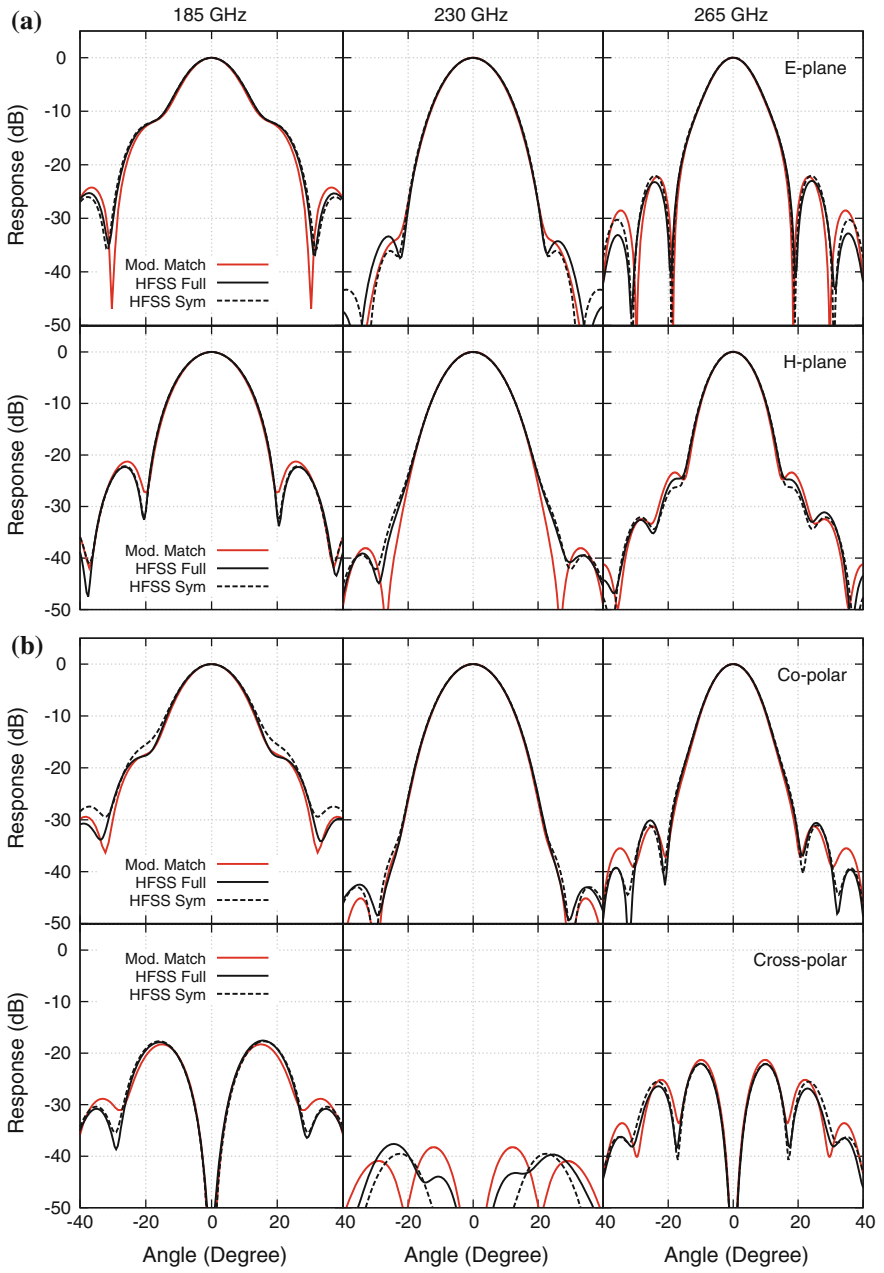

Fig. 2.14 Far-field patterns of a 3-section smooth-walled horn across the 230 GHz design wavebands, generated by *HornSynth*, a full-horn HFSS model and a simplified quarter-wedged horn HFSS model. **a** E- and H-plane. **b** Co- and cross-polarization

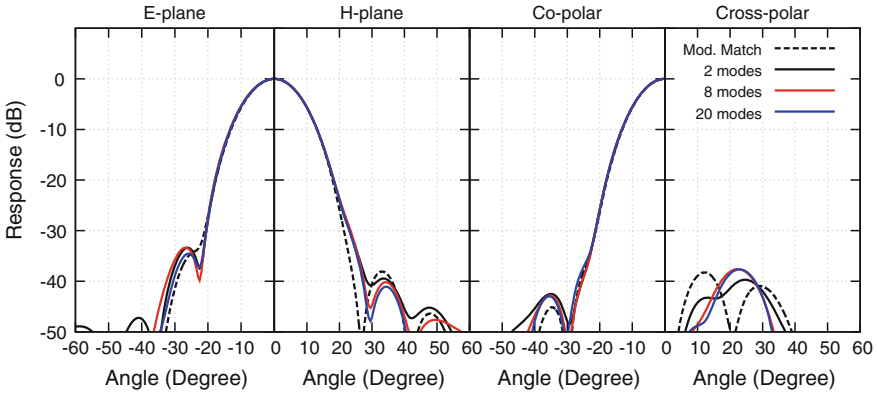

Fig. 2.15 Far-field patterns of a 230 GHz smooth-walled horn with 2, 8 and 20 modes, compared with the results from *HornSynth*

This again, shows that the HFSS has the limitation in accuracy for prediction of power levels below –40 dB, hence care should be taken when interpreting predictions at lower power levels.

Increasing the number of modes in the simulated wave port improves the accuracy of the HFSS model. However, this also increases the meshing frequency, hence effectively enlarges the electrical-size of the model. Figure 2.15 shows the comparison of simulating a 3-section smooth-walled horn with 2, 8 and 20 modes in the exciting port. As can be seen, the results in general were reasonable even when only using the TE_{11} and TM_{11} mode in the simulation. The main lobes match each other very well, but increasing the number of modes does help to improve the accuracy of the sidelobes. Nevertheless, increasing the number of modes more than 8 does not seem to show much improvement.

2.6.2 Tolerance Analysis

The use of HFSS to study the performance of a multiple flare-angle horn was largely motivated by the need for tolerance analysis to investigate the effect of lateral misalignment between the input waveguide and the horn. In Fig. 2.16, we have simulated this effect by setting the circular waveguide to be offset by 50–100 μm, and the simulated results were able to reproduce the asymmetry and the magnitude of the cross-polar patterns of the measured pattern with these settings. The smoothing of the dip in the cross-polarization pattern is also predicted correctly, especially in the case of Horn No. 2 from the first fabrication batch, where the offset is more severe. These results, together with the inspection of the horn interior, further confirmed that the lateral misalignment is the cause of the asymmetry and high cross-polar level measured previously in the first generation of the prototype horns.

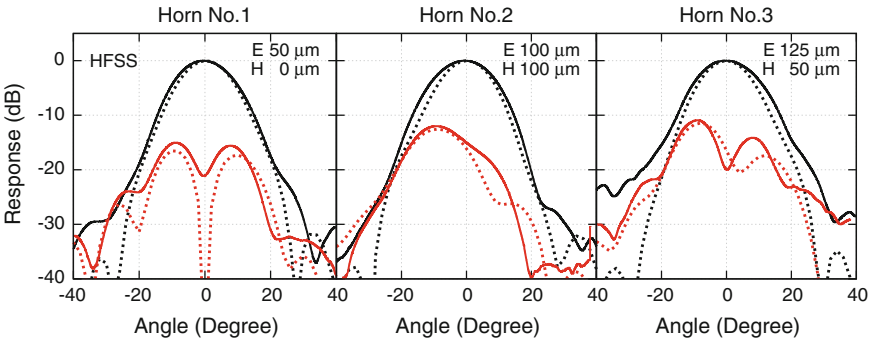

Fig. 2.16 Measurements of co- and cross-polarization for all three first generation prototype horns, comparing with HFSS simulation. The lateral misalignment used in the HFSS model are labelled on the *top right* of the panels, with E and H indicating the plane where the misalignment shifted, and the number indicating the amount of shifting. The *solid curves* are the measured data while the *dotted curves* are the computed patterns. The *black curves* represent the co-polarization patterns, while the *red curves* correspond to the cross-polarization patterns

2.6.3 Cross-Coupling Between Two Adjacent Horns

Cross-coupling between two adjacent horns within a focal plane array can greatly degrade the quality of astronomical data. In some cases such as CMB cosmology instruments, the level of cross-coupling must be well below –40 dB. In principle, the expected cross-coupling level can be estimated analytically (Olver et al. 1994) if the aperture fields of both feeds were known. However, this is complicated in general, as the aperture field of the horn is normally hard to describe accurately analytically, but this calculation can be easily done numerically using HFSS, utilising its full 3-D capability. Here, the cross-coupling level is defined as the ratio of the power received by one horn to the input power injected into the input of the adjacent one.

Figure 2.17 shows the cross-coupling of power between two adjacent horns, with 0.7 mm separation between the aperture edges of the two horns. HFSS predicts that the cross-coupling level is less than –50 dB across the required frequency band. The far-field pattern of the horn is not at all affected by this low level of coupling.

The simulated results were compared with the measured cross-coupling level between a two-horn array designed to operate from 210–250 GHz. Figure 2.18 shows the two adjacent horns that were milled directly into a single aluminium block with a 0.7 mm separation between the nearest edges of two horn apertures, a distance appropriate for a realistic packed array.

The cross-coupling measurement was performed using the ABmm® Vector Network Analyser (VNA) at Rutherford Appleton Laboratory, by measuring the power coupled between the transmitter and the receiver ports (see Fig. 2.18a). A carbon loaded epoxy cone was placed on top of the two-horn array to prevent the RF signal being reflected back to the receiver horn. The power measured by the VNA was then

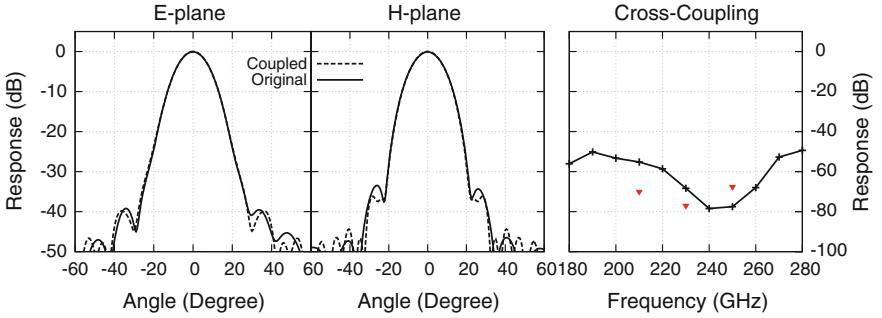

Fig. 2.17 The HFSS predicted far-field patterns of the radiating horn in the two-horn array, compared with the same patterns of a single horn. The panel on the *right* shows the comparison of HFSS predicted cross-coupling with the measured data. The *red triangle* indicates the measured response, while the *black thick line* represents the result predicted by HFSS

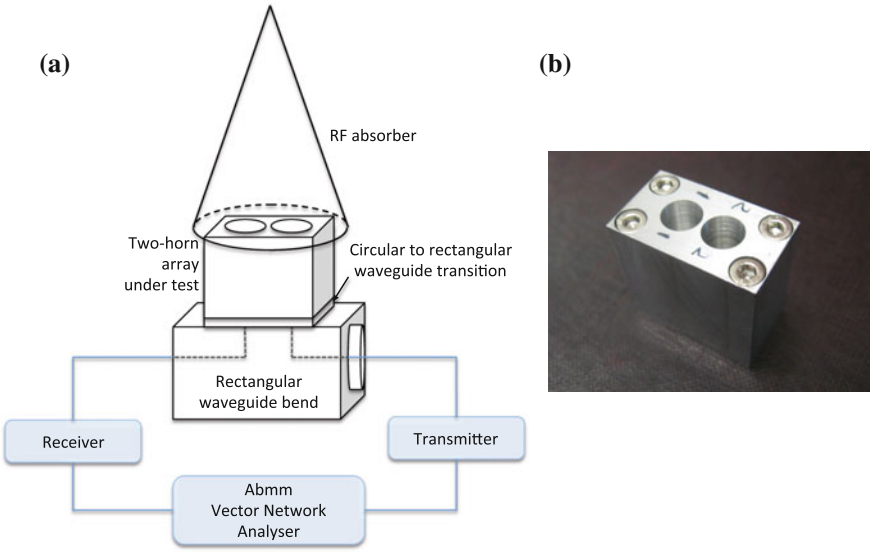

Fig. 2.18 **a** Schematic diagram showing the setup of Abmm® VNA to measure the cross-coupling between two horns. **b** Photo showing the two-horn array prototype

simply the cross-coupled RF power from the transmitter horn to the receiver horn caused by the fringing of the aperture fields.

Figure 2.17c, shows that the measured cross-coupling level agreed with the level predicted by HFSS, and was lower than –67 dB across the operating bandwidth. The measured far-field beam patterns of both horns showed high similarity as well (Leech et al. 2012), with the E- and H-plane measurements showing no deviation from the computed beam patterns of the individual horns. The very low level of cross coupling

between the two adjacent horn supported by the agreement with computed results demonstrates that smooth-walled horns fabricated by direct milling are suitable for employment in close packed focal plane arrays.

2.7 Summary

In this chapter, we have presented the design of a high performance multiple flare-angle horn that have radiation pattern similar to that of the conventional corrugated horn, but is much simpler to fabricate. The horn is suitable for producing a large number of feed horn for a closely packed focal plane arrays.

We have demonstrated that the multiple flare-angle design is feasible at frequencies as high as 700 GHz. The measured radiation patterns showed good performance and agreed well with modal matching across a bandwidth of 140 GHz, covering the entire astronomical window centred at 650 GHz. These results also demonstrate that the fabrication technology described above is effective in the sub-mm wavelength range.

We have also used HFSS to estimate and correctly predict the tolerances in fabrication that give rise to the asymmetry in the cross-polar patterns. This is important since conventional software packages cannot simulate non-axisymmetric errors. HFSS is also useful for estimating the cross-coupling level between two adjacent horns. We have measured the cross-coupling between two smooth-walled horns in an array and the results show a very low level of power coupling between the two horns, and good agreement with HFSS prediction.

References

Britton, J. W., Nibarger, J. P., Yoon, K. W., Beall, J. A., Becker, D., Cho, H. et al. (2010). Corrugated silicon platelet feed horn array for CMB polarimetry at 150 GHz. In *Society of Photo-Optical Instrumentation Engineers (SPIE) Conference Series*, vol. 7741.

Clarricoats, P. J. B. & Olver, A. D. (1984). *Corrugated horns for microwave antennas*. Peter Peregrinus Ltd.

Granet, C., James, G. L., Bolton, R., & Moorey, G. (2004). A Smooth-Walled Spline-Profile Horn as an Alternative to the Corrugated Horn for Wide Band Millimeter-Wave Applications. *IEEE Transactions on Antennas and Propagation*, *52*, 848–854.

Haupt, R. & Haupt, S. (1998). *Practical genetic algorithms.*. New York; Wiley-Interscience Publication.

James, G. L. (1981). Analysis and design of TE_{11}-to-HE_{11} corrugated cylindrical waveguide mode converters. *IEEE Transactions on Microwave Theory Techniques*, *29*, 1059–1066.

Kittara, P. (2002). *The development of a 700 GHz SIS mixer with Nb finline devices: Nonlinear mixer theory, design techniques and experimental investigation*. Ph.D. thesis, United Kingdom; University of Cambridge.

Kittara, P., Leech, J., Yassin, G., Tan, B. K., Jiralucksanawong, A. & Wangsuya, S. (2008). High performance smooth-walled feed horns for focal plane arrays. In *Proceedings of the Ninteenth International Symposium on Space Terahertz Technology*, 346–+.

Kittara, P., Yassin, G., Withington, S. & Smith, H. (2000). A pickett-potter horn-reflector antenna for submillimetre-wave applications. In *Eleventh International Symposium on Space Terahertz Technology*, pp. 589–598.

Kittara, P., Grimes, P., Yassin, G., Withington, S., Jacobs, K., & Wulff, S. (2004). A 700 GHz SIS antipodal finline mixer fed by a pickett-potter horn-reflector antenna. *IEEE Transactions on Microwave Theory Techniques*, *52*, 2352–2360.

Kittara, P., Jiralucksanawong, A., Yassin, G., Wangsuya, S., & Leech, J. (2007). The design of Potter horns for THz applications using a genetic algorithm. *International Journal of Infrared and Millimeter Waves*, *28*, 1103–1114.

Leech, J., Tan, B. K., Yassin, G., Kittara, P., Jiralucksanawong, A. & Wangsuya, S. (2010). Measured performance of a 230 GHz prototype focal-plane feedhorn array made by direct drilling of smooth-walled horns. In *Twenty-First International Symposium on Space Terahertz Technology*, pp. 114–119.

Leech, J., Tan, B. K., Yassin, G., Kittara, P., Wangsuya, S., Treuttel, J. et al. (2011). Multiple flare-angle horn feeds for sub-mm astronomy and cosmic microwave background experiments. *A&A*, *532*, A61+.

Leech, J., Yassin, G., Tan, B. K., Tacon, M., Kittara, P., Jiralucksanawong, A. et al. (2009). A new, simple method for fabricating high performance sub-mm focal plane arrays by direct machining using shaped drill bits. In *Proceedings of the 20th A International Symposium on Space Terahertz Technology*, 214–+.

Leech, J., Tan, B. K., Yassin, G., Kittara, P., & Wangsuya, S. (2012). Experimental investigation of a low-cost, high performance focal-plane horn array. *IEEE Transactions on Terahertz Science and Technology*, *2*(1), 61–70.

Ludwig, A. (1973). The definition of cross polarization. *IEEE Transactions on Antennas and Propagation*, *21*(1), 116–119.

Nelder, J. A., & Mead, R. (1965). A simplex method for function minimization. *The Computer Journal*, *7*(4), 308–313.

Olver, A. D., Clarricoats, P. J. B., Kishk, A. A., & Shafai, L. (1994). *Microwave horns and feeds*. Bath: Bookcraft.

Olver, A. D., & Xiang, J. (1988). Wide angle corrugated horns analysed using spherical modal-matching. *IEE Proceedings H: Microwaves Antennas and Propagation*, *135*, 34–40.

Pickett, H., Hardy, J., & Farhoomand, J. (1984). Characterisation of a dual mode horn for submillimetre wavelengths. *IEEE Transactions on Microwave Theory and Techniques*, *32*, 936–937.

Potter, P. (1963). A new horn antenna with suppressed sidelobes and equal beamwidths. *Microwave Journal*, *6*, 71–78.

Yassin, G., Kittara, P., Jiralucksanawong, A., Wangsuya, S., Leech, J. & Jones, M. (2007). A high performance horn for large format focal plane arrays. In *Proceedings of the Eighteenth International Symposium on Space Terahertz Technology*, 199–+.

Zeng, L., Bennett, C., Chuss, D. & Wollack, E. (2010). A low cross-polarization smooth-walled horn with improved bandwidth. In *IEEE Transactions on Antennas and Propagation*, *58*(4), 1383–1387. ISSN 0018-926X.

Chapter 3
SIS Mixer Theory

Overview: In this chapter, we review the fundamental SIS mixer theory, to provide a theoretical background for the subsequent studies presented throughout this thesis. This includes the quantum tunnelling mechanisms that occurs in an SIS junction, and the general principle of SIS heterodyne mixing theory. In particular, we will explain the various analysis techniques, such as impedance recovery, used extensively to assess the mixer performance.

3.1 Introduction

An SIS tunnel junction consists of two superconducting electrodes with a thin insulating barrier between them. Its operation as a heterodyne mixer relies on the quantum tunnelling of charge carriers through a physical barrier, typically a few tens of Å thick. This thin barrier allows the wave function describing the particle on one side of the barrier to have a finite probability amplitude at the opposite side, enabling the current to flow between two superconducting electrodes.

There exists two types of charge carrier in the superconductors, Cooper pairs and quasiparticles. In a superconductor below its critical temperature T_c, it is energetically favourable for two electrons with equal momenta but opposite spin to bind together and form a Cooper pair. The coupling between the pairs of electrons is mediated by their interaction with a phonon which allows them to condense to the lowest energy state. Quasiparticles, on the other hand, are single electron-like states. They arise when the Cooper pairs are broken by absorption of energy greater than their binding energy 2Δ, where Δ is the superconducting gap energy typically in the range of a few meV, corresponding to a few hundred GHz photons.

The excitation energy can be acquired through thermal absorption or an applied electromagnetic field. The gap energy can be expressed as a gap voltage using $V_{gap} = \frac{\Delta_1 + \Delta_2}{e}$, where Δ_1 and Δ_2 are the gap energies of each superconducting electrode across the barrier and e is the electron charge. In most cases, both electrodes are

B.-K. Tan, *Development of Coherent Detector Technologies for Sub-Millimetre Wave Astronomy Observations*, Springer Theses, DOI 10.1007/978-3-319-19363-2_3

made of the same superconductor, thus $V_{gap} = \frac{2\Delta}{e}$. The Bardeen-Cooper-Schrieffer (BCS) theory (Bardeen et al. 1957) reveals that the gap voltage is a strong function of physical temperature, for $T \approx T_c$

$$eV_{gap} \approx 3.52 k_B T_c \sqrt{1 - \frac{T}{T_c'}} \tag{3.1}$$

where k_B is the Boltzmann's constant and T is the physical temperature of the superconductor. The critical temperature T_c, and hence V_{gap} of a thin superconducting film, depend strongly on the quality of the superconductor. For an SIS junction, the gap voltage of the thin superconducting layer is slightly less than that of a bulk superconductor.

An important implication of the existence of a gap voltage is that it limits the highest frequency up to which the tunnel junction can still operate as a low-loss mixer. Beyond the gap frequency ($\upsilon_{gap} = \frac{eV_{gap}}{h}$), the incident photons break the Cooper pairs and the mixer circuits are no longer lossless. For niobium, this limit occurs at about 680 GHz. However, SIS junction can still operate up to twice this frequency limit (e.g.,Winkler and Claeson 1987; de Lange 1994), although the performance starts to deteriorate well above the superconducting gap frequency, due to the rapid rise of the superconductor's surface impedance, and hence the conduction loss.

Geometrically, an SIS tunnel junction forms a parallel plate capacitor. Hence, any RF signal across the junction will experience an intrinsic junction capacitance. This property influences both the RF and IF operation bandwidth of an SIS tunnel junction as a quantum mixer. This intrinsic capacitance can potentially short out the unwanted higher harmonics generated from the mixing process, but for maximum RF power coupling to the SIS junction, tuning structures are required to tune it out across the specific RF bandwidth (Raisanen et al. 1985; Kerr et al. 1988; Kerr and Pan 1990; Kerr et al. 1992).

3.2 Quasiparticle Tunnelling

From the BSC theory (e.g.,Cyrot and Pavuna 1992), the density of states for quasiparticles in a superconductor is given by

$$N(E) = \begin{cases} N(0)\dfrac{E}{\sqrt{E^2 - \Delta^2}}, & \text{if } E > \Delta \\ 0, & \text{if } E < \Delta \end{cases} \tag{3.2}$$

where $E = \sqrt{\varepsilon^2 + \Delta^2}$ and ε is the quasiparticle energy in normal state measured with reference to the Fermi level. Equation 3.2 clearly shows that no quasiparticles are allowed to exist within the gap. The density of state profile is illustrated graphically

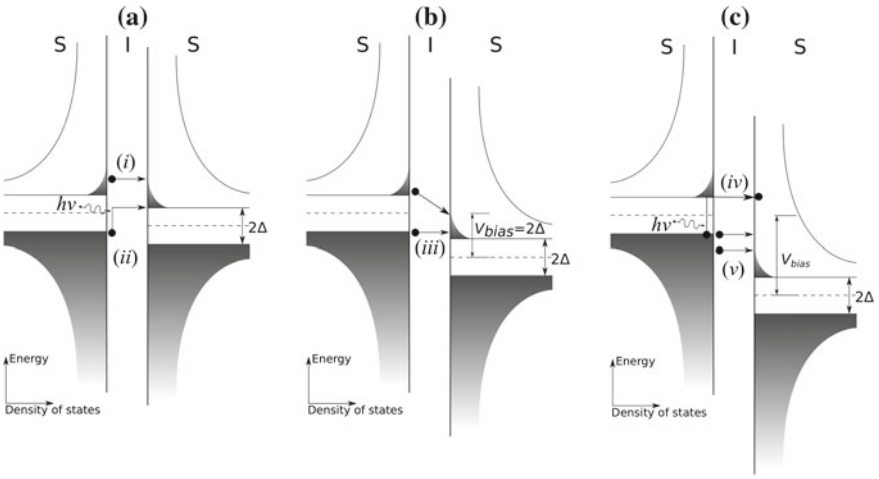

Fig. 3.1 Energy level diagrams illustrating how the potential difference and the absorption of photon energy influencing the magnitude of tunnelling current at various biasing stages. *i* Leakage current. *ii* Photon-assisted tunnelling before V_{gap}. *iii* Sudden rise in current at V_{gap}. *iv* Current suppression above the gap due to photon-absorbed quasiparticle reduces the number of empty state at the counter-electrode. *v* Linear increase in tunnelling current

in Fig. 3.1 using the so-called semiconductor picture, showing the density of states increasing sharply near the edge of the gap at both sides of the barrier. This causes a sudden rise in the nonlinearity of the SIS tunnel junction's IV characteristic, as shown in Fig. 3.2, and gives the SIS mixer superior mixing properties at high frequencies.

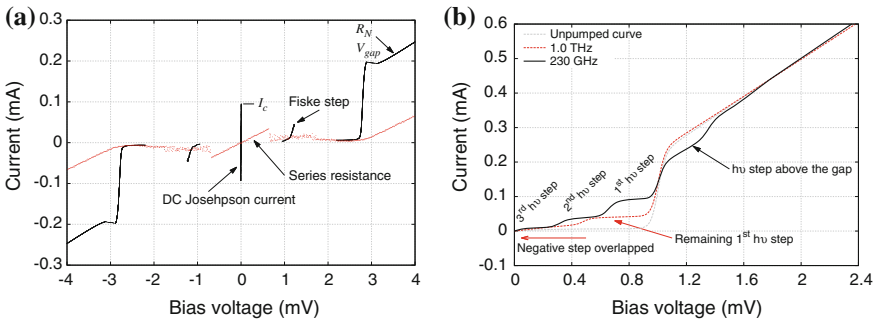

IV curves without LO illumination

LO pumped IV curves with magnetic field applied

Fig. 3.2 **a** *Black curve* Typical current-voltage (IV) characteristic curve of an SIS junction measured in a current-biased mode showing various features. *Red curve* IV curve of an SIS junction inflicted with a series resistance. **b** IV curves under illumination of 230 GHz and 1 THz LO signal showing the ordinary photon steps and the effect of negative step wrapping, respectively

When the tunnel junction is applied with a potential difference (V_b) across the barrier, the energy level of one electrode would be shifted with respect to the counter-electrode. The quasiparticle tunnelling current through the junction may then be calculated as (Tinkham 1996)

$$I(V_b) = C \int_{\infty}^{-\infty} \frac{\mathrm{d}N(E)}{\mathrm{d}E} \frac{\mathrm{d}N(E + eV_b)}{\mathrm{d}E} [f(E + eV_b) - f(E)] \, \mathrm{d}E, \tag{3.3}$$

where C is a constant representing the conductance of the junction at Ohmic state and the Fermi-Dirac distribution $f(E)$ is given by

$$f(E) = \frac{1}{e^{E/k_B T} + 1}. \tag{3.4}$$

Below the gap voltage, only a small number of thermally excited quasiparticles can tunnel across to the unoccupied states of the counter-electrode. This subgap current varies slowly with bias voltage at constant physical temperature, and is often referred to as the leakage current. When the bias voltage reaches V_{gap}, the large amount of empty states at the counter-electrode is suddenly available to the quasiparticles on the left, which gives rise to a rapid increase in the tunnelling current, resulting in an extremely nonlinear IV curve. Biasing beyond the gap voltage, the amount of quasiparticle tunnelling rises approximately linearly, following the normal resistance R_N, of the junction. In practice, the gap is broadened by several mechanisms such as the inhomogeneities within the junction area, the finite quasiparticle lifetime and the proximity effect, where part of the junction is not superconducting, forming micro SIN (superconductor-isolator-normal metal) junctions within the SIS junction. The latter effect shows up in the tunnel current above the gap as a small excess current.

3.2.1 Photon-Assisted Quasiparticle Tunnelling

Quasiparticles can tunnel through the barrier before $V_b = V_{gap}$, if they are illuminated with an external radiation of frequency υ, giving them enough energy to break the Cooper pairs. The condition for 'photon-assisted tunnelling' to happen is given by $nh\upsilon + eV_b > 2\Delta$, where n is an integer corresponding to the number of photons absorbed by a quasiparticle. For $n = 1$, the quasiparticles would be able to tunnel across the barrier before V_{gap} at $V_b > V_{gap} - \frac{h\upsilon}{e}$. This is shown as the first photon step just below V_{gap} in Fig. 3.2b. Quasiparticles can also absorb two or more photons but with much smaller probability, giving rise to second and higher order photon steps at much lower currents.

At bias voltages $V_{gap} + \frac{h\upsilon}{e}$ above the gap, a decrement in tunnelling current can be seen. The tunnelling of excited quasiparticles tunnel to the higher energy level at the counter-electrode reducing the number of empty states at the counter-electrodes available for fresh quasiparticles, hence lowering the magnitude of tunnelling current.

The limitation of SIS mixer operate to twice the gap frequency comes from the fact that the IV response of an SIS junction is antisymmetric. Obviously, the junction can still absorb photon energy $h\upsilon$ larger than the gap frequency. In this case, the first photon step will be extended to the negative biasing voltage side, as with the negative first photon step extends into the positive side. Due to the antisymmetric behaviour, this negative photon step will cancel out the positive photon step (Fig. 3.2b). In other words, the current flow from left-to-right is counter-balanced by the current flowing from right-to-left. This would reduce the size of the first photon step that is optimum for sub-mm mixing to region between the gap voltage and the end of the negative side photon step. This continues until the photon energy reaches twice the gap frequency. At this stage, the entire photon step is fully suppressed, and no biasing points will be available for mixing.

3.3 Cooper Pair Tunnelling

Both Cooper pairs and quasiparticles can tunnel across an SIS junction. Mixers employing Cooper pairs tunnelling are known as Josephson mixers to differentiate from SIS mixers that employ quasiparticles as the carrier. Early work that has been carried out on both types of mixers demonstrated that quasiparticle SIS mixers are superior in performance (sensitivity and stability) compared to Josephson mixers. Josephson mixers were therefore abandoned and it became customary to suppress pair tunnelling when operating the SIS mixers.

Cooper pair tunnelling currents, commonly referred to as Josephson tunnelling effect (Josephson 1962), can exhibit either a DC or AC behaviour. If no voltage is applied across an SIS junction, DC super current flows across the junction as a result of the direct tunnelling of Cooper pairs. The DC Cooper pairs tunnelling current can be described as $I = I_c \sin\varphi$, where I_c is the critical current given by $I_c \approx \dfrac{\pi V_{gap}}{4R_N}$, and φ is the superconducting wave function phase difference between the two superconductors. The phase φ can take any value between $\pm\pi$, hence the amplitude of the current can vary between $\pm I_c$ at 0 V. In normal circumstances, the DC super current is seen as a vertical line in the IV curve of an SIS junction (see Fig. 3.2a).

The AC Josephson effect occurs when a constant voltage is applied across the junction. The phase different now varies in time as

$$\frac{\mathrm{d}\varphi}{\mathrm{d}t} = \frac{2eV_b}{\hbar}, \qquad \text{thus} \qquad \varphi = \varphi_0 + \frac{2eV_b t}{\hbar}, \tag{3.5}$$

where V_b is the applied bias voltage. Inserting this time-varying phase difference into the DC tunnelling current equation gives $I = I_c \sin\left(\dfrac{2eV_b}{\hbar}t\right)$, which shows that the AC Josephson current oscillates at frequency $\upsilon = \dfrac{2eV_b}{h}$, corresponding to about 484 GHz/mV.

For normal photon-assisted SIS mixer operation, both types of Josephson current need to be suppressed, because they act as extra unstable current sources, hence add noise to the mixer. The junction's intrinsic capacitance can only partly short out these Cooper pairs currents, hence a magnetic field needs to be applied across the junction to suppress these unwanted currents. This technique is based on the fact that the critical current I_c have a strong dependence on magnetic field flux Φ. For a circular junction, I_c is modulated by Φ according to

$$I_c = 2I_c(0)\left|\frac{J_1(x)}{x}\right|, \quad x \sim \frac{\Phi}{\Phi_0} \tag{3.6}$$

where J_1 is the Bessel function of the first kind, and Φ_0 is the magnetic flux quantum $\frac{h}{2e}$ (Kooi 2008). The magnetic field strength required to generate the equivalent magnetic flux quantum is approximately $B = \frac{\Phi_0}{l(d+2\lambda)'}$ where l is the length of the junction size perpendicular to the direction of B-field, d the barrier thickness, and λ the magnetic penetration depth.

3.3.1 Fiske Steps and Shapiro Steps

As we have mentioned previously, the junction capacitance shorts out the AC Josephson current, except at the RF operating frequency where the junction capacitance is tuned out by the tuning circuit. Without the applied magnetic field, this allows the AC Josephson current to flow at these frequencies, and thus a gradual rise in the current near the middle of the subgap region as shown in the DC IV curve in Fig. 3.2a. This feature is normally referred to as the Fiske step (Fiske 1964). The value of the bias voltage that maximises the Cooper pair tunnelling current (V_{Fiske}) corresponds to the resonant frequency (f_{res}) of the tuning circuit, given by $f_{res} = \frac{2eV_{Fiske}}{h} \approx 484(\text{GHz/mV}) \times V_{Fiske}(\text{mV})$. This is a valuable tool which provides a first order assessment of the RF tuned frequency. Hence, the RF performance of the device under test can be probed quickly by wiring the device to an appropriate jig and dipping it into 4 K liquid helium to cool the device below its T_c.

Under the illumination of an RF power source, the AC Josephson oscillations can be excited at discrete voltage steps $S_n(mV) = \frac{nh\upsilon_{LO}}{2e} = \frac{n\upsilon_{LO}}{484(GHz)'}$ where n is an integer and υ_{LO} is the frequency of the RF source. These step features are known as Shapiro steps (Shapiro 1963). Shapiro steps have a sharp nonlinearity, and it is this sharp nonlinearity that is utilised in the Josephson mixer for high gain down-conversion. However, if the tunnel junction is configured to operate as an SIS mixer, biasing on Shapiro step normally causes large excess of noise in the mixer, resulting in unstable receiver behaviour. Thus, they are normally suppressed with the applied magnetic field, and the the mixer is biased at voltages distant away from these steps.

3.4 General Mixer Theory

A simple SIS mixer system can be represented using a Thevénin or a Norton equivalent circuit network, as shown in Fig. 3.3a. Here, the induced LO current source I_{LO} is connected in parallel with an embedding admittance Y_{emb}, while the SIS junction is represented by its intrinsic admittance Y_J. The two parameters I_{LO} and Y_{emb} are influenced by other components connected to the SIS junction, such as the tuning circuits, finlines, waveguide, etc. Since the electromagnetic behaviour of most of these external components are frequency dependent, the value of both I_{LO} and Y_{emb} vary with frequency. From this simple network representation, it is not hard to see that as long as I_{LO}, Y_{emb} and Y_J are known, the voltage V_J across the junction can be found, and thus the current I_J it generates.

Fundamental circuit theory requires that $Y_{emb} = Y_J^*$ for the maximum power transfer from the RF/LO to the SIS junction i.e., the junction capacitance is fully tuned out, leaving only an ohmic junction. If this condition is met, then the power absorbed by the junction is $P_{AV} = \dfrac{|I_{LO}^2|}{8G_{emb}}$, where G_{emb} is the real part of the source admittance, assuming the LO power is much stronger than the RF signal.

Let's us first consider the situation where the SIS junction is not illuminated with an LO and simply biased through an applied voltage across the junction and solve for the induced current generated in the junction. This can be obtained from Tucker's quantum detection theory (Tucker 1979; Tucker and Feldman 1985), which provides the fundamental framework for describing the behaviour of an SIS mixer. Its formulation is based mainly on the modified transfer Hamiltonian of tunnelling, where a term describing the effect of coupling across the barrier is added to the superconductor's quasiparticle Hamiltonian i.e.,

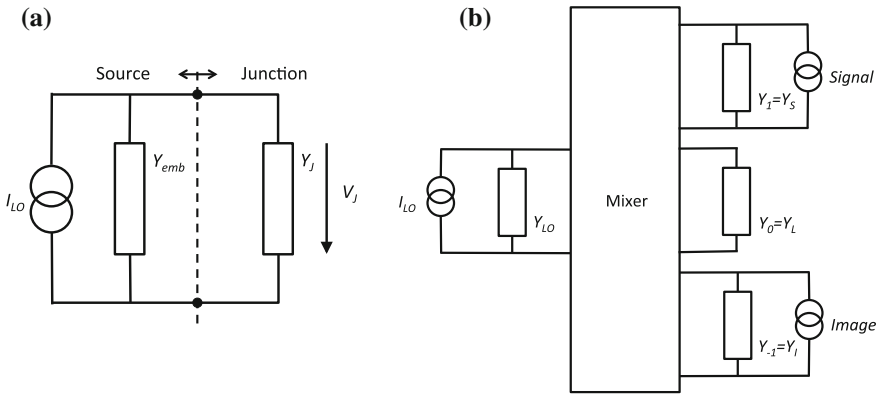

Fig. 3.3 A simple SIS mixer model represented as an equivalent Norton circuit. **a** Radiation source coupled to a junction as load admittance, **b** heterodyne mixer in 3-port approximation

$$H_T = \sum_{\kappa q \sigma} (T_{kq} c_k^\dagger c_q + T_{qk}^* c_q^\dagger c_k) = H_T^+ + H_T^-, \tag{3.7}$$

where c_k and c_q are the operators describing the Bloch states of the quasiparticles in both electrodes, and T_{kq} the matrix element representing the barrier penetration between states of comparable energy level. This Hamiltonian can be split into H_T^+ and H_T^-, where each term characterises the tunnelling of quasiparticles in either direction.

The effect of applied voltage $V(t)$ can be introduced coherently onto the wave function of the quasiparticle states on the ungrounded electrode as a modulation of its phase factor given by

$$f(t) = \exp\left[-\frac{ie}{\hbar}\int_0^t V(t')\mathrm{d}t'\right], \tag{3.8}$$

which can be Fourier transformed into $\int_{-\infty}^{\infty} W(\omega)e^{-i\omega t}\mathrm{d}\omega$ to give the phase factor $W(\omega)$. From this, the average quasiparticle tunnelling current can be evaluated as (Werthamer 1966)

$$\langle I(t)\rangle = \mathrm{Im}\int_{-\infty}^{\infty} W(\omega')W^*(\omega'')e^{-i(\omega'-\omega'')t}\, j\left(V_0 + \frac{\hbar\omega'}{e}\right)\mathrm{d}\omega'\mathrm{d}\omega'' \tag{3.9}$$

where V_0 is the bias voltage and $j(V)$ is the response function of the junction given by

$$j(V) = i I_{dc}(V_0) + I_{KK}(V_0), \tag{3.10}$$

where $I_{dc}(V_0) = \mathrm{Im}[j(V)]$ is the junction DC IV curve. The reactive tunnel current $I_{KK}(V_0)$ can be found via the Kramer-Kronig (KK) transform of $I_{dc}(V_0)$,

$$I_{KK}(V_0) = \mathrm{Re}[j(V)] = P\int_{-\infty}^{\infty} \frac{\mathrm{d}V'}{\pi}\frac{I_{dc}(V') - V'/R_N}{V' - V}, \tag{3.11}$$

where P is the Cauchy principle value for the integral, I_{dc} is the unpumped IV curve, V' is the IV curve voltage and R_N is the normal state resistance of the SIS junction.

3.4.1 Large Signal Analysis

Under the LO illumination, the potential difference across the junction can be modified to incorporate the periodic voltage induced by the LO source as

$$V(t) = V_0 + \sum_{p=1}^{\infty} V_p e^{-ip\omega t} \tag{3.12}$$

where V_p is the complex amplitude of the pth harmonic of the LO source. This changes the phase factor of the quasiparticle Bloch states into

$$f(t) = \exp\left[-i\sum_{p=1}^{\infty}\alpha_p \sin(p\omega t + \phi_p)\right] = \prod_{p=1}^{\infty}\sum_{n=-\infty}^{\infty} J_n(\alpha_p)e^{-inp(\omega t+\phi_p)}. \tag{3.13}$$

Here, $\alpha_p = \dfrac{\omega_{gap}|V_p|}{p\omega} = \dfrac{|V_p|}{pV_{ph}}$ is a dimensionless quantity describing the level of LO driving power at pth harmonic, $V_{ph} = \dfrac{\omega}{\omega_{gap}}$ is the normalised photon voltage, ϕ_p is the phase of the voltage at pth harmonic and J_n is the nth order of the Bessel function of the first kind. Assuming the higher harmonics of the LO are all shorted out, the junction drive level can be simplified to $\alpha_p = \dfrac{eV_{LO}}{h\upsilon}$.

Inserting Eq. 3.13 into 3.8 and solving for 3.9, we obtain

$$I_{LO}(t) = \mathrm{Im}\sum_{n,m=-\infty}^{\infty} J_n(\alpha)J_{n+m}(\alpha)e^{-im\omega t}\, j\left(V_0 + \frac{n\hbar\omega}{e}\right). \tag{3.14}$$

Given that the junction capacitance practically shunts the second and higher LO harmonics, we can limit our calculation to the value of $m = -1, 0, 1$. The LO pumped DC IV curve of the junction can now be written with $m = 0$ as

$$I_{dc}(V_0, V_{LO}) = \sum_{n=-\infty}^{\infty} J_n^2(\alpha) I_{dc}(V_0 + \frac{n\hbar\omega}{e}), \tag{3.15}$$

while the complex tunnelling current induced by the LO in the SIS junction can now be defined as $I_{LO}^{\omega} = I'_{LO} + i\,I''_{LO}$, where

$$I'_{LO}(V_0, V_{LO}) = \sum_{n=-\infty}^{\infty} J_n(\alpha)[J_{n-1}(\alpha) + J_{n+1}(\alpha)]I^0_{dc}(V_0 + \frac{n\hbar\omega}{e}), \tag{3.16}$$

$$I''_{LO}(V_0, V_{LO}) = \sum_{n=-\infty}^{\infty} J_n(\alpha)[J_{n-1}(\alpha) - J_{n+1}(\alpha)]I_{KK}(V_0 + \frac{n\hbar\omega}{e}). \tag{3.17}$$

3.4.2 Small Signal Analysis

The above analysis dealt with only the direct current induced from a single frequency component, the LO signal, and did not include the effect of mixing of the LO with the RF signals at the USB and LSB frequencies. To evaluate the mixer behaviour in

the present of weak RF radiation and a strong LO signal at frequency ω_{LO}, we have to replace the 'one-port' model of the junction shown in Fig. 3.3a with the 'four-port' model in Fig. 3.3b.

In principle, each sideband signal at a frequency $\omega_m = m\omega_{LO} + \omega_0$ will mix with the LO and its harmonics, down-converting them to the same intermediate frequency $\omega_{IF} = \omega_0$. Nevertheless, as we have already mentioned, we shall only concentrate on the frequency components $m = \pm 1$, assuming that all the higher harmonics are shorted by the SIS junction's intrinsic capacitance. In the following discussion, we shall assume the useful RF signal is in the USB, hence $\omega_{+1} \equiv \omega_S$ is the signal and the LSB $\omega_{-1} \equiv \omega_I$ is the image sideband.

In this 'four-port' model, the junction is connected with four frequency ports at the signal, LO, image, and the IF frequency ports. Similar to the LO source, the signal and image port are connected to an equivalent power source (representing the RF signal or white noise), while the IF port is terminated with a load of conductance G_L. For a DSB mixer, the electrical properties of the RF signal from the sky is thus the sum of both sidebands, given by

$$V_{RF}(t) = \mathrm{Re} \sum_{m=-\infty}^{\infty} V_m e^{i\omega_m t} \quad \text{and} \quad I_{RF}(t) = \mathrm{Re} \sum_{m=-\infty}^{\infty} I_m e^{i\omega_m t} \quad (\text{for} \quad m \neq 0). \tag{3.18}$$

Both voltage and current component of each sideband can therefore be related linearly in term of $I_m = \mathrm{Re} \sum_{m'} Y_{mm'} V_{m'}$, via the admittance matrix $Y_{mm'} = G_{mm'} + i\,B_{mm'}$, where $Y_{mm'}$ is the matrix elements that sums up all the interaction of the tunnel junction with the different frequencies given by

$$\begin{pmatrix} I_1 \\ 0 \\ I_{-1} \end{pmatrix} = \begin{pmatrix} Y_{1,1} + Y_{USB} & Y_{1,0} & Y_{1,-1} \\ Y_{0,1} & Y_{0,0} + Y_L & Y_{0,-1} \\ Y_{-1,1} & Y_{-1,0} & Y_{-1,-1} + Y_{LSB} \end{pmatrix} \begin{pmatrix} V_1 \\ V_0 \\ V_{-1} \end{pmatrix} \tag{3.19}$$

where I_1, Y_{USB} and I_{-1}, Y_{LSB} are the amplitude and internal impedance of the equivalent signal source at the USB and LSB frequency, Y_L is the load impedance at the IF port, and V_1, V_0 and V_{-1} are the voltages across the different ports. This conversion matrix $Y_{mm'}$ entirely describes the mixing behaviour of the device, where the real and imaginary part of $Y_{mm'}$ were derived by Tucker and Feldman (1985) as

$$\begin{aligned} G_{mm'} = \frac{e}{2\hbar\omega_{m'}} \sum_{n,n'=-\infty}^{\infty} J_n(\alpha) J_{n'}(\alpha) \delta_{m-m',n'-n} [I_{dc}(V_0 + \frac{\hbar}{e}(n'\omega + \omega_{m'})) \\ - I_{dc}(V_0 + n'\frac{\hbar\omega}{e}) + I_{dc}(V_0 + n\frac{\hbar\omega}{e}) - I_{dc}(V_0 + \frac{\hbar}{e}(n\omega - \omega_{m'}))], \end{aligned} \tag{3.20}$$

and

$$B_{mm'} = \frac{e}{2\hbar\omega_{m'}} \sum_{n,n'=-\infty}^{\infty} J_n(\alpha) J_{n'}(\alpha) \delta_{m-m',n'-n} [I_{KK}(V_0 + \frac{\hbar}{e}(n'\omega + \omega_{m'})) - I_{KK}(V_0 + n'\frac{\hbar\omega}{e}) + I_{KK}(V_0 + n\frac{\hbar\omega}{e}) - I_{KK}(V_0 + \frac{\hbar}{e}(n\omega - \omega_{m'}))]. \tag{3.21}$$

To obtain $Y_{mm'}$, one could expands the total current through the barrier $\langle I(t)\rangle = I_{LO}(t) + I_{RF}(t)$ and the total voltage across the barrier $V(t) = V_0 + V_{LO}(t) + V_{RF}(t)$, or through the measured DC IV curve and its KK transformation, since they in principle contains all the information regarding both quantities of interest.

3.4.3 Impedance Recovery

Analysis of the mixer behaviour requires the measurement of the pumped DC current $I_{dc}(V_0, V_{LO})$ and the unpumped IV curve ($\alpha = 0$). From this, we can solve for the pump parameter α at each bias point. Once α is known, the current I^{ω}_{LO} generated from the SIS junction can be calculated. Referring back to Fig. 3.3a, we can see that the only remaining unknown parameters now are Y_{emb} and I_{LO}, since the equivalent circuit can be described by

$$I_{LO}(V_0, V_{LO}) = Y_{emb} V_{LO} + I^{\omega}_{LO}(V_0, V_{LO}). \tag{3.22}$$

Both of these parameters can be recovered following the method first described by Skalare (1989). This method matches the RF voltage across the junction $V_{LO} = \frac{\alpha\hbar\omega}{e}$ at a certain bias point. Therefore, at each of this bias points, we are provided with an independent equation in the form of Eq. 3.22. By solving (or minimising the error of)

$$|I_{LO}(V_0, V_{LO})|^2 - |Y_{emb} V_{LO} + I^{\omega}_{LO}(V_0, V_{LO})|^2 = 0 \tag{3.23}$$

for several bias points (typically on the linear portion of the first photon step) iteratively, the parameters Y_{emb} and I_{LO} can be found.

In our analysis, we have used SuperMix[1] to implement impedance recovery. Here, the SuperMix circuit model consists of only the equivalent circuit i.e., a linear source impedance and an embedding impedance to be found, connected to an SIS tunnel junction. By supplying this simple model with experimentally measured pumped

[1]The software library developed by the California Institute of Technology's Submillimeter Astrophysics Group (Caltech) specifically to aid the calculation and analysis of high-frequency SIS mixer circuits (Ward et al. 1999; Rice et al. 2000). It can be downloaded from https://www.submm.caltech.edu/supermix.

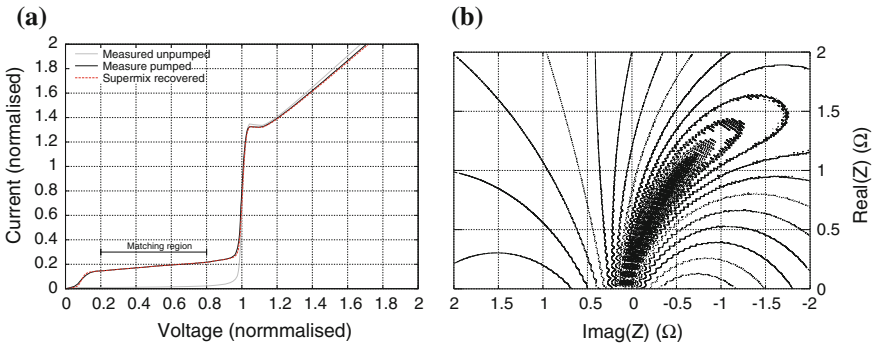

Fig. 3.4 Example of embedding impedance recovery using SuperMix of a slightly capacitively tuned device. **a** Recovered IV curve, **b** contour of the error surface

and unpumped IV curves, it can be coded such that a range of bias points are swept through, to find a combination of α, Y_{emb} and I_{LO} that match the theoretically generated pumped IV curve with the experimentally obtained one. This is normally done across a portion ($\sim$90 %) of the first photon step, as shown in Fig. 3.4.

Even without complicated computational calculation, one can in fact estimate to first order the embedding impedance by simply observing the slope of the first photon step. This results from the fact that the susceptance of a perfectly tuned junction shifts from capacitive to inductive at the first photon step, as shown in Fig. 3.5a. If the junction capacitance is not fully cancelled out i.e., a slightly capacitive device (Fig. 3.5b), the residual embedding capacitance resonates with the inductive susceptance of the junction near the rear edge of the first photon step. This results in stronger absorption of the LO power toward the gap, hence the positive slope of the first photon step. On the other hand (Fig. 3.5c), if the junction capacitance is over-compensated at a certain frequency, the situation is just the opposite. Closer to the gap, there would be a large mismatch between the inductive source and the junction inductive susceptance. This reduces the LO power absorbed by the junction, hence the negative slope of the first photon step.

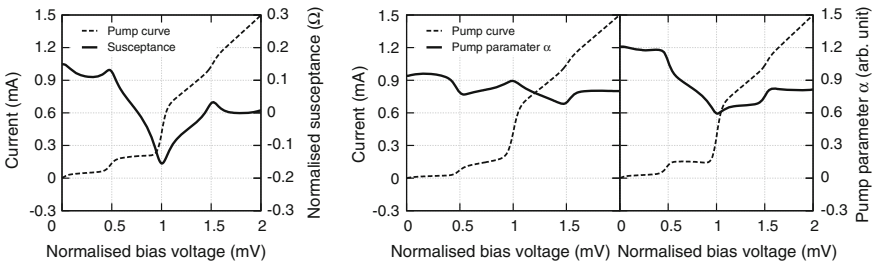

Fig. 3.5 (*Left panel*) Examples showing the pumping level and the normalised susceptance of a tuned SIS mixer pumped at 345 GHz. (*Right panel*) show the pumped curves and how the pump parameter for a slightly capacitive (*left*) and a slightly inductive (*right*) SIS mixer varies against the bias voltages

3.5 Measurement of the SIS Mixer Performance

3.5.1 Y-Factor Noise Temperature Measurement

An SIS mixer can in principle achieve conversion gain $G_0 > 1$, and its sensitivity is commonly defined by the amount of noise power (P_N) generated by the mixer device. This noise power is related approximately to its equivalent noise temperature T_N via the Rayleigh-Jeans (R-J) approximation, $P_N = k_B T_n \delta_\upsilon$, where δ_υ is the bandwidth of the receiver. The noise power P_N of an SIS mixer can be estimated using the standard Y-factor method, by measuring the mixer's output power at two different input power levels. The two power levels are typically generated using radiating/absorbing loads at room temperature (293 K, hereinafter the hot load) and at the boiling point of liquid nitrogen (77 K, hereinafter the cold load). The measured noise power is then given by

$$P_N = \frac{P^{in}_{hot} - Y P^{in}_{cold}}{Y - 1}, \qquad \text{or equivalently,} \qquad T_N = \frac{T_{hot} - Y T_{cold}}{Y - 1}. \tag{3.24}$$

Here, T_{hot} and T_{cold} are the radiation temperature of the hot and cold loads, and $Y = \frac{P^{out}_{hot}}{P^{out}_{cold}}$, where $P^{out}_{hot} = G_0(P^{in}_{hot} + P_N)$ and $P^{out}_{cold} = G_0(P^{in}_{cold} + P_N)$. Strictly speaking, these sets of equations are only valid at low frequency, where the R-J approximation still holds. At higher frequencies, a more accurate expression (Callen and Welton 1951) is available but, as shown in e.g., Kittara (2002) and Grimes (2006), the difference at 700 GHz is only about 1.5 %. Hence throughout this thesis, we will only use the R-J approximation.

Y-factor measurements estimate the overall noise temperature added by the whole receiver, which does not include only the SIS junction, but all the losses contributed by the other components forming the complete receiver. To understand the noise contribution from these various components, we can represent the receiver as a simple cascaded circuit made up of noisy electrical components. The receiver noise temperature can then be written as

$$T_N = T_1 + \frac{T_2}{G_1} + \frac{T_3}{G_1 G_2} + \cdots + \frac{T_n}{G_1 G_2 \ldots G_{n-1}}, \tag{3.25}$$

where $T_1, T_2, \ldots, T_n$ are the input noise temperatures and, $G_1, G_2, \ldots, G_n$ are the gain of each component respectively, assuming a perfect impedance match between the components. The overall system gain is then simply $G_0 = G_1 G_2 \ldots G_n$. For passive components, the effective noise temperature is given as $T_{eff} = \left(\frac{1}{G} - 1\right) T$, where T is the physical temperature and $1/G$ is the attenuation (loss).

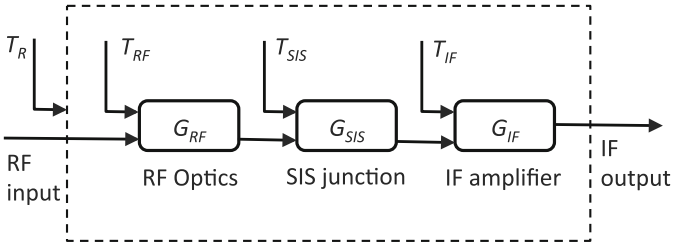

Fig. 3.6 Diagram showing the various components in an SIS receiver that contribute to the overall noise temperature

An effective way to estimate the receiver noise temperature is to break the complete receiver into three main sub-systems: the RF, the IF and the junction itself. This is shown in Fig. 3.6, which expresses the receiver's noise temperature as

$$T_N = \left(\frac{1}{G_{RF}} - 1\right) T_{RF} + \frac{T_{SIS}}{G_{RF}} + \frac{T_{IF}}{G_{RF} G_{SIS}}. \tag{3.26}$$

This example assumes that the first stage cryogenic IF amplifier has a very large gain that would makes the noise contribution from the subsequent components negligible.

In the above formulation, the RF noise contribution is given by all the components before the SIS junction (i.e., optics and transmission line losses), while the IF contribution is the noise temperature of the various amplification stages and other IF components after the junction. There exist several experimental techniques (Ke and Feldman 1994; Buffey 1999; Woody et al. 1985) for estimating the noise contribution of these sub-systems independently, which shall be described below.

3.5.1.1 RF Noise Contribution

We can simplify Eq. 3.26 as

$$T_N = T' + \frac{T_{IF}}{G_{RF} G_{SIS'}} \quad \text{where} \quad T' = \left(\frac{1}{G_{RF}} - 1\right) T_{RF} + \frac{T_{SIS}}{G_{RF}} \tag{3.27}$$

is now the total RF noise contribution in front of the junction, including the junction noise. If a load at temperature T_{in} is placed in front of the mixer, the power output per unit instantaneous bandwidth can be written as $P_{out}(T_{in}) = k_B(T_N + T_{in})G_0$, where $G_0 = G_{RF} G_{SIS} G_{IF}$. Substituting for T_N, we have $P_{out}(T_{in}) = k_B(T' + T_{in})G_0 + k_B T_{IF} G_{IF}$. If we plot P_{out} against T_{in}, we obtain a straight line with a slope of $k_B G_0$ and y-axis interception at $k_B(T_{IF} G_{IF} + T' G_0)$.

It is well known that the mixer gain G_{SIS} (and hence G_0) is a strong function of the LO pump level, whereas the mixer noise T_{SIS} varies only slowly with the LO power level below the peak gain (Ke and Feldman 1994). Hence, assuming that

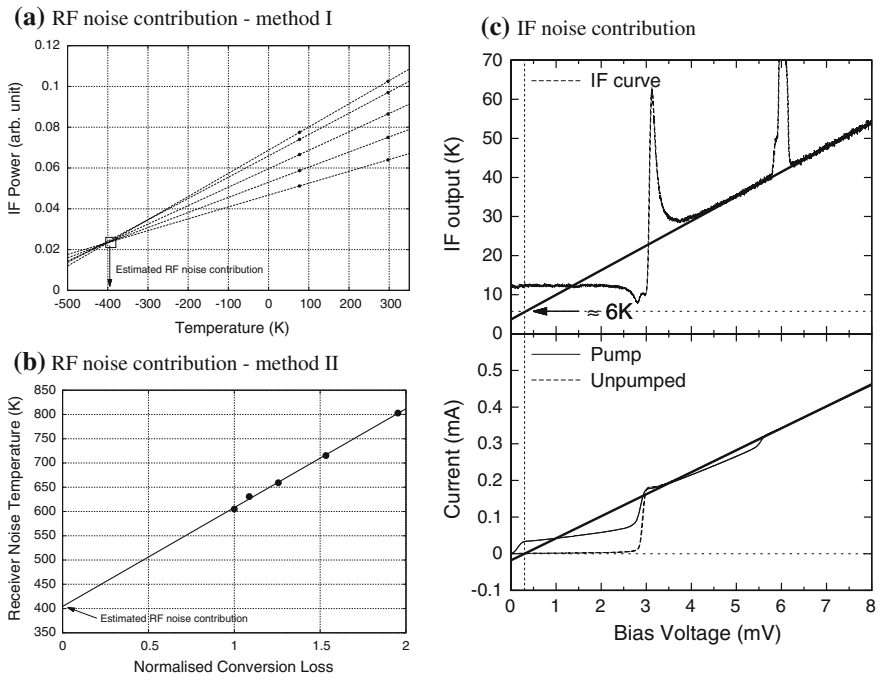

Fig. 3.7 Examples showing **a** and **b** the intersecting line methods for estimating the total contribution of RF losses to the mixer noise temperature, and **c** IF gain calibration method for estimating IF noise

T_{SIS} remains constant, we can plot a series of straight lines by varying the LO power level (hence $k_B G_0$), with $T_{in} = T_{in,hot}$ and $T_{in} = T_{in,cold}$ for the two data points that defines the straight line. All these lines will intersect at $T_{in} = -T'$, with $P_{out} = k_B T_{IF} G_{IF}$. This graphical method, as illustrated in Fig. 3.7a, provides a convenient mean to estimate the RF noise.

Another way to visualise this is by plotting the normalised conversion loss $(1/G_0)$ against the measured noise temperature (Tong et al. 2008), as depicted in Fig. 3.7b. This technique is based on the formulation where we could rewrite Eq. 3.27 as $T_N = \frac{G_{IF} T_{IF}}{G_0} + T'$, by replacing $G_{RF} G_{SIS} = \frac{G_0}{G_{IF}}$. Now, if we plot T_N versus $1/G_0$, we would obtain a straight line with a slope of $G_{IF} T_{IF}$ and a y-axis intersection at T', which is the estimated RF noise contribution.

3.5.1.2 Conversion Gain and If Noise Contribution

The conversion gain of the SIS mixer can be estimated experimentally using the shot noise property of the junction itself (Woody et al. 1985). The shot noise contribution from an unpumped SIS junction can be written as (Rogovin and Scalapino 1974)

$$T_{shot} = \frac{1}{2k_B} e I_{DC} R_{dyn} \coth\left(\frac{eV_b}{2k_B T_{phys}}\right), \tag{3.28}$$

where I_{DC} is the DC tunnelling current, R_{dyn} is the dynamic impedance of the junction, and T_{phys} is the physical temperature of the system, at bias voltage V_b. Above the gap, the tunnelling current rises approximately linear with bias voltage. The IF output in this region arises from the shot noise generated by the junction itself. Equation 3.28 at this linear portion of the DC IV curve can then be simplified to

$$T_{shot} \approx \frac{e I_{DC} R_N}{2k_B} + \text{constant} \approx 5800 \times V_b + \text{constant}, \tag{3.29}$$

where R_N is the normal resistance of the junction, the bias voltage $V_b = I_{DC} R_N$, and its gradient approximates to 5.8 K/mV. Dividing this with the gradient measured from the IF output curve (in arbitrary units (au) per mV) above the gap voltage region, gives the scaling factor X_{IF} in the units of K/au. The reciprocal of this scaling factor is in fact, the gain of the IF components, $G_{IF} = \frac{1}{X_{IF}}$, in the unit of au/K, since it represents the measured output power of the IF system, with reference to the known junction's shot noise power at the IF input port.

Now consider a simple two component system, consisting of only the SIS mixer (ignoring the passive RF components) connected to an IF amplifier (concatenation of various IF amplification stages). Using the R-J approximation, we can write the output power at the output port of the SIS mixer (or input power for the IF amplifier) and the measured output power from the IF amplifier as

$$P_{out,mix} = G_{mix} k_B (T_{in,hot} - T_{in,cold}) \quad \text{and,} \quad P_{out,final} = k_B (T_{out,hot} - T_{out,cold}), \tag{3.30}$$

respectively. Note that here, G_{mix} is actually the product of $G_{RF} G_{SIS}$, not just the actual gain of the SIS junction itself, if the RF components are included in the calculations. Since IF amplifier gain G_{IF} is already known, we can now estimate the mixer conversion gain i.e.,

$$G_{IF} = \frac{P_{out,final}}{P_{out,mix}} = \frac{T_{out,hot} - T_{out,cold}}{G_{mix}(T_{in,hot} - T_{in,cold})} \qquad \text{hence,}$$
$$G_{mix} = \frac{1}{G_{IF}} \times \frac{T_{out,hot} - T_{out,cold}}{T_{in,hot} - T_{in,cold}}. \tag{3.31}$$

We can also use the shot noise property of the SIS junction to estimate the noise contribution of the IF sub-system. The shot noise current does not start to flow before a finite voltage $V_{I=0}$ is reached. $V_{I=0}$ can be found by extrapolating the linear portion (above the gap) of the junction's unpumped DC IV curve back to the zero current axis (Woody et al. 1985). At this point, the shot noise contribution from the junction is zero, therefore the IF output power generated by the junction must also be zero. Performing the same extrapolation on the IF curve and measuring the output power

at $V_{I=0}$, we can find the additional noise generated by the IF system itself. This method for estimating the IF noise contribution is illustrated graphically in Fig. 3.7c.

3.5.2 Noise Temperature and Gain Correction for Optical Losses

The warm optical components in front of the mixer i.e., beam splitter, Dewar window and infrared (IR) filter, can account for a large portion of the RF loss. To obtain a closer estimate of the mixer's actual performance, we often correct the measured T_N for these losses.

The optical properties of both the beam splitter and the Dewar window can be calculated by considering them as a Fabry-Perot interferometer as described in Goldsmith and Button (1982). For the beam splitter, the transmission coefficient at several hundred GHz is approximately inversely proportional to its thickness, which is generally around a few tens of microns. Dewar windows, on the other hand, have to be made much thicker (in the range of several hundred microns) so that they are strong enough to withstand the atmospheric pressure against the vacuum inside the Dewar. They are normally made out of polyethylene, and since their thicknesses are closed to the wavelength of the GHz signal, they have to be designed such that they would have the maximum transmission near the mixer operating frequency band. Figure 3.8 shows some examples of the calculated reflection losses from the beam splitters with various thickness, and a flat 660 μm thick HDPE window. Note that these calculations do not take into account the absorption losses due to the water content which could be significant, especially in the case of beam splitters that are exposed to the moist atmosphere. Direct measurements of beam splitter losses made by Isaak (1995) at 550 GHz show that the measured value can sometimes be higher than the theoretical prediction by about 13 %.

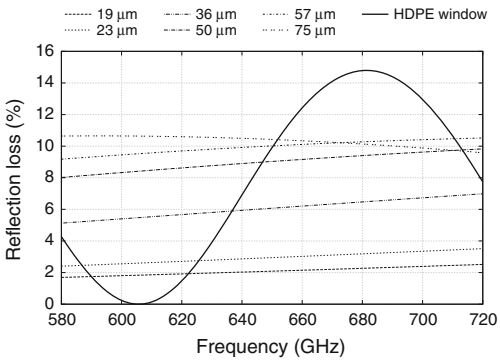

Fig. 3.8 Reflection loss of beam splitter with various thickness and a 660 μm thick HDPE Dewar window without corrugation

As for the IR filter, a few layers of Zitex® membrane are normally used to reduce the heat loading. These thin flaps of Teflon have a reflective index of about 1.22 (Kooi 2008). At low frequencies, they are almost transparent to the LO irradiation, but at wavelength shorter than 450 μm, they can easily give rise to 5–10 % of transmission loss, as measured by Benford et al. (2003).

Optical losses can be corrected from the measured noise temperature using Eq. 3.26, since the gain and the R-J temperature of each component can be estimated theoretically or experimentally using the methods described above. If we know the predicted optical loss, we can also correct for the measured mixer conversion gain. Recall that G_{mix} in Eq. 3.31 is in fact $G_{SIS} \times G_{RF}$, thus by simply calculating $G_{SIS} = \dfrac{G_{mix}}{G_{RF}}$, we would have a better estimate of the actual mixer conversion gain.

3.6 Summary

In this chapter, we have outlined the fundamentals of quantum detection theories that govern the behaviour of the SIS tunnel junction mixer. We have also summarised several experimental techniques used frequently to assess the performance of the SIS mixer, such as the impedance recovery, SIS mixer noise temperature measurement and techniques for estimating the RF and IF noise contributions.

References

Bardeen, J., Cooper, L., & Schrieffer, J. (1957). Theory of superconductivity. *Physical Review*, *108*(5), 1175–1204.

Winkler, D., & Claeson, T. (1987). High-frequency limits of superconducting tunnel junction mixers. *Journal of Applied Physics*, *62*, 4482–4498.

de Lange, G. (1994). Quantum limited heterodyne detection of 400–840 GHz radiation with superconducting nb tunnel junctions. Ph.D. thesis, University of Groningen, The Netherlands.

Raisanen, A., McGrath, W. R., Richards, P. L., & Lloyd, F. L. (1985). Broad-band RF match to a millimeter-wave SIS quasi-particle mixer. *IEEE Transactions on Microwave Theory Techniques*, *33*, 1495–1500.

Kerr, A. R., Pan, S. K. & Feldman, M. J. (1988). Integrated tuning elements for SIS mixers. *International Journal of Infrared and Millimeter Waves*, **9**, 203–212. ISSN 0195-9271. http://dx.doi.org/10.1007/BF01010970. 10.1007/BF01010970.

Kerr, A. R., & Pan, S. K. (1990). Some recent developments in the design of SIS mixers. *International Journal of Infrared and Millimeter Waves*, *11*, 1169–1187.

Kerr, A., Pan, S.-K., Lichtenberger, A., & Lea, D. (1992). Progress on tunerless SIS mixers for the 200–300 GHz band. *IEEE Microwave and Guided Wave Letters*, *2*(11), 454–456.

Cyrot, M. & Pavuna, D. (1992). *Introduction to superconductivity and high-Tc materials*. New Jersy NJ: World Scientific Pub. Co. Inc.

Tinkham, M. (1996). *Introduction to Superconductivity*. New York NY: Dover Publications Inc.

Josephson, B. D. (1962). Possible new effects in superconductive tunnelling. *Physics Letters*, *1*, 251–253.

Kooi, J. W. (2008). *Advanced receivers for submillimeter and far infrared astronomy*. Ph.D. thesis, University of Groningen, The Netherlands.

Fiske, M. D. (1964). Temperature and magnetic field dependences of the josephson tunneling current. *Reviews of Modern Physics*, *36*, 221–222.

Shapiro, S. (1963). Josephson currents in superconducting tunneling: the effect of microwaves and other observations. *Physical Review Letters*, *11*, 80–82.

Tucker, J. (1979). Quantum limited detection in tunnel junction mixers. *IEEE Journal of Quantum Electronics*, *15*(11), 1234–1258.

Tucker, J. R., & Feldman, M. J. (1985). Quantum detection at millimeter wavelengths. *Review Modern Physics*, *57*, 1055–1113.

Werthamer, N. R. (1966). Nonlinear self-coupling of Josephson radiation in superconducting tunnel junctions. *Physical Review*, *147*, 255–263.

Skalare, A. (1989). Determining embedding circuit parameters from dc measurements on quasiparticle mixers. *International Journal of Infrared and Millimeter Waves*, *10*, 1339–1353.

Ward, J., Rice, F., Chattopadhyay, G., & Zmuidzinas, J. (1999). *SuperMix: A Flexible Software Library for High-Frequency Circuit Simulation*. In Tenth International Symposium on Space Terahertz Technology: Including SIS Mixers And Superconducting Elements. (vol. 268).

Rice, F., Ward, J., Zmuidzinas, J. & Chattopadhyay, G. (2000). SuperMix Now Available. In *Eleventh International Symposium on Space Terahertz Technology*, (vol. 341).

Callen, H. B., & Welton, T. A. (1951). Irreversibility and generalized noise. *Physical Review*, *83*, 34–40.

KITTARA, P., 2002. *The development of a 700 GHz SIS mixer with Nb finline devices: Nonlinear mixer theory, design techniques and experimental investigation*. Ph.D. thesis, University of Cambridge, UK.

Grimes, P. (2006). *Design and analysis of 700 GHz Finline Mixers*. Ph.D. thesis, University of Cambridge, UK.

Ke, Q., & Feldman, M. (1994). A technique for noise measurements of SIS receivers. *IEEE Transactions on Microwave Theory and Techniques*, *42*(4), 752–755.

Buffey, M. (1999). *Submillimetre-wave technology for extragalactic spectral-line astronomy*. Ph.D. thesis, University of Cambridge.

Woody, D. P., Wengler, M. J., & Miller, R. E. (1985). 85–115-GHz receivers for radio astronomy. *IEEE Transactions on Microwave Theory Techniques*, *33*, 90–95.

Tong, C.-Y. E., Hedden, A. & Blundell, R. (2008). An empirical probe to the operation of SIS receivers—revisiting the technique of intersecting lines. In *Proceedings of 19th International Symposium Space THz Technology*, (pp. 314–318).

Rogovin, D., & Scalapino, D. (1974). Fluctuation phenomena in tunnel junctions. *Annals of Physics*, *86*(1), 1–90.

Goldsmith, P., & Button, K. (1982). *Quasi-optical technique at millimetre and submillimetre wavelengths*. IR and MM Waves: International Journal, (vol. 6).

ISAAK, K. G., 1995. *Low-Noise Intrumentation and Astronomical Observations of High-Redshift Objects at Submillimetre Wavelengths*. Ph.D. thesis, University of Cambridge, UK.

Benford, D. J., Gaidis, M. C., & Kooi, J. W. (2003). Optical properties of Zitex in the infrared to submillimeter. *Applied Optics*, *42*, 5118–5122.

Chapter 4
Design of Unilateral Finline SIS Mixer

Overview: This chapter describes the designs of niobium based single-ended SIS mixers optimised to work in the frequency range of 600–700 GHz. We will first review the various design variations, followed by a detailed discussion of each circuit component that comprises the final mixer design, supported by the rigorous electromagnetic simulations. Finally, the full mixer chip's performance predicted using SuperMix will be presented.

4.1 Introduction

All the SIS mixer designs described in this thesis employ a unilateral finline taper as the waveguide-to-planar circuitry transition. An important advantage of unilateral finline taper is that it provides an extremely wide band and smooth transition from the waveguide impedance to a low slotline impedance (Yassin et al. 2008). The transition from slotline to microstrip can be achieved relatively easy and can be made to exhibit broadband performance as well. Once the RF power is coupled to the microstrip mode, the finline chip does not need the waveguide anymore, hence all the additional circuits can elegantly be fabricated using microstrip.

As explained in Chap. 1, the design of a unilateral finline taper is straightforward and its electromagnetic behaviour can easily be simulated. Unilateral finline SIS mixer chips have large substrate area which is very useful for circuit integration, and require only a simple mixer block design without any mechanical tuners, as all the superconducting circuits can be deposited on-chip using planar circuit technology. One should be aware however, that this large planar circuit chip can present high capacitance at IF frequencies, but with careful design, the performance can be optimised for wide IF bandwidth operation (e.g., >10 GHz).

B.-K. Tan, *Development of Coherent Detector Technologies for Sub-Millimetre Wave Astronomy Observations*, Springer Theses, DOI 10.1007/978-3-319-19363-2_4

4.1.1 Silicon-On-Insulator (SOI) Technology

Conventional SIS mixers at sub-mm frequencies have usually been deposited on ~100 μm thick quartz, or silicon substrates that has a relatively high dielectric constant. Finline chips in particular require grooves of significant depth and height to be machined in the waveguide wall in order to support the mixer chip in the E-plane of the waveguide. This can potentially excite higher order modes, hence limiting the mixer operation at higher frequency band.

The introduction of the Silicon-on-Insulator (SOI) technology (Westig et al. 2011) allows the finline mixer to be fabricated on an extremely thin silicon substrate (~3–15 μm), hence extending their employment to the THz region. The very thin substrate presents light loading to the incoming waveguide signal, hence avoids the excitation of higher order modes within a relatively large bandwidth. It also helps to reduce planar circuit losses incur by the substrate loading. The required mixer block design is extremely simple, consisting of only two halves of a rectangular waveguide. This is because the light chip will no longer need a deep groove in the waveguide wall but can now be supported by gold beam leads deposited on-chip. These beam leads also provide an easier mean to position the mixer chip within the waveguide via shallow locating pockets. Since the beam leads are only a few microns thick, these shallow pockets have negligible effect on the RF performance of the SIS mixer.

The SOI mixer chips are also markedly easier to handle. Once the SOI chips are fabricated, they are ready to be mounted; compared to the quartz or silicon substrate chips that are required to be thinned and diced individually. SOI devices can easily be dropped into the waveguide, and bonded directly on to the surface of the mixer split block, without the need of bond wires. This is important as it simplifies the mounting process, which is highly desirable if a large number of mixer chips are to be populated across a large focal plane array. It also eliminates the additional inductive effect from the bonding wires affecting the IF performance of the mixer chip. The wide beam leads provide large contact area between the mixer chip and the mixer block, which leads to better cooling of the mixer chip, hence improving the mixing performance. Avoiding the dicing and thinning process also reduces significantly the possibility that the mixer chips being damaged during these hazardous mechanical handling procedures.

In the new mixer layout, the unilateral finline taper and the entire superconducting circuit are designed to be deposited on a 15 μm thick SOI substrate (hereinafter *SOI mixers*). In addition to the SOI mixers, we have also fabricated a batch mixers with similar circuit design on a conventional 60 μm thick quartz substrate (hereinafter *quartz mixers*). This allows us to better understand the behaviour of the new design features and to verify the performance of the on-chip planar circuits irrespective of the substrate material or configuration. Although the exact dimensions of the various features are altered slightly to suit the substrate, the tested results should in principle be able to provide a good comparison between the SOI and quartz devices.

4.2 Mixer Design

We have developed four different designs of the single-ended 700 GHz unilateral finline SIS mixers. They differ in the use of two different types of finline-to-microstrip transitions, and the use of two different substrates (Tan et al. 2010, 2012).

Figure 4.1 shows all the four design variations and the basic components of the unilateral finline mixer chip. Each design comprises 6 major sections, in the direction of the RF signal propagation: a matching notch, a unilateral finline taper, a finline-to-microstrip transition, a superconducting tuning circuit, an RF chokes and an IF bonding pad or IF beam lead. A major topological difference between the quartz and the SOI mixers is the need for serrated chokes in the former and the employment of gold beam leads in the later.

Apart from the substrates, the design layouts differ mainly in the method used to couple power from the finline to the microstrip. The first design employs a direct slotline-to-microstrip transition (hereinafter the *direct-mixer*) and the second utilises an intermediate coplanar waveguide sections to better match the impedance of the slotline to the microstrip (hereinafter the *CPW-mixer*).

All the mixers are designed to work in conjunction with a circular Nb/AlO_x/Nb (niobium/aluminium-oxide/niobium) SIS tunnel junction with the total area of 1 μm^2. This corresponds to a normal resistance of approximately 20 Ω and junction capacitance of 75 fF, giving $\omega R_n C \simeq 6$ at 650 GHz. Table 4.1 summarises the material and dimensions of the common structures used in all mixer designs. The Nb ground plane film which forms the two fins is separated from the Nb wiring film forming the microstrip by a 475 nm silicon monoxide (SiO, dielectric constant = 5.8) insulating layer. The design procedure is summarised as follows:

1. The profile of the unilateral finline taper was determined using Oxford's *FinSynth* package (North et al. 2006) and verified with HFSS, together with the design of the matching notch.
2. Transition from finline to microstrip, mixer tuning circuit, IF choke and other superconducting circuits were designed using Ansys Designer and HFSS.
3. Superconductivity was included by inserting the superconducting surface impedance to the perfect conductor structure in HFSS.[1]
3. Complete mixer chip simulation were performed in HFSS, with further alterations on the various circuit components for optimised RF performance.
4. Mixing performance was verified using Caltech's SuperMix package by cascading the scattering matrices of the electromagnetic circuit components exported from HFSS.

[1] This is done by approximating the characteristic of the superconducting surface impedance with a polynomial equation, but not from the full Mattis-Bardeen equation. This approximate equation is inserted as the frequency dependent surface impedance of the perfect conductor used to construct the circuit in HFSS.

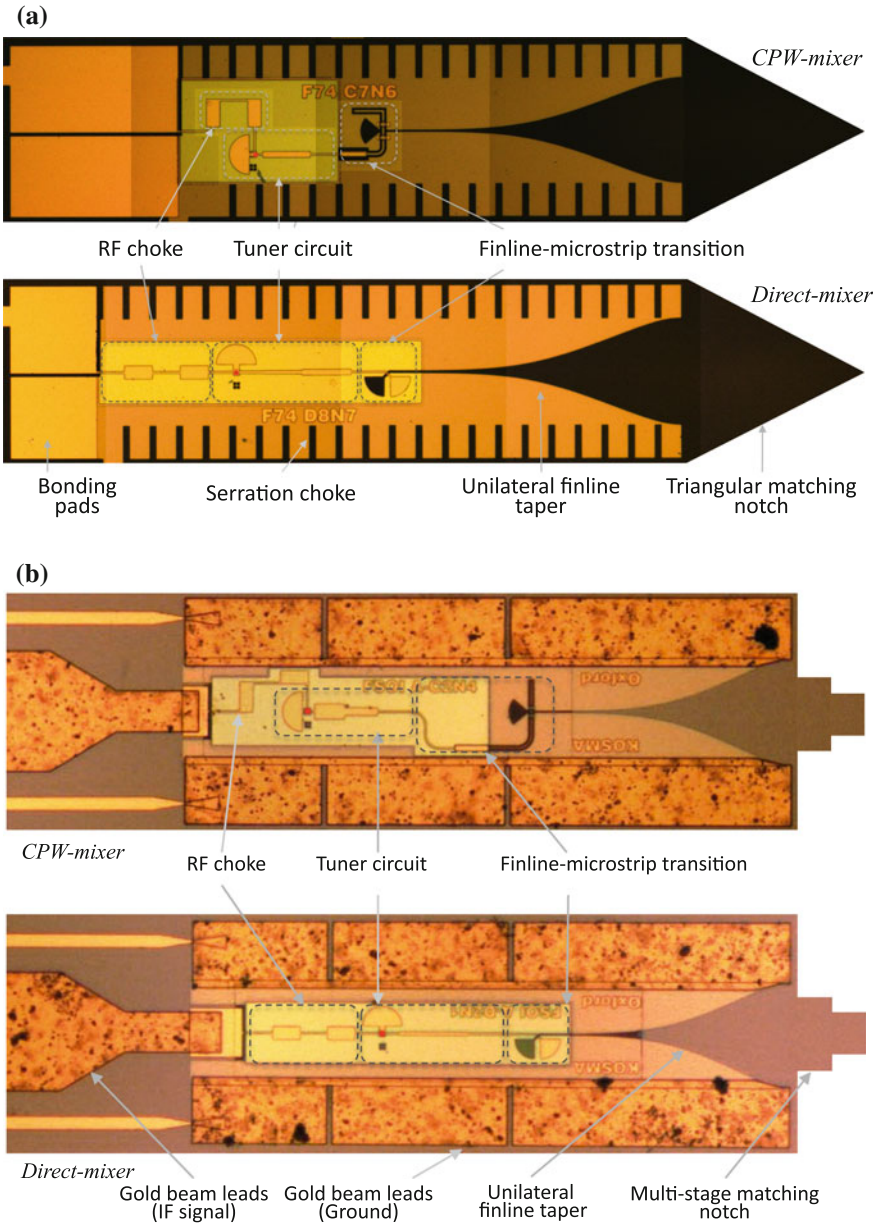

Fig. 4.1 Overview of the unilateral finline mixer designs, with two different types of finline-to-microstrip transition and two different types of substrate, showing the different components of the complete mixer chip. The *red dot* near the half-moon stub indicates the location of the SIS tunnel junction. **a** Quartz mixers. **b** SOI mixers

Table 4.1 Materials and dimensions of components used in our SIS mixer chips

Structure	Material	Dimension
SIS junction	Nb/AlO_x/Nb	1 μm^2
Substrate	Silicon	15 μm
	Quartz	60 μm
Ground plane	Niobium	250 nm
Dielectric layer	Silicon monoxide	475 nm
Signal layer	Niobium	400 nm
Waveguide	Copper	320 $\times$ 160 μm

In the following sections, we describe the design and simulation of the individual passive components of the mixer chip. Since the design procedure for the quartz and the SOI mixers is similar, only the SOI mixer design will be described in details.

4.2.1 Waveguide-to-Slotline Transition

The profile of the unilateral finline taper was carefully calculated using *FinSynth*, an Oxford software package written by North et al. (2006). *FinSynth* uses the Optimum Taper Method to search for a unilateral finline profile that has minimum length for a required return loss. The profile of the taper is synthesised by converting the computed cutoff frequency taper into a slotline taper. The final design is checked with Ansys HFSS for a full 3-D electromagnetic simulation to include the effect of superconductivity surface impedance, the enclosing waveguide, and the matching notches.

As seen from Fig. 4.2a, a unilateral taper transforms the RF power from the waveguide mode into a slotline with a simple single layer structure. The slot width

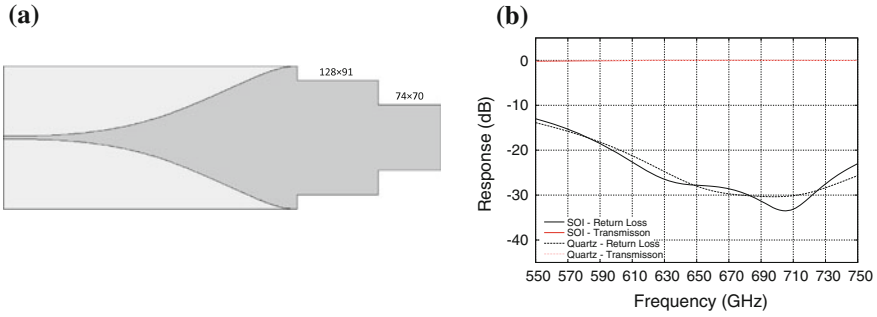

Fig. 4.2 **a** Layout of the unilateral finline taper with a 2-step notch to match the impedance of the unloaded waveguide to the 15 μm SOI substrate. The quoted dimensions of the matching notches are in width $\times$ length, in μm. **b** Return loss and coupling efficiency across the designated RF bands for both the quartz and the SOI substrates

needs to be tapered from 160 μm (waveguide width) to approximately 2.5 μm, in order to reduce the from ∼500 Ω to the values comparable for CPW or microstrip matching (∼20–30 Ω).

A matching notch is required before the finline to match the impedance of the substrate loaded waveguide to the empty waveguide. For the quartz mixer, a simple triangular $\sim \lambda_g/4$ notch (optimised to 240 μm) is sufficient for a good return loss performance. However, for substrates with higher dielectric constant, such as silicon substrates, multiple notch transformers should be used. Thus for the SOI mixers, we use a 2-step rectangular notch (approximately $\lambda_g/4$ long) to form the transformer for broader RF band performance.

Figure 4.2b shows the computed scattering parameters of the unilateral finline taper with the appropriate matching notches for both the 15 μm SOI and the 60 μm quartz substrate. The performance is excellent with return loss below −20 dB over more than 150 GHz bandwidth.

4.2.2 Slotline-to-Microstrip Transition

Since the SIS junction is fabricated across a microstrip line, a transition from slotline to microstrip line is required. This transition can be realised either through direct coupling across the dielectric layer, or more efficiently via intermediate CPW sections. The need for the intermediate CPW sections arises because even for a very narrow slot (3 μm), the impedance of the slotline is still much higher than the 20 Ω value presented by a very narrow (3 μm) microstrip, feasible for photolithography fabrication. Nevertheless, we used both types of transitions to design the new finline mixers, and the advantages and limitations of each option will be discussed below.

4.2.2.1 Direct Slotline-to-Microstrip Transition

Figure 4.3a shows the layout of the direct slotline-to-microstrip transition. Both transmission lines are connected to a 90° radial stub of approximately $\lambda_g/4$ in radius. At the crossing plane between the slotline and the microstrip, the slotline's radial stub is designed to appear as open-circuit, and the microstrip's radial stub as a short. This combination guides the RF signal to propagate from the slotline to the microstrip, as illustrated in Fig. 4.4b, where the field lines gently fold-over from tangential to vertical mode.

The advantage of the direct-transition is that the layout is simple. Different material layers are clearly separated, as shown in Fig. 4.4a, thus avoiding potential shorting during fabrication. The RF path can also be arranged easily to align along the central axis to the chip. However, the large difference in the characteristic impedance between a slotline and a microstrip, requires more careful considerations. For example, the choice of a junction normal impedance of 20 Ω is compatible to a microstrip width of about 2–3 μm (with a silicon monoxide SiO isolating layer of

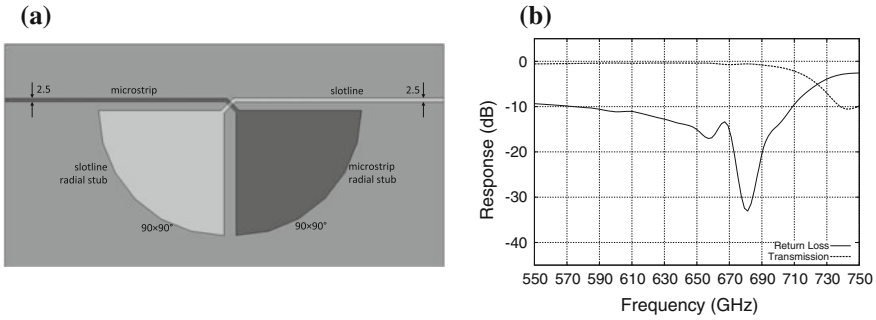

Fig. 4.3 **a** Layout of the direct slotline-to-microstrip transition. **b** The return loss and coupling efficiency across the designated RF band for the SOI design. The dimensions for the radial stubs are in radius (μm) × angle (°)

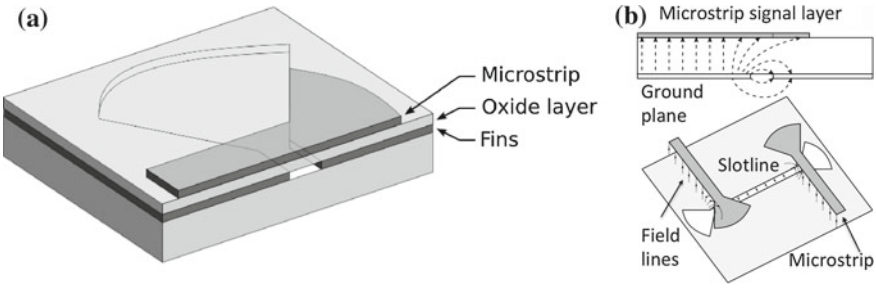

Fig. 4.4 **a** The layer structure of the transition from slotline to microstrip. **b** Diagrams showing how the field lines transit from the slotline to microstrip. Images courtesy of Yassin et al. (2008)

475 nm thick), which can just about be fabricated using standard photolithography. A slotline of width 2.5 μm on a 15 μm silicon substrate however, has an impedance of ∼65 Ω, and decreasing the impedance requires even narrower slots which is not practically feasible.

Figure 4.3b shows the HFSS calculated transmission and return loss of the transition, with a 2.5 μm slotline and microstrip with the same width, on a 15 μm SOI substrate. As can be seen, the performance is reasonable but not excellent (return loss is mostly between −10 and −20 dB). To further reduce the return loss without changing the size of the slotline and microstrip, one generally have to increase the size of the radial stub, but this might induce large capacitance at IF frequencies, and limits the IF operating bandwidth. One way to circumvent this problem is to use multi-stages transformer to bridge the impedance to the SIS junction, as shall be seen later in Sect. 4.2.3.

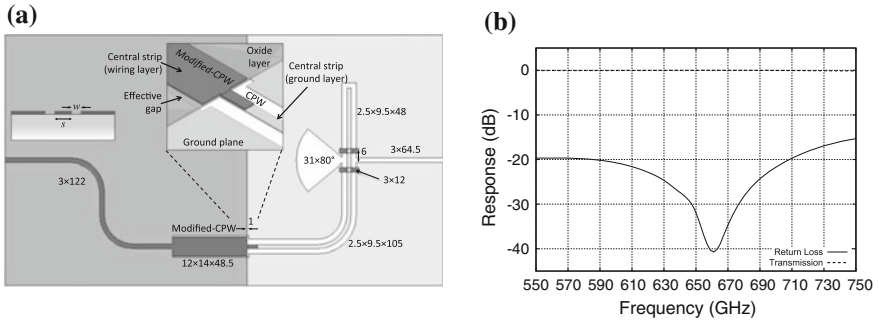

Fig. 4.5 **a** Layout of the slotline-to-microstrip transition via CPW sections. An enlarged 3-D view of the modified-CPW cross-over is shown in the inlet for clarity view. The dimensions for most structures are in width × length. For CPW, the quoted dimensions are in $s \times (2w + s) \times$ length, in μm. **b** Return loss and coupling efficiency across the designated RF band

4.2.2.2 Transition via Coplanar Waveguide

CPW offers a wide range of impedance values that can easily be exploited to bridge the slotline-microstrip mismatch. Neglecting the fringing effects, its characteristic impedance is determined mainly by the ratio of the central strip width (s) to the gap width (w) between the central strip and the ground plane. Using the quasi-static approximation and assuming the substrate is infinitely thick, its characteristic impedance can be estimated as $Z_{cpw} = \frac{30\pi}{\sqrt{e_{eff}}} \frac{K'(k)}{K(k)}$ where $k = \frac{s}{s+2w}$, $K(k)$ is the complete elliptic integral of the first kind, $K'(k) = K(\sqrt{1-k^2})$, and e_{eff} is the effective dielectric constant, averaging that of the air and the dielectric slab.

Figure 4.5a shows the layout of slotline-to-microstrip transition with CPW sections. The RF power is guided from the slotline to CPW using the same method as the direct-transition, but here, the radial stub is replaced by a standard quarter-wavelength CPW stub (Tan et al. 2010). Two short air-bridges are deposited across the CPW near the slotline-CPW junction to make sure that the ground planes are equipotential. The central strip and the ground plane are also fabricated simultaneously in one photolithography step to ensure better symmetrical alignment. As seen from Fig. 4.5b, the performance of this transition is much better than the direct-transition, having more than 160 GHz of bandwidth with less than −20 dB return loss.

We should point out that the section labelled 'Modified-CPW' in Fig. 4.5a is in fact a modified CPW structure. The central strip and the ground plane are separated by a thin 475 nm oxide layer. Since the impedance of a CPW is insensitive to the thickness of the substrate, such a thin layer does not modify the impedance significantly. The gap is thus defined by the effective distance between the edge of the central strip on top of the oxide layer, and the edge of the ground plane beneath the oxide layer. This arrangement is made for two reasons. Firstly, to bring the CPW central strip over the top of the oxide layer, preparing it to form a microstrip line. Secondly, it allows a very narrow CPW gap to be employed without the potential of shorting the

central conductor to the ground plane. The narrow gap is needed to achieve lower impedance without widening the central strip too much. Note that the central strip of this modified-CPW section was fabricated as part of the wiring layer, instead of the ground layer. Its length was slightly extended and overlapped on top of the central strip of the preceding CPW section to ensure good electrical contact. Forming a microstrip line from this modified CPW section is straightforward: change the width of the central strip to the required microstrip width and merge the two ground plane sections of the CPW.

4.2.3 Tuning Circuit

The successful operation of an SIS mixer requires the parasitic capacitance of the tunnel junction to be tuned out to prevent shorting of the RF signal. The conventional method uses an inductive strip terminated by a stub (Jacobs et al. 1992) to eliminate the capacitance at a particular frequency. This results in narrow band operation, determined primarily by the $\omega R_n C$ constant (Kerr 1995). A broader band performance can be obtained by utilising the twin-junction method (Belitskii et al. 1992; Grimes 2006), transforming the complex impedance of one junction to the complex conjugate of the other using a microstrip transformer. But this method is often limited by the difficulty to fabricate both junctions identically.

Our tuning circuit comprises four parts: an inductive strip with a half-moon stub, an inductive strip before the junction, a multi-sections transformer and an RF choke (Tan et al. 2010, 2012). The lumped element equivalent circuit is shown in Fig. 4.6a.

In order to match the junction impedance across a broader bandwidth, two inductive strips, one in series and another parallel to the junction, are used to provide two sharp tuning dips on the matching diagram. Both inductors are chosen to be tuned at two slightly different frequencies on either side of the centre frequency. As we shall see later, this method broadens the tuning response by about a factor of two compared to a single tuning stub.

The first inductor (*Tuner 1* in Fig. 4.6a), is a microstrip terminated with a $\sim \lambda_g/4$ half-moon stub which acts as a short at RF frequencies. The short microstrip line transforms the short-circuit stub into the inductance (seen by the junction) that is required to tune out the junction capacitance, at a particular frequency ω_1. To first order, the width and the length of this microstrip can be calculated using the expression $\beta l \approx Z_0 \omega_1 C$, where $\beta = \dfrac{2\pi}{\lambda}$ is the guided wavenumber, C is the capacitance of the junction, Z_0 is the characteristic impedance of the microstrip (a function of the width of the line), and l is the length of the microstrip in the unit of electrical wavelength.

The second inductive microstrip (*Tuner 2* in Fig. 4.6a) is placed before the junction to tune out the residual capacitance at a slightly shifted frequency ω_2. The width and the length of this microstrip section can be determined using the standard transmission

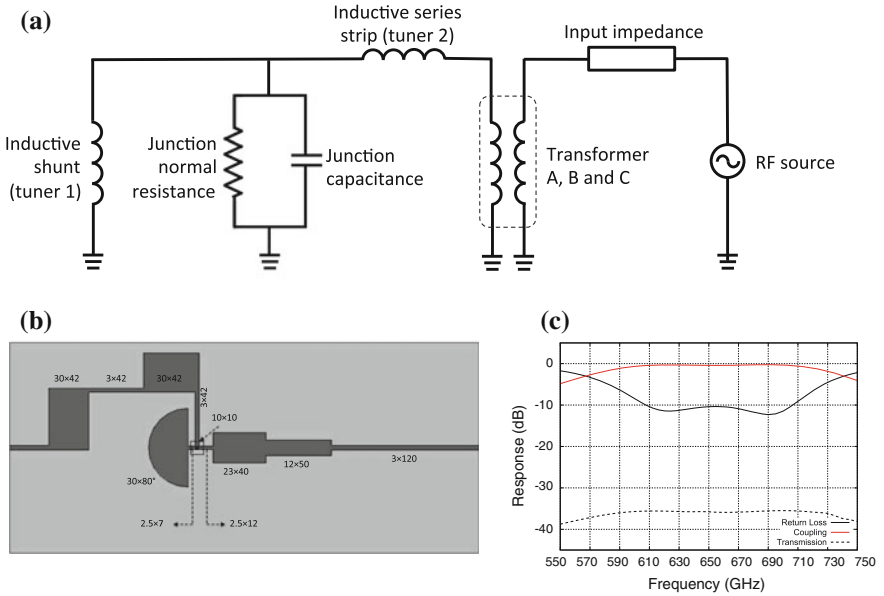

Fig. 4.6 **a** Electrical diagram representing the RF tuning circuit of the finline mixer. **b** Layout of the RF tuning circuit with an RF choke to prevent RF leakage to the IF port. The dimensions for various structures are similar to the previous figures. **c** Return losses and coupling efficiency of the tuning circuit across the designed RF band

line equation, $Y_s = \dfrac{(Y_l + iY_0 \tan \beta l)}{(Y_0 + iY_l \tan \beta l)}$, where Y_s is the source admittance, Y_l is the load admittance, $\dfrac{1}{Y_0}$ is the characteristic impedance of the line and βl is the propagation constant. By setting the imaginary part of Y_s to zero, the length of the microstrip can be obtained in terms of βl. The value of Y_0 is determined by the chosen width of the microstrip. Connecting both inductive strips with the junction, the overall reactance should be tuned to zero at two frequencies, giving the two poles in the matching diagram.

To match the impedance of this sub-circuit (the SIS junction with two inductive strips) to the output of the slotline-to-microstrip transition, a 3-step transformer is employed. The initial dimensions of the transformer can be estimated by using the standard multi-$\dfrac{\lambda_g}{4}$-step, or a Chebyshev design. We would like to emphasise that the final design of this transformer and the two inductive microstrips were eventually optimised using HFSS, including the effect of the complex surface impedance of the superconductor material, dielectric thickness, loss tangent, and other factors that cannot accurately be calculated from standard transmission line theory.

Finally, a 5-section RF choke, consisting of alternating high and low impedance $\lambda_g/4$ sections of microstrip, is placed after the SIS junction to provide high rejection of the RF signal across the operating bandwidth. This prevents the RF power leaking

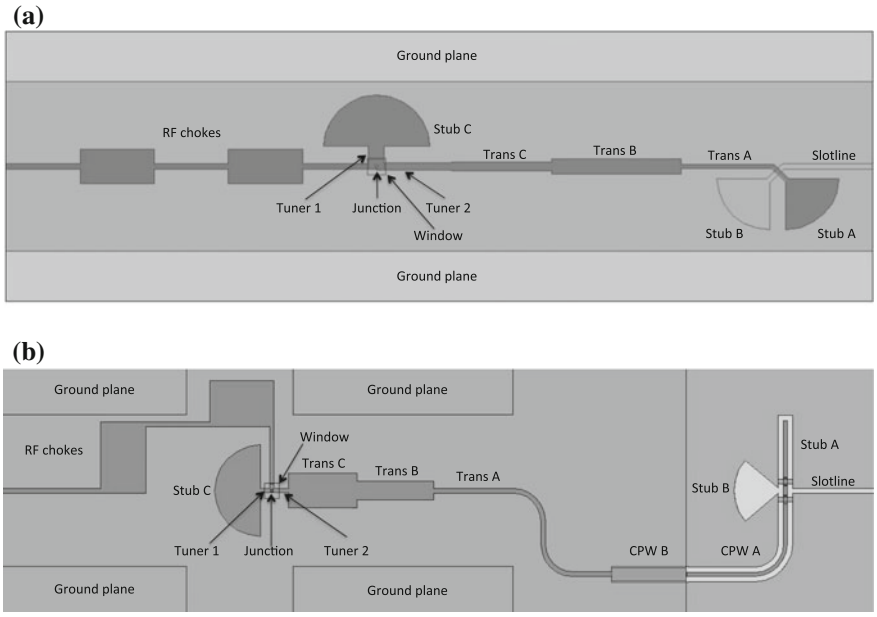

Fig. 4.7 Two different types of unilateral finline SIS mixer employing SOI substrates. The "ground planes" in the figure are the locations where the gold beam leads will be deposited to carry and earth the chip. **a** Direct finline-to-microstrip transition. **b** Transition via coplanar waveguide

into the IF path, to ensure that most of the RF power is coupled to the SIS tunnel junction. The widths of these sections are chosen such that they are not too large to introduce high IF capacitance, but at the same time, not too narrow for the fabrication tolerances of modern photolithography. These RF chokes therefore serve both as a channel to deliver the IF signal from the junction to the IF circuits, as well as delivering the bias DC current to the SIS junction. Together with the various transitions reported earlier, this completes the entire planar circuit structure of the mixer chip, as shown in Fig. 4.7, excluding the finline taper.

4.3 Full RF Mixer Chip Simulations

We combined all the passive circuit components discussed above and simulated them as one complete structure in HFSS (as shown in Fig. 4.7[2]), to take into account the effect of all interfaces. The dimensions of the various structures were then fine-tuned to optimise the performance. This is crucial for the direct-mixer design because the

[2]The unilateral finline is excluded and added in at later stage, after all the dimension of the planar circuit is finalised. This is to shorten the HFSS simulation time and thus speed up the turn-over time required for each design iteration.

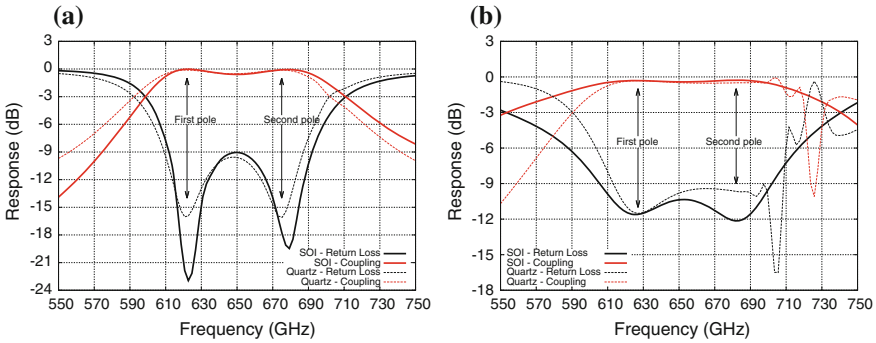

Fig. 4.8 HFSS simulation showing that the tuner design exhibiting broad bandwidth of 100 GHz centred at 650 GHz. **a** Direct finline-to-microstrip transition. **b** Transition via coplanar waveguide

large impedance mismatch between the microstrip and the slotline has to be modelled as part of the transformer design in the tuning circuit.

Figure 4.8 shows the return loss and coupling efficiency of the complete RF designs predicted by HFSS. Both direct- and CPW-mixer designs yield about 100 GHz RF bandwidth centred at 650 GHz. The power coupled to the junction is better than −0.5 dB in all cases. The tuning dips mentioned above can clearly be seen in the return loss curve which resonates around 620 and 680 GHz. Away from the designated operating band, the performance of the CPW-mixer deteriorates slower than the direct-mixer, mainly due to the large mismatch in the direct slotline-to-microstrip transition at these frequencies. Table 4.2 and Table 4.3 list all the critical dimensions (refer to Fig. 4.7) of the final mixer designs optimised with HFSS simulations.

4.4 IF Matching

To design the IF matching circuit, the mixer chip is modelled as an equivalent RLC circuit, which is a justified approximation at IF frequencies. The output impedance of this circuit was calculated and matched to the 50 Ω input impedance of the low-noise amplifier (LNA) within a given IF bandwidth (i.e., 4–14 GHz). The design procedure is fairly simple, using standard transformer design method, and can be optimised using conventional circuit design packages. We used HFSS to provide the flexibility of including structures such as the bonding wires and bond pads, to make certain that the effective impedances induced by these structures are included in the design of the matching transformer. The procedure of designing the IF transformer following the mixer chip RF simulation may be summarised as follows[3]:

[3]The detail description of each of these step can be found in Tan et al. (2014).

Table 4.2 Dimension of the tuning circuits, including the finline-to-microstrip transition, of direct-mixer design, referring to Fig. 4.7a

		Stub A	Stub B	Stub C	Slotline	Trans A	Trans B	Trans C	Tuner 1	Tuner 2	RF Chokes
Quartz	Width/Radius	30	30	30	3.0	2.5	8.5	5.0	9.0	4.0	20/3
	Length/Angle	90°	90°	180°	60.0	61.5	73.5	56.0	12.0	43.0	42.0
SOI	Width/Radius	30	30	30	3.0	2.5	3.5	5.5	8.5	3.0	20/3
	Length/Angle	90°	90°	180°	60.0	48.5	64.0	104.5	11.5	26.5	42.0

All dimension are in μm, otherwise stated

Table 4.3 Dimension of the tuning circuits, including the finline-to-microstrip transition, of CPW-mixer design, referring to Fig. 4.7b

		Stub A	Stub B	Stub C	Slotline	CPW A	CPW B	Trans A	Trans B	Trans C	Tuner 1	Tuner 2	RF Chokes
Quartz	Width/Radius	3.0	30.0	30.0	3.0	3.0	8.0	2.5	9.0	–	5.0	2.5	30/3
	Length/Angle	73.5	80°	180°	60.0	55.7	40.0	45.0	71.0	–	8.0	12.5	42.0
	CPW gap width	3.5	–	–	–	3.5	6.0	–	–	–	–	–	
SOI	Width/Radius	2.5	31.0	30.0	3.0	2.5	8.5	3.0	12.0	23.0	2.5	2.5	30/3
	Length/Angle	46.0	80°	180°	65.0	111.4	49.0	154.83	50.0	45.0	7.5	11.0	42.0
	CPW gap width	3.5	–	–	–	3.5	1.0	–	–	–	–	–	

All dimension are in μm, otherwise stated

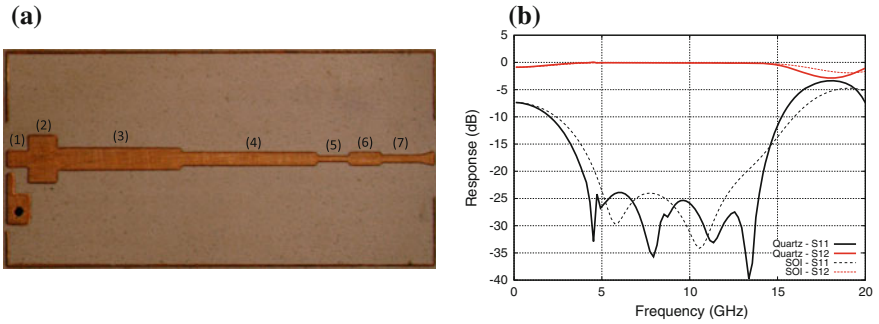

Fig. 4.9 IF transformer for matching the output complex impedance of the mixer chip to a 50 Ω port. The numbers in diagram (**b**) correspond to the numbers assigned to each transformer section tabulated in Table 4.4. HFSS simulations show that the return loss is better than −25 dB in the 4–14 GHz IF band. **a** Layout of the actual IF transformer board. **b** Insertion and return loss

1. Obtain the IF termination output impedance of the mixer chip from the SuperMix package, or from the Ansys Designer's lumped circuit model.
2. Find the RLC equivalent circuit of the RF mixer chip. Use Designer or any other circuit simulator to design the impedance matching transformer.
3. Improve the design by including the bond wires (or gold beam leads for SOI devices) and the bonding pads using HFSS.
4. Export the scattering matrix into SuperMix to verify the final full mixer IF performance including the influence of quantum mixing (see Sect. 4.5).

Figure 4.9a shows the actual IF transformer board. The final section of the microstrip is set to 50 Ω with 0.2 mm width and was flared wider (approximately 30°) towards the end to provide extra area for soldering contact with the pin of the SMA (SubMiniature version A) connector. Figure 4.9b shows the simulation results of the 6-step transformer, for both the quartz and SOI mixer designs, where the insertion loss is flat from 4–14 GHz. This bandwidth was chosen to match the operating bandwidth of the LNA, and is wide enough for most astronomical requirements. Both the direct- and CPW-mixers on the same substrate share the same IF transformer design, since the physical dimensions and the junction sizes (hence the IF impedance) of both designs are rather similar. The final optimised dimensions of both the IF transformers are listed in Table 4.4. Note that the actual dimensions between the two

Table 4.4 Dimensions of the optimised IF transformer on a 7.0 mm × 11.15 mm, 254 μm thick Duroid 6010 printed circuit board

		Section 1	Section 2	Section 3	Section 4	Section 5	Section 6	Section 7
quartz	Width	0.40	1.30	0.60	0.36	0.15	0.36	0.20
	Length	0.60	0.80	3.50	3.80	0.90	0.90	1.50
SOI	Width	0.40	1.31	0.60	0.36	0.14	0.35	0.20
	Length	0.50	0.70	3.34	3.64	0.79	0.78	1.50

All dimensions are in mm

designs differ only slightly. This difference arises mainly from the use of bond wire or beam leads as the IF connection for quartz and SOI devices, respectively.

4.5 Full Mixer Chip SuperMix Simulations

Following the rigorous simulation of the various mixer components with HFSS, the scattering matrices of these components were exported into SuperMix to assess the gain, noise temperature and other heterodyne properties of the mixer. In this way, the ability of SuperMix as a quantum mixing simulation package was enhanced by a more accurate description of the electromagnetic behaviour from HFSS. The SuperMix equivalent mixer circuit is shown in Fig. 4.10a.

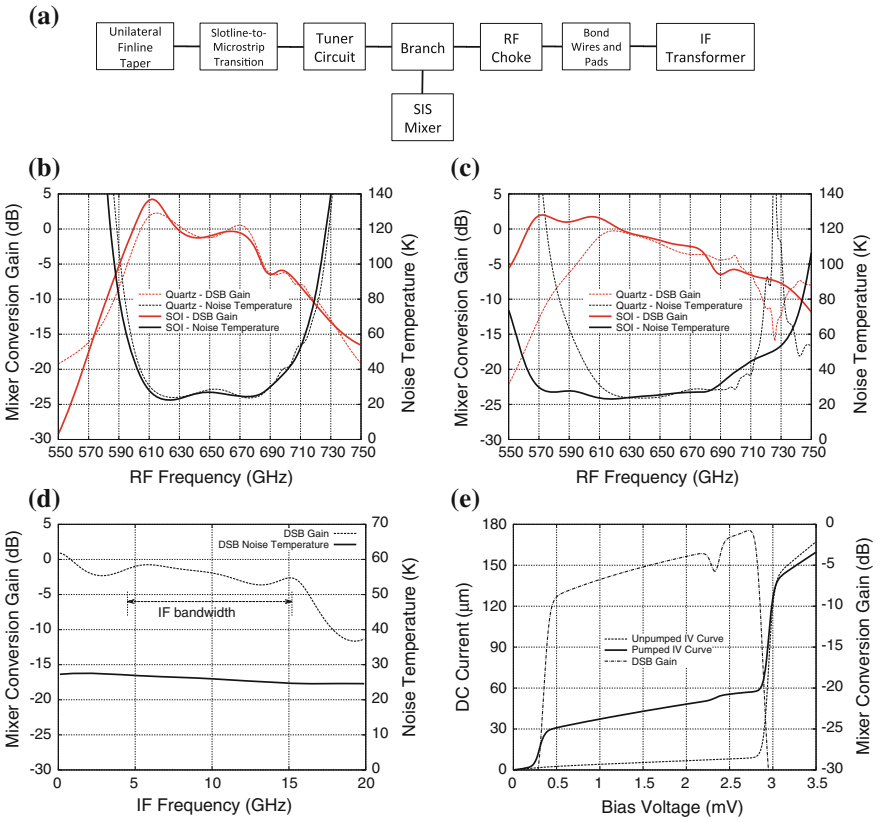

Fig. 4.10 **a** Block diagram showing the various components included in the SuperMix simulation. **b–e** The predicted behaviour of the final mixer chip designs. All the response curves were generated using the following setting except the x-axis parameters: bias voltage at 2.7 mV, pumped at 650 GHz with an LO power of 180 nW and IF frequency set at 5.0 GHz. **a** Block diagram of SuperMix model. **b** RF response for direct-mixers. **c** RF response for CPW-mixers. **d** IF response for direct-mixers (SOI substrate). **e** Bias response for direct-mixers (SOI substrate)

Examples of these calculations for the final mixer designs including the IF transformer are shown in Fig. 4.10. These results were simulated using an unpumped DC IV curve computed theoretically (Ward et al. 1999). The analysis is used to verify the details of the design and to serve as a guide in understanding the experimental results. As expected, the computations predict good RF conversion gain and low DSB noise temperature across the entire RF band. The design of the IF matching is validated by noting that the noise temperature remains flat, from 4 to 14 GHz.

4.6 Summary

In this chapter, we presented the designs of the broadband unilateral finline SIS mixer near the niobium superconducting gap frequency. Four designs were developed: a direct-mixer and a CPW-mixer on a 15 μm SOI substrate, and the same chip designs on a 60 μm quartz substrate. Their performance was fully simulated using rigorous electromagnetic methods, exported into SuperMix package, and the heterodyne performance has been computed. The RF noise temperature was found to be low and flat over a wide range of frequencies. The RF gain was also flat across a 100 GHz bandwidth and the IF performance satisfactory from 4–14 GHz.

4.7 Postscript

The discussion in Sect. 4.4 may imply that we can always match the output of the SIS mixer to a 50 Ω input impedance regardless of the equivalent lumped capacitance and inductance of the chip. This however is not straightforward and it turns out that considerable care needs to be taken during the RF design in order to avoid resonances at the IF frequencies. This, and the Bode-Fano limit, imposes a fundamental limit for broadband matching any capacitive devices (Kerr 1995).

To illustrate this point, we plotted the embedding impedance of the mixer chip (without the IF transformer) over a large frequency range as shown in Fig. 4.11a. We can clearly notice that both the real and the imaginary parts of the impedance go to zero at a certain frequency ν_0, in this case, around 44 GHz. This is due to the intrinsic circuit of the mixer chip creating a reactive shunt at that particular frequency. Another way of looking at it is that the equivalent RLC circuit of the mixer resonates at ν_0. This practically shorts the entire mixer, and the mixer gain drops to zero at this point, as shown in Fig. 4.11b. Since the device is entirely shorted, it is impossible to tune out the impedance at this point.

In the example shown in this thesis, the 650 GHz mixer chip has a relatively small size, hence a small planar circuit area. Therefore, the total capacitance seen at the IF port is relatively small too. Consequently, the frequency at which the equivalent circuit resonates ($\nu_0 \approx 44$ GHz), is well outside the targeted IF band. However, if the mixer chip were to be designed at a much lower RF frequency, say around

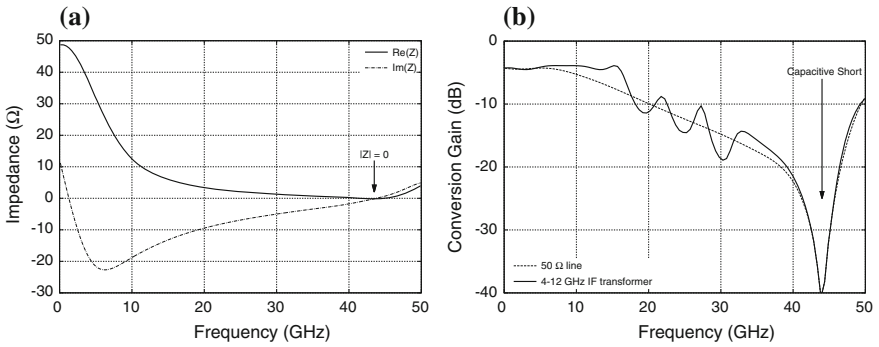

Fig. 4.11 The complex embedding impedance of the mixer chip and the mixer gain as a function of frequency showing a zero value near 44 GHz

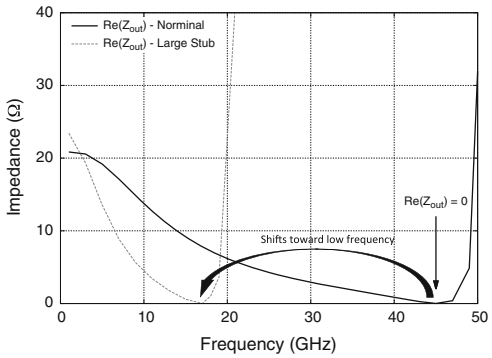

Fig. 4.12 The IF output resistance of the mixer chip shorted to zero at the same frequency. With a three times larger planar circuit area, the zero-gain point would be shifted to lower frequency at 18 GHz

230 GHz, the mixer chip planar circuit area would be approximately three times larger and the lumped element capacitance will also be larger. This would shift the zero-gain point towards the lower frequency end, hence constitutes an important limiting factor on the IF bandwidth achievable by low frequency mixers. This is illustrated in Fig. 4.12 where the zero-gain point has moved from around 44 GHz to ∼18 GHz when the lumped element capacitance was increased by a factor of three. Hence, for low frequency mixers, the RF circuit must be carefully designed so that the resonant frequency is pushed outside the high frequency end of the IF bandwidth by decreasing the equivalent lumped element capacitance and inductance of the RF circuit.

References

Belitskii, V. I., Tarasov, M. A., Kovtoniuk, S. A., Filippenko, L. V., & Kaplunenko, O. V. (1992). Low noise completely quasioptical SIS receiver for radioastronomy at 115 GHz. *International Journal of Infrared and Millimeter Waves*, *13*, 389–396.

Grimes, P. (2006). *Design and analysis of 700 GHz finline mixers*. Ph.D. thesis, University of Cambridge, United Kingdom.

Jacobs, K., Kotthaus, U., & Vowinkel, B. (1992). Simulated performance and model measurements of an SIS waveguide mixer using integrated tuning structures. *International Journal of Infrared and Millimeter Waves*, *13*, 15–26.

Kerr, A. R. (1995). Some fundamental and practical limits on broadband matching to capacitive devices, and the implications for SIS mixer design. *IEEE Transactions on Microwave Theory Techniques*, *43*, 2–13.

North, C., Yassin, G., & Grimes, P. (2006). Rigorous analysis and design of finline tapers for high performance millimetre and submillimetre detectors. In *Seventeenth International Symposium on Space Terahertz Technology*, (pp. 284–287).

Tan, B.-K., Yassin, G., Grimes, P., & Jacobs, K. (2010). Designs of broadband unilateral finline SIS mixers employing 15 μm silicon-on-insulator substrate at THz frequencies. In *Twenty-First International Symposium on Space Terahertz Technology* (pp. 204–211).

Tan, B.-K., Yassin, G., Grimes, P., Leech, J., Jacobs, K., Withington, S., Tacon, M., & Groppi, C. (2010). A 700 GHz unilateral finline SIS mixer fed by a multi-flare angle smooth-walled horn. In *Society of Photo-Optical Instrumentation Engineers (SPIE) Conference Series* (Vol. 7741).

Tan, B.-K., Yassin, G., & Grimes, P. (2014). Ultra-wide intermediate bandwidth for high-frequency SIS mixers. *Terahertz Science and Technology, IEEE Transactions on*, *4*(2), 165–170.

Tan, B.-K., Yassin, G., Grimes, P., Leech, J., Jacobs, K., & Groppi, C. (2012). A 650 GHz unilateral finline SIS mixer fed by a multiple flare-angle smooth-walled horn. *IEEE Transactions on Terahertz Science and Technology*, *2*(1), 40–49.

Ward, J., Rice, F., Chattopadhyay, G., & Zmuidzinas, J. (1999). SuperMix: A flexible software library for high-frequency circuit simulation. In *Tenth International Symposium on Space Terahertz Technology: Including SIS Mixers And Superconducting Elements* (p. 268).

Westig, M. P., Jacobs, K., Stutzki, J., Schultz, M., Justen, M., & Honingh, C. E. (2011). Balanced superconductor-insulator-superconductor mixer on a 9 μm silicon membrane. ArXiv e-prints.

Yassin, G., Grimes, P. K., King, O., & North, C. E. (2008). Waveguide-to-planar circuit transition for millimetre-wave detectors. *Electronics Letters*, *44*(14), 866–867.

Chapter 5
Single-Ended Mixer Tests

Overview: This chapter describes the mixer fabrication, mixer assembly, experimental setup and, focuses on the mixer test results and analysis. We will show that both SOI and quartz mixers, yield good noise temperature performance, but that they seem to have different contributions to their receiver noise. The performance of the quartz devices were affected by the larger-than-designed junction size, while the sensitivity of SOI devices was degraded by the misalignment of the junction with the planar microstrip definition. These arguments will be supported by comparing the experimental results with the theoretical models from HFSS and SuperMix. The best noise temperatures obtained were 143 K at 600 GHz for the quartz device, and 345 K at 595 GHz for the SOI device.

5.1 Introduction

The quartz devices and the SOI devices were fabricated separately in two runs, with both the direct and the CPW designs fabricated on the same substrate wafer. All the mask definitions were drawn in-house using AutoCAD® by Dr. Paul Grimes and myself. The mask fabrication for the quartz wafer was done by Mr. Ernst Otto at the University of Chalmer, while the SOI mask was fabricated by Rose Fotomasken in Germany. All the wafer fabrication were done at the I. Physikalisches Institut, University of Cologne, Germany. The quartz devices were fabricated by the Dr. Paul Grimes, with the support and guidance of the KOSMA group led by Dr. Karl Jacobs, while the SOI devices were fabricated jointly by Dr. Karl Jacobs and Dr. Paul Grimes.

5.2 Device Fabrication

The most commonly used fabrication scheme for niobium based SIS devices is the Self-align Niobium Etch Process (SNEP), and the detailed description of the processing steps can be found in Grimes (2006) and Pütz (2004). Here, we shall

B.-K. Tan, *Development of Coherent Detector Technologies for Sub-Millimetre Wave Astronomy Observations*, Springer Theses, DOI 10.1007/978-3-319-19363-2_5

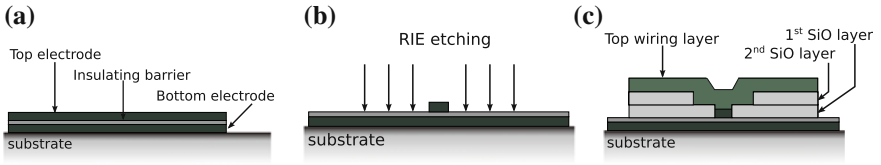

Fig. 5.1 Diagrams illustrating the various photolithography steps used in fabrication of the SIS devices. **a** Trilayer. **b** RIE etching to define tunnel junction. **c** Deposition of SiO layers and the wiring layer to complete the planar circuit

only briefly summarise the main processing steps that form the planar circuits of our mixer chips, regardless of the substrate used. These processing steps are illustrated graphically in Fig. 5.1. They comprise 5 stages, using 4 lithography masks:

1. The ground niobium layer which forms the unilateral finline is sputtered across the wafer, and ionised immediately to form the AlO_x barrier. The top niobium electrode is then deposited to form a Nb-AlO_x-Nb trilayer. (Mask No. 1)
2. The SIS junction is defined using Reactive Ion Etching (RIE), by removing the top niobium electrode across the wafer, except the junction area. (Mask No. 2)
3. Using the same mask in step 2, the first layer of the SiO insulation layer is deposited.
4. The second layer of SiO is deposited. (Mask No. 3)
5. Finally, the niobium wiring layer is deposited to form a contact with the top niobium electrode on the SIS junction, and the transmission lines of the mixer chip. Additional wiring is added, connecting the devices to the contact pads for on-wafer DC testing. (Mask No. 4)

Note that the patterning process described in the second step is etched using electron-beam lithography, while the remaining steps employ standard photolithography. Electron-beam lithography produces sharper pattern with much better accuracy than photolithography, which is essential for the precise definition of the junction. We should point out that two separate insulation layers are required here because a 20 Ω microstrip line (to match the normal resistance of the SIS junction) with minimum width compatible with photolithography, requires thicker SiO ($\varepsilon_r = 5.8$) layer due to its high dielectric constant. Also, the second (top) SiO layer clears a square area ($\sim 10 \times 10\,\mu$m) around the junction to ensure that the wiring layer has a good contact with the SIS junction.

Since the fabrication of SIS mixers on an SOI substrate is a new technology, we shall briefly summarise the major steps involved in the processing. For detailed descriptions, the readers are referred to Westig et al. (2011). The SOI wafer normally comes with a thick silicon handling wafer and a buried oxide (BOX) layer (hence silicon-on-insulator), which will be etched away at the end of the processing steps to release the fabricated mixer chips. For clarity, each steps tabulated below refers to a sketch in Fig. 5.2 labelled with the corresponding step number:

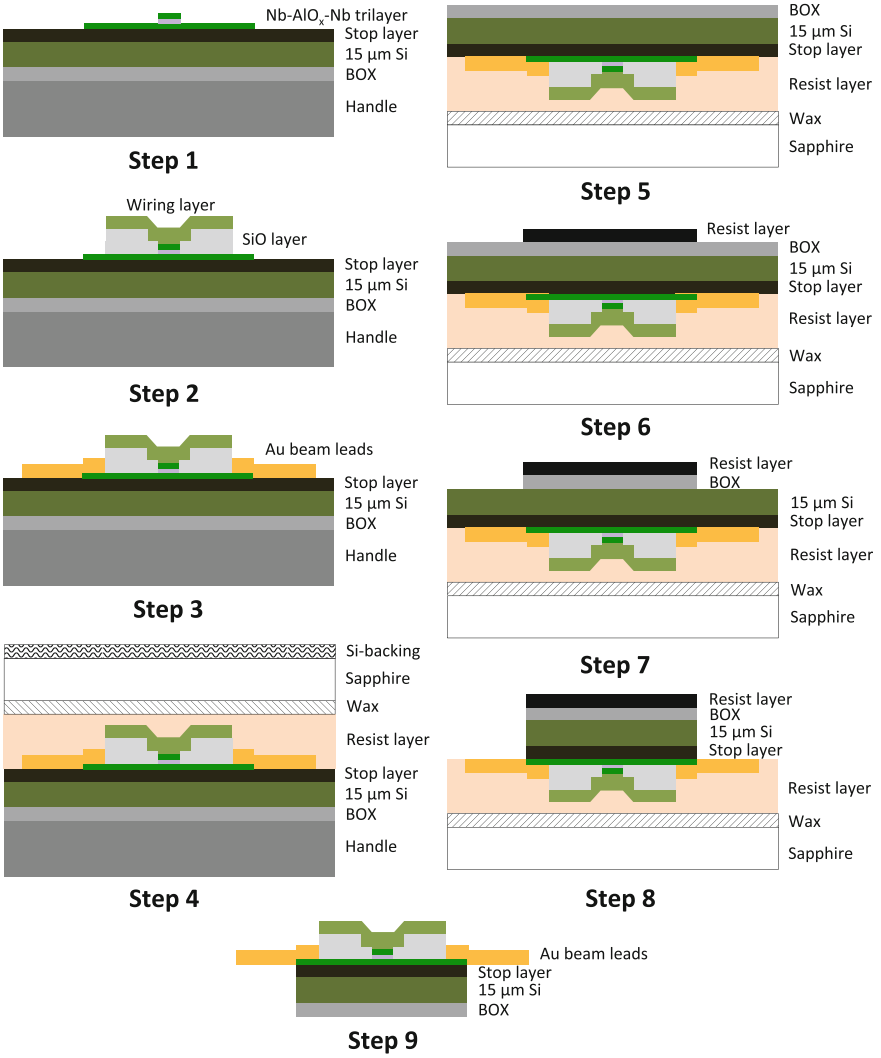

Fig. 5.2 Drawings depicting the important stages involved in the fabrication of SIS mixers on a 15 µm thick SOI substrate

1. The trilayer is formed by DC magnetron sputtering with optical lithography patterning, while the top layer defining the junction is patterned using electron-beam lithography.
2. The SiO layers and the Nb wiring layer are deposited as described earlier.
3. The gold beam leads are deposited with a separate mask.
4. At this stage, the entire structure on the device wafer is mounted on a backing wafer using wax and a front-side resist layer.

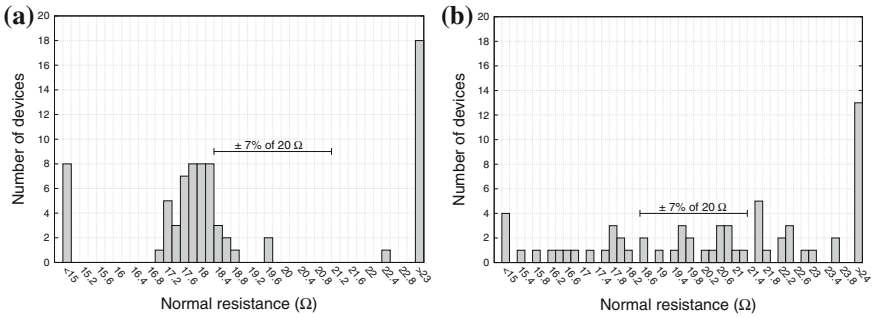

Fig. 5.3 Normal resistance of all the quartz and SOI mixer that have a live junction. **a** Quartz devices. **b** SOI devices

5. The whole structure is flipped upside-down to etch away the handle layer with DRIE (Deep Reactive Ion Etching), together with the silicon-backing.
6. Then a resist layer defining the device partitioning is deposited using another mask.
7. Using the same mask, the BOX layer is removed and device wafer is remounted on the backing wafer for transport.
8. The 15 μm silicon substrate and the stop layer are etched out to define the devices.
9. Finally, the fabricated devices are released by removing the front-side resist layer and wax.

Figure 5.3 shows the distribution of the normal resistance (R_N) for all the devices fabricated on the quartz and the SOI substrates that have a live junction. One immediately notices from the histogram that the normal resistance of a large number of quartz devices were concentrated around 18 Ω instead of the design value of $R_N = 20\,\Omega$. In fact, none of the devices turned out to have a normal resistance of 20 Ω. This unfortunately indicates that the junctions sizes were fabricated ∼10 % larger than expected across the entire wafer, pulling the tuning frequencies below 600 GHz.

In light of this experience, for the subsequent fabrication of the SOI devices, we intentionally designed 25 % of the junctions to have a 10 % larger than the nominal 1 μm^2 and 25 % of the junctions were designed at 10 % smaller. This strategy aimed at a larger variation of junction size spread across the wafer to increase the chances of having devices with the intended junction size. As seen from Fig. 5.3b, this has indeed produced a handful of devices with the normal resistance close to the nominal value.

5.3 Mixer Assembly

Both the quartz and the SOI mixer blocks were fabricated at the School of Earth and Space Exploration, Arizona State University, by Dr. Christopher Groppi, using a 6-axis Computer Numerical Control (CNC) micro-machining machine. The individual

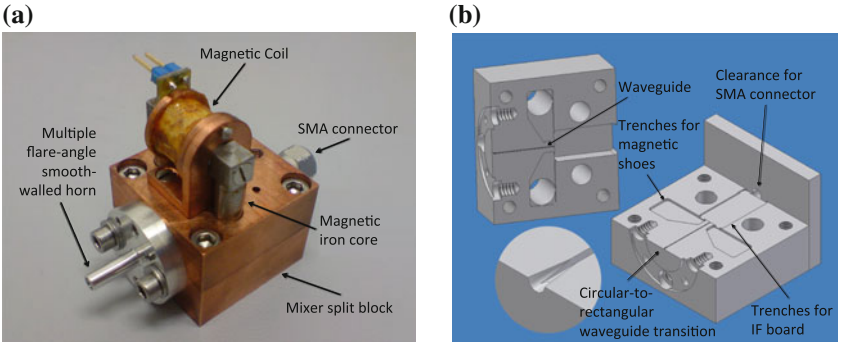

Fig. 5.4 Assembly of the 650 GHz mixer block enclosing a unilateral finline mixer, fed by a multiple flare-angle smooth-walled feed horn. The superconducting coil used to suppress the Josephson tunnelling can be clearly seen on top of the block. The butterfly-wing structures are used to hold the magnetic shoes that direct the magnetic field from the coil, fed by the two iron cores on top of the mixer block. The IF output will be tapped from the IF board using standard SMA connector at the back of the mixer block. The IF board is placed in a trench immediately after the rectangular waveguide. **a** Quartz mixer block. **b** Mechanical drawing of SOI mixer block

block is split into two halves along the E-plane of the rectangular waveguide, with the device located in a groove in the bottom-half.

In Fig. 5.4, we show the photograph and the mechanical drawing of the blocks. Each block accommodates a straight rectangular waveguide (160 μm wide × 320 μm high), a trench for the IF transformer board, two sockets for the magnetic shoes to direct the magnetic field line towards the mixer chip, and a circular-to-rectangular transition to taper smoothly the feed's circular waveguide output to the rectangular waveguide in the block. This transition is realised by milling a 13° semi-flare angle cone into the inlet of the rectangular waveguide. This simple method of making a transition was modelled using HFSS and was found to give a return loss better than –20 dB within the operating band.

All the single-ended mixer blocks presented in this chapter were fed by the multiple flare-angle smooth-walled horn discussed in Chap. 2. These feed horns were machined separately and bolted to the front of the waveguide via a UG-387/U (modified) flange.

The magnetic field required to suppress the Josephson current was supplied by a small superconducting coil, with a ferro-magnetic iron core penetrating through the upper split block (see Fig. 5.4) to the ferro-magnetic shoes positioned besides the mixer chip. The coil had 2,000 turns of 50 μm diameter copper-clad NbTi superconducting wire on a former of 7.0 mm diameter. With this arrangement we were able to induce a magnetic field sufficient to sweep the tunnel junction through several Josephson nulls with a current of 0–300 mA. The magnetic field applied is normally set at the second minima or higher, as the first Josephson null is usually insufficient to completely suppress the Josephson current. Higher order minima can of course be applied, but this would suppresses the gap nonlinearity and leads to a reduction in the mixer conversion gain.

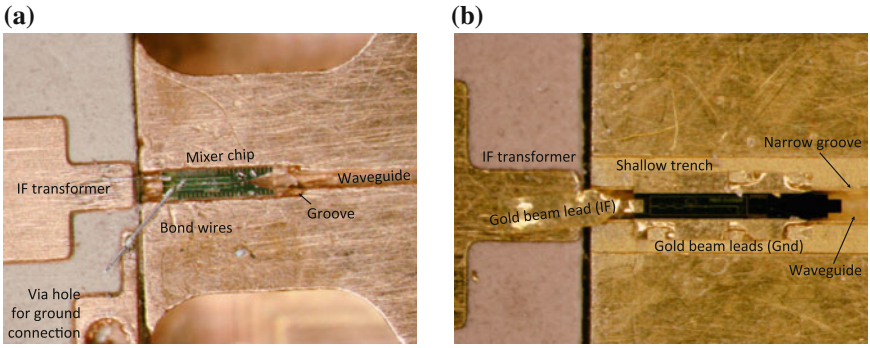

Fig. 5.5 **a** A photo showing the quartz mixer chip sitting in the groove inside the waveguide. Two bond wires were used to connect the mixer chip bonding pads to the IF transformer board. **b** A similar photo showing an SOI mixer chip mounted on the E-plane of the waveguide. The gold beam leads were bonded directly to the surface of the mixer split block without any bond wires

In Fig. 5.5, we show examples of quartz and SOI mixer chips mounted in their respective mixer blocks. The substrate, which carries the superconducting circuit, is located in the E-plane of the waveguide near the rear end. For the quartz mixer chip, we used a bond wire to connect the IF signal from the mixer chip bonding pads to the IF transformer board, which is connected to the bias tee by a standard SMA connector. This wire bonding step is not required for SOI devices, since they were fabricated with beam leads that contact the IF board and the body of mixer block directly. The DC bias voltage is supplied to the SIS junction via the same IF path. The mixer block for both mixers are largely similar, except for a few specific features, and these differences are listed in Table 5.1.

Table 5.1 The major structural differences between the quartz and the SOI mixer's block

Quartz	SOI
Split copper block without gold plating	Split block was gold plated for better bonding contact with the beam leads
Mixer chip was supported by deep groove of 65 μm wide and 80 μm deep to accommodate the mixer substrate and the serrated choke	Narrow groove of 15 μm wide and 35 μm deep to ease the positioning of device into the waveguide and shallow trench of 165 μm wide and 4 μm deep for the gold beam leads
IF transformer board needs small island with via holes for ground bonding	Ground contact is provided by the direct bonding of the beam leads to the body of the block
On-chip serrated choke is needed	No serrated choke required
Bonding using aluminium bond wire with diameter of 25 μm	Contact via gold beam leads with thickness of 2 μm

5.3.1 Device Handling

As the mixer chips are tiny (less than 1 mm in length), they can be picked up conveniently using the whiskers of a paint brush. Despite the different nature of the quartz and SOI chips, the handling processes are rather similar. Both types of devices were first picked up from the anti-static box and placed near the waveguide using the paint brush. We then used two sharpened wooden sticks to carefully push and move the mixer chip into the waveguide slot and to further align it.

For the SOI devices, after the mixer chip was well positioned within the waveguide, small patches of solid crystal bond fragments were placed on top of the ground beam leads. The mixer block was then heated to about 60–80 °C, to melt the crystal bond. In most cases, the liquefied crystal bond flows on top and underneath the beam leads, holding the mixer chip in position. The mixer block was then left to cool down before the bonding. At this stage, we usually cleaned off the excessive crystal bond using acetone.

The bonding of SOI chips was done without any bond wire—instead, the wedge of the bonding machine was used to force a contact between the beam leads and the gold plated mixer block ultrasonically at about 60 kHz. The bonding strength applied was adjusted to ensure that the thin crystal bond layer underneath the beam leads has penetrated through and a solid electrical contact was created between the beam leads and the mixer block or the IF transformer. This arrangement greatly reduced the probability of cracking the mixer chip, since the entire bonding process was completed without any pressure applied on the substrate itself.

For quartz devices, we used the ordinary cyanoacrylate based superglue instead of crystal bond. Due to the smaller contact area (within the 50 μm groove instead of the 120 μm wide beam leads), we found that crystal bond is not strong enough to hold the thick quartz mixer chip in good contact with the mixer block. To mount the quartz devices after locating the chip inside the waveguide groove, we first dropped a small blob of superglue on top of the surface of the split block using a wire with an appropriate diameter (depending on the size of the drop required), along the edge of the groove. We then carefully slid the liquefied glue over the chip, covering parts of the serrated chokes on both sides of the chip. This process has to be done quickly to allow the capillary effect to guide the glue into the gap between the groove and the mixer chip, as well as underneath the chip.

5.4 Mixer Test Setup

Figure 5.6 shows the block diagram describing the experimental setup for performing the mixer tests, together with the picture of the actual test bench and the inner working area of the cryostat. The test receiver comprises the following subsystems: 1. a cryostat housing the mixer block and the cold electronics, 2. a room temperature

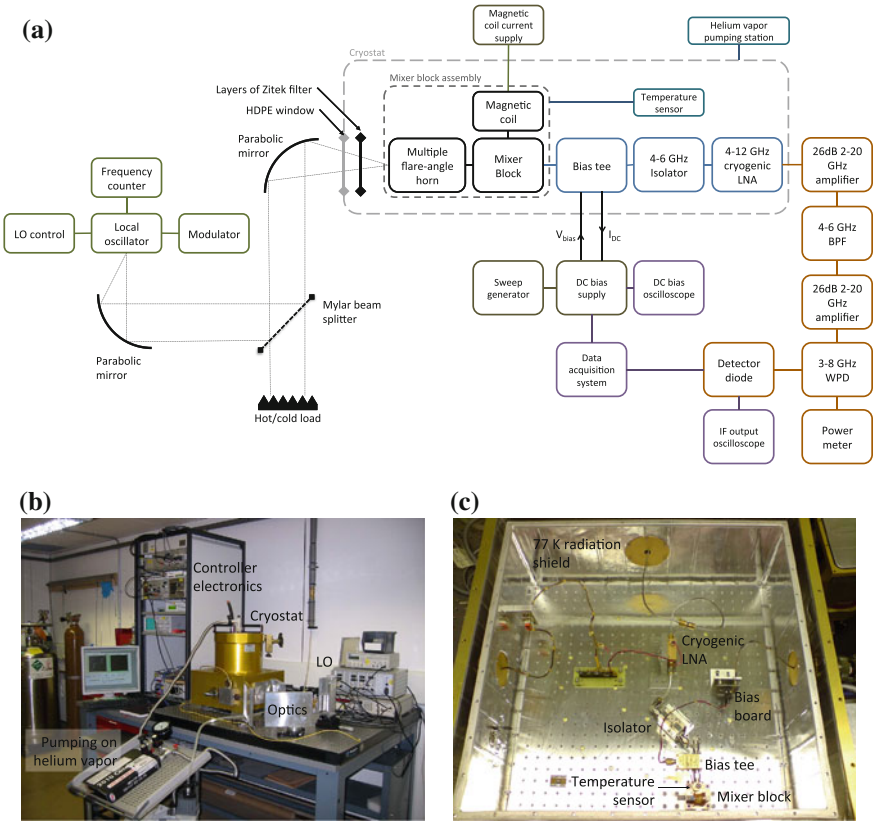

Fig. 5.6 Experimental setup measuring mixer performance using Y-factor method. **a** Block diagram of the test system. **b** Actual experimental setup without the liquid nitrogen bucket. **c** Working area of the Dewar

IF chain, 3. the bias circuitry and control electronics,[1] 4. the optics for feeding the LO and the RF signals, and 4. a data acquisition system.

The mixer assembly, including the first-stage cryogenic IF amplifier, was cooled to ∼4.2 K within an IR-Lab cryogenic Dewar. The mixer block was mounted via a bracket attached to the cold plate behind the 77 K stage opening, with the feed horn pointing directly towards the Dewar window. Temperature sensors were mounted on various stages, e.g. the mixer block, the cold plate and the 77 K stage cold shield. For operation below 4.2 K, we pumped on the helium vapour to lower the pressure and the liquid temperature down to ∼3.5 K.

The IF output signal and the biasing to the mixer block was connected through an SMA connector, to a 0–12 GHz bias tee, which in turn connected to an isolator

[1] Designed and built by Dr. David T. Smith and Mr. Rik Elliott of Oxford Physics Central Electronics Group.

via a semi-rigid SMA cable. The isolator was used to reduce the reflections from the first-stage amplifier coupling back to the mixer. The IF amplifier is a 4–12 GHz low noise amplifier fabricated in California Institute of Technology. The average noise temperature of the amplifier at cryogenic temperature is less than 4 K, and the average gain is ∼37 dB.

The down-converted IF power was detected through the output of a 4–6 GHz warm (room temperature) IF amplifier chain, consisting of two 26 dB warm broadband 2–20 GHz amplifiers and a 4–6 GHz bandpass filter. All of these components were designed and fabricated in-house. The output IF power was calibrated using a power diode detector, which allows us to display the IF output against the bias voltage when the mixer was radiated with either a hot (297 K), or cold (77 K) load. The noise temperature and IF contribution of the receiver were then found using the standard hot and cold load measurement technique (Woody et al. 1985), described in Chap. 3. Our cold load was made of an open-topped filled liquid nitrogen bucket lined with Eccosorb® AN-72 microwave absorber. A 45° plane mirror was mounted on top of the bucket to direct the horizontal beam into the bucket. Our hot load consist of a few layers of stacked Eccosorb® at room temperature, placed in front of cold load mirror.

The LO power and the blackbody load radiation were injected into the optical path by means of a partially reflecting Mylar beam splitter, whose surface is aligned at 45° with respect to the signal's direction of propagation. Care should be taken for high frequency operation such as around 700 GHz, since water absorption by the beam splitter can cause further signal attenuation. The beam splitter therefore should be kept in the dry atmosphere of a desiccator at all times.

Our LO power was supplied by a ×6 frequency-multiplied Gunn oscillator with a ferrite modulator, which could provide ∼100 μW of power over the frequency range of 630–700 GHz, but much less power was available below 620 GHz. The LO signal was focused onto the cryostat window by two off-axis parabolic mirrors (off-axis focal length 80 mm), forming a Gaussian telescope configuration. The optical setup was designed using single mode Gaussian beam quasioptics Goldsmith (1997). The cryostat window was made of a 660 μm thick high density polythene (HDPE) sheet and several layers of Zitek PTFE G-110 infrared filter were mounted on the 77 K stage to reduce the heat loading of the cold plate.

5.5 Results and Analysis

We have successfully tested 4 quartz devices, and 5 SOI devices. We will first present the test results of the quartz mixers, and then focus on the measured performance of SOI devices. We shall highlight the observations and interesting results obtained from particular devices, while the rest of the measured data can be found in Appendix A.

Table 5.2 Overview of the mixer test results for various quartz devices

Device	f_{LO} (GHz)	R_N (Ω)	d_{bs} (μm)	$T_{N(c)}$ (K)	$G_{R(c)}$ (dB)	imag (Z_{rec})
F74 A-D7N2[a]	–	–	–	–	–	–
F74 A-D7N1	660	17.9	57	765	−10.8	−10.8
F74 A-D4N1	660	17.9	50	327	−8.4	−10.3
F74 C-D7N6	600	18.2	75	143	−4.9	0.1

For each device, only the best results are shown. The reader is referred to Appendix A for the full tabulation of the test results
[a]No data available

5.5.1 Quartz Devices

Table 5.2 summarises the measurement results for each of the tested quartz devices. The quoted DSB noise temperature and the conversion gain were only corrected for the beam splitter losses, hence includes all other losses e.g., optical components, transmission line, and mixer conversion loss. The symbols used in tables and the discussion below are defined as follows:

Device	The unique device identity number.
f_{LO}	The LO frequency.
R_N	The normal state resistance of the device measured during DC testing after fabrication.
d_{bs}	The thickness of beam splitter.
T_N	The recorded receiver DSB noise temperature. The subscript (c) is used to denote the noise temperature corrected for the beam splitter losses.
G_R	The measured conversion gain of the mixer. The subscript (c) is used to denote the gain corrected for the beam splitter losses.
$imag(Z_{rec})$	The recovered embedding reactance from SuperMix.
T	The physical temperature of the mixer block.
f_{Fiske}	The resonance frequency estimated by observation of the Fiske step on the DC IV curve of the mixer.

In general, the mixer design assumed junctions with current density of ∼14 kA/cm^2 and an area of 1 μm^2. However, embedding impedance recovery Skalare (1989); Withington et al. (1995) calculations have shown that the tuning was in general shifted below 600 GHz. Considering that the normal resistance of the junctions has often came below the design value of 20 Ω, the low tuning frequency could be explained by a larger than designed tunnel junction area. This conclusion was supported by HFSS simulations which showed that an increase in the junction capacitance narrows down the operating bandwidth and shifts the frequency tuning range downwards. The SuperMix model constructed with a larger junction area showed similar behaviour to the HFSS model (see Fig. 5.7). Unfortunately, our LO did not produce much power below 620 GHz, hence thick beam splitter is needed to be used to pump the mixer.

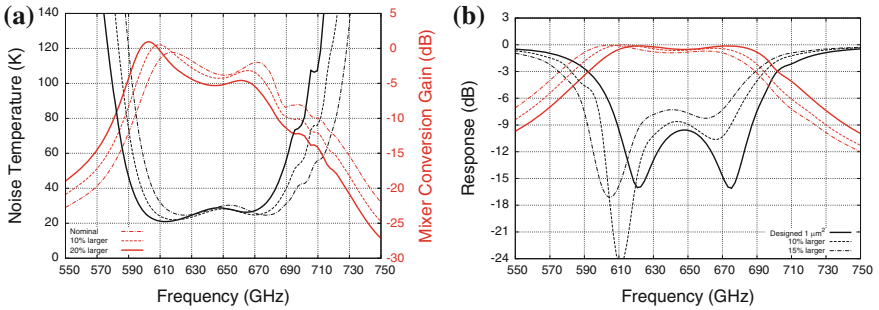

Fig. 5.7 SuperMix and HFSS simulating the effect of a direct quartz mixer design with larger than designated junction size. **a** SuperMix prediction. **b** HFSS simulation

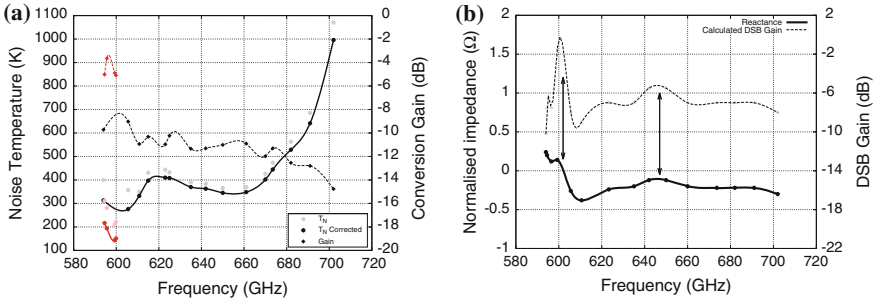

Fig. 5.8 **a** Frequency response of the tested F74 C-D7N6 quartz mixer. The two tuning dips are clearly observed around 600 and 650 GHz. The *red curves* indicate measurement done at bias voltage close to the actual first photon step. **b** Embedding impedance and DSB gain recovered using SuperMix across the operating RF bandwidth

The following section focus on the tested performance of the F74 C-D7N6 quartz device, as this particular device had been tested most extensively and has showed the best measured performance. The Y-factor of the mixer was measured over the frequency range where the LO power was sufficient to pump the device to an acceptable level. In Fig. 5.8, we show the measured DSB gain and receiver noise temperature as a function of frequency between 595–702 GHz (see Table A.3 in the Appendix A for the tabulation of the corresponding measured quantities).

The best noise temperature measured for this device is at 600 GHz, significantly lower than the designed tuning central band (650 GHz), for reasons we have explained earlier. Nevertheless, the tuning double dips can clearly be seen in the plot and appear to be located around 600 and 650 GHz. The noise temperature below the superconducting gap was measured below 400 K. This is well above what can be achieved by modern mixers at these frequencies but is consistent with the behaviour of an untuned mixer. This argument is supported by the result at 600 GHz where the noise temperature dropped to $\sim$145 K if corrected against the beam splitter thickness, and yet included all the other noise contributions. Below 600 GHz, the mixer performance

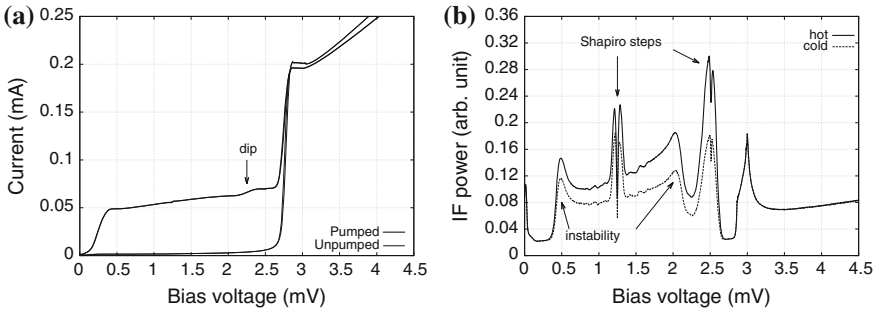

Fig. 5.9 IV characteristic of the tested mixer pumped with a 600 GHz RF signal and the measured hot and cold loaded IF responses. The mixer was pumped at $\alpha_1 = 0.407$. **a** IV curves. **b** IF curves

deteriorated rapidly due to the lack of LO power to pump the mixer. The poor performance above 670 GHz is expected as the superconducting losses increase sharply at these frequencies near the niobium superconducting gap, and is almost moving out from tuning band.

We have investigated the behaviour of the imaginary part of the recovered junction embedding impedance as a function of frequency (Fig. 5.8b). The effect of the tuning circuit designed to resonate at two particular frequencies can clearly be seen. As we move across the band towards high frequencies, the reactance changes from being inductive to capacitive, and stays slightly capacitive throughout the band. The reactance curve crosses the zero point near ~600 GHz. This value is compatible with the measurements in Fig. 5.8a and coincides with the frequency where the best noise temperature was measured. The second dip in the tuning circuit near 650 GHz can also be seen in the plot, where the imaginary part of the impedance moves again towards zero, corresponding again to the region where the noise temperatures has clearly improved.

In Fig. 5.9, we have plotted in the left frame, the pumped and unpumped IV curves as a function of the biased voltage at 600 GHz. In the right frame, we show the hot and cold IF responses used to calculate the receiver noise temperature. The Shapiro steps can clearly be seen on top of the photon step, indicating an incomplete suppression of the Josephson pairs current. The Josephson features can be further suppressed by increasing the magnetic field across the junction, but would resulting in a slight suppression of the superconducting gap. Notice that in the right frame, the existence of a dip in the pumped IV curve at a bias voltage of 2.3 mV which reflects the wrapping of the second photon step from the negative to the positive side of the display, as discussed in Sect. 3.2.1 in Chap. 3. In other words, the first photon step region is reduced to the range of bias voltages between the location of the dip and the superconducting gap Salez et al. (1994). Therefore, the best noise temperature values are obtained at bias voltage values in this first photon step region, which can clearly be seen (indicated by the red points) from Fig. 5.8a and the IF conversion plots in Fig. 5.9b.

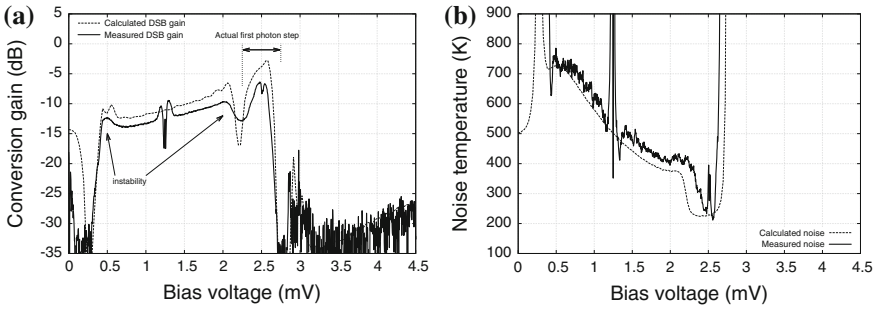

Fig. 5.10 Measured gain curve and noise temperature at 600 GHz in comparison with SuperMix model computed from the recovered impedance for F71 C-D7N6. **a** Gain at 600 GHz. **b** Noise temperature at 600 GHz

To further analyse the experimental results, we used the SuperMix model configured to determine the embedding impedance (as described in Chap. 3) to simulate the performance of the mixer using the pumped IV curve measured at 600 GHz, where the best noise temperature was located. Figure 5.10 compares the measured gain and noise temperature curves at 600 GHz with the theoretically computed values by the SuperMix model. Since the SuperMix model did not include losses apart from those due to mismatches, we calibrated the height of the computed curves by a multiplication factor (without changing the features). The shape of the measured and the computed curves then matched very well, including the subtle features, as can be seen in Fig. 5.10. The Shapiro features do not appear in the theoretical curve since SuperMix assumes full suppression of Josephson pair tunnelling. The instability shoulders near 0.5 and 2.0 mV in the measured curve are well predicted, so is the dip resulting from the wrapping of the second negative photon step to the positive side.

Finally, we used the techniques described in Chap. 3 to estimate the RF and IF noise contributions, and recover the actual noise generated by the junction itself. For this particular device, we see that the intersecting lines method estimates the noise seen before the junction at around 130 K (uncorrected, Fig. 5.11), and the IF noise contribution after the junction to be low (∼5 K). With this figures and the measured conversion gain, we arrived at the actual mixer noise of ∼40 K at 600 GHz (Table 5.3), which is very close to quantum limited performance.

5.5.2 SOI Devices

We have tested 5 SOI devices and a summary of the measurements is shown in Table 5.4. In general, the noise temperature measured was around 350–400 K for most devices. However, these measured performances appeared to show no correlation with the R_N value, as was the case of quartz devices. For example, the results given

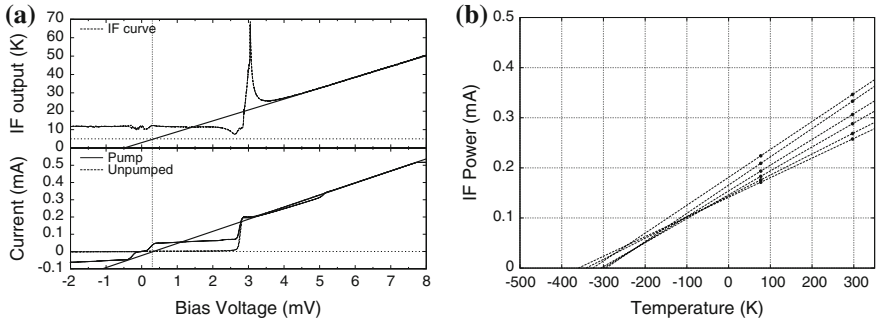

Fig. 5.11 **a** RF and **b** IF noise contributions estimated from the unpumped IV and IF curves

Table 5.3 Noise temperature (uncorrected) breakdown by estimating the optical, IF and mixer conversion loss at 600 GHz

Component	Optics	Mixer	Isolator	LNA	Warm IF chain	Total
Noise (K)	133.0	41.5	13.2	22.3	0.3	210.3

Table 5.4 Overview of the mixer test results for various SOI mixers

Device	F_{LO} (GHz)	R_N (Ω)	d_{bs} (μm)	$T_{N(c)}$ (K)	$G_{R(c)}$ (dB)	imag (Z_{rec})
FSOI A-D2N8	670	19.2	50	363	−11.4	−0.14
FSOI A-C2N7	595	16.7	75	343	−10.9	NA
FSOI A-C2N8	660	20.5	75	1272	−13.6	−0.08
FSOI F-D2N2	634	22.4	36	382	−9.9	−0.12
FSOI A-D2N1	605	20.7	75	399	−8.9	−0.28

For each device, only the best result measured at that particular RF frequency is shown. Readers are to refer to Appendix A for the full tabulation of the test results

in Fig. 5.12 show that FSOI A-C2N8 which had an R_N that is very close to the nominal 20 Ω value, had its measured noise temperature higher than 1,000 K throughout the operating bandwidth. On the other hand, FSOI A-C2N7 which had an R_N well below 20 Ω gave a reasonably good noise temperature around 400 K. This device also showed the typical behaviour of an untuned mixer (similar to F74 C-D7N6 above), where larger than designated junction size shifted the tuning towards lower frequencies.

The comparison between these two devices is interesting, as they both employ the same CPW-transition design. For one, we were able to pump FSOI A-C2N7 to saturation easily and measure reasonable noise temperature performance, as good as the other direct-mixer devices, which demonstrates that the CPW-transition can indeed perform as well as the direct slotline-to-microstrip transition design.

Second, FSOI A-C2N8 was noticeably harder to pump at all frequencies, compared to FSOI A-C2N7 despite the fact that they have exactly the same design. The first photon step current measured was less than half of that of the latter, even though

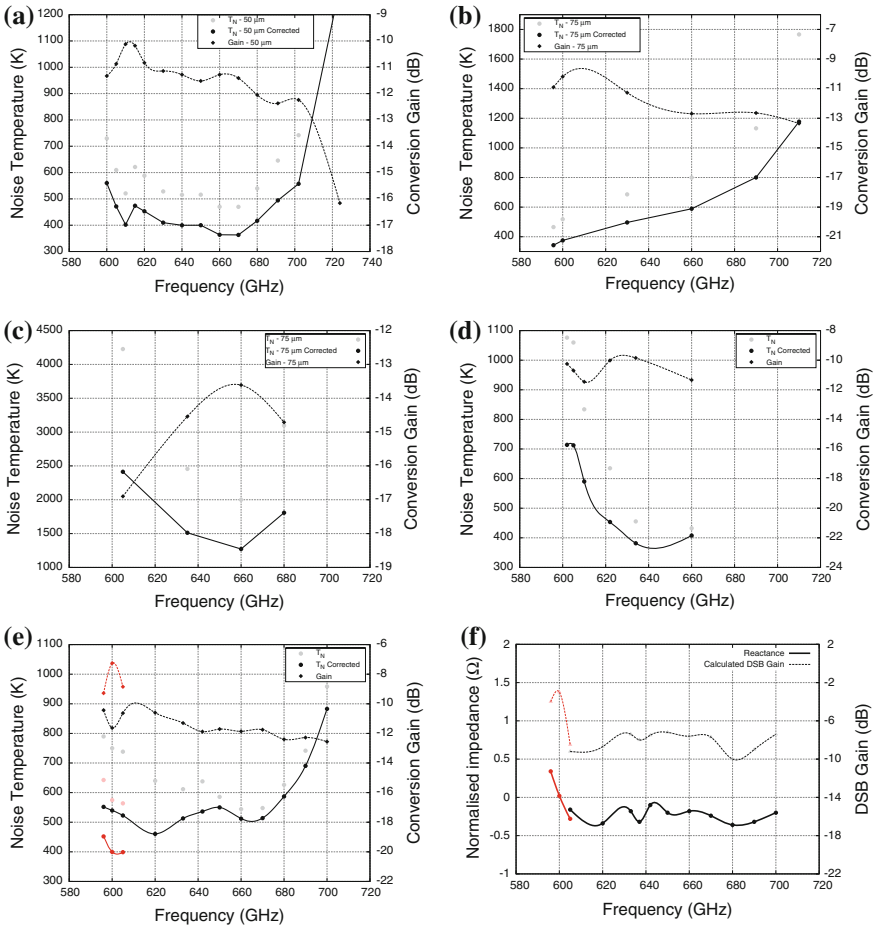

Fig. 5.12 Frequency response of all SOI devices tested so far, in terms of measured conversion gain and noise temperature.The grey points are the uncorrected measurements. The *red and pink points* are those measured on the real first photon step i.e., between the dip shown in Fig. 5.9 and the gap voltage. **a** FSOI A-D2N8. **b** FSOI A-C2N7. **c** FSOI A-C2N8. **d** FSOI F-D2N2. **e** FSOI A-D2N1. **f** Impedance recovery FSOI A-D2N1

the same optical setup was used in these tests. This suggests that the power coupling deficiency in FSOI A-C2N8 must be mainly related to the tunnel junction itself.

We believe that the higher than expected noise temperature was caused by the sensitivity of the mixer being degraded by the misalignment of the SIS tunnel junction with the wiring layer's definition. This resulted in an effective optical loss, caused by the reduction in RF and LO power coupling to the junction. In Fig. 5.13 it is shown that some junctions were shifted up to 1.2 μm away from the design position, in arbitrary directions. Given that the microstrip width around this area is narrow (2.5–4.0 μm), the effect of this offset can degrade the mixer performance significantly.

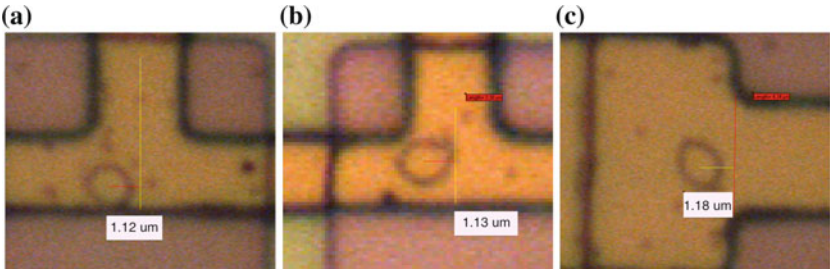

Fig. 5.13 Microscope photos showing the junction was not aligned to the microstrip as designed. **a** FSOI A-C2N2. **b** FSOI D-C2N2. **c** FSOI A-D1N2

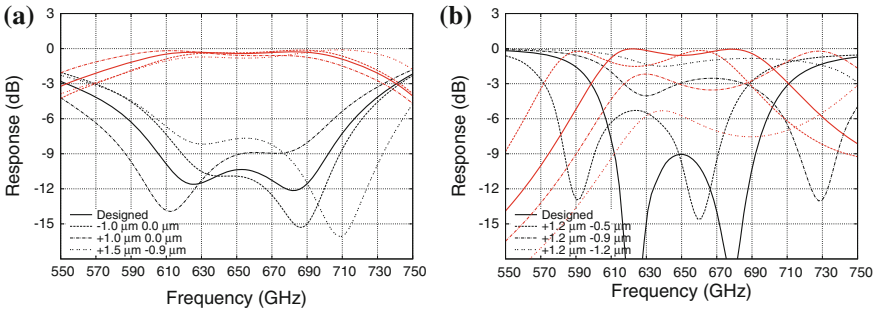

Fig. 5.14 HFSS simulating the effects of junction misalignment to the power coupling. The value in the legend corresponding to the magnitude of offset along (*horizontal*) and orthogonal (*vertical*) to the finline axis. The couplings to the junction are plotted with *red lines*, while the *black lines* representing the return losses. **a** CPW devices. **b** Direct devices

To understand how the junction offset affects the coupling to the junction, we have modelled the fabricated chip using HFSS simulations. Figure 5.14 shows that the magnitude of the RF power coupling is indeed affected by the offset, especially when the junction was simulated to be partially outside the microstrip area. In that case, the coupling level could be attenuated by as much as 7–8 dB, seriously reducing the LO and RF pumping level of the mixer chip. This result can explain why FSOI A-C2N8 was significantly harder to pump and had poor measured sensitivity, despite it having a normal resistance that was close to the design 20 Ω value.

During the experimental characterisation, we have also observed that the SOI devices were particularly susceptible to magnetic field effect and trapped fluxes. The Josephson features were especially harder to suppress compared to the quartz devices. In certain cases, the magnetic field had to be applied at the third Josephson null to reduce the Shapiro steps substantially, and consequently rounding out the sharp nonlinearity of the gap. This effect was especially notable for FSOI A-C2N8, where the gap was rounded even at the first magnetic null.

As with the quartz devices, we have estimated the noise contribution of various components within the tested SOI mixer chip. We have selected FSOI A-D2N1 for this exercise, but we expect similar behaviour for the other tested SOI mixers.

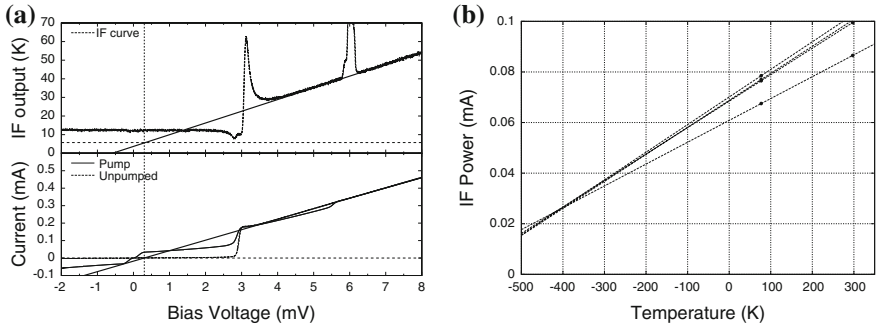

Fig. 5.15 **a** RF and **b** IF noise contributions estimated from the unpumped IV and IF curves of FSOI A-D2N1

Table 5.5 Noise temperature breakdown by estimating the optical, IF and mixer conversion loss at 600 GHz, using data from FSOI A-D2N1

Component	Optics	Mixer	Isolator	LNA	Warm IF chain	Total
Noise (K)	406.0	67.9	37.3	63.0	0.9	575.1

As can be seen from Fig. 5.15 and Table 5.5, the RF noise was estimated to be above 400 K, while the noise contribution from the LNA around 5 K, as expected. This estimation appears to agree well with the argument we presented earlier, indicating that the majority of the loss for SOI devices were mainly coming from the poor optical coupling caused by the junction shifting problem.

In short, the measured performance for this batch of SOI devices were compromised due to the junction offset inducing unexpectedly high optical loss to the mixer. Moreover, the Shapiro step was hard to suppressed and this have made the first photon step region that was not wrapped, unavailable for noise temperature measurement.

5.6 Summary

We have presented the measured performance of both the quartz based and SOI based unilateral finline SIS mixer, fed by the multiple flare-angle feed horn. In general, most of the tested devices could be pumped easily and showed promising noise performance. This demonstrates the integrity of the mixer designs presented in Chap. 4. The measured performance for the quartz devices agreed well with the software predictions but the performance was degraded at the high frequency end by a significantly larger than designed tunnel junction. The best receiver noise temperature of 143 K was measured at 600 GHz. The measured noise temperature for the SOI devices was higher than 350 K, but we believe that this was caused by the junction shifted with respect to the wiring layer, causing severe loss of optical coupling to the junction.

An important conclusion from this chapter is that the finline mixer design can indeed be extended to work at THz frequencies, in conjunction with the very thin substrates produced using the SOI technology.

5.7 Postscript

Since the completion of the thesis, we have managed to test a few more SOI devices with a slightly different design layout, and we also managed to measure the IF performances of these SOI devices. The results from these measurements have been reported in Tan et al. (2013), and therefore we shall present here only a summary as an update to the chapter.

Figure 5.16 shows the layout of these SOI mixers. These SOI devices were fabricated on the same wafer as the SOI mixers reported earlier, hence they suffers from the similar junction shifting and alteration with the junction size problem. The mixer circuit design is basically similar to the direct-mixer on SOI substrate depicted in Fig. 4.1 of Chap. 4, except that the half-moon stub is now also acts as an RF choke, replacing the alternating high and low impedance quarter-wavelength microstrip RF choke design. However, due to the difference in the positioning of the half-moon stub in relation with the tunnel junction, this design happened to be more tolerable to the junction shifting problem. This is due to the fact that the junction is now shifted

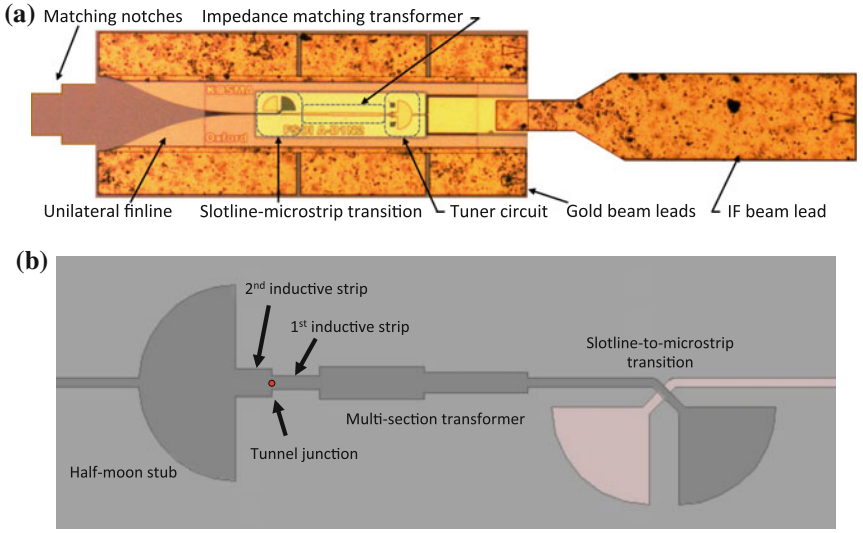

Fig. 5.16 **a** The planar circuit mixer chip comprising the finline taper, slotline-to-microstrip transitions, tuner circuit, RF choke, and gold beam leads for grounding and IF connections. **b** Layout of the RF tuning circuit and the slotline-to-microstrip transition. The *red dot* shows the location of the tunnel junction. The layout is a zoom on the circuit shown in (a)

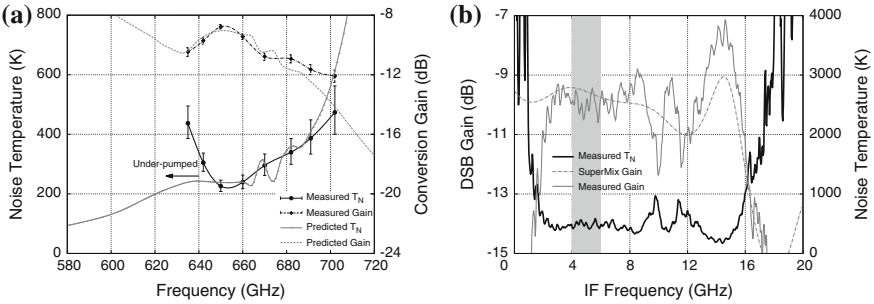

Fig. 5.17 **a** Measured and computed T_N, and receiver gain curves, across the LO frequency range. The computed gain curve by SuperMix was slightly shifted to compensate for losses not included in the model. **b** The measured DSB T_N and gain against the IF frequency at 4.5 K, showing the ultra-wide operating bandwidth of the new mixer. The SuperMix simulated gain curve was shifted to account for losses not included in the model

along the direction of the tuning stub (hence shifting the tuning frequencies), rather than shifted away from the tuning stub. In the latter case, the tuning stub would only be presented partially to the junction, hence severely deteriorating the performance of the mixer chip.

We measured the noise temperature of these SOI mixers against frequency over the 630–702 GHz range and obtained a best value of $T_N = 226 \pm 20$ K and DSB gain of -8.7 ± 0.15 dB, as shown in Fig. 5.17a. The quoted values are corrected for the beam splitter loss but include the contributions from the IF system, the Dewar window, and other optical losses. This again shows that the performance of the SOI mixer is similar to that of the conventional waveguide mixers. We were also able to reproduce the measured results using SuperMix software, by taking into account the fabricated errors. In these simulations, we assumed that the fabricated junction size was about 10 % smaller than the nominal design value and its position was offset by $\sim 1\,\mu$m from the designated position. As can be seen in Fig. 5.17a, including these fabrication errors in the simulations allow us to reproduce accurately the measured behaviour of the tuning circuits, where the best performance of the mixer was shifted towards lower frequencies end. The predicted gain curve also matches very well with the measured gain profile across the band, therefore further validating our mixer design procedure.

The IF output of the mixer chip was also matched to the 50 Ω IF amplifier chain through a multi-stage IF transformer PCB board Tan et al. (2014), for best performance between 4–12 GHz. Figure 5.17b shows the measured IF performance of the mixer, taken without any bandpass filter in the IF chain. One can see that the mixer has an operating IF bandwidth from about 2 GHz to 15 GHz. The deterioration of the performance below 2 GHz was simply due to the lower limit set by the IF amplifier chain. In Fig. 5.17b we also plotted the DSB gain predicted by SuperMix, and again we can see that the measured performance agreed well with simulation predictions, for example the slight deterioration in gain around 10–12 GHz that was correctly

predicted by the SuperMix model. This result in important, as it shows that we are able to extend the IF bandwidth of an existing SIS mixer from the original 4–6 GHz to approximately 2–15 GHz, by simply adding an additional IF transformer optimised to match the mixer's output impedance to 50 Ω over this IF bandwidth as described in Chap. 4.

References

Grimes, P. (2006). *Design and analysis of 700 GHz Finline Mixers. Ph.D. thesis*. UK: University of Cambridge.

Pütz, P. (2004). *Fabrication of superconductor-insulator-superconductor devices for heterodyne mixer applications with electron beam lithography. Ph.D. thesis*. Germany: Universität zu Köln.

Westig, M. P., Jacobs, K., Stutzki, J., Schultz, M., Justen, M. & Honingh, C. E. (2011). *Balanced superconductor-insulator-superconductor mixer on a* 9 μm *silicon membrane*. *ArXiv e-prints*.

Woody, D. P., Wengler, M. J., & Miller, R. E. (1985). 85–115-GHz receivers for radio astronomy. *IEEE Transactions on Microwave Theory Techniques*, *33*, 90–95.

Goldsmith, P. F. (1997). *Quasioptical systems: gaussian beam quasioptical propagation and applications*. Wiley-IEEE Press.

Skalare, A. (1989). Determining embedding circuit parameters from dc measurements on quasiparticle mixers. *International Journal of Infrared and Millimeter Waves*, *10*, 1339–1353.

Withington, S., Isaak, K. G., Kovtonyuk, S. A., Panhuyzen, R. A., & Klapwijk, T. M. (1995). Direct detection at submillimetre wavelengths using superconducting tunnel junctions. *Infrared Physics and Technology*, *36*, 1059–1075.

Salez, M., Febvre, P., McGrath, W. R., Bumble, B., & Leduc, H. G. (1994). An SIS waveguide heterodyne receiver for 600 HGz-635 GHz. *International Journal of Infrared and Millimeter Waves*, *15*, 349–368.

Tan, B.-K., Yassin, G., Grimes, P., & Jacobs, K. (2013b). 650 GHz SIS mixer fabricated on silicon-on-insulator substrate. *Electronics Letters*, *49*(20), 1273–1275.

Tan, B.-K., Yassin, G., & Grimes, P. (2014). Ultra-Wide Intermediate Bandwidth for High-Frequency SIS Mixers. *Terahertz Science and Technology, IEEE Transactions on*, *4*(2), 165–170.

Chapter 6
Single-Chip Integrated Balanced SIS Mixer

Overview: This chapter describes the design, mixer assembly, experimental setup, and experimentally measured results of the integrated balanced SIS mixers operating near 700 GHz. The new design retains the same fabrication requirements as the single-ended SOI mixers, with all the circuit components integrated onto a single chip using planar circuit technology. This results in a significantly simpler balanced mixer block design than the conventional balanced mixers.

Preliminary testing of the balanced devices resulted in a best noise temperature of 714 K measured at 635 GHz, and remained at a similar level throughout the operating frequency band. As this initial batch of balanced mixers was fabricated on the same wafer as the single-ended SOI mixers, they also suffered from the same junction shifting problem. This and various other losses, including RF beam truncations and difference in junction size, gave rise to a higher than expected noise temperature. Nevertheless, independent testing of the on-chip RF quadrature hybrid, and the DC/IF blocks showed that they have performed well. Before concluding the chapter, we present the analyses and simulations using HFSS and SuperMix, to assess these measurements.

6.1 Introduction

The major advantage of a balanced mixer over a single-ended mixer is its ability to reject LO sideband noise and to harness all the available LO power, by eliminating the use of a beam splitter. In principle, one can form a balanced mixer by simply connecting two reverse-biased SIS mixers to the output ports of a 180° or 90° RF hybrid, and then combining the down-converted IF outputs of both mixers. Here, we chose to use a quadrature RF hybrid for its compactness, in conjunction with a 180° IF hybrid. As shown in Fig. 6.1, our balanced mixer comprises 6 major RF components: unilateral finline tapers with matching notches, finline-to-microstrip

B.-K. Tan, *Development of Coherent Detector Technologies for Sub-Millimetre Wave Astronomy Observations*, Springer Theses, DOI 10.1007/978-3-319-19363-2_6

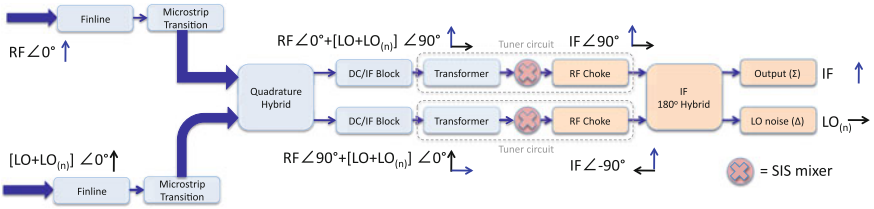

Fig. 6.1 Block diagram showing the components needed for a balanced mixer design. The phasors for the LO components are shown in *black arrows*, while the RF phasors are in *blue*. The 0° phase is referenced to the upward pointing direction and clockwise for positive phase shift

transitions, an RF quadrature hybrid, DC/IF blocks, superconducting tuning circuits with SIS junctions, and RF chokes terminated with an IF bonding pad (Tan et al. 2013, 2012).

The simplest way to understand the working principle of a balanced mixer is by considering the phases of the LO and the RF signal, with an additional LO noise component $LO_{(n)}$ in-phase with the LO power (Kerr 1998; Kooi et al. 2012). For simplicity, we have assumed that all these incoming GHz signals have the same phase at 0°. The RF signal from the sky and the LO power, coupled separately through two sets of finline and microstrip transition, enter the RF quadrature hybrid, to produce two merged GHz signals that have a 90° phase difference between the RF and the LO signals. These are written as $\mathrm{RF}\angle 0° + (\mathrm{LO} + \mathrm{LO}_{(n)})\angle 90°$ at the upper branch and $\mathrm{RF}\angle 90° + (\mathrm{LO} + \mathrm{LO}_{(n)})\angle 0°$ at the lower branch of Fig. 6.1.

Before feeding these GHz signals into two individual SIS junctions, two DC/IF blocks are placed between the RF hybrid and the tuning circuits leading to the junctions, to prevent signal leakage and interaction between the SIS junctions. From each mixers, we now have IF outputs that are ±90° phase-shifted between the signals of two branches. It can be seen immediately that the LO (and the LO noise components) are now 180° out of phase with the RF signals at the output of both mixers. Hence, when these two down-converted IF signals are combined at the 180° IF hybrid, we obtain the IF signal at the `sum` (Σ) port without LO noise, and all the LO noise components appear at the `difference` (Δ) port.

The configuration shown in Fig. 6.1 assumes that both SIS mixers are biased with the same polarity. If they are biased with opposing polarity, one simply has to flip the polarity of the IF output of one of the mixers, since the IV characteristic of an SIS junction is anti-symmetric. In this case, the `sum` port would be the LO noise output, while the `difference` port is the desired IF signal.

6.2 Design of the RF Passive Circuit Components

Conventionally, the main components of balanced SIS mixers were constructed with waveguide-machining technology, which is challenging in the THz region. In particular, they often required the careful selection of two identical single-ended SIS mixer

chips, where the mixer blocks and other RF waveguide components (e.g., RF hybrid) are mechanically attached together (Serizawa et al. 2008; Kooi et al. 2010; Justen et al. 2008; Shitov et al. 2006; Claude et al. 2000). Aligning these component blocks accurately at high frequencies is not a simple task. Furthermore, this method results in a bulky and complicated waveguide component block assembly and a crowded receiver. In recent years, there has been a lot of enthusiasm to simplify these designs to enable deployment of more advanced SIS mixers into compact detector arrays (Grimes et al. 2005; Kerr and Pan 1996; Kerr et al. 2000; Westig et al. 2011).

In our design, we chose to use only planar circuit technology to ensure that the mixer block is kept as simple as possible. All the RF circuit components required are integrated on a 15 μm SOI substrate. We aimed to retain the same fabrication processing steps as those employed for the single-ended mixer chip described in Chap. 5, without the use of any lumped element components. The simple configuration consisted of only an SOI substrate, a niobium ground layer (250 nm), a silicon monoxide dielectric layer (475 nm) and a niobium wiring layer (400 nm). The smallest dimension of any planar circuit structure on chip is 2.5 μm, complying with the limits of standard photolithography.

An important advantage of integrated planar circuits over waveguide technology is that it only requires one magnetic coil since all the SIS junctions are in close proximity to one another. The entire mixer block required for the mixer is therefore greatly simplified and reduced in size. Only a straight rectangular waveguide connected with two feed horns and a pocket for the IF board are needed in the final mixer block module, closely resembling the single-ended mixer block presented in Chap. 5. In addition, planar circuit technology allows us to scale a successful design to other frequency ranges in a straightforward manner (see Appendix D).

With SOI technology, one can easily shape the mixer chip into any required planar form using a direct etching technique. This gives greater freedom in designing the mixer block, and simplifies the positioning procedure when mounting the device in the block (Belitsky et al. 2011). In our design, two unilateral finline tapers are deposited back-to-back, as shown in Fig. 6.2, while the remaining superconducting circuits are fabricated on the central part of the chip, connecting the two finline tapers. This simple layout allows us to use only a straight rectangular waveguide in the mixer block. The signal from the sky is coupled to the chip from one side of the block via a feed horn, while the LO power is coupled from the other end via a similar feed horn. The important advantage of this configuration is that it eliminates the need for a beam splitter that normally wastes 90 % or more of the available LO power. This reduces the stringent power requirement on the LO source, and opens up the opportunity of using a photonic mixing LO source (Huggard et al. 2002, 2004, 2006) instead of the commonly used solid state sources. All of these advantages are not only confined to balanced mixers, but are equally important for more complicated mixer designs, such as the sideband separating and balanced with sideband separating mixer designs (see Chap. 7).

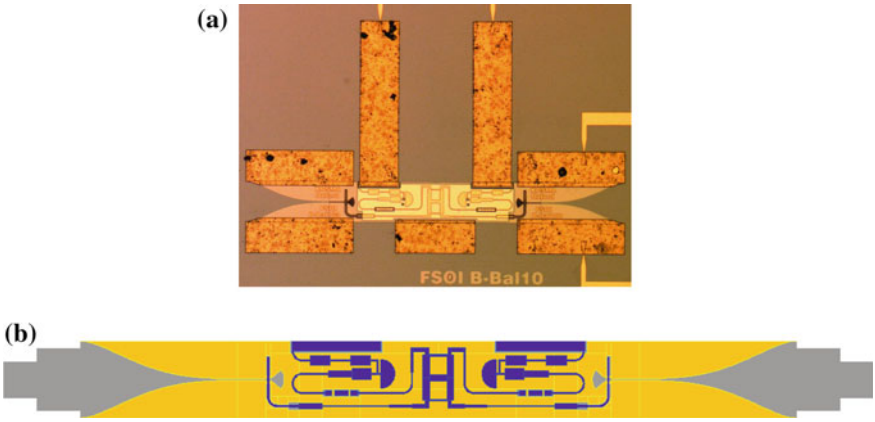

Fig. 6.2 **a** Photo showing the complete balanced SIS mixer chip before the final SOI etching to define the chip size and the matching notches. **b** AutoCad drawing drafted without the dielectric layers and beam leads for clarity

Our balanced SIS mixers presented in this chapter are designed to work in conjunction with a circular Nb/AlO_x/Nb SIS tunnel junction that has an area of 1 μm^2. This corresponds to a normal resistance of approximately 20 Ω (with a current density of approximately 14 kA/cm^2) and junction capacitance of 75 fF. All the individual on-chip RF circuit components are made to match with a system-wide characteristic impedance of 20 Ω (a 3 μm wide microstrip line) at the input and output ports, to ease the integration of the various planar components into the complete circuit. The designated operating frequency band is from 600–700 GHz.

In the following sections, we will describe in detail the design of each circuit component and present full 3-D electromagnetic simulation results from HFSS. We have predominantly used microstrip as the main transmission line, and for all the mixers reported here, we did not include an IF matching circuit. The final optimised dimensions of various structures are tabulated alongside the corresponding figures using the same notation as laid out in Chap. 4. The finline-to-microstrip transition employed here is the same as the single-ended mixer design, but here we only used the transition design that employs CPW sections (i.e., the CPW-design in Chap. 4). The output microstrip width is modified to 3 μm to ease the integration with other circuit components. The tuning circuit used is also similar to the one employed in the single-ended mixer, except that the transformer is now matched to a 20 Ω input microstrip port.

6.2.1 RF Quadrature Hybrid

For planar circuit on-chip integration, we used a microstrip branch line hybrid with a 90° phase difference between the two output arms as shown in Fig. 6.3. To increase

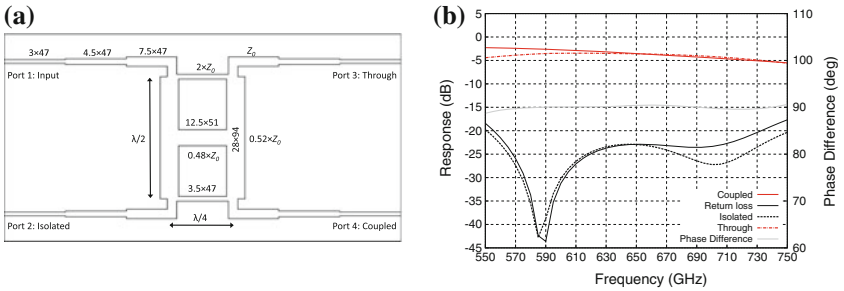

Fig. 6.3 **a** Layout of the 90° RF quadrature hybrid, with the dimension optimised by HFSS. **b** The S-parameters and the phase difference between the `coupled` and `through` arm of the hybrid across the designed RF band

the bandwidth, we used two cascaded hybrids at the expense of slight amplitude imbalance between the `through` and the `coupled` arms. This however does not effect the performance of the mixer significantly, since balanced (and sideband separating) designs often have a high degree of tolerance for both amplitude and phase imbalances (Claude et al. 2000).

The highest impedance branch lines (and therefore the narrowest sections) in the hybrid were chosen to be $2Z_0 \approx 20\,\Omega$, where Z_0 is the characteristic impedance of the four input/output arms of the hybrid. This corresponds to a microstrip width of about 3 μm, well within the limit of standard photolithographic fabrication. A transformer is then used to transform the 10 Ω input/output microstrip back to 20 Ω line. The distance between each T-junction is close to $\lambda_g/4$ in length. All the dimensions were optimised in the final design using HFSS for the widest bandwidth.

As shown in Fig. 6.3b, the return loss and the coupling between the two input ports are less than −20 dB across the operating frequency band. The coupling to the `coupled` and the `through` arms is close to −3 dB, with only a small variation of ±0.5 dB. The mild roll off from low to high frequency is due to the superconducting surface impedance variation from low to high values as a function of frequency. The phase difference between these two output arms is constant at 90° ± 0.5° across the entire band.

6.2.2 DC/IF Block

The DC/IF block is used to DC isolate the two SIS tunnel junctions and to prevent IF power leakage between the two mixers. Normally, a series capacitor is employed for this purpose; either by means of a lumped element metal-insulator-metal (MIM) capacitor or a planar interdigit capacitor. The former have the disadvantage of increasing the complexity of the fabrication process, whilst the later has a large size and

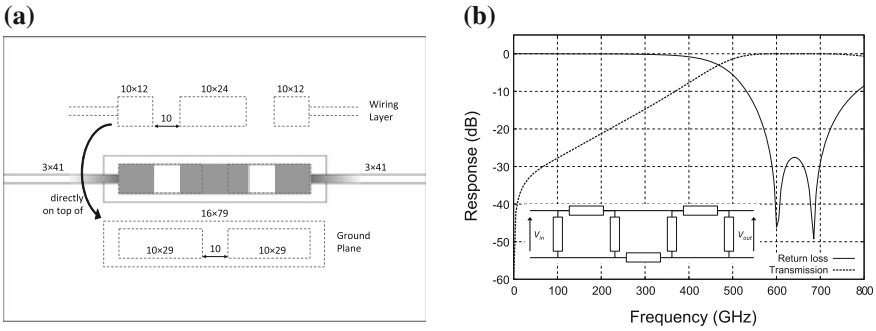

Fig. 6.4 **a** Layout of the broadside coupler as DC/IF block. Panel **b** shows the equivalent circuit, and the transmission and the return loss simulated using HFSS

the gap between the interdigit arms are often too small to be fabricated at THz frequencies.

Our design employs a broadside coupler as DC/IF block. The RF power is coupled from the microstrip to the underlying CPW, both separated by an oxide layer, and back to the microstrip, as shown in Fig. 6.4a. The overlapping region between the microstrip with the central strip of the CPW determines the parallel capacitance between the input and the output ports, while the gap between the microstrips, and the gap between CPW stages gives the series capacitance (see the circuit diagram in the inlet of Fig. 6.4b). To first order, the required capacitance of the structure can be estimated from the overlapping areas and gap distances. This initial value is then optimised within the HFSS model to include the effects of the inductance of the transmission lines. Since both transmission lines are not in contact with each other, they are therefore always DC isolated, and only the RF power within the resonant frequency band is allowed to pass through with minimum return loss. In circuit terms, it acts like a bandpass filter at RF frequencies, as shown in Fig. 6.4b. Again, we cascaded two broadside couplers to widen the operating RF bandwidth.

6.2.3 IF Hybrid

The 180° IF hybrid used later in the balanced mixers performance test was reported previously (Grimes 2006), hence only the layout and the simulated performance results from the Ansoft Designer are reproduced here for completeness, as shown in Fig. 6.5.

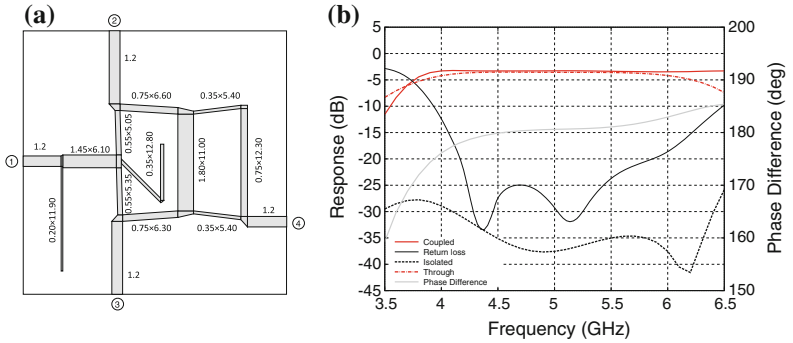

Fig. 6.5 **a** Image (courtesy of P. Grimes) shows the layout of the 180° IF hybrid, where Port 2 & 3 are the input ports, while port 1 is the `sum` and port 4 is the `difference` port. **b** The S-parameters and the phase difference between the `sum` and `difference` port of the hybrid across the designed IF band

6.3 Balanced Mixer Simulations

In order to optimise the RF performance of the complete full mixer chip, we would normally combine all the RF circuit components and simulate the chip in HFSS. However, for a balanced design (and for all the advanced mixer designs presented later in Chap. 7) the entire mixer chip is electrically too large for HFSS simulations. Consequently, we approached this problem with two alternative techniques. In the first method, we only combined a subsection of the RF chip that includes the RF quadrature hybrid, the DC/IF blocks and the tuner circuits, without the finline taper and the microstrip transition, since we know that their performance is good within the operating band. Secondly, we exported the S-parameters of each RF circuit component simulated by HFSS into Ansoft Designer to form a complete RF mixer chip model. Both methods allow us to predict the RF performance of the mixer, but do not provide the means for full optimisation. Nevertheless, as shall be seen later, even by simply cascading the required components to form the complete mixer chip, the final performance is good enough within the operating waveband, with insignificant effects from the interfaces.

Figures 6.6 and 6.7 show the outcomes of the simulations from HFSS and Ansoft Designer, respectively. One notices immediately that the results obtained by both packages agree well with each other. The power coupling to the two SIS junctions is almost identical, averaging at -4 ± 1 dB from 600–700 GHz. The mild roll off from the low to high frequencies is caused mainly by the RF quadrature hybrid (see Sect. 6.2.1). The phase difference between the two IF outputs from the SIS mixers is also kept to within $90 \pm 2°$ from 580–720 GHz, while the return loss and isolation between the two input ports remains below -10 dB for about 120 GHz.

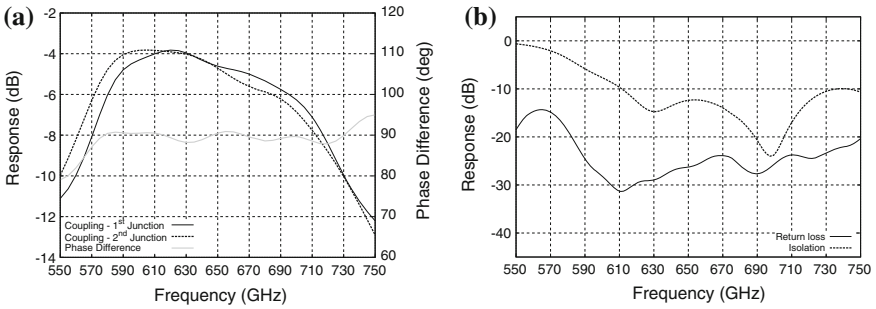

Fig. 6.6 HFSS simulation of a subsection of the mixer chip including the RF quadrature hybrid, the DC/IF blocks and the tuner circuits. **a** Coupling and phase difference. **b** Return losses and isolation

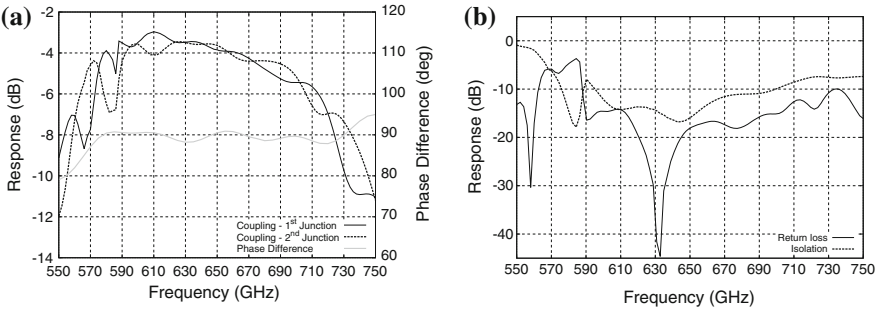

Fig. 6.7 Ansoft Designer simulations of the full balanced chip by importing various S-parameters from HFSS. The phase different is adapted from HFSS simulation with only the quadrature hybrid, DC/IF block and the tuner circuits. **a** Coupling and phase difference. **b** Return losses and isolation

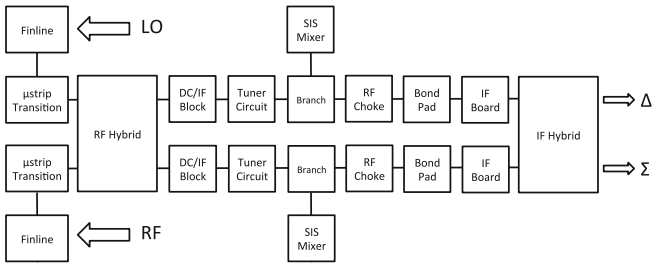

Fig. 6.8 Block diagram shows the various components included in the SuperMix simulation

For estimating the heterodyne mixing performance of the final balanced mixer, we followed the method described in Chap. 4, forming a full-chip SuperMix model via

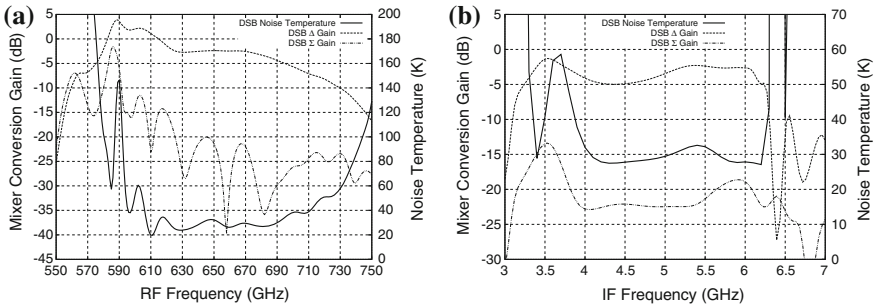

Fig. 6.9 SuperMix simulations showing the predicted behaviour of the final design of the balanced mixer chip. **a** RF response: fixed bias points at 2.4 mV with IF frequency set at 5.5 GHz. **b** IF response: fixed bias points at 2.4 mV with RF frequency at 650 GHz

the HFSS generated S-parameters of individual circuit components.[1] In Fig. 6.9, we show an example of these calculations. As expected, the performance is good from 600–700 GHz. The best performance appears to have shifted upward by ∼10 GHz, which is not surprising, since all the circuit components were simply cascaded together without further optimisation. Note that no IF transformer is included in these SuperMix calculations (the same applies to the other advanced mixer designs in the next chapter), since we did not use any IF transformer to match the IF impedance. The IF operating bandwidth is defined by the bandwidth of the IF hybrid (4–6 GHz), where the IF response is flat at ∼30 K, as shown in Fig. 6.9b.

6.4 Device Fabrication

The performance of a well-designed balanced mixer relies critically on the quality of the two SIS junctions. Ideally, both junctions need to be fabricated not only close to the designated size with the correct normal resistance and capacitance for the tuning circuit to work, but what is especially important for the balanced mixer operation is that both junctions have to be fabricated as identical as possible.

Since our balanced mixer design has the same fabrication requirements as the single-ended SOI devices, we fabricated these double-ended mixers on the same 15 μm SOI wafer. Fabrication of the mixer chip follows the same procedure used for the standard finline mixer described in Chap. 5. Figure 6.10 shows the layout of both mixers on the same wafer, where the balanced mixers were populated at the centre column, while the single-ended devices on either side of the wafer.

[1] The 180° IF hybrid was generated through Ansoft Designer. This can be done using HFSS too, but since the IF hybrid does not operate in a superconducting state and the fringing effects are negligible, it is easier to use the simpler 2-D planar circuit software.

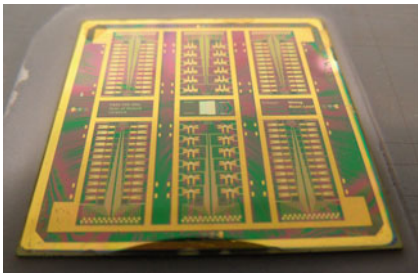

Fig. 6.10 Photograph showing the layout of balanced and single-ended devices on the same SOI wafer, after the front side processing

There were 24 balanced mixers in total, but only 15 of them had both junctions fabricated successfully. As shown in Fig. 6.11, out of these 15 devices only 5 devices had both junctions fabricated to within ±7 % of the 20 Ω normal resistance, and 4 devices had less than 7 % difference between the normal resistances of the two junctions. Consequently, we were left with only 3 devices that satisfied the requirements stated above.

Since these balanced mixers were fabricated on the same wafer as the single-ended SOI devices, all of these balanced devices suffered from the same junction shifting problem (see Chap. 5), which is particularly detrimental for the balanced mixers. Recall from the earlier sections that the two tuning circuits of our back-to-back balanced design were positioned as a mirror image of each other with respect to the hybrid. This implies that if one junction is shifted towards the radial stub (i.e., tuned to higher frequency), the other is shifted away from its radial stub. Hence, at any operating point, neither junction would be able to operate with similar performance to the other junction, producing an intrinsically imbalanced configuration. Figure 6.12 shows an example of the junctions shift in one of the balanced mixers to demonstrate the magnitude of shifting.

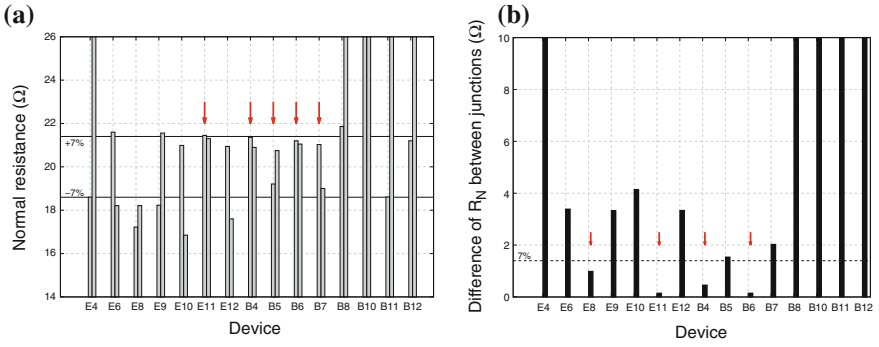

Fig. 6.11 Normal resistance of all the surviving SOI balanced mixers that had both junctions fabricated. **a** Normal resistance of both junctions. **b** Difference of normal resistance between the two junctions

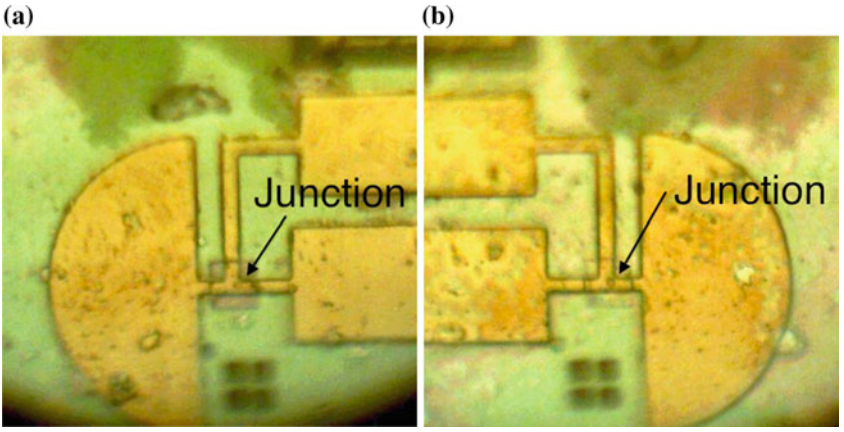

Fig. 6.12 Photograph showing both junctions of the same device shifted rightwards. **a** Junction a shifted away from the half-moon stub. **b** Junction b shifted towards the half-moon stub

6.5 Experimental Setup

Before proceeding to describe in detail the experimental setup, we would like to emphasis that the entire system setup, including the cryogenic Dewars, the LO source, the mixer block and the ancillary electronics, was built previously by the Detector Physics Group from University of Cambridge to test a different batch of balanced mixers. The apparatus was originally constructed to test a 60 μm thick quartz antipodal finline balanced mixer at 700 GHz, designed and fabricated by Dr. Paul Grimes (Grimes 2006). Using this existing system enabled us to assess the performance of the new balanced mixers immediately, but at the expense of not having all components optimised to work with the new design, especially the mixer block which had a deep groove in the waveguide wall designed for the quartz mixers.

Figure 6.13 shows the experimental setup comprising the mixer block, bias tees, IF hybrid, isolator and cryogenic amplifier, all housed within the cryogenic Dewar. The cryostat itself was a square Dewar with two windows, and a circular cold plate. The mixer block was mounted on an elongated bracket which was in turn bolted down to the Dewar's cold plate, along with the IF components and biasing circuits. Two bias supplies, temperature sensors readout electronics and the power supply to the IF amplifier and magnetic coil were all connected through the Dewar using several multiple pin connectors. The IF components, including the isolator, the 4–12 GHz cryogenic amplifier, and the warm IF system, are similar to the ones used in the single-ended mixer tests described in Chap. 5.

The LO and RF signals enter the cryostat separately through two HDPE windows (460 μm thick) mounted on the outer wall of the cryostat, as shown in Fig. 6.14. Three layers of Zitex® were installed on the 77 K stage inner shield as infrared filters. The

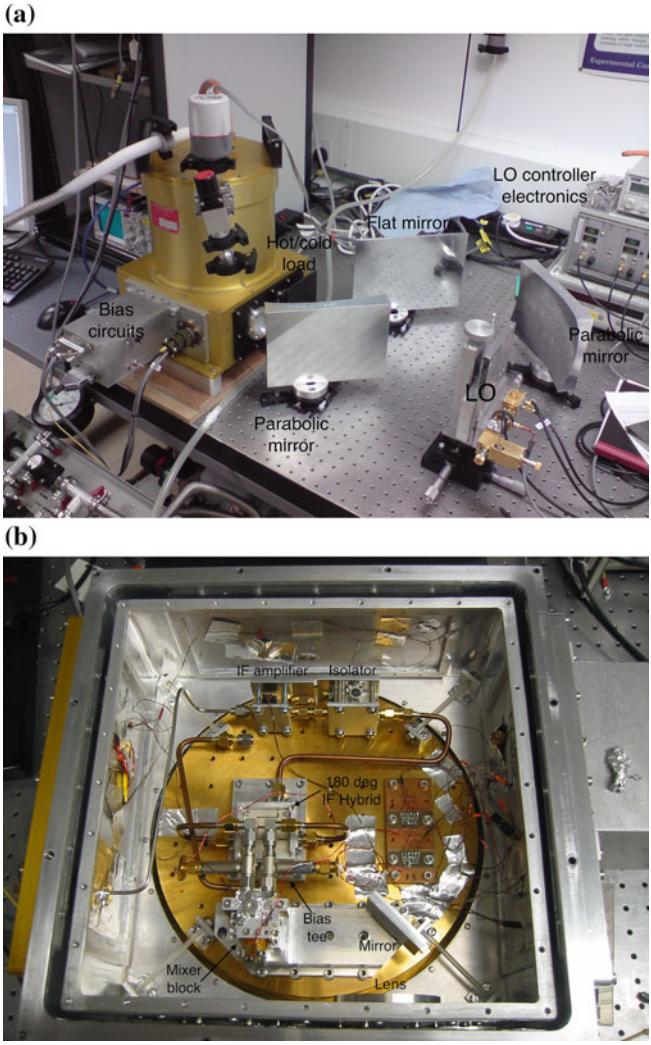

Fig. 6.13 Experimental setup for testing the balanced mixer performance. **a** Actual experimental setup. **b** Working area of the Dewar

LO (or RF) beam is injected to the mixer block via two flat mirrors and a Pickett-Potter horn reflector antenna, while the RF signal (or LO) is coupled straight into the other end of the mixer block via an identical horn reflector antenna. However, due to the relatively large distance between the mixer block and the Dewar window at the LO optics path, the beam was truncated due to the small diameter of the cryostat window. Hence, a dielectric terahertz lens was installed to minimise this truncation and to improve the LO power coupling. Nevertheless, any loss or changes in the LO

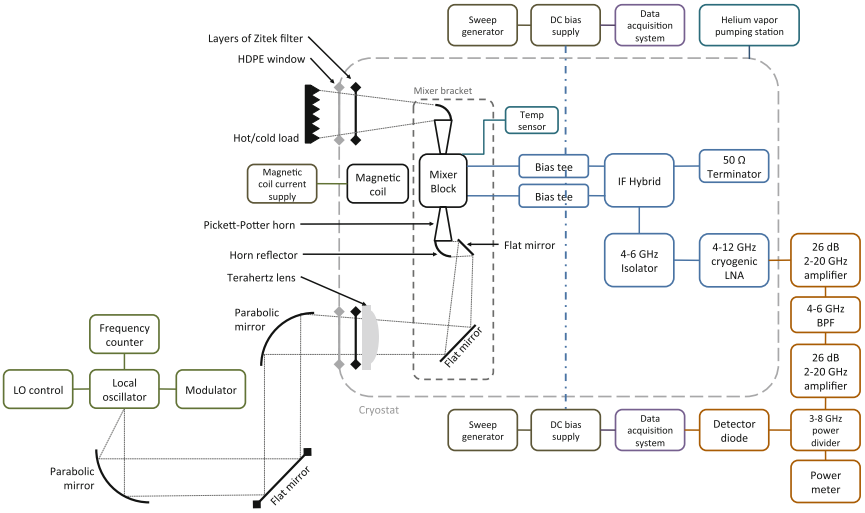

Fig. 6.14 Block diagram of the balanced mixer test setup

signal path should not affect the mixer performance significantly, since the RF signal is coupled along a completely separate path and the direct injection of the LO signal (without beam splitter) should ensure that there is a large excess of available LO power. Stray reflection of LO signal within the Dewar, however, may couple into the RF path and degrades the mixer performance. Such effects should be detectable by swapping the RF and LO input path, and could be improved by placing Eccosorb® at critical areas inside the Dewar.[2]

6.5.1 Mixer Assembly and Device Mounting

Due to the time constraints, we did not design and fabricate a dedicated mixer block for these new balanced devices. Instead, we made use of an existing balanced mixer block, inherited from the previously described experimental system setup. A detailed description of the mixer block has been reported previously by Grimes (2006), hence only a short description is given here for completeness. It comprises a 160 µm × 320 µm rectangular waveguide with two 55 µm wide by 65 µm deep slots machined into the E-plane of the waveguide for holding the quartz mixer chip. Two back-to-back Pickett-Potter horns, connected to the two ends of the waveguide via circular-to-rectangular waveguide transitions, were manufactured as part of the mixer block. These were designed to work with a pair of horn reflector antennas to

[2]In fact, we did observed hints of this LO stray reflection effect during experiments, though no further effort had been made yet to completely eliminate these reflections.

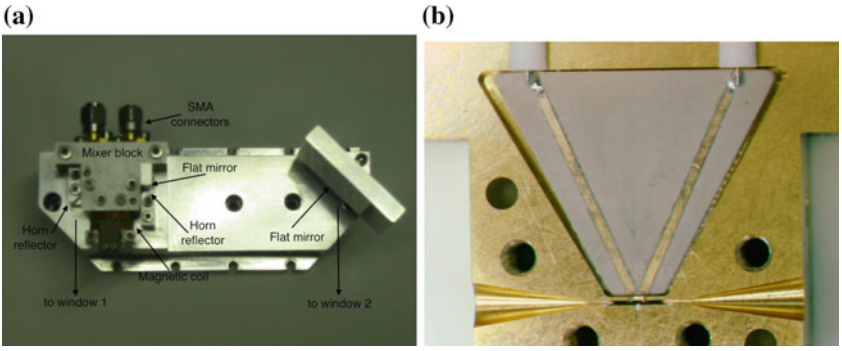

Fig. 6.15 **a** Photograph showing the mixer block and the ancillary relay optics affixed on the bracket. **b** Internal view of the mixer block, with two back-to-back Pickett-Potter horn fabricated as part of the mixer block

reduce the divergence of the outgoing/incoming beams and help to reduce the beam waist radius outside the cryostat. A detailed analysis of the horn and the reflector antenna can be found in Kittara (2002). Both the mixer block and the horn reflectors were mounted on an elongated bracket, together with the magnetic coil and the two flat mirrors as shown in Fig. 6.15a.

The IF board was mounted in a pocket alongside the waveguide, and the end of the microstrips were soldered to two 50 Ω coaxial SMA connectors mounted on the back of the block. The 50 Ω microstrip line (0.6 mm wide) was manufactured on a 1.27 mm thick RT/duroid 2010LM substrate, with a dielectric constant of 10.2 and a dielectric loss tangent of $\tan\delta \approx 0.0023$. The IF signals generated by the balanced mixer were fed through two bias tees and subsequently to the IF hybrid via a pair of equal length semi-rigid coaxial cables. In principle, two sets of IF chains would be needed to connect both the output ports of the IF hybrid into two separate cryogenic pre-amplifiers. However, as explained earlier, one can utilise the anti-symmetry of the biasing response of the balanced SIS mixer, to measure both the Δ and Σ ports simultaneously by sweeping the mixer from both negative and positive voltages. Hence, for simplicity, we opted to connect only one output port from the IF hybrid to the cold IF chain, while terminating the other port with a 50 Ω load. The cold IF chain consisted of an IF isolator and an LNA, mounted separately on the Dewar cold plate. The output of the amplifier was connected through stainless steel semi-rigid coaxial cable to SMA connector mounted outside the Dewar.

Since the new balanced mixer did not need any bond wires, we simply clamped the ground beam leads on both sides of the balanced device between the two split blocks for supporting and grounding of the mixer. Figure 6.16a shows the top-down view of an SOI device mounted on the lower half of the split mixer block. Installing the SOI device in the 'Cambridge' block was not problem free. This is because of the deep grooves (approximately 65 μm in depth) which were originally designed to accommodate a serrated quartz balanced chip. The total width of the SOI chip (about 360 μm) including the beam leads, is only marginally wider than the total

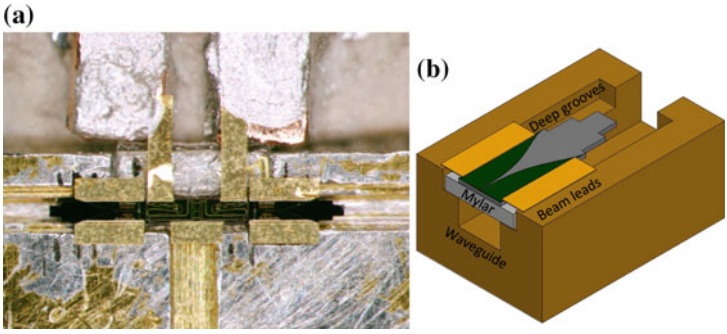

Fig. 6.16 **a** Photo showing a balanced SOI device mounted on the quartz mixer block. **b** Diagram illustrate the position of the mixer chip relative to the waveguide groove

width (270 μm) of the waveguide slots (including the 2×55 μm grooves on each side of the 160 μm wide waveguide). In other words, only a very narrow area was available for the beam leads to hang above both ends of the waveguide groove and hold the chip in level with the surface of the block. Therefore, in order to strengthen the support for the SOI chip, we cut a small piece of Mylar (36 μm thick), and placed it underneath the central part of the mixer chip, with the Mylar hanging across the deep waveguide groove, supporting and holding the mixer chip in position with the help of crystal bond and also levelling the beam leads with the surface of the split block (Fig. 6.16b). We ensured that the Mylar was only a fraction of the length of the entire mixer chip, and was positioned away from the finline and slotline portion of the chip to avoid unwanted loading of the waveguide near the finline tapers.

It should be noted that the narrow strip area available for the beam leads eliminated the possibility of directly bonding the beam leads to the block. Hence, we had to rely on a mechanical contact of the bare beam leads to the upper and lower split block to provide grounding. The advantage of this simple mounting process was that the mixer chip would not be damaged upon de-mounting. While the beam leads could be slightly distorted, the chip could be used again for subsequent tests, if needed.

6.6 Results and Analysis

At the time of writing, there were only three balanced devices that have been successfully tested. The first (Bal-B05) and second (Bal-B07) device had a slightly different normal resistance between the two junctions, compared to the last tested device (Bal-B04). Hence, in what follows, we will focus mainly only on the measured performance of Bal-B04 which gave the best measured noise temperature so far, and present the measured data of the former two devices in Appendix B. We will highlight the measured results for the RF hybrid and in particular, discuss the various sources of noise contributions supported with extensive simulations, and present further analysis and suggestions for future improvements.

6.6.1 Measured Performance of the RF Hybrid and the DC/IF Block

The two most important circuit components in the balanced mixer design, compared to the single ended devices, are the RF quadrature hybrid and the DC/IF block. To assess the performance of the RF quadrature hybrid, we made use of the two SIS junctions as direct detectors, and measured the LO coupling level to the two junctions simultaneously to verify the power coupling of the hybrid. We made sure that the pumped current levels of the first photon step were maintained below a third of the gap current to guarantee operation in the linear regime of the SIS junctions.

Figure 6.17a shows the experimentally measured LO coupling to both junctions of Bal-B05. This plot was made without taking into account other losses in the circuit, hence we assume that all the LO power is fully delivered to both junctions. Also shown in the figure is the simulated performance from HFSS, taking into account the difference in the junction sizes, but not the junction shifting effect since this is hard to simulate in HFSS. Note that the HFSS model is not a complete mixer chip, as mentioned earlier, but simply the cascading of the most important components i.e., the quadrature hybrid, the DC/IF block and the tuning circuits, assuming the transmission of the finline and the slotline-to-microstrip transition are the same on both branches.

From Fig. 6.17a, one immediately notices the striking similarity in the general trend of the HFSS model curve and the measured power coupling between the two output arms of the RF hybrid. This demonstrates the integrity of the design, and indeed the successful operation of the RF hybrid. Note that the simulated curves in Fig. 6.17a have been shifted upward by about 7 GHz, and away from each other by about 1 dB to account for the unknown imbalanced coupling due to the junctions dislocation and other unknown losses. This adjustment also indirectly indicates that there is about 1 dB imbalance in the hybrid power coupling because of the junction's offset in position.

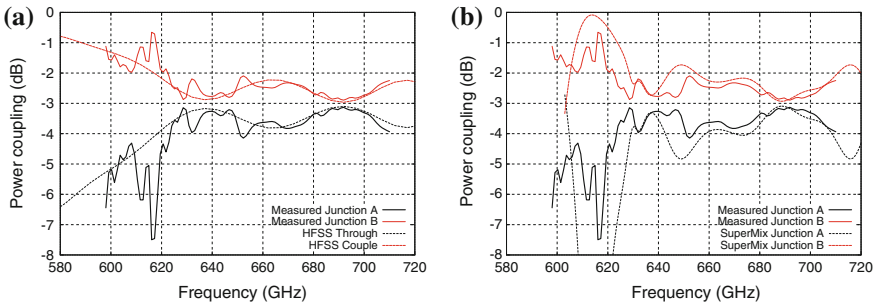

Fig. 6.17 **a** Comparison of the measured performance of the hybrid to the HFSS simulations, with junction size corrected to 0.975× and 1.025× the designated 1 μm^2 area (corresponding to 19.5 and 20.5 Ω). **b** Similar simulation performed using SuperMix full chip model

Using the SuperMix full-chip model to cross check the result from HFSS yields a similar degree of agreement as well, as shown in Fig. 6.17b. The SuperMix simulated curves also exhibit details which are more closely resemble the features found in the measured curve, such as the two humps near the centre of the frequency band. This improvement in agreement is mainly due to the fact that the SuperMix model takes into account the junction shifting and is a full chip model.

The ability of both HFSS and SuperMix models to reproduce the measured results indicates that the original RF hybrid design would work very well, if the SIS junctions were identical and correctly positioned. The fact that both of these junction fabrication abnormalities affect the coupling efficiency of the RF hybrid is hardly surprising, since they not only affect the power coupling to the junction itself, but also affect the effective impedance seen by both output arms of the hybrid.

Finally, the fact that two independent junctions on the same balanced chip could be biased separately without any interferences or cross-talk, points to the successful operation of the DC/IF block to DC isolate the two junctions. The IF leakage of the component is hard to measured quantitatively, but if the IF blocking was not working well, one would have seen the IF noise increase significantly when one of the junctions was biased above the gap—this was not seen in our experiment.

6.6.2 Balanced Mixer Performance

The initial assessments of the first three tested balanced mixers have shown promising performance. However, note that they were not the three best balanced mixers available in this initial batch as indicated in Fig. 6.11, except Bal-B04 (the other two are Bal-B06 and Bal-E11). Before we discuss in detail the performance of Bal-B04, we first summarise the measured gain and noise temperature of all the three tested balanced devices in Table 6.1 to give an overview. The quoted DSB noise temperature ($T_{N(c)}$) and the conversion gain ($G_{R(c)}$) were corrected for various known or estimated RF losses. These include the loss of the HDPE resonant window (without anti-reflection coating) and the losses incurred from the Teflon used as an infrared filter. These losses were calculated using the method described in Chap. 5. We also

Table 6.1 Results of balanced mixer tests carried out on 2012-03-09 and 2012-03-19 for FSOI Bal-B04

Device	f_{LO} (GHz)	T_N (K)	G_R (dB)	NR (dB)	$G_{R(c)}$ (dB)	$T_{N(c)}$ (K)		
						HDPE 460 μm	Zitex and Teflon	WG groove
Bal-B04	635	879	−11.6	10.3	−8.3	867	844	714
Bal-B05	595	1169	−12.8	6.8	−5.6	1045	1028	961
Bal-B07	605	1279	−10.1	–	−3.1	1178	1159	1093

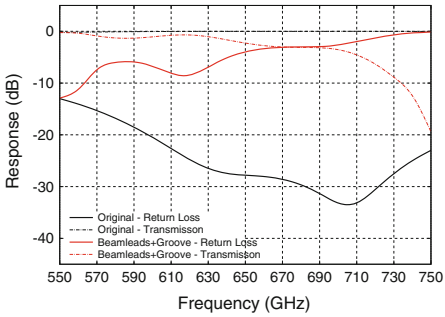

Fig. 6.18 Changes in the power coupling behaviour of the finline taper and the matching notches due to the existence of the waveguide groove

assumed there was a frequency independent 3 % loss from the Zitex® filter, following the investigation by Benford et al. (2003) which indicates that the G-110 Zitex® we used could have loss as high as 5–10 % near 700 GHz.

To obtain a better understanding of the actual noise from the balanced mixer itself, we also corrected the measured performance for the additional loss caused by the deep groove in the waveguide wall. We initially expected that mounting the thin SOI substrate on a mixer block designed for quartz mixers should present rather light loading to the unloaded waveguide. However, HFSS simulations show that the deep groove would in fact alter the performance of the finline taper and the matching notches substantially, as shown in Fig. 6.18. This is most probably due to two factors. First, the SOI matching notches were not originally optimised for this waveguide slot width, and secondly, it could be caused by the gold beam leads hanging across the E-plane of the mixer block. This configuration virtually creates a resonant cavity between the beam leads and the groove (see Fig. 6.16b), and could possibly lead to a resonance of higher order modes generated by the waveguide groove, thus subsequently degrading the quality of RF power coupling to the mixer chip.

This simulated result is in fact consistent with our observations during experiment, where direct injection of LO without beam splitter was still unable to saturate the mixer, apart from at several specific frequencies. Comparing this to the much higher level of LO power coupling measured with single-ended SOI device, where the matching notches and the finline taper were of the same design, supports the argument that the deep groove in the waveguide wall was indeed producing extra RF losses.

6.6.2.1 Bal-B04 Device

The following section focuses on the tested performance of the Bal-B04 balanced mixer. In Fig. 6.19 and Table 6.2, we show the measured DSB gain and receiver noise temperature as a function of frequency between 595–701 GHz. The best noise temperature measured for this device is 714 K at 635 GHz. The overall performance across the operating frequency band also seems to be consistent except for a mild roll off towards the high frequency end. As expected, this was caused by the

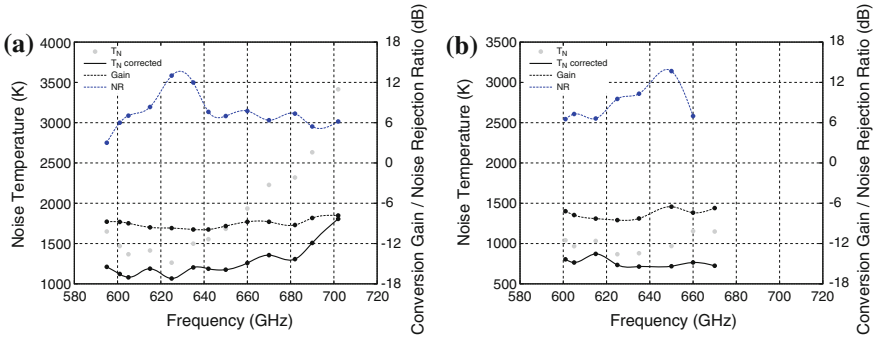

Fig. 6.19 Measured noise temperature and DSB gain for FSOI Bal-B04. **a** 4.5 K. **b** 3.5 K

superconducting circuit surface impedance loss at high frequencies near the gap, which becomes less significant when the mixer is further cooled down to 3.5 K.

The highest noise rejection ratio (defined as the ratio between the measured Y-factor of the `difference` and `sum` port at the same bias voltage) measured for this particular device was around 13 dB, slightly lower than what can be achieved by a well-tuned balanced mixer. This result however was quite acceptable considering both junctions were shifted in opposite directions. The best noise rejection ratio measured also did not occur at the location where lowest noise temperature was measured, since this parameter measures the ability of the balanced mixer to reject the LO amplitude noise, and is not directly related to the intrinsic sensitivity of the individual junction itself.

Generally, we attribute the high noise temperature measured to the non-identical junctions and the relative shifting of the junction positions. The former factor could result in one junction producing more noise when the other is biased at its optimum operating point. Combining this effect with the junction offset in opposite directions relative to the tuning circuit could make the two SIS mixers to have different and opposite tuning behaviours. This would also affect the equality in power coupling to the junctions as well.

We have also noticed that the unwanted Josephson current was rather difficult to suppress simultaneously for both junctions. This is shown in Fig. 6.20, where one can clearly see that when the magnetic coil was adjusted to suppress the Josephson effect completely in the first junction, the second junction was still affected by the Shapiro steps effect. This results in the final combined IF outputs from the IF hybrid having a strong Josephson noise contribution, and unavoidably degrades the measured sensitivity.

Another factor that must have degraded the receiver sensitivity is the beam truncation at the RF optical path for RF power coupling. As mentioned earlier, due to the long optical path inside the Dewar and the small cryostat window, the LO and RF beams were partially truncated. The truncation was lower on the shorter optical path as shown at the top half of Fig. 6.14. Therefore, we chose to couple the hot/cold

Table 6.2 Results of balanced mixer tests carried out on 2012-03-09 and 2012-03-19 for FSOI Bal-B04

$T = 3.6\,\mathrm{K}$, $R_N = 21.36\,\Omega$ and $20.90\,\Omega$							
f_{LO} (GHz)	T_N (K)	G_R (dB)	NR (dB)	$G_{R(c)}$ (dB)	$T_{N(c)}$ (K)		
					HDPE 460 μm	Zitex and Teflon	WG groove
601	1041	−11.3	6.5	−7.2	944	901	803
605	966	−11.4	7.3	−7.8	886	849	764
615	1033	−11.8	6.6	−8.3	976	949	871
625	867	−11.4	9.5	−8.5	839	819	734
635	879	−11.6	10.3	−8.3	867	844	714
650	969	−11.3	13.7	−6.5	969	926	718
660	1155	−12.8	7.0	−7.4	1151	1077	765
670	1149	−12.5	–	−6.7	1132	1037	724
$T = 4.75\,\mathrm{K}$							
595	1649	−14.0	3.0	−8.7	1483	1398	1211
601	1468	−13.5	6.0	−8.8	1340	1277	1122
605	1367	−13.3	7.1	−9.0	1261	1209	1080
615	1414	−13.6	8.3	−9.6	1341	1303	1188
625	1263	−13.3	13.0	−9.7	1225	1196	1066
635	1498	−14.3	12.0	−9.9	1480	1440	1203
642	1554	−14.6	7.6	−9.9	1548	1495	1187
650	1683	−14.9	7.0	−9.4	1683	1605	1175
660	1934	−15.3	7.7	−8.8	1928	1805	1258
670	2227	−16.0	6.4	−8.8	2197	2013	1356
682	2319	−16.4	7.4	−9.2	2240	1999	1306
690	2632	−16.4	5.4	−8.2	2498	2219	1507
702	3413	−17.4	6.2	−7.8	3148	2777	1806

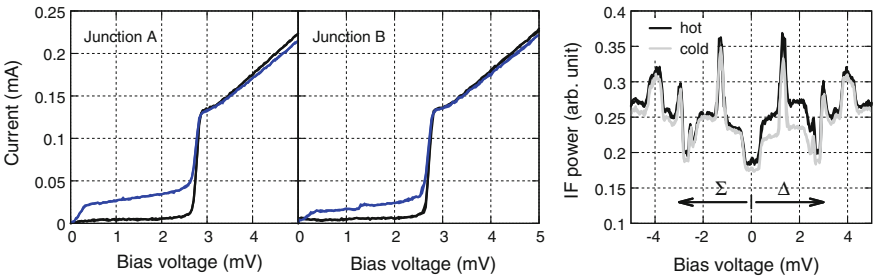

Fig. 6.20 Example of IV and IF curves measured from FSOI Bal-B04

load signal through the shorter path, and rely on the terahertz lens to improve the LO coupling for the longer path. Following standard Gaussian beam analysis, the power coupling through the window for the longer path improved significantly with the help of the lens, but the RF port was still truncated at about 9 dB edge taper due to the lack of additional focusing element. Furthermore, it was rather difficult to carefully check the alignment of the entire optical system, since they were all affixed to the bracket, and were confined within the cryostat itself, preventing any further adjustment during the experiment. Imperfect optical alignment could cause stray reflection within the cryostat, introducing unwanted power coupling to the mixer.

Comparing the 800 K measured noise temperature for the balanced mixer to the 400–500 K noise temperature measured in the single-ended SOI device gives us a perspective on their relative performance. Given that these measured noise temperatures were already subjected to several known RF loss, we believe that the extra ∼300 K noise was caused by the RF beam truncation problem mentioned above. An imperfect impedance match RF hybrid could also cause reflection of RF power back to the hybrid, cancelling out part of the incoming RF power, since the reflecting signal would be 180° out of phase with the input RF power. However, this loss mechanism must be insignificant compared to the beam truncation problem, because these are losses at 4 K, and the magnitude of power reflection into the hybrid should be rather small. This was demonstrated when the redundant junction was biased at different voltages to assess its effect on the tested junction. No significant increase in noise temperature was observed. This simple experiment also indirectly demonstrates that the IF leakage between the junctions was minimum, as mentioned in Sect. 6.6.1.

We would like to emphasis that, apart from the higher than expected noise temperature, the mixer chip has in fact operated successfully as a balanced mixer. This is most clearly demonstrated in Fig. 6.20, where the difference between the `sum` (negative biasing) and `difference` (positive biasing) on the photon step is obvious. For example at bias voltage $V_b = \pm 2$ mV, we can see that the difference in hot and cold loaded IF curve at the Δ port is significantly higher than the Σ port, indicating that the balanced mixer had successfully separate the required IF signals from the LO noise, and injected them into two different ports.

6.6.2.2 Comparison with Theoretical Model

To verify the impact of junction shifting and size difference on the measured noise temperature performance, we ran a SuperMix simulation taking into account both effects. In Fig. 6.21a, we plotted the SuperMix predicted response across the operating frequency band in comparison with the measured performance at 3.5 K. Even though the predicted noise temperature was much lower than the measured one, the general behaviour were very similar. This indicates that the additional noise could be caused by a relatively frequency-independent loss mechanism such as the RF beam truncation and incomplete Josephson noise suppression. SuperMix also predicted that the non-optimised junction configuration could alter the behaviour of the

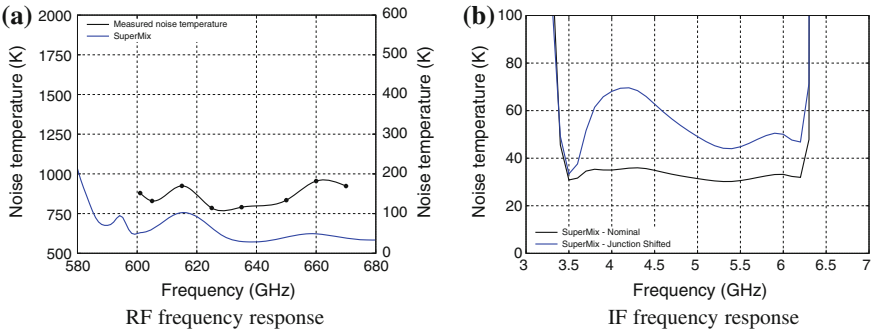

Fig. 6.21 SuperMix model prediction of **a** RF response in comparison with the measured data, and **b** a two fold increase in noise temperature across the IF band due to the junction shifting and size difference

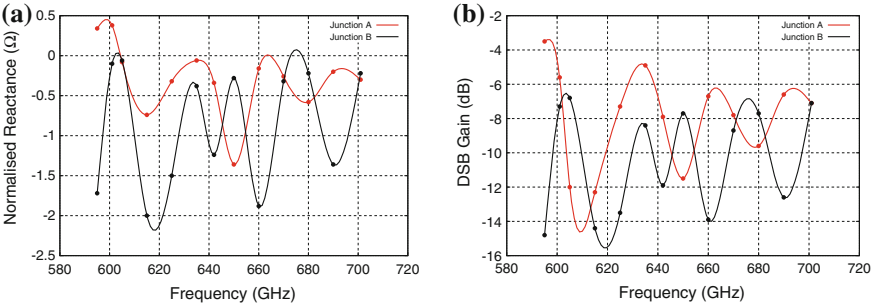

Fig. 6.22 Embedding impedance and DSB gain recovered from SuperMix model. **a** Recovered reactance. **b** Recovered DSB gain

IF response of the balanced mixer. As shown in Fig. 6.21b, this could potentially double the measured noise temperature across the IF frequency band.

In order to further understand the intrinsic tuning behaviour of the individual junction from the balanced test data, we performed the SuperMix calculations described in Chap. 3 to recover the embedding impedances of each junction. Figure 6.22 shows the imaginary part of the embedding impedance and the DSB gain recovered from SuperMix based on the measured IV curves.

Interestingly, one notices immediately that the two junctions exhibit a different tuning behaviour, as if the two mixers that are tuned 'out-of-phase' in frequency. We believe that this effect is largely due to the oppositely shifted junctions with respect to the tuning stubs. Relating this to the measured noise temperature performance, we see that at 635 GHz, the reactance of both junctions was close to zero, and the DSB gain of both junctions was high. This coincides exactly with the frequency at which the best noise temperature was measured. The fact that the measured performance stays almost constant throughout the frequency band is also not hard to explain, as

one can see from these plots, almost at all frequencies, the good performance of one junction is degraded by the relatively inferior performance of the other junction. For example, Fig. 6.22a, b both show that the embedding reactance and DSB gain of the two junctions are most different at 615 and 660 GHz. This translates directly to the relatively poor measured performance at both of these frequencies, compared to the average measured noise temperature.

6.6.3 Single Junction Noise Temperature

With proper configuration, it is possible to measure the sensitivity of individual junction fabricated on the balanced mixer. This test is useful since it can reveal information about the integrity of the design and the loss mechanism that are not directly related to the balanced operation. We approached this by fabricating a new bracket to direct the feed horn pointing straightly outwards the Dewar window, while covering the aperture of the other feed horn with an absorbing material attached to mixer block wall. All the remaining optics, including the horn reflectors, were removed to minimise the optical complexity. The LO power was coupled through a beam splitter in the similar fashion described in Chap. 5 for testing the single-ended SIS devices. Only the IF output from one of the junctions under test was connected directly to the cold IF sub-system, without the IF hybrid. The other redundant junction was terminated with a 50 Ω load. The IF connections were simply swapped for testing the other junction independently.

Figure 6.23a, Tables 6.3 and 6.4 show the measured sensitivities for both junction A and B of Bal-B04. After correcting for the RF losses, and taking the 3 dB coupling from the RF quadrature hybrid into account, we arrived at an average noise temperature of around 800–1200 K, and DSB gain of about −10 to −12 dB. Note that due to the waveguide groove problem indicated earlier, the LO coupling was rather

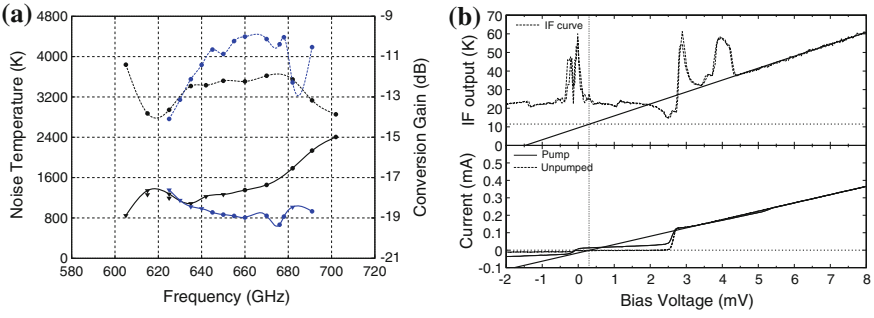

Measured gain and noise temperature IF contribution

Fig. 6.23 **a** DSB gain (*dashed line*) and noise temperature (*solid line*) of Bal-B04a (*black curves*) and Bal-B04b (*blue curves*) measured independently. **b** IF noise contribution estimated experimentally showing high IF noise at ∼12.5 K

Table 6.3 Results of balanced mixer tests carried out on 2012-03-26 for FSOI Bal-B04a

$T = 4.5\,\mathrm{K}$, $R_N = 21.36\,\Omega$								
f_{LO} (GHz)	T_N (K)	G_R (dB)	$G_{R(c)}$ (dB)	$T_{N(c)}$ (K)				
				75 µm BS	HDPE 460 µm	Zitex	WG groove	RF Hybrid
625	3513	−21.3	−14.1	3113	3032	2944	2471	1357
630	2999	−20.5	−13.1	2649	2601	2526	2059	1151
635	2712	−19.9	−12.1	2397	2370	2303	1783	1024
640	2684	−19.7	−11.4	2371	2358	2292	1679	987
645	2533	−19.3	−10.7	2237	2233	2171	1514	910
650	2624	−19.6	−10.9	2320	2320	2254	1461	866
655	2574	−19.4	−10.2	2275	2274	2210	1385	840
660	2586	−19.4	−10.0	2287	2280	2216	1326	808
670	2860	−19.8	−10.1	2538	2505	2434	1383	842
676	2470	−19.4	−10.4	2188	2138	2076	1136	666
678	2873	−19.8	−10.0	2549	2483	2413	1355	826
682	3963	−21.7	−12.3	3535	3419	3319	1784	1016
691	3411	−20.7	−10.5	3042	2882	2801	1539	931

Table 6.4 Results of balanced mixer tests carried out on 2012-04-19 for FSOI Bal-B04b

$T = 4.5\,\mathrm{K}$, $R_N = 21.36\,\Omega$								
f_{LO} (GHz)	T_N (K)	G_R (dB)	$G_{R(c)}$ (dB)	$T_{N(c)}$ (K)				
				75 µm BS	HDPE 460 µm	Zitex	WG groove	RF Hybrid
605	2199	−18.8	−11.4	1935	1793	1742	1464	849
615	3426	−21.1	−13.8	3033	2891	2808	2426	1343
625	3267	−20.9	−13.6	2890	2813	2732	2298	1274
635	2908	−20.3	−12.5	2569	2540	2468	1907	1087
642	3466	−21.0	−12.4	3070	3058	2972	2125	1226
650	3916	−21.6	−12.2	3478	3478	3379	2172	1266
660	4593	−22.3	−12.2	4087	4077	3961	2311	1352
670	5115	−22.7	−12.0	4560	4503	4376	2447	1454
682	6399	−23.7	−12.1	5725	5542	5387	2985	1785
691	8191	−24.9	−13.2	7342	6976	6778	3666	2135
702	10605	−26.2	−13.9	9538	8837	8583	4199	2406

poor in this configuration, since a beam splitter only couples a small percentage of the LO power available from the source, hence at certain frequencies the mixer was relatively underpumped. These were shown as triangle points in Fig. 6.23a.

An interesting feature in Fig. 6.23a is that one can see clearly that one of the junction was tuned towards the lower frequency end, while the other performed better at the high frequency end. This in fact validates our earlier suggestion that the dislocation of the junction position shifted the tuning of the two mixers towards opposite frequency ends. Thus, even if the RF power could be coupled equally to both junctions, the good performance of one junction at a particular frequency would certainly be degraded by the inferior performance of the second junction. This can clearly be seen in the frequency range from 640–690 GHz where the noise temperature measured for junction B is almost double that of junction A.

It is interesting to note that the measured performance of the individual junctions was slightly inferior compared to the balanced mixer performance. This could be attributed to the ability of the balanced mixer to reject the LO amplitude noise. However, the improvement was not vastly significant, as the balanced mixer performance was degraded by the additional noise from the non-optimised combined junctions' performance, as explained earlier.

Calculation of the noise contributed by the IF sub-system indicates that there existed a higher than expected IF noise compared to the single-ended devices, as shown in Fig. 6.23b. This observation indicates that the lack of impedance matching between the IF port of the mixer to the IF amplifier chain might have contributed to higher noise temperature performance. Note that this IF noise contribution calibration methods only works if the balanced mixer is configured for testing the single junction independently, because the method relies on calibration against the shot noise of the individual junction (see Chap. 3).

6.7 Summary

We have presented the design of a wideband unilateral finline balanced SIS mixer at 700 GHz using SOI and planar circuit technology. The design results in an easy to fabricate mixer chip and mixer block with elegant yet fully integrated planar circuits. The performance was fully simulated using rigorous electromagnetic package in conjunction with the quantum mixing package, SuperMix.

Preliminary assessment of the initial batch of the balanced mixers show promising performance. We measured a DSB noise temperature of about 700 K at 635 GHz. Although the measured noise temperature are higher than expected, we attribute most of the losses to the difference in tuning behaviour between the two junctions, due to the junction shifting and changes in junction size. These discrepancies made it impossible to tune the two junctions simultaneously, equalise the coupling and suppress the Josephson noise from pair tunnelling. Another significant loss is the RF beam truncation caused by the long optical path between the feeds and the Dewar window.

Nevertheless, we have shown that the two key circuit components, the DC/IF block and the RF quadrature hybrid, performed well to specification. The measured results were reproduced using SuperMix and HFSS models, thus validating the integrity of the designs. Consequently, this balanced mixer design could now be re-fabricated to alleviate the junction offset and size problems without altering the chip design, hence enabling reuse of the existing mask. Moreover, a suitable mixer block and matched IF circuit need to be fabricated, in addition to improving the optical design inside the Dewar. With these basic modifications, we expect a substantial improvement on the balanced mixer sensitivity while retaining all the novel features of this design.

References

Belitsky, V., Desmaris, V., Dochev, D., Meledin, D., & Pavolotsky, A. (2011). Towards multi-pixel heterodyne terahertz receivers. In *22nd International Symposium on Space Terahertz Technology*, 26–28 April 2011 at Tucson, AZ, USA.

Benford, D. J., Gaidis, M. C., & Kooi, J. W. (2003). Optical properties of Zitex in the infrared to submillimeter. *Applied Optics*, *42*, 5118–5122.

Claude, S. M. X., Cunningham, C. T., Kerr, A. R., & Pan, S. K. (2000). Design of a sideband-separating balanced SIS mixer based on waveguide hybrids. In *ALMA Memo*, p. 316.

Grimes, P. (2006). *Design and analysis of 700 GHz finline mixers*. Ph.D. thesis, University of Cambridge, United Kingdom.

Grimes, P., Yassin, G., Jacobs, K., & Withington, S. (2005). A 700 GHz single chip balanced SIS mixer. In *Sixteenth International Symposium on Space Terahertz Technology*, pp. 46–52.

Huggard, P. G., Azcona, L., Laisné, A., Ellison, B. N., Shen, P., Gomes, N. J., & Davies, P. A. (2004). Integrated 1.55 μm photomixer local oscillator sources for heterodyne receivers from 70 GHz to beyond 250 GHz. In *Society of Photo-Optical Instrumentation Engineers (SPIE) Conference Series* (Vol. 5498, pp. 596–604).

Huggard, P. G., Ellison, B. N., Fontana, A.-L., Lazareff, B., & Navarrini, A. (2006). Focal plane heterodyne SIS receiver array with photonic LO injection. In *Seventeenth International Symposium on Space Terahertz Technology*, p. 153.

Huggard, P. G., Ellison, B. N., Shen, P., Gomes, N. J., Davies, P. J., Shillue, W. P., et al. (2002). Efficient generation of guided millimeter-wave power by photomixing. *IEEE Photonics Technology Letters*, *14*(2), 197–199.

Justen, M., Honingh, C. E., Tils, T., & Jacobs, P. P. K. (2008). Balanced SIS mixer system with modular design for 490 GHz. In W. Wild. (Ed.), *Ninteenth International Symposium on Space Terahertz Technology*, pp. 444–+.

Kerr, A. (1998). On the noise properties of balanced amplifiers. *IEEE Microwave and Guided Wave Letters*, *8*(11), 390–392. ISSN 1051-8207.

Kerr, A. R., & Pan, S.-K. (1996). Design of planar image-separating and balanced SIS mixers. In *Seventh International Symposium on Space Terahertz Technology*, pp. 207–+.

Kerr, A. R., Pan, S.-K., Lichtenberger, A. W., Horner, N., Effland, J. E., & Crady, K. (2000). A single-chip balanced SIS mixer for 200-300 GHz. In *Eleventh International Symposium on Space Terahertz Technology*, pp. 251–259.

Kittara, P. (2002). *The development of a 700 GHz SIS mixer with Nb finline devices: Nonlinear mixer theory, design techniques and experimental investigation*. Ph.D. thesis, University of Cambridge, United Kingdom.

Kooi, J. W., Monje, R. R., Force, B. L., Rice, F., Miller, D., & Phillips, T. G. (2010). Measurement results of the caltech submillimeter observatory 230 GHz and 460 GHz balanced receivers. In *Twenty-First International Symposium on Space Terahertz Technology*, pp. 138–+.

Kooi, J., Chamberlin, R., Monje, R., Force, B., Miller, D., & Phillips, T. (2012). Balanced receiver technology development for the caltech submillimeter observatory. *IEEE Transactions on Terahertz Science and Technology*, *2*(1), 71–82.

Serizawa, Y., Sekimoto, Y., Kamikura, M., Shan, W., & Ito, T. (2008). A 400–500 GHz balanced SIS mixer with a waveguide quadrature hybrid coupler. *International Journal of Infrared and Millimeter Waves*, *29*, 846–861.

Shitov, S. V., Koryukin, O. V., Uzawa, Y., Noguchi, T., Uvarov, A. V., & Cohn, I. A. (2006). Development of balanced SIS mixers for ALMA band-10. In *Seventeenth International Symposium on Space Terahertz Technology*, pp. 90–93.

Tan, B.-K., Yassin, G., Grimes, P., Jacobs, K., & Withington, S. (2012). Design of a 650 GHz planar circuit balanced mixer. In *Twenty-third International Symposium on Space Terahertz Technology*.

Tan, B.-K., Yassin, G., Grimes, P., Jacobs, K., & Withington, S. (2013). Preliminary measurement results of a 650 GHz planar circuit balanced SIS mixer. *IEEE Transactions on Terahertz Science and Technology*, *3*(1), 32–38.

Westig, M. P., Jacobs, K., Stutzki, J., Schultz, M., Justen, M., & Honingh, C. E. (2011). Balanced superconductor-insulator-superconductor mixer on a 9 μm silicon membrane. ArXiv e-prints.

Chapter 7
Design of 700 GHz Single Sideband SIS Mixers

Overview: This chapter focuses on the design of the 700 GHz single sideband SIS mixers, where the USB and the LSB are separated at the IF output. Similar to the balanced mixer design, the RF and LO powers are fed separately through two back-to-back unilateral finline tapers deposited on a 15 μm SOI substrate. The designs include a sideband separating mixer and a balanced with sideband separating mixer. All the RF circuit components are integrated on-chip, and their designs will be discussed in detail. For each mixer, the required circuit components are combined to form a full mixer chip model within SuperMix, and the predicted performances will be presented.

7.1 Introduction

In Chaps. 4 and 6, we have described in detail the design of the single-ended and the balanced SIS mixers on a 15 μm thick SOI substrate, and have shown that these mixers have promising performances. Building on these results, we have developed a sideband separating, and a balanced with sideband separating (hereinafter balanced-2SB) SIS mixers that cover a similar RF range from 600–700 GHz. The design methodology follows closely that of the single-ended and balanced SIS mixer, and we opt to retain the same fabrication process as those mixers reported previously. Both of the sideband separating and balanced-2SB mixer designs have their own advantages and limitations, as discussed below.

7.1.1 Sideband Separating Mixer

The balanced mixer concept described in Chap. 6 has some well-known disadvantages. The IF output remains unseparated, hence the image sideband (where the spectral signal is usually absent) only contributes to noise, and thus degrades the sen-

B.-K. Tan, *Development of Coherent Detector Technologies for Sub-Millimetre Wave Astronomy Observations*, Springer Theses, DOI 10.1007/978-3-319-19363-2_7

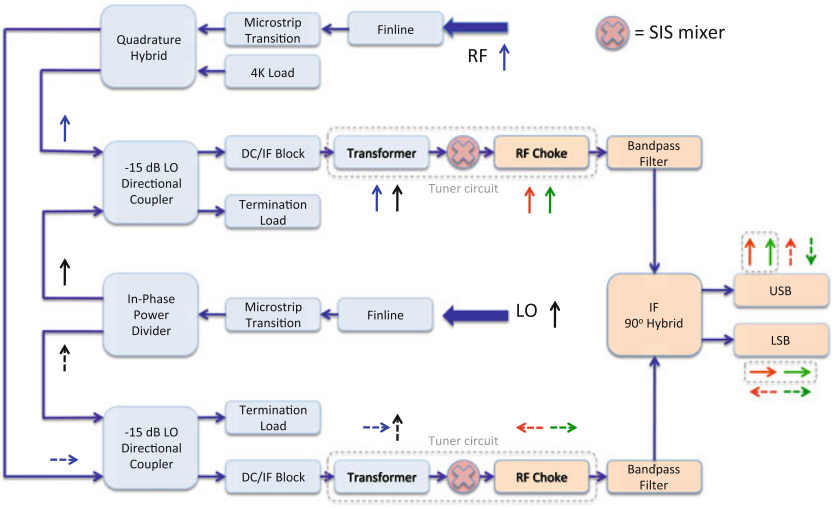

Fig. 7.1 Block diagram showing the components needed for a sideband separating mixer. The notation for the various phasors are: *LO* in *black*, *RF* in *blue*, *USB* in *red*, *LSB* in *green*, *upper branch IF* in *solid arrow*, and *lower branch IF* in *dashed arrow*. All phasors are referenced to the upward pointing direction as 0° and clockwise for a positive phase shift

sitivity of the mixer. A sideband separating receiver, on the other hand, is designed to separate the signal and image sideband at the mixer's IF port. Both upper (USB) and lower sidebands (LSB) are detected simultaneously, but the image sideband is terminated on a 4 K load, thus providing better noise reduction over a double sideband (DSB) receiver.

The sideband separating mixer requires three additional RF circuit components. These are the in-phase power divider, the LO directional couplers, and the 4 K termination loads. Unlike the balanced mixer, the RF power is divided via a quadrature hybrid to produce a 90° phase difference RF output, while the LO power is split through an in-phase power divider.[1] Both the RF and LO power are then combined through two directional couplers (upper and lower branch of Fig. 7.1), where the LO power is delivered to the SIS junctions at about –15 dB level. This helps to minimise the warm LO noise contribution to the final mixing output. The excess LO power (with a small amount of RF signal) at each branch is terminated at a 4 K load, which in our case, is a dummy SIS junction biased above the gap voltage (see Sect. 7.2.3). The unused input port of the RF quadrature hybrid is also terminated with a similar dummy tunnel junction acting as a 4 K load. The bias voltage for all these dummy junctions can be applied directly through the bonding pad connected to the junction, since the junctions are isolated by the DC/IF blocks, and thus can be biased separately.

[1] Note that the operation of a sideband separating mixer remains the same even if these two ports are swapped.

The combined RF/LO power from both branches are mixed separately using two identically tuned SIS tunnel junctions. The down-converted IF output from each mixer still contain both the USB and LSB. They are separated through a 90° IF hybrid with an operating bandwidth of 4–6 GHz (King 2009), where the USB is combined in phase and the LSB 180° out of phase, at the USB port. Similarly, at the LSB port, USB is combined anti-phase and LSB in phase. The only drawbacks of the sideband separating design compared to the balanced mixer design is the loss of immunity to LO noise, the requirement of higher LO power and a slightly more complicated design.

7.1.2 Balanced with Sideband Separating Mixer

Having designed a balanced SIS mixer and a sideband separating mixer using the cascading method of individual RF planar circuit components, the next step is to combine both designs to produce a more advanced balanced-2SB SIS mixer. Interestingly, this mixer design is in fact a simpler planar circuit compared to sideband separating mixer design, since it does not need a –15 dB LO directional coupler. This is because the balanced circuit has already cancelling out the LO noise and thus the LO power can now be fully utilised without worrying about the impact of additional LO noise. An additional bonus is that only one 4 K termination load is now required, at the input port of the RF quadrature hybrid. However, this design needs four operating SIS junctions which ideally have to be fabricated identically.

A straightforward way of implementing a balanced-2SB mixer is by splitting both the RF and the LO power equally into two balanced mixer chips.[2] The LO (or RF) is fed in-phase to both the balanced mixer chip, while the RF (or LO) is coupled through a quadrature hybrid to produce a 90° phase difference between the two balanced mixers. This power splitting scheme leads naturally to the conventional way of constructing a waveguide-based balanced-2SB mixer, where both signals are fed into two identical balanced mixer blocks and combined mechanically using a waveguide RF hybrid and an in-phase power divider.

In our design, we opt for incorporating all the RF components onto a single mixer chip. The RF and LO power injection method are the same as the sideband separating mixer described above. The key difference here is that the –15 dB LO directional coupler is now replaced by the second stage RF quadrature hybrid, with the subsequent circuit components remain exactly the same as a balanced mixer on each branch. The down-converted IFs from the `difference` port of these 'balanced' mixers are then combined through a 180° IF hybrid, to produce the USB and LSB outputs that are free of LO noise (these unwanted noise was diverted into the `sum` port

[2]Notice that the upper and the lower branches of Fig. 7.2 are in fact identical to those in Fig. 6.1 for a balanced mixer.

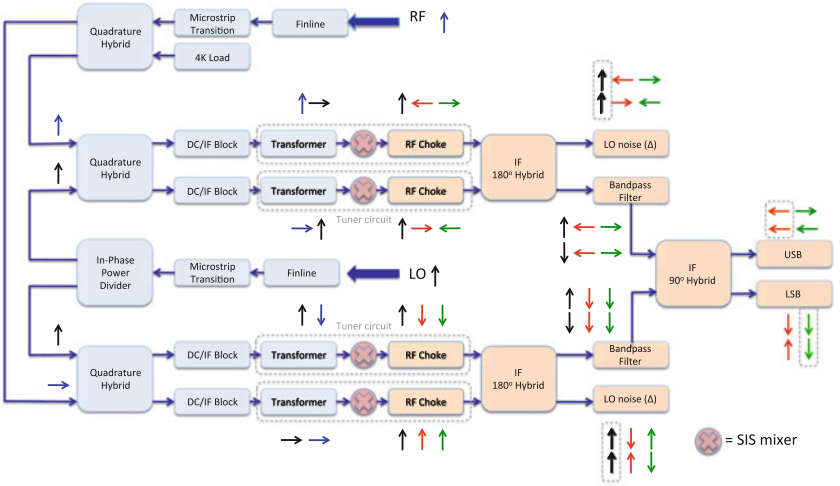

Fig. 7.2 Block diagram showing the components needed for a balanced mixer design with sideband separating capability. The notation for various phasors are: *LO* in *black*, *RF* in blue, *USB* in *red* and *LSB* in *green*. All phasors are referenced to the upward pointing direction as 0° and clock-wise for positive phase shift

of each 'balanced' mixer). The readers are encouraged to follow through the phasor diagram in Fig. 7.2, starting from the LO and RF port towards the final IF outputs of the mixer, to see how these USB and LSB splitting scheme works in principle.

7.2 Design of the RF Passive Circuit Components

A few additional circuit components, such as the in-phase power divider, the directional coupler and the 4 K termination loads, are required for these advanced mixer designs. Following the design of the balanced mixer, we used only planar circuit technology here, and all the RF circuit components are integrated onto a 15 μm SOI substrate. These planar circuit components are made out of 250 nm niobium ground layer, 475 nm silicon monoxide dielectric layer and 400 nm niobium wiring layer. No lumped elements were used, and all the circuit components are matched to a 20 Ω input and output microstrip. The finline taper, the finline-to-microstrip transition, the RF quadrature hybrid and the DC/IF block retain the same design as the balanced mixer design, and both sideband separating and balanced-2SB design are based on the 1 μm^2 Nb/AlO_x/Nb SIS tunnel junctions with 20 Ω normal resistance and junction capacitance of 75 fF.

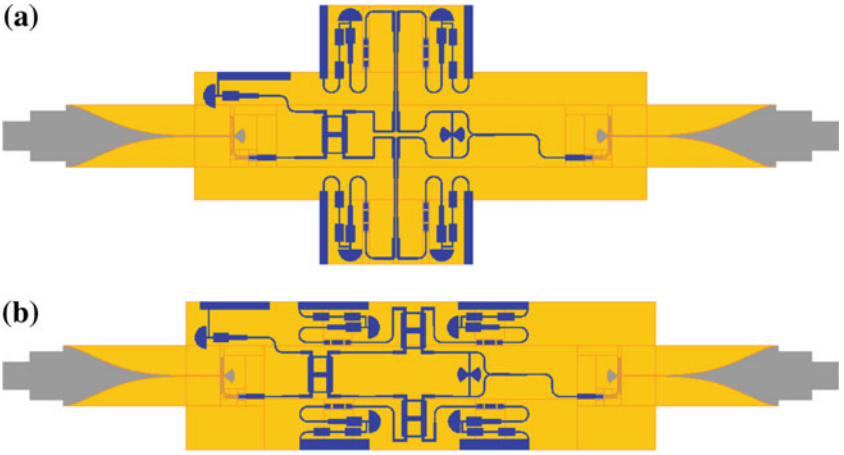

Fig. 7.3 AutoCAD layout of the complete sideband separating and balanced-2SB SIS mixer chip. These drawings were drafted without the dielectric layers for clarity. **a** Sideband separation mixer. **b** Balanced with sideband separation mixer

7.2.1 In-Phase Power Divider

Both sideband separating and balanced-2SB mixer require a 3-port in-phase power divider, in addition to the 90° RF hybrid, for their operation. The fundamental property of a lossless reciprocal 3-port device implies that the input/output impedance of all three ports cannot be simultaneously matched unless a resistor is introduced to compensate for the coupling between the output ports. The standard Wilkinson-type power divider design, therefore requires the use of a lumped resistor that would require additional fabrication steps, (e.g., Kerr and Pan 1996). Alternatively, a Y-junction waveguide can be employed (Claude et al. 2000), but this is often bulky and required high precision mechanical machining. Vassilev et al. (2001) used two probes (pointing against each other) hanging across the E-plane of a waveguide, to split the input RF signal equally between two output ports. However, this design is not suitable for the back-to-back architecture since the 90° phase shifted RF hybrid would no longer be easily incorporated on-chip without a complicated circuit arrangement (Fig. 7.3).

In order to maintain elegant planar circuit integration, we opted for a design that allow some power coupling between the two output ports i.e., $S_{23} \neq 0$, but does not degrade the performance significantly. Following Vassilev et al. (2001), we set the allowed trade-off of $S_{22} = S_{33} = S_{23} = S_{32} = -6\,\text{dB}$. This would have negligible effect on the overall mixer performance, as the reflected LO power is normally absorbed by the 4 K termination load via the RF quadrature hybrid (depending on the mixer design). The LO power which is reflected back to the LO source is also insignificant since it is in-phase with the incoming LO radiation (Claude et al. 2000).

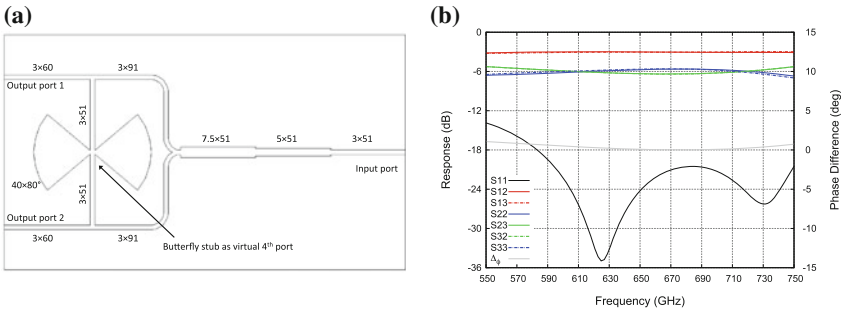

Fig. 7.4 **a** Layout of the in-phase power divider. **b** The S-parameters of the structure and the phase difference ($\pm 0.5°$) between the two output arms simulated using HFSS

Our design employs a microstrip Y-split with the impedance of both the output ports (set to 20 Ω) made approximately double that of the input port impedance. This arrangement allows the two output ports to be seen as connected in parallel from the input port, and thus matches the impedance. The simple Y-split innately split the incoming power evenly (–3 dB) between two output ports due to its balanced feature. Again, a quarter-wavelength transformer is then used to transform the characteristic impedances of the input ports back to a 20 Ω line. Unfortunately, this transformer also changes the impedance seen by the output ports, hence the limitation of simultaneously matching all three ports in a lossless reciprocal three-port device.

In order to circumvent this predicament, we connected a microstrip section, with a butterfly stub in the middle, between the two output arms, as shown in Fig. 7.4a. This extra branch line provided an extra degree of freedom for impedance matching. In principle, this transforms the simple 3-port power divider into a 4-port branch-line circuit, with the butterfly stub acting as a virtual opened (`isolated`) fourth port. By altering the length of this fourth branch line, and the distance between the `isolated` port to the input and output ports, we managed to achieve an operating bandwidth as wide as 200 GHz, as shown in Fig. 7.4b.

7.2.2 –15 dB LO Directional Coupler

A sideband separating mixer requires a directional coupler to couple only a small amount of LO power into the RF path, to ensure that the warm (room temperature 300 K) LO noise is not fully injected into the junction. Conventionally this was realised using a waveguide structure, with holes between two adjacent waveguides; or using CPWs with air bridges connecting the central strip of the two CPW lines (Kerr and Pan 1996; Claude et al. 2000; Vassilev et al. 2001). In our design, we used a microstrip-based directional coupler for ease of integration, as shown in Fig. 7.5. The coupling of field lines between two microstrip lines depends strongly on the

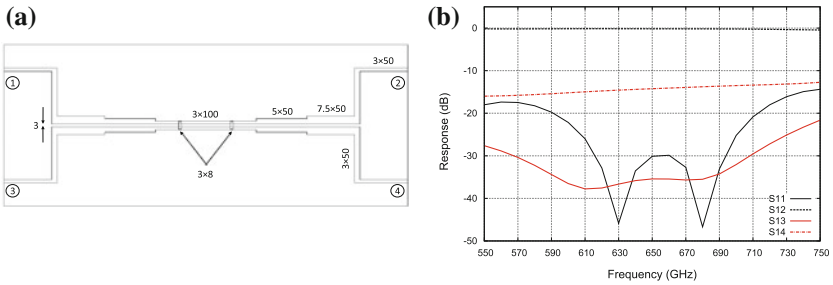

Fig. 7.5 **a** Layout of the –15 dB LO directional coupler. **b** The S-parameters of the structure across the designated bandwidth simulated using HFSS

gap between them. Given that the smallest gap convenient for photolithography is ∼3 μm, and the thickness and material of the dielectric layer is pre-determined, the coupling efficiency would be too small for operating at sub-THz frequencies. To increase the coupling, we cut out two openings at the ground plane underneath the two coupled microstrips. They can be seen in the centre of Fig. 7.5a, shown as two small boxes between the two microstrips. These small ground plane gaps force the field lines adjacent to the neighbour microstrip to cross over, hence achieving a better coupling efficiency. The amount of coupling is mainly controlled by the length of these openings, which lent itself to a convenient way for designing the required coupling level. Again, the coupled lines are cascaded to achieve a wider bandwidth.

Our directional coupler was designed to couple –15 dB of LO power to the adjacent microstrip, and as shown in Fig. 7.5b, the final optimised coupler design indeed gives a coupling (S_{41}) close to the design value from 600–700 GHz. The return loss is less than –20 dB, with leakage between the two input ports (S_{31}) less than –30 dB across the band.

7.2.3 4 K Termination Cold Load

Both sideband separating and balanced-2SB mixer designs need a 4 K load incorporated into the quadrature hybrid or to the fourth arm of an LO coupler as a cold load termination. Since most of the quadrature hybrids or LO couplers used to date are of a waveguide type, the most natural way of utilising a 4 K load is simply to embed a piece of RF absorber material within the waveguide arm. For planar circuit design, using either a capacitively loaded coplanar waveguide (CLCPW) or microstrip as transmission line, a simple thin film lumped resistor can be employed. To keep the fabrication process identical to that of a single-ended mixer, we avoided the use of the thin film resistor and instead used an SIS tunnel junction biased above the gap as a 4 K load.

To achieve this, we bias this idle junction separately at a constant voltage above the gap voltage i.e., at ±6 mV, while the working junctions are biased below the gap voltage as required for normal mixer operation. Above the gap voltage, an SIS junction simply acts as a resistive load, generating no IF signal. The only main source of noise would be the shot noise, and its contribution should be minimal since the junction is physically kept at 4 K. The mixer chip therefore needs to be separately biased at two different voltages, which is feasible since the working SIS junctions are DC isolated using the DC/IF block described in Chap. 6.

7.3 Mixer Simulations

7.3.1 Sideband Separating Mixer

Due to the large number of components in the sideband separating mixer design, it is not feasible to simulate even some of the important parts of the RF circuit in HFSS, because of computer memory constraints. However, as we had demonstrated in Sect. 6.3 of Chap. 6, Ansoft Designer with the S-parameters of the individual RF circuit components imported from HFSS can produce adequate prediction of the RF performance of the final mixer chip. The RF performance of the full sideband separating mixer chip is therefore analysed using this method. Figure 7.6 shows the power coupling to the two identical SIS junctions, and the return loss and isolation between the two input ports of the sideband separating mixer simulated using Ansoft Designer. The predicted performance is as good as expected from 600–700 GHz. The return loss remains below –10 dB from 590–720 GHz, while the difference in the power coupling between the two SIS junctions is less than ±1 dB.

As in the case of the balanced mixers, the performance of the sideband separating mixer chip was simulated using SuperMix after importing the S-parameters of individual components from HFSS. In these SuperMix simulations, the actual 90°

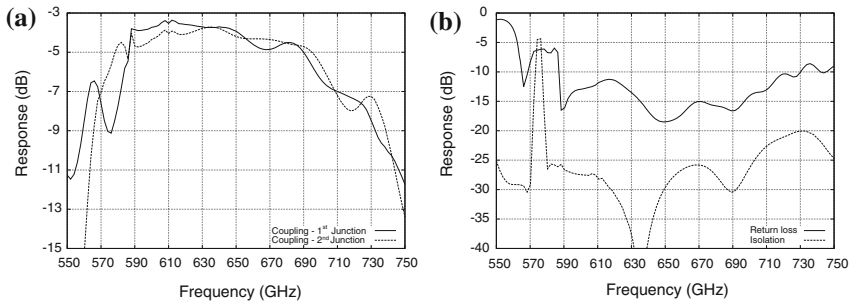

Fig. 7.6 Ansoft Designer simulation of the full sideband separating mixer chip by importing various S-parameters from HFSS. **a** Coupling and phase difference. **b** Return losses and isolation

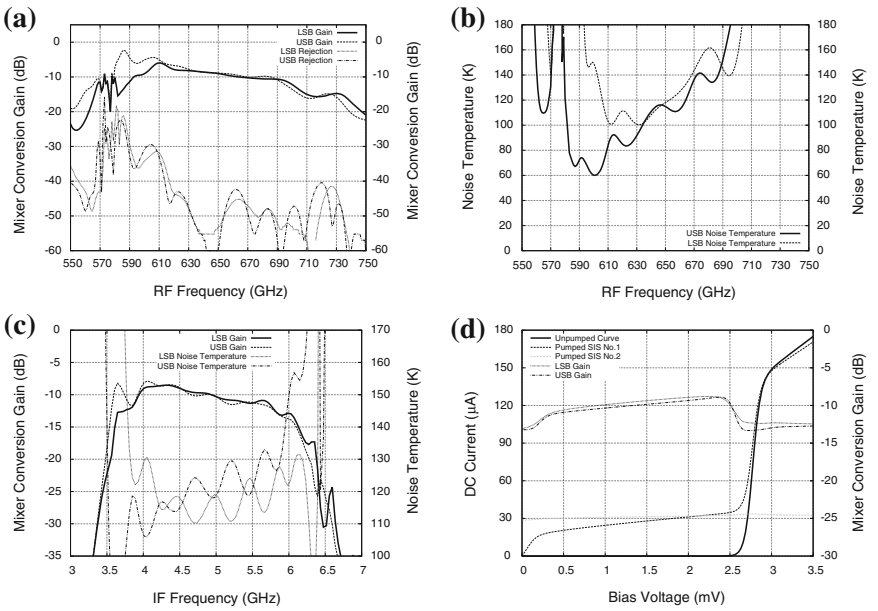

Fig. 7.7 SuperMix simulations showing the predicted behaviour of the final design of the sideband separating mixer chip. **a** RF response: fixed bias points at 2.4 mV with IF frequency set at 4.5 GHz. **b** RF response: fixed bias points at 2.4 mV with IF frequency set at 4.5 GHz. **c** IF response: fixed bias point at 2.4 mV with RF frequency at 650 GHz. **d** Bias response: at 650 GHz with IF frequency set at 4.5 GHz

IF hybrid is simply replaced by the S-parameter matrix of an ideal 90° IF hybrid created artificially within SuperMix. Note that the performance of an actual hybrid should not be the limiting factor in the final mixer performance.

From Fig. 7.7, it can be seen that the sideband rejection ratio is very good, below –50 dB level across the entire band, but the mixer conversion gain is almost half of that of the balanced mixer, while the predicted noise temperature is nearly quadruple. The increase in noise temperature by a factor of two is not surprising since the balanced mixer has a DSB response while the output of a sideband separating mixer is split into USB and LSB bands. The additional loss of performance is therefore mostly attributed to two factors. The warm LO amplitude noise is still coupled to the SIS junctions even though the impact had been largely reduced; and part of the RF signal is lost in the –15 dB LO directional coupler. Furthermore, referring back to Fig. 7.3, one can see that the superconducting circuits employed are almost double the size compared of those used in the balanced mixer design. This inevitably increases the superconducting losses, especially when the mixer is operating near its superconductor's gap frequency. Nevertheless, the performance is good for a preliminary design without any extensive optimisation. Given the complexity of the circuit, there should be much room for further performance improvements, before being finalised for mixer fabrication and testing.

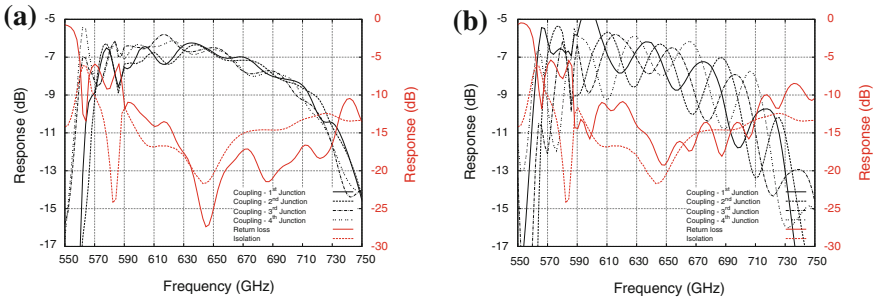

Fig. 7.8 Designer simulation of the full balanced with sideband separating chip by importing various S-parameter from HFSS. **a** The coupling and return loss from the LO port and its isolation from the RF port. **b** The coupling and return loss from the RF port and its isolation from the LO port

7.3.2 Balanced-2SB Mixer Design

Figure 7.8a and b show the Ansoft Designer predicted RF performance of the final balanced-2SB mixer chip from the LO and RF port, respectively. Here, the LO coupling to each of the 4 junctions drops to about –7 dB compared to the –4 dB of the sideband separating mixer. This is to be expected since the LO is now split equally through the RF hybrids to 4 SIS junctions where each of them is connected to a tuning circuit that suffers from imperfect coupling efficiency. The isolation between the RF and LO ports however remains lower than –10 dB across the operating bandwidth, as does the return loss of both input ports, except for a slight deterioration below 630 GHz. The 180° phase difference between the LO coupling to the two sets of SIS junctions (the ripples) in Fig. 7.8a points to a good LO sideband noise rejection ratio, since they are expected to cancel each other out through the IF hybrid. An interesting observation here is that the 90° phase difference (quarter wavelength shift of the ripples) of all 4 SIS junctions in Fig. 7.8b is in fact purely the result of the cascade of two RF quadrature hybrids on the RF path.

As usual, we simulated the heterodyne mixing performance of the mixer design using SuperMix. A noticeable change shown in Fig. 7.9b is that compared to the sideband separating mixer, the predicted sidebands noise temperature is now improved by a factor of two. This improvement comes from the rejection of the additional LO amplitude noise, resulting in USB and LSB noise temperatures about double those of the DSB noise temperature of a balanced mixer. This effect is clearly shown in Fig. 7.9a, where only the USB and LSB sidebands now have a higher conversion gain than the other ports, since the output of the remaining sidebands is now simply the residue LO sideband amplitude noise. These theoretically calculated good performances of this preliminary balanced-2SB design demonstrate that the design is promising for further improvements with minor adjustment to the various circuit components.

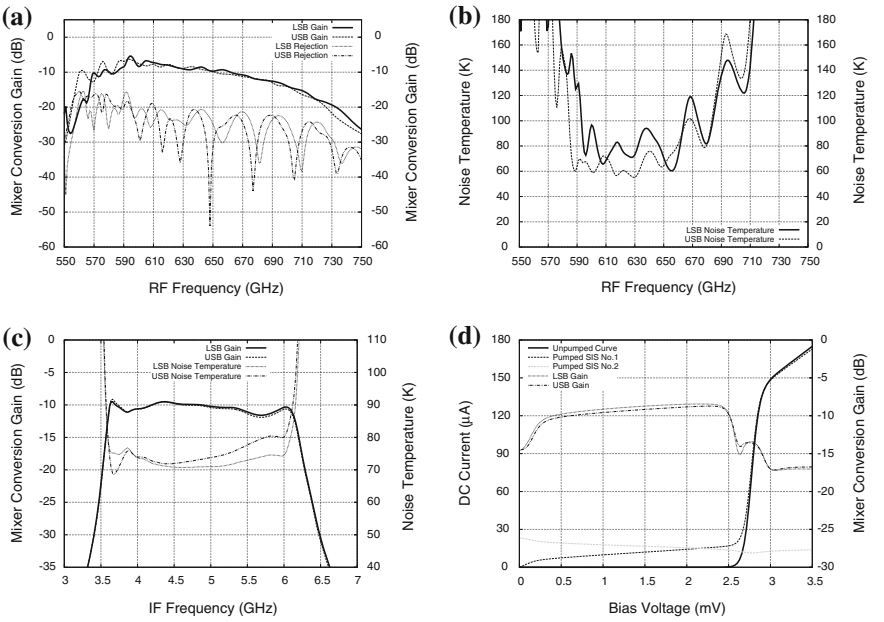

Fig. 7.9 SuperMix simulations showing the predicted behaviour of the final design of the balanced with sideband separating mixer chip. **a** RF response: fixed bias points at 2.4 mV with IF frequency set at 4.5 GHz. **b** RF response: fixed bias points at 2.4 mV with IF frequency set at 4.5 GHz. **c** IF response: fixed bias point at 2.4 mV with RF frequency at 650 GHz. **d** Bias response: at 650 GHz with IF frequency set at 4.5 GHz

7.4 Summary

This chapter presents the design of two single sideband SIS mixer based on the SOI substrate technology. They are the sideband separating mixer and the balanced-2SB mixer. All mixer designs presented here have their required superconducting circuits integrated on-chip, thus greatly simplifying the requirements of the accompanying mixer block. The designs also take into account the complications which can arise in fabrication, and we chose to use the simplest fabrication steps, similar to those of the single-ended and balanced SIS devices.

For designing these advanced mixers, we have introduced a simple method for calculating and simulating the performance of the final mixer design. First, we designed and optimised each required RF circuit components separately using a 3-D electromagnetic simulator. We then made sure that both the input and output ports of each component are matched to the system-wide 20 Ω microstrip line, to facilitate the integration of various RF components for forming a complete working mixer chip. As demonstrated in this chapter, this method works very well, although there are still rooms for improvements upon these preliminary designs.

References

King, O. (2009). *C-BASS: The C-band all-sky survey*. Ph.D. thesis, University of Oxford.

Kerr, A. R. & Pan, S. -K. (1996). Design of planar image-separating and balanced SIS mixers. In: *Seventh International Symposium on Space Terahertz Technology* (pp. 207–219).

Claude, S. M. X., Cunningham, C. T., Kerr, A. R. & Pan, S. K. (2000). Design of a sideband-separating balanced SIS mixer based on waveguide hybrids. In: *ALMA Memo* (p. 316).

Vassilev, V., Belitsky, V., Urbain, D. & Kovtonyuk, S. (2001). A new 3-dB power divider for millimeter-wavelengths. *Microwave Wireless Components Letters, IEEE*, **11**(1), 30–32. ISSN 1531-1309.

Chapter 8
The Characteristics of an SIS Junction Near Its Superconducting Gap

Overview: In this chapter, we present two new studies investigating the behaviour of a tunnel junction operating near its superconducting gap, which can not be easily deduced from standard mixer theory. Firstly we used the current-voltage (IV) characteristic of an SIS mixer to study the localised heating effect of the tunnel junction by the tunnelling currents, and from this we were able to extract a fundamental physical property of the superconductor. Secondly, we studied the influence of the Josephson pair tunnelling on the sensitivity of an SIS mixer, where we observed that under certain circumstances, the pair tunnelling seems to improve the noise temperature performance of an SIS mixer.

8.1 Local Tunnelling Heating Effect in SIS Junction

In Chap. 3, we introduced a function relating V_{gap} with the physical temperature of the SIS mixer (i.e., $V_{gap} \approx 3.52 k_B T_c \sqrt{1 - \frac{T}{T_c}}$). As well as the physical temperature, the gap voltage V_{gap} of an SIS mixer operating near its superconducting energy gap also depends strongly on the LO pumping level, as a result of heating effects taking place in the junction (Leone et al. 2000; Dieleman et al. 1996). The implication of this effect on mixer performance is worth studying since accurate determination of the energy gap is central to the performance of the mixer. Here, we present a simple formulation for studying this heating effects in SIS tunnel junctions near the energy gap, and demonstrate that the electron-phonon interaction time (τ_{eph}) of the superconducting material can be directly recovered from the DC pumped IV curves of an SIS device (Tan et al. 2009).

B.-K. Tan, *Development of Coherent Detector Technologies for Sub-Millimetre Wave Astronomy Observations*, Springer Theses, DOI 10.1007/978-3-319-19363-2_8

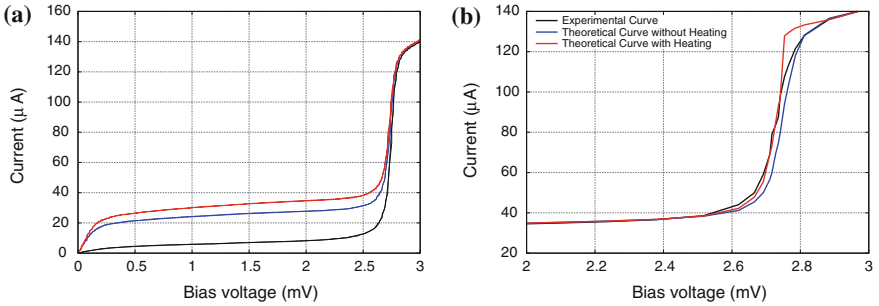

Fig. 8.1 **a** The measured IV curves at different LO pump levels. **b** The matching of simulated IV curves with and without the heating effect with the experimental IV curve

8.1.1 Method of Analysis

The DC pumped IV curves used in our calculations were taken by Kittara (2002) using a 700 GHz niobium-based antipodal finline mixer with a 1 μm^2 Nb-AlO_x-Nb junction. The Josephson current was fully suppressed by a magnetic field during these measurements and the critical temperature of Nb used throughout this section is assumed to be 9.3 K. The IV curves measured at different pump levels are shown in Fig. 8.1a and the gap depression with increasing pump level can be clearly seen, which is typically ~0.1 mV.

Although the heating effect by RF signals for hot electron bolometers (HEBs) have been widely studied, there is relatively limited information reported on the effect in SIS junctions. Leone et al. (2001) have previously reported electron heating of a niobium SIS mixer, using niobium titanium nitrate (NbTiN) stripline with Nb-Al-AlO_x-Nb junction. They attributed the mechanism responsible for the heating to the energy gap discontinuity at the Nb/NbTiN interface. We believe however, that the heating effect in our all Nb-based SIS mixer is different and can be resulted from different mechanisms i.e., heat dissipation in the electrodes but not the heating caused by the Andreev reflection effect as described by Leone et al. (2001), although there are some similarities to the mechanisms found in HEBs.

As excited quasiparticles tunnel through the junction barrier, power is dissipated in the junction. At steady state, this power is transferred by thermal conduction through the superconducting ground film to the substrate. The heat transfer from the junction to the bath can be described phenomenologically using an effective heat transfer coefficient, η, which may be written as

$$P_{total} = \eta(T_e) wlt(T_e^{n_i} - T_b^{n_i}), \tag{8.1}$$

where P_{total} is the total power coupled the junction, T_e is the effective electron temperature (junction temperature), T_b is the bath temperature, w, l and t are the width, length and thickness of the junction defining its volume and n_i is an index

which depends on the model used for heat transfer. Equation (8.1) is in fact a rather general equation that can be used to describe any heat transfer process. The heat transfer coefficient $\eta(T_e)$, is a temperature dependent parameter defined as

$$\eta(T_e) = \frac{C_e}{n_i T_e^{n_i - 1} \tau_{eph}}, \tag{8.2}$$

where C_e is the electron heat capacity and τ_{eph} is the electron-phonon interaction time. In order to incorporate the temperature dependent effect of the heat capacity into the final equation, the low temperature limit heat capacity equation is used to calculate C_e (Duzer and Turner 1981) as

$$C_e = \frac{2N(E_F)\Delta^2}{T_e} \exp\left(\frac{-\Delta}{k_B T_e}\right), \tag{8.3}$$

where $N(E_F)$ is the density of states at the Fermi level and Δ is the superconducting energy gap.

From the BCS equations, the DC and RF power dissipated in the junction at each bias point are given by,

$$P_{rf} = \sum_{n=-\infty}^{n=+\infty} \frac{n\hbar\upsilon}{e} J_n^2\left(\frac{eV_{LO}}{\hbar\upsilon}\right) I_{dc}\left(V + \frac{n\hbar\upsilon}{e}\right) \quad \text{and} \quad P_{dc} = V_b \times I_{dc} \tag{8.4}$$

respectively, where J_n is the nth order Bessel function of the first kind and V_{LO} is the voltage across the junction. We have used impedance recovery described in Sect. 3.4.3 of Chap. 3 to find V_{LO}, assuming that the heating effect is negligible. This is a justified assumption, since only part of the first photon step region away from V_{gap} is used for impedance recovery. Recall that I_{dc} is given by

$$I_{dc} = \frac{1}{eR_N} \int_{-\infty}^{\infty} N(E)N(E - eV_b)[f(E - eV_b) - f(E)]\mathrm{d}E, \tag{8.5}$$

where R_N is the junction normal state resistance, $f(E)$ is the Fermi-Dirac distribution function and $N(E)$ describes the density of states. Note that both functions, $f(E) = \left[\exp\left(\frac{E}{k_B T_e}\right) + 1\right]^{-1}$ and $N(E) = \frac{E}{\sqrt{E^2 - \Delta^2(T_e)}}$, are explicit functions of the electron temperature.

We start our formulation with an initial guess of τ_{eph} and index n_i, and make use of both equations in (8.4) to give P_{total} in Eq. (8.1). By substituting Eqs. (8.2) and (8.3) into (8.1), we can then solve for T_e. The new gap voltage Δ is then numerically re-computed using the standard temperature dependent expression,

$$\frac{1}{N(E_F)V} = \int_0^{\hbar\upsilon_c} \frac{1}{\sqrt{E^2 + \Delta^2}} \tanh\left(\frac{1}{2k_B T_e}\sqrt{E^2 + \Delta^2}\right) \mathrm{d}E \tag{8.6}$$

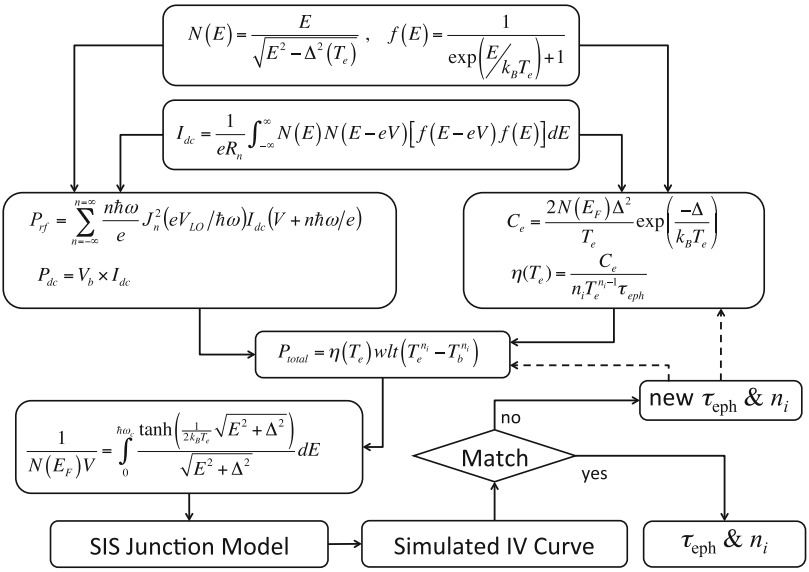

Fig. 8.2 Diagram showing the flow of the method used to recover the τ_{eph} and index n_i

where V is the attractive potential, and $\hbar\upsilon_c$ is the Debye frequency.

Since all the junction parameters found using SuperMix are normalised to the gap voltage, the theoretical current calculated using the recovered LO power and embedding impedance must be multiplied with the gap current given as $\frac{V_{gap}}{R_N}$. This entire simulation procedure, given as a flow chart in Fig. 8.2, was repeated throughout the whole range of bias voltages. The generated IV curve was then compared to the measured curve, and both τ_{eph} and index n_i were optimised simultaneously until both theoretical and measured curves were matched. The following summarises the steps involved:

Step 1: From the experimental pumped and unpumped IV curves, recover the junction embedding impedance and the LO power.
Step 2: Start from $V_b = 0$, find the power dissipated in the junction.
Step 3: Using the heat balance equation and the initial guess value of τ_{eph} and index n_i, find the effective electron temperature.
Step 4: Find the new gap voltage with the effective electron temperature.
Step 5: Use the SuperMix model to recalculate the current.
Step 6: Repeat step 2–5 throughout the whole range of bias voltages.
Step 7: Compare the simulated IV curve with the measured IV curve.
Step 8: Optimised τ_{eph} and index n_i, and repeat step 2–8 until both curves are matched.

8.1.2 Results and Discussion

We shall now show an example of using the method described above to deduce the electron-phonon interaction time of niobium from the pumped IV curve of our Nb-AlO_x-Nb SIS junction. We shall use the IV response with the highest pumping level shown in Fig. 8.1a, and try to match this with the theoretically generated IV curve, paying particular attention to the agreement of the calculated V_{gap} compared to the measured one.

Figure 8.1b shows the theoretical IV curves calculated using embedding parameters recovered by the SuperMix model with and without the heating effect. Without using the heating parameters in the calculation, one notice immediately that the generated IV curve has a V_{gap} higher by about 0.1 mV than the measured value. After optimising for $\tau_{eph} = 7.8$ ns and index $n_i = 4$, this V_{gap} discrepancy between the calculated and the measured V_{gap} becomes much smaller. This leads us directly to the recovered value of τ_{eph} that we were seeking in the first instance, in conjunction with the index n_i. This recovered $\tau_{eph} = 7.8$ ns is in fact rather consistent with the values measured for niobium with different thickness reported in the literaturem (Gershenzon et al. 1990; Prober 1993; Dieleman et al. 1996; Araújo et al. 2000), which are mostly within a few ns range.

The glitch in the heated curve near the knee of the gap voltage is probably due to the electron temperature being calculated without the rounding of the gap voltage in Eq. (8.6). This can potentially be corrected by incorporating the imaginary lifetime-broadening parameter (Γ) in the density of states equation (Dynes et al. 1978; Mitrović and Rozema 2008). Unfortunately, the value of this parameter for niobium is difficult to obtain from the literature. The same sudden step change is also seen in Fig. 8.3a, where T_e, gap voltage and power across the junction are plotted as a function of bias voltage. In this figure, one can also clearly see that the power $(P_{rf} + P_{dc})$ coupled to the junction is in fact a function of the bias voltage. The

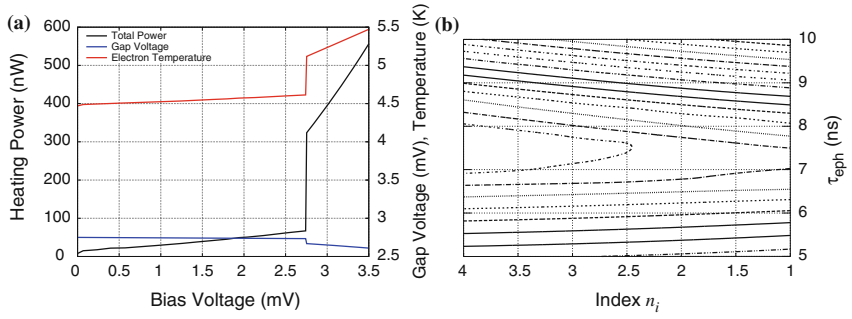

Fig. 8.3 **a** The heating power coupled to the junction as a function of bias voltage. Shown together are the junction temperature and the gap voltage change corresponding to the bias voltage. **b** Contour of the error surface with different guess value of τ_{eph} and index n_i

effective electron temperature thus rises slowly with the bias voltage, resulting in the gradual suppression of the gap.

Figure 8.3b shows the error surface contour of different trial values of n_i and τ_{eph}. It is obvious from the figure that changes in n_i had little effect on the error surface function. In other words, the index n_i is not as significant as τ_{eph} in determining the efficiency of heat transfer process. This can easily be explained if we assume the difference between T_e and T_b is small compared to either T_e or T_b in Eqs. (8.1) and (8.2). The term $\dfrac{(T_e^n - T_b^n)}{nT_e^{n-1}}$ can then be approximated as $T_e - T_b$, without the index n_i, giving

$$P_{total} = \frac{C_e}{\tau_{eph}} wlt(T_e - T_b), \tag{8.7}$$

which depend only on the effective electron temperature and the electron-phonon interaction time τ_{eph}.

It should be noted that heating parameters can also be recovered solely from the unpumped IV curve. A procedure similar to the one described above can be employed, with the junction model replaced by a modified temperature dependence polynomial equation and P_{total} now consist of only the P_{dc} component. The results obtained with this method can be compared with those obtained using the pumped IV curve to give better constraints on the heating parameters recovered.

8.2 Josephson Effects on the Sensitivity of an SIS Mixer

In normal mixer operation, the mixer is biased at a voltage point that is clearly distant from the Shapiro steps. At frequencies approaching the gap however, this becomes difficult to achieve. To explain this, consider the curve in Fig. 8.4a where we have measured the pumped and unpumped IV curves of an SIS mixer irradiated

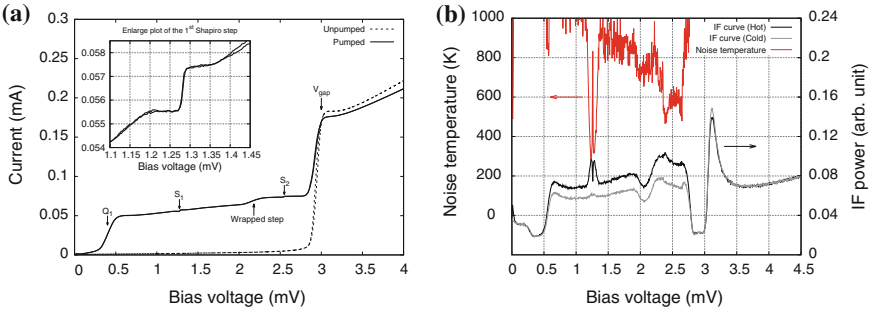

Fig. 8.4 **a** IV curve showing the step wrapping, the Shapiro steps and the photon step at 634 GHz. **b** Calculated noise temperature using the hot and cold load IF curves

with a 634 GHz LO signal. The Cooper pair nonlinearities (Shapiro steps) and the quasiparticle nonlinearities (photon steps) are clearly seen in the pumped curve. The steps labelled as S_n are the Shapiro steps and they are labelled sequentially as they appear above the DC Josephson nonlinearity at 0 V. As stated in Sect. 3.3.1 in Chap. 3, they are separated in voltage by $\frac{h\upsilon}{2e}$ (1.31 mV at 634 GHz), the energy of the photon divided by the charge of the carrier. The quasiparticles steps are labelled as Q_n and are numbered sequentially away from V_{gap}. Their spacing in voltage is $\frac{h\upsilon}{e}$ (2.62 mV at 634 GHz), twice as large as Shapiro step spacing since the quasiparticle carrier charge is half of that of the Cooper pair. When operating at 634 GHz, there is only one quasiparticle step and two Shapiro steps below V_{gap}.

The Cooper pair current is very sensitive to magnetic field strength, whereas the quasiparticle current is less influenced by it. Hence, in normal operation, a magnetic field is applied to control the amplitude of the Cooper pair tunnelling. The existence of a step in the pumped IV curve shown in Fig. 8.4a at 2.2 mV reflects the wrapping of the second photon step from the negative to the positive side of the IV curve. This effect would be less noticeable if the LO power was insufficient to excite the negative higher-order photon steps, and at frequencies significantly lower than the gap frequency ω_{gap}, as the negative higher-order photon steps would remain at the opposite voltage region. Clearly, the best noise temperature values are obtained at bias voltage across the first photon step region, which can also clearly be seen from Fig. 8.4b. However, the step wrapping effect becomes more restrictive as the operating frequency approaches or above ω_{gap}. The negative second photon step would become entirely coincident with the positive first photon step, reducing the unsuppressed first positive photon step region to a negligible width. Moreover, a Shapiro step would occupy the centre of this narrow region making it even harder to obtain a clean measurement on the first photon step without degrading the mixer by the application of a strong magnetic field.

8.2.1 Josephson Current Enhancing SIS Mixer Performance

In an ideal SIS mixer, the Josephson current is fully suppressed by the external magnetic field. In that case, the best performance of the SIS mixer is obtained at DC bias points near the V_{gap} on the first photon step. Figure 8.4 however shows that the Josephson features cannot easily be fully suppressed and unexpectedly, we notice that the noise temperature measured near the first Shapiro step (S_1) is actually better than at bias points near V_{gap}. It is not completely clear to us if this reflects a truly improved sensitivity of the mixer but if this is indeed the case, the enhanced sensitivity could be attributed to the incomplete suppression of Josephson current, which under carefully chosen conditions enhances the mixing performance (Tan and Yassin 2011).

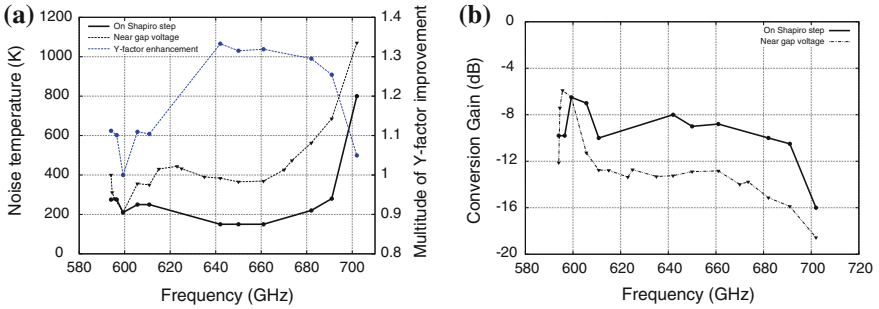

Fig. 8.5 **a** Y-factor and noise temperature improvement when biasing at S_1 compared to the conventional bias point near the V_{gap}. **b** Same as *left panel*, but plotting for the conversion gain improvement

We further measured the noise temperature at bias point near S_1 and near V_{gap} across the designated waveband of the mixer, from 600 to 700 GHz. As shown in Fig. 8.5, the improvement in noise temperature measured near S_1 is obvious, except at the lower frequency end where the non-wrapped first photon step is readily available for a good noise temperature measurement.

This behaviour of enhancing mixing performance near S_1 seems to indicate that the tunnel junction is now behaving as a dual-charge-carrier mixer where the SIS mixer is working in parallel with a Josephson mixer, in which both are operating at their optimum biasing point. The mixing is now occurring through both Cooper pair and quasiparticle tunnelling. If the Josephson mixer could be removed completely by suppressing pair tunnelling and the noise temperature of the SIS mixer could be measured at the unwrapped first photon step, the operation of a single SIS mixer is certainly superior. If on the other hand, Josephson tunnelling could not be completely suppressed, it will inevitably contribute to the receiver noise. In that case, optimising the pair tunnelling signal can improve the SIS mixer's performance, in particular relative to the noise temperature measured at the wrapped photon step region.

It is worthwhile noting that effects similar to this behaviour have been reported previously (Vystavkin et al. 1994; Wengler et al. 1992). Vystavkin et al. (1994) noticed that the mixer conversion gain measured using the hot and cold load technique was highest near the Shapiro step regions. They confirmed their observation by replacing the Y-factor measurement with direct injection of two LO signals into the tunnel junction to perform a coherent measurement. However, Wengler et al. (1992) argued that the Y-factor measurement in this case is misleading and the Josephson pair tunnelling should always be suppressed. They attributed this to the nonlinear response of the SIS mixer to the blackbody illuminating it, where the SIS mixer is acting as a noise source in which the magnitude of the generated noise increase with the temperature of the blackbody. They have also supported their claim using similar coherent measurements. Hence, we believe that we could resolve this ambiguity if

the experiment is repeated using a gas cell to measure the Y-factor noise temperature from a spectral line, rather than the incoherent broad continuum radiation from a blackbody load.

8.3 Summary

In this chapter, we have presented two effects related to the behaviour of an SIS mixer near its superconducting gap. The first effect is related to the heating of the SIS junction with LO power. Here, we constructed a simple model to measure the electron-phonon interacting time of a superconductor by recovering the change in the electron temperature from the experimentally pumped IV curve. Our results show that in our system, the heat transfer equation does not depend on the index n_i.

The second effect is the apparent enhancement of the measured gain of an SIS mixer operating near the superconducting gap, when the Y-factor was measured near a Shapiro step. This observation was noted when it was difficult to suppress the Josephson effect completely and when step wrapping combined with Josephson features did not allow measurement of the Y-factor on the first photon step.

References

Araújo, H. M., Puplett, E. F., & White, G. J. (2000). Optimizing phonon-cooled Nb hot-electron bolometers. *Journal of Applied Physics*, *88*, 6801–6807.

Dieleman, P., Klapwijk, T. M., Kovtonyuk, S., & van de Stadt, H. (1996). Direct current heating in superconductor-insulator-superconductor tunnel devices for THz mixing applications. *Applied Physics Letters*, *69*(3), 418.

Duzer, T. V., & Turner, C. W. (1981). *Principles of superconductive devices and circuits*. New York, Oxford: Elsevier.

Dynes, R. C., Narayanamurti, V., & Garno, J. P. (1978). Direct measurement of quasiparticle-lifetime broadening in a strong-coupled superconductor. *Physical Review Letters*, *41*(21), 1509–1512.

Gershenzon, E. M., Gershenzon, M., Gol'tsman, G., Lyul'kin, A., Semenov, A., & Sergeev, A. (1990). Electron-phonon interaction in ultrathin niobium films. *zh. eksp. teor. fiz.97*, 901–911.

Kittara, P. (2002). *The development of a 700 GHz SIS mixer with Nb finline devices: Nonlinear mixer theory, design techniques and experimental investigation*. Ph.D. thesis, University of Cambridge, UK.

Leone, B., Gao, J. R., Klapwijk, T. M., Jackson, B. D., & amd G. de Lange, W. M. L. (2001). Hot electron effect in terahertz hybrid devices. *IEEE Transactions on Applied Superconductivity*, *11*(1), 649–652.

Leone, B., Jackson, B. D., Gao, J. R., & Klapwijk, T. M. (2000). Geometric heat trapping in niobium superconductor-insulator-superconductor mixers due to niobium titanium nitride leads. *Applied Physics Letters*, *76*(6), 780–782.

Mitrović, B., & Rozema, L. A. (2008). On the correct formula for the lifetime broadened superconducting density of states. *Journal Physics: Condense Matter*, *20*, 15215–15218.

Prober, D. E. (1993). Superconducting terahertz mixer using a transition-edge microbolometer. *Applied Physics Letters*, *62*, 2119–2121.

Tan, B. K., Yassin, G., Kittara, P. & Leech, J. (2009). Measurement of electron-phonon interaction time of niobium using heating effect in SIS tunnel junction. In: *Proceeding of the Twentieth International Symposium on Space Terahertz Technology*, 275–+.

Tan, B.-K., & Yassin, G. (2011). Josephson pair tunnelling influence on the performance of an SIS mixer near its superconducting gap. *International Journal of Terahertz Science and Technology*, *4*, 123–127.

Vystavkin, A., Tarasov, M., Prokopenko, G., Shitovl, S., Jacobsson, S., Koshelets, V., Kovtonyuk, S., Holmstedt, C., Filippenko, L., Lapitskaya, I. & Kollberg, E. (1994). Studies of Josephson mixing in SIS junctions. In *24th European Microwave Conference, 1994*, vol. 2, 1949–1954.

Wengler, M., Dubash, N., Pance, G. & Miller, R. (1992). Josephson effect gain and noise in SIS mixers. *IEEE Transactions on Microwave Theory and Techniques*, *40*(5), 820–826. ISSN: 0018-9480.

Chapter 9
Generation of Local Oscillator Signal via Photomixing

Overview: This chapter investigates the possibility of down-converting the output of two commercially available infrared lasers to generate a local oscillator (LO) signal at sub-mm wavelengths, for working in conjunction with balanced SIS mixers. The main motivation here is to utilise the ability of a balanced mixer to reject the LO amplitude noise, which may prevent the use of a photonically generated LO signal as part of a heterodyne receiver system. In the first part of this chapter, we shall introduce the principle of photomixing for generating LO signals, and report on the successful operation of using the photonic LO to pump a 230 GHz single-ended SIS mixer. We will then describe an attempt for locking the two lasers to produce a stabilised LO output.

9.1 Introduction

The local oscillator source is a major component in a heterodyne receiver system. For radio/sub-mm astronomy applications, low frequency LOs are generally commercially available. They are mainly based on yttrium iron garnet (YIG) or Gunn effect electronics with waveguide resonant cavity, or direct up-converting a low frequency synthesiser signal via chains of frequency multipliers. Conventionally, these solid-state LO source can generate power up to a few hundred GHz, but for application at the higher end of sub-mm spectrum up to 1 THz, several stages of frequency multipliers are required. In the frequency regime above several THz, quantum cascade or molecular vapour lasers are normally the preferred choice. The major drawback of the multiplied LO generation methods is often the low power output at high frequencies end, especially approaching THz regime, and the enhancement of phase noise (or line width in spectroscopic term) due to the frequency multiplier chain. They may also be rather complicated with mechanically variable tuners, and have limited operating bandwidths.

B.-K. Tan, *Development of Coherent Detector Technologies for Sub-Millimetre Wave Astronomy Observations*, Springer Theses, DOI 10.1007/978-3-319-19363-2_9

9.1.1 Optical Heterodyning

Generating a sub-THz signal via beating two infrared lasers in a photodiode or photoconductor has been studied for over a decade (e.g., Brown et al. 1993). But only recently, when this method has been deployed to provide a stable sub-THz synthesiser signal for the phase locking of several receivers in ALMA, has it excited interest among sub-mm astronomers to explore the use of photonic source as an LO.

The main advantages of photonically generated LO sources are the low attenuation of optical fibres and the wide bandwidth operation. In addition, the technology offers the potential to deliver a compact and lightweight LO source. This is especially important for an interferometer, such as ALMA, where all the lasers driven sub-systems can be centralised at location remote from the individual antenna, and only biasing electronics and photomixers are required near the receivers. The signal from the lasers can easily be distributed via networks of low-loss optical fibres. For example, this architecture had been proposed for the Millimeter Array (MMA, precursor of ALMA) to generate photonic LO source from 30 GHz to approximately 900 GHz (Payne et al. 1998).

The principle of down-converting optical signals to produce GHz waves is similar to the operation of an SIS junction as a mixer. Coherent waves from two infrared lasers, oscillating at two slightly different frequencies, are combined through an optical coupler, and fed into a photodiode or photoconductor which acts as a photomixer, to produce difference frequencies that are in the sub-THz range. Normally the line width of the lasers is excellent, with a high side mode suppression ratio, so that the photomixer only generates a single tone. This is an advantage over multiplied sources, where it is difficult to eliminate unwanted harmonics. Waveguide filters are in theory feasible, but they are difficult to make and may be ineffective if the multiplier needs a reasonable tuning bandwidth. Infrared lasers are generally tuneable by a small fraction of their centre wavelength via varying temperature and drive current. Since the down conversion is so large, typically from $\lambda \approx 1\,\mu$m to $\lambda \approx 1$ mm, this results in a tuning range in the LO signal of typically several hundred GHz. The challenge is therefore to design an efficient and broadband photomixer.

Generating LO signal at millimetre and sub-mm wavelengths has been attempted and reported successfully by various groups (Verghese et al. 1999; Matsuura et al. 2000; Takano et al. 2003; Kimberk et al. 2006). Nevertheless, to achieve comparable performance to the existing frequency multiplied diode oscillator technology, the amplitude noise from the photonic LO should be stable to at least 1 dB with the line width (or phase noise) around a few kHz. This amplitude noise and phase noise depend largely on the quality of the laser source. Narrowing the laser lines, and reducing the drifting in laser wavelengths caused by environmental effects, such as thermal variations, also needs to be achieved by using frequency or phase locking schemes.

9.2 Generation of Local Oscillator Signal

The advantage of using a photonic LO source with a balanced SIS mixer is that some of the requirements listed above can be relaxed, since a balanced mixer has the ability to reject the sideband noise from the LO. Depending on the application, some astronomical instruments might not require the ultra narrow line widths needed for interferometry, such as wide band, low resolution spectroscopy. For example, HARP-B instrument on the James Clerk Maxwell Telescope (JCMT) has a back-end resolution of about 500 kHz, limited by the spectrometers, and a photonic LO source with a balanced SIS mixer should in principle be able to produce LO signal with a phase noise less than this resolution. The only additional scheme needed is the frequency or phase locking technique to ensure that the LO frequency stays stable throughout the instrument operation.

Our objective (in collaboration with the Millimetre Technology (MMT) Group from the STFC Rutherford Appleton Laboratory) was to demonstrate the feasibility of using a photonic LO source with a 230 GHz SIS mixer. This will serve as the first step, towards building up a future experimental setup for deploying the system to work with the 700 GHz balanced SIS mixers reported in Chap. 6. In the following sections, we shall briefly describe several key components and steps in the development of the photonic LO system assembled for this purpose.

9.2.1 Photomixer and System Setup

A critical component of a photonic LO system is the photomixer, and the MMT Group has considerable expertise in this area. For example, they currently have responsibility for delivering photomixers for the ALMA observatory. They have demonstrated previously a 75–170 GHz photomixing source by beating two commercially available 1.55 μm communication lasers using an InGaAsP (Indium-Gallium-Arsenide-Phosphide) photodiode. The group has also investigated the possibility of extending the system up to 600 GHz (Huggard et al. 2002a, b) and a similar system operating cryogenically at 77 K had also been used as an LO for a linear receiver array (Fontana et al. 2007).

Figure 9.1a, b show the current system setup and the internal construction of a photomixer block. Near-infrared light from two lasers combined within an optical fibre coupler enters the photomixer block along a single mode optical fibre , shown at the right side of Fig. 9.1a. An adjustable stage was used to bring the cleaved fibre end to within a few tens of μm of the input facet of the photodiode chip. Light is then conveyed to the 5 μm × 20 μm photodiode by means of a rib waveguide . The fibre was held in a ferrule which was fixed by epoxy resin to the block, where the photodiode was supported on a 200 μm thick InP (Indium-Phosphide) chip.

The photodiode sub-mm wave output was transmitted via a planar gold transmission line at the end of the InP chip. The transmission line was connected to a

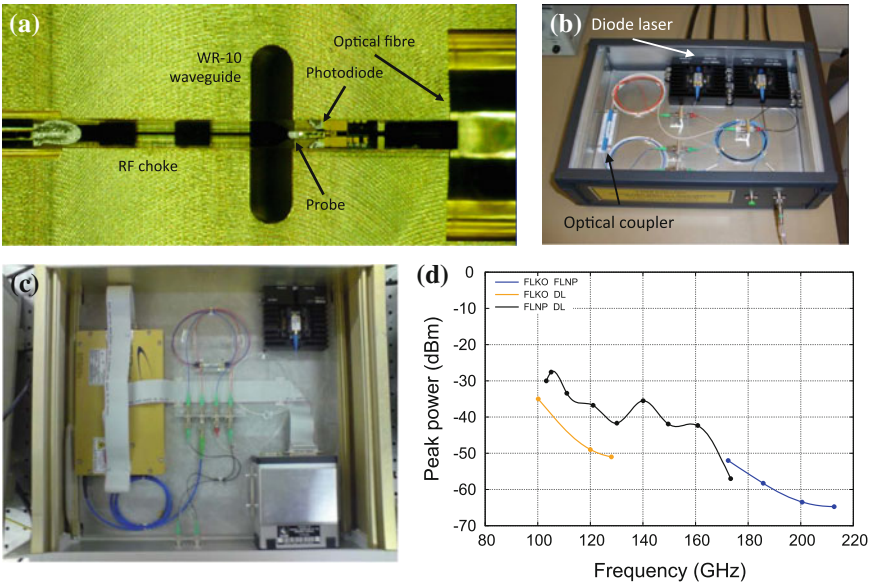

Fig. 9.1 **a** Internal structure of a photomixer block. **b** System setup consisting two distributed feedback (DFB) diode lasers generating a GHz frequency tone. **c** An NP Photonic fibre laser enclosed together with a DFB diode laser. **d** The output power of the photomixer plotted against the down-converted frequencies

gold-on-quartz probe, which extended across the WR-10 output waveguide. Bias voltage for the device was applied from the opposite end of the block through an RF choke deposited on the 200 μm thick quartz substrate. This bottom split block was capped with a top half of the block through which the WR-10 waveguide continues. This capped block is provided with a sliding backshort that provides means for adjusting the embedding impedance presented to the photodiode and therefore optimising the power transfer.

The photomixer itself was capable of delivering an output of about 100 μW, with an input power of about 10 mW. However, the power output is largely frequency dependent. This particular setup was designed to operate within W-band (75–110 GHz), but the output power is still detectable up to about 625 GHz (Huggard et al. 2002a). The power output varies approximately as the inverse fourth power of frequency. This is a combination of two inverse square dependencies, one due to photodiode capacitance, and the other due to carrier transit time in the device.

9.2.2 *Infrared Lasers*

There are two main types of laser suitable for constructing a compact photonic LO system using the photodiodes described above: distributed feedback (DFB) diode lasers and fibre lasers. Diode lasers are the cheaper option among the two, and they are easy to operate and have wide tuning ranges. However, they tend to have broad emission line widths, generally in the MHz range, due to the phase fluctuation intrinsic to the diode itself. In some circumstances, this type of laser can be servo-locked to an external ultra-high finesse Fabry-Perot cavity to narrow down the line width. The tuning of the diode laser wavelengths is normally achieved by varying their temperature and/or laser driving current, for coarse and fine tuning respectively.

Fibre lasers, on the other hand, offer narrow line width operation at some tens of kHz, but they have limited adjustability which results in narrow tuning ranges. They normally make use of a piezo-electric transducer to stretch the optical fibre for fine frequency tuning, while the coarse frequency adjustment can be done through the thermal contraction/expansion of the cavity i.e., the fibre length.

Table 9.1 and Fig. 9.2 show the specifications of the several infrared lasers we acquired for constructing a new photonic LO system, alongside the tuning range available from these lasers. The two fibre lasers were a Koheras BASIK™ module

Table 9.1 Specification of the three infrared lasers we acquired

Laser	λ_c (nm)	λ_{min} (nm)	λ_{max} (nm)	Δf (GHz)
Diode laser	1550.000	1548.500	1551.500	375.0
Fibre laser (Koheras)	1550.207	1550.081	1550.333	30.0
Fibre laser (NP Photonic)	1548.174	1548.630	1547.718	135.4
Piezo tuning	1548.174	1548.400	1548.430	3.0

Here the lasers central wavelength is denoted λ_c, the maximum and minimum tunable wavelength is given as λ_{min} and λ_{max}, and the tunable frequency range is denoted as Δf

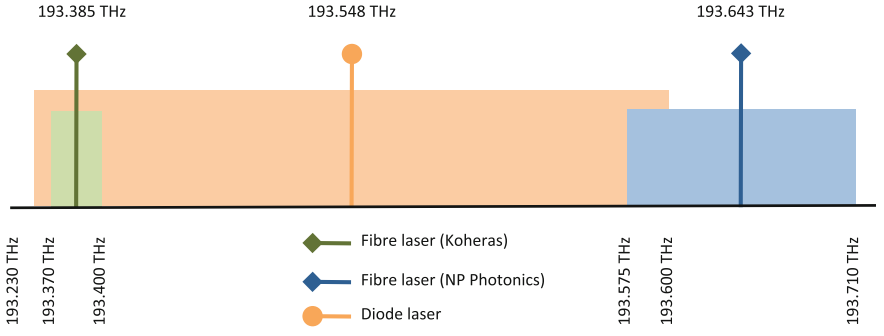

Fig. 9.2 Diagram showing the centre frequency and the tuning range of the three lasers

Table 9.2 Table showing the range of down-converted GHz signals made by beating two different lasers

Laser combination	Δf_{min} (GHz)	Δf_{max} (GHz)	*FWHM* (MHz)	P_{peak} (dBm)	f_{meas} (GHz)
FLKO + FLNP	175.0	340.0	∼0.5	−52	172.4
FLKO + DL	25.0	480.0	∼2	−35	100.17
FLNP + DL	140.0	230.0	∼2	−30	103.25

The full-width half-maximum frequency *FWHM* and the peak power P_{peak} quoted here were measured at the f_{meas} frequency

and an NP Photonics Erbium Micro Fiber Laser module, while the diode laser was from Eblana Photonics, a 1550 nm narrow line width laser.

As can be seen in Table 9.2, with different combination of lasers, we could cover the difference frequency range from about 25 GHz up until about 480 GHz. We thus performed a preliminary test using the W-band photomixer described above to check the available output power by down-mixing the beating tones of various two laser combinations. The similar output power dependence on frequency as reported before is clearly seen in Fig. 9.1d. The down-converted line has a typical peak power in the range of −50 to −30 dBm, but the line width varies depending on the lasers used. In general, beating two fibre lasers with a photomixer results in a slightly narrower down-converted line width, compared to combinations using a diode laser. The latter options typically had about 4× broader line width at ∼2 MHz, while the fibre lasers could produce ∼500 kHz line width signals. Without any locking scheme, the output signal also tended to jitter around the tuned frequency by about 3 MHz, and we also observed a slower long term drifting due mainly to thermal effects.

Figure 9.3a shows an example of the down-converted output from beating two lasers together with the W-band photomixer. One sees immediately the typically ∼2 MHz line width down-converted signal from the diode lasers. But this GHz tone was affected by a noise characterised by the current supply that drove the diode lasers. A shoulder of about 6 MHz width is clearly seen on both sides of the main tone, at about 20 dB below the peak of the main tone. Nevertheless, by replacing the main AC driven current supply with a battery powered lower noise diode laser supply, we did successfully generate a cleaner down-converted RF without any additional noise feature.

9.2.3 Pumping an SIS Mixer with a Photonic LO Source

Using the photonic LO system described above, we successfully pumped a 230 GHz SIS mixer on an initial trial. The IV responses from the SIS device are shown in Fig. 9.3b. As clearly seen, we managed to pump the device to a reasonable level for normal SIS receiver operation. In this particular experiment, the LO power was

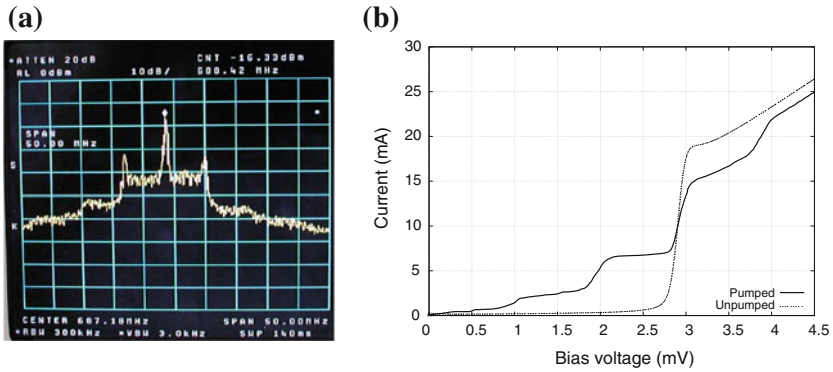

Fig. 9.3 **a** Beat note from a narrow line fibre laser and a narrow line diode laser. The factory specification of line width is about 10 kHz for the fibre laser, however the spectrum of the down-converted signal shows additional noise from the laser power supply. **b** The pumped and unpumped IV curves of a 230 GHz SIS mixer illuminated with a photonic LO source

coupled directly to the SIS mixer through free-space optics, without the use of any beam splitter. But considering the photomixer and the housing WR-10 waveguide block were optimised for W-band operation, we could optimistically expect a 3–4 fold improvement in the power output from the photonic LO system, if the photomixer were to be replaced by one that is optimised specifically for 230 GHz operation. In fact, the MMT group have already demonstrated a 230 GHz photomixer with output powers in the 10 μW region.

9.3 Frequency Stabilisation Schemes

As mentioned before, the down-converted GHz signal from beating two infrared lasers results in typical line widths of several hundred kHz to several MHz. The effect of the slightly larger phase noise could be minimised if the LO were to be used with a balanced SIS mixer. However, it is preferable that the fast jittering and slow drifting of the down-converted signal can be eliminated to enable use with single-ended mixers. There are various ways of achieving good stabilisation, and the most common approach is via frequency or phase locking electronics.

In principle, a frequency/phase locking loop adjusts the tuning of one of the two infrared lasers, to compensate for any offset from the output signal away from the desirable frequency/phase. As shown in Fig. 9.4, a small output signal from the photomixer is tapped out to feed into a harmonic mixer for down-converting the GHz output signal into the MHz range. This MHz signal is then compared with a reference source from a stable synthesiser via frequency/phase error detector electronics. This generates an error signal that is then used to correct one of the laser frequencies via a transducer. Depending on the type of laser to be adjusted, different transducers are

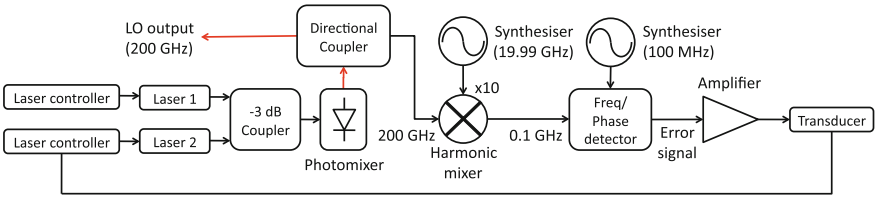

Fig. 9.4 Graphical description of phase-locking two lasers

available. For example, for stabilisation of a fibre laser, a piezoelectric transducer can be used to fine tune the frequency to counter-balance the drift of output GHz signal. This method is relatively simple, but is limited in bandwidth to tens of kHz by the piezo-transducer.

We had tried several approaches previously for stabilising the down-converted output from the two fibre lasers. First, we combined the Phase Matrix 588C frequency counter to down-convert the GHz signal to IF and used a Phase Matrix 578B module for source locking. Unfortunately, this combination of modules had very limited efficiency at frequencies higher than 170 GHz. Secondly, we approached the problem using an amplitude modulator to introduce sidebands on a laser line. The idea here is to lock the MHz tone created by beating a high order sideband with the other laser. Unfortunately, due to the limited modulating efficiency of the modulator unit, the optical power in the sideband was again too low to generate a difference signal that the locking electronics could detect.

Finally, we chose to use an XL Microwave 800A Gunn Phase Lock Module to replace the Phase Matrix source locking frequency counter modules. In the first instance, we down-converted a signal at ~180 GHz from the photomixer using a harmonic mixer fed through a diplexer. The harmonic mixer generated the difference between the 180 GHz signal and a multiple of the LO signal from a 20 GHz synthesiser. The beat signal at around 200 MHz was used for locking by the XL 800A module. With this setup, we successfully generated the IF signal in the MHz range, but unfortunately the signal was too weak to be detected by the XL 800A module, as the power output from the W-band photomixer and the harmonic mixers was limited at these frequencies.

To improve the situation, we replaced one of the fibre lasers with a DFB diode laser to achieve a wider tuning frequency range in the expense of broader line width output. The main reason for this alteration is that the XL Microwave 800A Gunn Phase Lock Module and the subsequent system components were mostly optimised for lower frequency operation. We thus re-ran the system for a 90 GHz down-conversion signal, and the XL 800A module successfully detected the IF signal. Unfortunately, due to the very narrow locking range of the XL 800A (approximately 1 MHz), and the wide line width from the diode laser, this phase-lock module was unable to locate and thus phase-lock the source.

In order to circumvent the narrow locking range problem, we replaced the XL Microwave 800A Gunn Phase Lock Module with a newly purchased TOPTICA

mFALC 110 proportional-integral-derivative (PID) controller module, which is a flexible wide bandwidth analog phase locking module. This is capable of taking in an RF input signal and providing an error correction within a 100 MHz bandwidth. In order to better understand this module, we decided to skip the entire GHz down-mixing chain temporarily. Instead, we beat the DFB diode laser with the fibre laser at an offset of around 100 MHz using a 1 GHz bandwidth photodiode. This enabled us to test and understand the working principle of the mFALC 110. With this simple setup, we finally managed to frequency stabilise the down-converted GHz signal to the kHz range. This demonstrates the ability of the new module to detect the broad down-converted signal and stabilise it, which is only a step away from phase-locking the lasers. To our understanding, to achieve further phase locking, we need to connect the output of the mFALC module directly to the photodiode, instead of via the current supply that drives the diode laser. This will enable the full bandwidth of the error signal to be applied to the source. Unfortunately, due to the time constraints, this upgrade has yet to be completed at the time of writing.

9.4 Summary

In this chapter, we have concentrated on the photonic method of generating a local oscillator signal at sub-THz frequency range, for work with a balanced SIS mixer. This LO signal is created by beating the output tones from two infrared lasers using a photodiode as a mixer to generate a GHz down-converted signal. We have successfully setup an initial system for characterising the down-converted output signals, using different combinations of lasers. We also managed to pump an SIS mixer at 230 GHz using the system, thus demonstrating the feasibility of using such an LO system in conjunction with an SIS receiver.

For stabilising the output of the photonic LO, we managed to frequency-lock the lasers for a stable frequency operation, although the system is not yet in a packaged final delivery form. Even though a frequency stabilised operation is sufficient for the operation of a balanced SIS mixer, we believe a phase-locked signal from the current photonic LO system could be achieved with a custom designed photomixer module and a transducer circuit for delivering the error signal from the mFALC 110 phase-locking module to drive the fibre laser directly.

References

Brown, E. R., Smith, F. W., & McIntosh, K. A. (1993). Coherent millimeter wave generation by heterodyne conversion in low temperature grown GaAs photoconductors. *Journal of Applied Physics*, *73*(3), 1480–1484. ISSN 0021-8979.

Fontana, A., Bortolotti, Y., Lazareff, B., Navarrini, A., Huggard, P., & Ellison, B. (2007). Cryogenic photonic local oscillator for 2 mm band SIS heterodyne astronomical receiver array. *Electronics Letters*, *43*(20), 1121–1123.

Huggard, P. G., Ellison, B. N., Shen, P., Gomes, N. J., Davies, P. J., Shillue, W. P., et al. (2002a). Efficient generation of guided millimeter-wave power by photomixing. *IEEE Photonics Technology Letters*, *14*(2), 197–199.

Huggard, P. G., Ellison, B. N., Shen, P., Gomes, N. J., Davies, P. J., Shillue, W. P., et al. (2002b). Generation of millimetre and sub-millimetre waves by photomixing in a 1.55 μm-wavelength photodiode. *Electronics Letters*, *38*(7), 327–328.

Kimberk, R., Hunter, T., Tong, C. Y. E., & Blundell, R. (2006). A photonic mm wave local oscillator. In *Proceedings of the 17th International Symposium on Space Terahertz Technology* (pp. 206–209).

Matsuura, S., Blake, G. A., Chen, P., Wyss, R. A., Pearson, J. C., Pickett, H. M., et al. (2000). *A photonic local oscillator source for far-IR and sub-mm heterodyne receivers*. Report, The Institute of Space and Astronautical Science, p. 14.

Payne, J. M., D'Addario, L., Emerson, D. T., Kerr, A. R., & Shillue, B. (1998). Photonic local oscillator for the millimeter array. *MMA Memo*, #200.

Takano, S., Ueda, A., Yamamoto, T., Asayama, S., Sekimoto, Y., Noguchi, T., et al. (2003). The first radioastronomical observation with photonic local oscillator. *Publications of the Astronomical Society of Japan*, *55*, 53–56.

Verghese, S., Duerr, E. K., McIntosh, K. A., Duffy, S. M., Calawa, S. D., Tong, C.-Y. E., et al. (1999). A photomixer local oscillator for a 630-GHz heterodyne receiver. *IEEE Microwave and Guided Wave Letters*, *9*(6), 245–247.

Chapter 10
$CO_{(3\rightarrow 2)}$ Observations of NGC 2976 and NGC 3351

Overview: In this chapter, we present ^{12}CO $J = 3\rightarrow 2$ maps of NGC 2976 and NGC 3351 obtained using the James Clerk Maxwell Telescope (JCMT), both early targets of the JCMT Nearby Galaxy Legacy Survey (NGLS). We combine the present data with the ^{12}CO $J = 1\rightarrow 0$ data to derive ^{12}CO line ratios and find that the spatial distribution of the line ratio correlates more closely with the ^{12}CO $J = 3\rightarrow 2$ line strength compared to ^{12}CO $J = 1\rightarrow 0$. Using a generic line ratio of 0.6, a typical line ratio for Galactic and extragalactic Giant Molecular Cloud (GMC), we calculate a total *dense* molecular gas mass (M_{H_2}) for both galaxies. We compare these results with the M_{H_2} derived using the galaxy average line ratio and a theoretically derived CO(3→2)-to-H_2 conversion factor. Using the neutral atomic hydrogen (H_1) data from the THINGS (The H_1 Nearby Galaxy Survey) survey, we investigate the correlation between H_1 and H_2 with star formation rate density (SFRD). We find that the agreement between the relation of $H_1 + H_2$ with SFRD between the two galaxies is better compared to the relation with H_2 gas mass alone. Finally, we compare the ^{12}CO $J = 3\rightarrow 2$ intensity with the PAH 8 μm surface brightness. The results suggest that the correlation is good in the high surface brightness regions. We extend this study to include 25 galaxies within the NGLS sample and find a tight correlation at large spatial scales, as both PAH 8 μm and ^{12}CO $J = 3\rightarrow 2$ are likely to originate in the proximate site of active star formation.

10.1 Introduction

Observations of molecular gas are essential for understanding the role of star formation in the evolution of galaxies. However molecular hydrogen (H_2), a major constituent of the interstellar medium (ISM), lacks a permanent electric dipole moment, making it difficult to observe directly in external galaxies. In contrast, carbon monoxide (CO) rotational lines, a very convenient tracer of molecular hydrogen, can be observed easily from the ground.

B.-K. Tan, *Development of Coherent Detector Technologies for Sub-Millimetre Wave Astronomy Observations*, Springer Theses, DOI 10.1007/978-3-319-19363-2_10

Many extra-galactic surveys of low rotational transitions (low-J) of CO have been conducted and reported before (e.g., Sage 1993; Braine et al. 1993; Young et al. 1995; Elfhag et al. 1996; Meier et al. 2001; Albrecht et al. 2004; Israel 2005). Most of these surveys are single pointing observations using single-dish telescopes with large beam sizes, leading to a rather limited understanding of the spatial distribution of the molecular gas within individual galaxies. High angular resolution interferometric surveys have also been conducted (e.g., Sakamoto et al. 1999; Regan et al. 2001; Helfer et al. 2003) to study the smaller scale structure, but these surveys have been mostly constrained to the central regions of the galaxies due to the limited field size. This often results in incomplete mapping of nearby galaxies which are larger than the interferometer's restricted field of view. Multiple pointing data from single-dish telescopes are available, but usually only with a few pointings along the major and minor axes, rather than fully sampled maps. A new generation of high-sensitivity multi-pixel array receivers mounted on single-dish telescopes are now providing much faster mapping speeds, and are thus very efficient at mapping complex structures in the ISM across entire galactic disks. Two surveys using this type of focal plane array receivers were carried out, one by Leroy et al. (2009) using HERA (Heterodyne Receiver Array) on the IRAM (Institut de Radio Astronomie Millimétrique) 30 m telescope to map ^{12}CO $J = 2\rightarrow 1$ and another by Kuno et al. (2007) using BEARS (Beam Array Receiver System) on NRO (Nobeyama Radio Observatory) to map ^{12}CO $J = 1\rightarrow 0$, in nearby galaxies.

The Nearby Galaxy Legacy Survey (NGLS) (Wilson et al. 2009, 2012) uses the James Clerk Maxwell Telescope (JCMT) to map ^{12}CO $J = 3\rightarrow 2$ emission from nearby galaxies. The ^{12}CO $J = 3\rightarrow 2$ transition traces the warmer and denser regions of the molecular gas and may be more directly correlated with star forming regions (and references therein Wilson et al. 2009) compared to the lower transitions, such as ^{12}CO $J = 1\rightarrow 0$ which traces more diffuse gas. The entire JCMT NGLS sample consists of 155 nearby galaxies, each with spectral line observations at 345 GHz, and continuum observations at 450 and 850 μm. The spectral line observations were made with the HARP-B (Heterodyne Array Receivers Program for B-band) receiver (Smith et al. 2003), whereas the continuum observations will be made with the recently commissioned SCUBA-2 (Submillimetre Common User Bolometer Array 2) camera (Robson and Holland 2007). The NGLS sample includes 47 *Spitzer* Infrared Nearby Galaxies Survey (SINGS) galaxies (Kennicutt et al. 2003) and 108 randomly selected galaxies from a H_1 flux-limited sample, 36 from the Virgo cluster and 72 field galaxies. The distances of all selected galaxies are limited to within 25 Mpc so that the resolved spatial scales are small enough (between 0.2–2 kpc) to study the physics of the interstellar molecular gas and dust content. So far, the survey has completed the HARP-B ^{12}CO $J = 3\rightarrow 2$ observations for all the galaxies in the survey. The final phase of the survey will be the SCUBA-2 dust continuum observations for the entire sample.

NGC 2976 and NGC 3351 are two galaxies both observed near the beginning of the NGLS survey. The two galaxies offer an interesting contrast in both morphology and likely star formation activity. NGC 2976 is a dwarf galaxy on the outskirts of the M81 group in a weak tidal interaction with the group (Appleton et al. 1981; Yun

1999); whereas NGC 3351 is a starburst galaxy with ring structures (Colina et al. 1997; Elmegreen et al. 1997; Swartz et al. 2006; Hägele et al. 2007). NGC 2976 has mostly an older stellar population and the galaxy is thought to be at the end of an episode of star formation. However, there are indications (Williams et al. 2010) that there are still sites of intense star formation within the inner disk, fuelled by molecular hydrogens as they funnelled from the outer disk after the recent interaction with the tidal stream from M81. On the other hand, NGC 3351 has mainly a very young starburst population. It is thus interesting to understand the effect of such different environments on the behaviour and physical conditions of the molecular component of the ISM within these two galaxies.

Using the improved spatial resolution of the NGLS ^{12}CO $J = 3\rightarrow2$ survey, we can resolve the sites with *warmer*, *denser* molecular hydrogen which often coincide with sites of intense star formation activity, and investigate the correlation of this observable with other components of the ISM observed in different wavebands. The ratio between the higher-J ^{12}CO $J = 3\rightarrow2$ transition and the commonly observed ^{12}CO $J = 1\rightarrow0$ allows us to constrain the physical gas conditions. By comparing this spatially resolved line ratio with various line ratios obtained from the literature, normally averaged over a larger beam area within the galaxy, we can study the effect of spatial resolution on the variation of the line ratio distribution within the galactic disc. Using the galaxy disc-averaged ratio, we also investigate the derived molecular gas mass and study its relation to the star formation rate density (SFRD), in conjunction with data providing the neutral atomic hydrogen (H_1) gas mass.

One of the scientific motivations of the NGLS is to understand the relationship between dust and gas within nearby galaxies. Globally integrated mid-infrared line emission from Polycyclic-Aromatic-Hydrocarbons (PAHs) is often used as an indicator of star formation (Zhu et al. 2008; Kennicutt et al. 2009) and is associated with continuum emission from the cold dust (Haas et al. 2002; Bendo et al. 2008). Results from SINGS, a comprehensive infrared imaging and spectroscopic survey of 75 nearby galaxies using the *Spitzer* Space Telescope (hereinafter *Spitzer*) indicate that the relation of PAHs and star formation holds true to spatial scales of greater than 1 kpc, although the relation breaks down on smaller spatial scales (Calzetti et al. 2005, 2007; Bendo et al. 2006, 2008; Prescott et al. 2007; Kennicutt et al. 2009; Zhu et al. 2008). On the other hand, Regan et al. (2006) and Bendo et al. (2010) using radial average values, found that in nearby galaxies PAH emission and CO spectral lines are closely correlated. The origin of this relation between the two components remains unclear (e.g., Bendo et al. 2010). As the CO emission lines are often associated with the gas reservoir involved in star formation, we investigate this relation between PAH and CO spectral line strengths using SINGS and NGLS data, to further understand whether the two components may be linked through a common excitation source, i.e. star forming activity.

In this chapter, we report the ^{12}CO $J = 3\rightarrow2$ measurements of NGC 2976 and NGC 3351, both targets of early HARP-B observations. We describe the basic properties of the two galaxies in Sect. 10.2. The details of the observations and data reduction are presented in Sect. 10.3. We present our results and discussion in Sect. 10.4 where we calculate ^{12}CO $J = 3\rightarrow2$ to ^{12}CO $J = 1\rightarrow0$ line ratios, derive the molecular

gas masses and study the correlation between the ^{12}CO $J = 3\rightarrow2$ line emission and emission from PAHs. Finally, we summarise our conclusions in Sect. 10.5.

10.2 Target Galaxies

NGC 2976 is an SAB(s:)d peculiar dwarf galaxy (Buta 2013) in the M81 group. In the optical (Frei et al. 1996; Abazajian et al. 2009), it appears as a pure disk system showing neither bulge nor bar. However, in many other wavebands including H_1 (Walter et al. 2008) and the ^{12}CO maps, shown in Fig. 10.1, two bright regions near the ends of the major axis (hereinafter the bright end regions) can clearly be seen. Single-beam ^{12}CO $J = 3\rightarrow2$ and ^{12}CO $J = 2\rightarrow1$ data have been collected by Israel (2005) using the JCMT and the ^{12}CO $J = 1\rightarrow0$ emission has been mapped at high resolution by Simon et al. (2003) using the BIMA (Berkeley-Illinois-Maryland Association) interferometer. These observations, however, concentrate mainly on the central region of the galaxy and the BIMA map only partially includes the bright end regions. The NGLS ^{12}CO $J = 3\rightarrow2$ maps cover a rectangular area corresponding to $D_{25}/2$, and are therefore wide enough to include both bright complexes.

NGC 3351 is an SB(r)b spiral galaxy (Buta 2013) displaying high-mass star formation in a $15.3'' \times 11.2''$ circumnuclear ring (hereinafter the $15''$ ring) (Alloin and Nieto 1982; Buta and Crocker 1993; Colina et al. 1997; Elmegreen et al. 1997) fuelled by gas accreted through a stellar bar (Swartz et al. 2006). Most of the studies of NGC 3351 made so far concentrate on this bright central region of the galaxy. However, the optical image (Frei et al. 1996; Abazajian et al. 2009) shown in Fig. 10.2a shows a faint ring of $\sim2'$ diameter (hereinafter the $2'$ ring) encircling the bar, with signs of spiral arms extending from this ring towards the outermost pseudo-ring feature (major axis diameter $\sim5.5'$, minor axis $\sim3.6'$) (Buta and Crocker 1993). All these features are within the area covered by our ^{12}CO $J = 3\rightarrow2$ map of NGC 3351 presented here.

The general properties of NGC 2976 and NGC 3351 taken from de Vaucouleurs et al. (1991) (unless otherwise stated) are summarised in Table 10.1.

10.2.1 Archival Data

Both NGC 2976 and NGC 3351 are part of the SINGS survey (Kennicutt et al. 2003) and have rich multi-wavelength ancillary data available. Although a number of ^{12}CO data sets at various transitions are available, most of these are single-beam data and thus the comparison with our ^{12}CO $J = 3\rightarrow2$ maps is challenging. For NGC 3351, ^{12}CO $J = 1\rightarrow0$ maps are available from the single-dish Nobeyama Radio Observatory (NRO) (Kuno et al. 2007)[1] and the BIMA Survey of Nearby

[1] http://www.nro.nao.ac.jp/nro45mrt/COatlas/.

Table 10.1 General properties of NGC 2976 and NGC 3351 taken from the literature

General properties	NGC 2976	NGC 3351
Type	SAB(s:)d pec	(R')SB(r,nr)a
R.A. (J2000)	09:47:15.6	10:43:58.0
Dec (J2000)	+67:54:50	+11:42:15
Distance (Mpc)	3.56	9.33
Incl. angle	54°	39°
$D_{25}/2$ (′)	2.9 × 1.5	3.8 × 2.2

Reference for the distance to NGC 2976 is from Karachentsev et al. (2002) and for NGC 3351 is from Freedman et al. (2001). The inclination angle is from Blok et al. (2008) and value of $D_{25}/2$ from Buta et al. (2007)

Galaxies (SONG) (Helfer et al. 2003). We used ^{12}CO $J = 1 \rightarrow 0$ maps from NRO as these are single-dish data and their beam size (15″) closely matches the ^{12}CO $J = 3 \rightarrow 2$ beam size of HARP-B on the JCMT. NGC 2976, however, was not included in the NRO survey. Hence, the ^{12}CO $J = 1 \rightarrow 0$ map for NGC 2976 was retrieved only from the BIMA SONG survey.[2] The *Spitzer* IRAC (Infrared Array Camera) 3.6 and 8 μm data and MIPS (Multiband Imaging Photometer for *Spitzer*) 24 μm data used in this study were downloaded from the SINGS survey website.[3] The optical images for both galaxies were retrieved from the seventh data release of the Sloan Digital Sky Survey (SDSS).[4] The H_1 images were downloaded from The H_1 Nearby Galaxy Survey (THINGS)[5] and the ultraviolet (UV) images used to produce the SFR surface density images, in conjunction with the 24 μm data, were retrieved from the Galaxy Evolution Explorer (*GALEX*) data release.[6]

10.3 Observations and Data Reduction

The ^{12}CO $J = 3 \rightarrow 2$ (rest frequency 345.796 GHz) observations for NGC 2976 were carried out over two nights between November 2007 and January 2008, while observations for NGC 3351 took place over two observing runs in January 2008. The instrument used was HARP-B which has 16 SIS heterodyne mixers arranged in a 4×4 array with 30″ row and column separation. This corresponds to a 2′ square footprint on the sky. HARP-B operates over a frequency range of 325–375 GHz and the average FWHM (Full Width Half Maximum) beamwidth is 14.5″. The receiver operates with the ACSIS (Auto-Correlation Spectrometer and Imaging System Buckle et al. 2009) as the back-end. The observations for both galaxies were made using a 1 GHz

[2] http://nedwww.ipac.caltech.edu/level5/March02/SONG/SONG.html.

[3] http://sings.stsci.edu/.

[4] http://www.sdss.org/.

[5] http://www.mpia.de/THINGS/Data.html.

[6] http://galex.stsci.edu/GR4/.

Table 10.2 Observation dates and parameters used in the observing runs for NGC 2976 and NGC 3351

Parameters	NGC 2976	NGC 3351
Observing dates	25 Nov 2007	07 Jan 2008
	06 Jan 2008	12 Jan 2008
Position angle (major axis)	143°	13°
Height of map	294″	348″
Width of map	210″	252″
T_{sys}	341 K	409 K
ΔT_A^*	13.3 mK	16.2 mK

ACSIS bandwidth with a spectral resolution of 0.488 MHz. The main beam efficiencies (η_{MB}) used to convert the corrected antenna temperature (T_A^*) to the main beam brightness temperature (T_{mb}) were determined from observations of bright planets. All data presented in here were calibrated to the T_{mb} scale using $\eta_{MB} = 0.6$.

Both NGC 2976 and NGC 3351 were raster scanned using a basket-weave technique with half array steps (58.2″, Warren et al. 2010). This ensured that all of the area within the target scan region, defined to include all of the optical galactic emission, was fully sampled. These fully sampled maps were made repeatedly until the target root-mean-square (RMS) noise of the combined scans (less than 19 mK at the T_A^* scale) was achieved within a frequency bin of 20 km s^{-1} resolution. The observational details for each galaxy are summarised in Table 10.2.

10.3.1 Data Reduction

The spectral data reduction and analysis was done mainly using the *Starlink*[7] software packages (Jenness et al. 2009). We used KAPPA (Kernel Application Package)[8] and SMURF (Sub-Millimetre User Reduction Facility) applications within *Starlink* as the main reduction tools. GAIA (Graphical Astronomy and Image Analysis Tool) and SPLAT (Spectrum Analysis Tool) were used for analysis and visualisation purposes. Data collected under the NGLS survey were processed primarily following the steps outlined in Warren et al. (2010), with some modifications depending on the characteristics of the individual galaxy and the quality of the observed data.

When comparing our ^{12}CO $J = 3\rightarrow2$ data with the interferometric ^{12}CO $J = 1\rightarrow0$ data, we convolved the ^{12}CO $J = 1\rightarrow0$ data with a two-dimensional Gaussian profile, using the KAPPA routine `gausmooth`.[9] This allowed the ^{12}CO $J = 1\rightarrow0$

[7] *Starlink* is maintained by the Joint Astronomy Centre (JAC) (http://www.starlink.ac.uk).

[8] http://docs.jach.hawaii.edu/star/sun95.htx/sun95.html.

[9] This step was skipped for NRO ^{12}CO $J = 1\rightarrow0$ map because the beam size of NRO (15″) is very close to the beam size of HARP-B.

data to be matched to the 14.5″ HARP-B resolution (Bendo et al. 2010). For single pointing ^{12}CO $J = 1 \rightarrow 0$ data that have larger beam than 14.5″, we matched the ^{12}CO $J = 3 \rightarrow 2$ to the larger beam size.

The point spread function (PSF) of *Spitzer* images are highly non-Gaussian. We thus created convolution kernels, following recipes from Gordon et al. (2008) and Bendo et al. (2010), to match the PSFs to those of HARP-B. These kernels were created, for each waveband, using the STinyTim[10] package (Krist 2002), and convolved with the *Spitzer* images to match the HARP-B beam. We used the KAPPA routine `convolve` for this task. Further details of the PSF matching for HARP-B and *Spitzer* images can be found in Bendo et al. (2010).

10.3.1.1 R_{31} Line Ratio

We derived the line ratio of ^{12}CO $J = 3 \rightarrow 2$ to ^{12}CO $J = 1 \rightarrow 0$ (hereinafter R_{31}) by simply dividing the ^{12}CO $J = 3 \rightarrow 2$ integrated intensity with the ^{12}CO $J = 1 \rightarrow 0$ integrated intensity, after matching the beam. For single-beam observations, the ^{12}CO $J = 3 \rightarrow 2$ spectra from the pixel corresponding to the coordinate of the ^{12}CO $J = 1 \rightarrow 0$ pointing was extracted and re-binned to 10 km s^{-1} channels. We used the SPLAT package to inspect the spectra and discard the line-free region. The remaining spectra were then integrated over the velocity axis to derive ^{12}CO $J = 3 \rightarrow 2$ line intensity, and this was divided by the corresponding ^{12}CO $J = 1 \rightarrow 0$ integrated intensity to produce R_{31}. For deriving R_{31} map, we re-gridded the ^{12}CO $J = 1 \rightarrow 0$ to match our pixel size and calculated the R_{31} ratio by performing a pixel-by-pixel division of the resulting ^{12}CO $J = 3 \rightarrow 2$ and ^{12}CO $J = 1 \rightarrow 0$ maps.

10.3.1.2 8 μm Data and Radial Profile

The IRAC 8 μm band samples emission from both stars and PAHs. To produce a clean 8 μm image with surface brightness due to PAHs only, the stellar contribution needs to be removed using the 3.6 μm image (Helou et al. 2004; Smith et al. 2007). We downloaded the 3.6 and 8 μm images from the SINGS website. The description of the pipeline data reduction steps can be found in Regan et al. (2006).

For the production of the clean 8 μm image, we followed the steps outlined in Bendo et al. (2010). First, we determined and subtracted the residual background of both the 3.6–8 μm images by fitting a smoothed gradient of the background brightness outside the galaxy disk. Regions with 3.6–8 μm surface brightness ratio ≥ 5 were masked out as bright foreground stars. The effective aperture corrections were then applied to both images by multiplying the correction factors, 0.944 for the 3.6 μm image and 0.737 for the 8 μm image respectively, following the calibration recommendation in Reach et al. (2005). Finally, we subtracted the stellar continuum (represented by the final 3.6 μm image) from the 8 μm surface brightness images

[10] http://ssc.spitzer.caltech.edu/archanaly/contributed/browse.html.

(Helou et al. 2004) using

$$I_{8\,\mu m}^{clean} = I_{8\,\mu m}^{raw} - 0.232 I_{3.6\,\mu m}^{raw} \tag{10.1}$$

where $I_{8\,\mu m}^{raw}$ and $I_{3.6\,\mu m}^{raw}$ are the raw 8 and 3.6 μm intensity map from the IRAC pipeline, and $I_{8\,\mu m}^{clean}$ is the final clean 8 μm intensity map. Note that the IRAC 8 μm image of NGC 3351 is affected by the Muxbleed artefact (Laine 2011). Hence, the affected area has been masked out, except the bright circumnuclear region.

To create the radial profiles, we binned the corresponding maps into a number of elliptical annuli. The ellipticity of the annuli are defined by the ratio of the galaxy's major and minor axis lengths. The width of the annuli was about 14.5″ for ^{12}CO $J = 3\rightarrow2$ data and 5.25″ for PAH 8 μm data, defined along the major axis of the galaxy. The radial surface brightness was then the average of the brightness within each elliptical.

10.3.1.3 SFR Surface Density

To produce SFR surface density maps, we combined the *GALEX* far ultraviolet (FUV) data with the *Spitzer* 24 μm maps to account for both the exposed and the embedded star formation activity. The 24 μm waveband traces the dust emission from the young stars embedded within, and the FUV detects the photospheric emission from the O and B star which relates to the unobscured star formation. However, it is worthwhile noting this approach does include some faint emission that are unrelated to star formation, as discussed by Kennicutt et al. (2009) and Foyle et al. (2012). We estimated the surface density of SFR using

$$\Sigma_{SFRD} = 8.1 \times 10^{-2} I_{FUV} + 3.2 \times 10^{-3} I_{24}, \tag{10.2}$$

from Leroy et al. (2008), where Σ_{SFR} is the estimated SFR surface density having units of $M_\odot$ kpc^{-2} year^{-1} and both FUV and 24 μm intensity (I_{FUV} and I_{24} respectively) are in MJy sr^{-1}. We refer the reader to the appendix of Leroy et al. (2008) for details of the calibration steps.

10.4 Results and Discussion

In Figs. 10.1 and 10.2, we show the reduced ^{12}CO $J = 3\rightarrow2$ map of NGC 2976 and NGC 3351 respectively, together with the ancillary maps of ^{12}CO $J = 1\rightarrow0$, IRAC 8 μm, optical image from SDSS, H_1 image from THINGS and SFR surface density map. All maps shown are in their native resolution (except the SFRD map that has been convolved to the HARP-B beam size), overlaid with the contours of our NGLS ^{12}CO $J = 3\rightarrow2$ data.

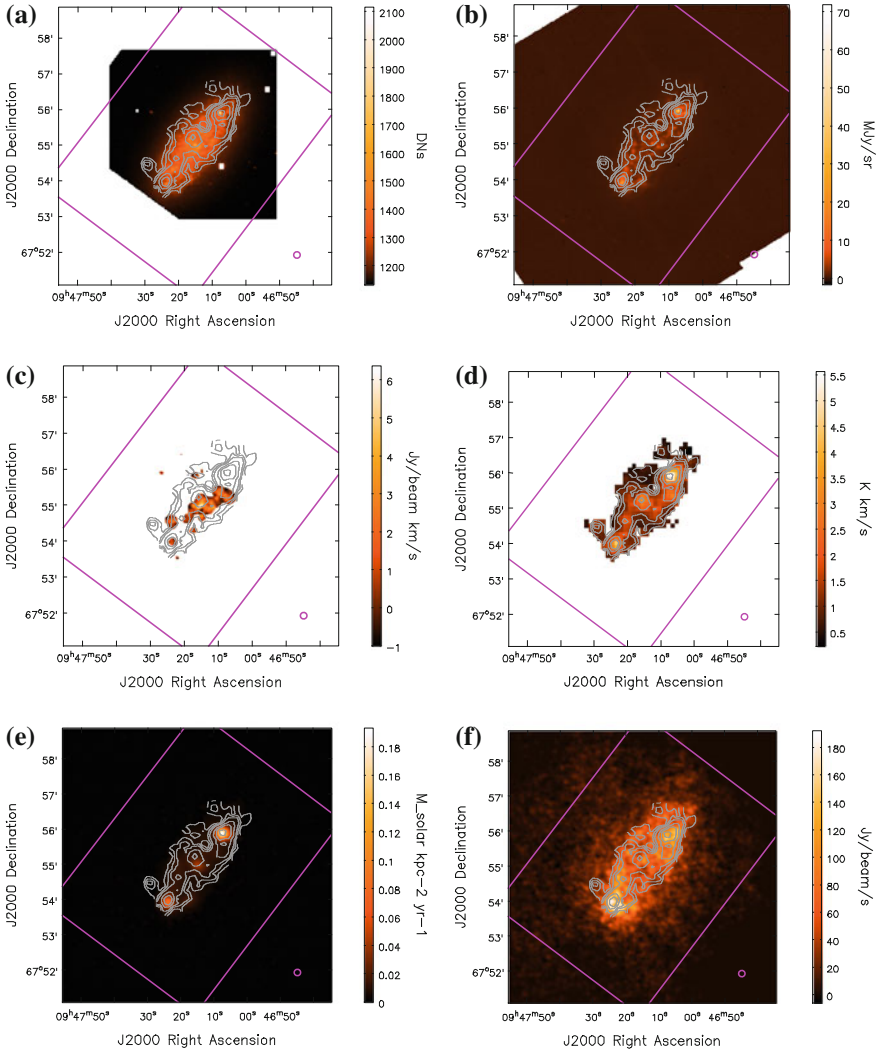

Fig. 10.1 Contours of the ^{12}CO $J = 3 \rightarrow 2$ data of NGC 2976 overlaid on the corresponding ancillary images from the archives. The contour levels are 0.36 (3σ), 0.72, 1.08, 2.0, 3.0 and 5.0 K km s^{-1} (temperature in T_{mb}). In all panels, a *magenta box* is drawn to show the region mapped by HARP-B, and a *magenta circle* to indicate the 14.5″ angular resolution of the ^{12}CO $J = 3 \rightarrow 2$ data. All images are oriented North up and East to the *left*, with the inclination angle of 54°. The image representing Σ_{SFR} had been convolved to the HARP-B beam size. **a** Optical (SDSS). **b** 8 μm (*Spitzer* IRAC). **c** ^{12}CO $J = 1 \rightarrow 0$ (BIMA). **d** ^{12}CO $J = 3 \rightarrow 2$ (JCMT NGLS). **e** Σ_{SFR} (*Spitzer* MIPS 24 μm and *GALEX* FUV). **f** H_1 (THINGS)

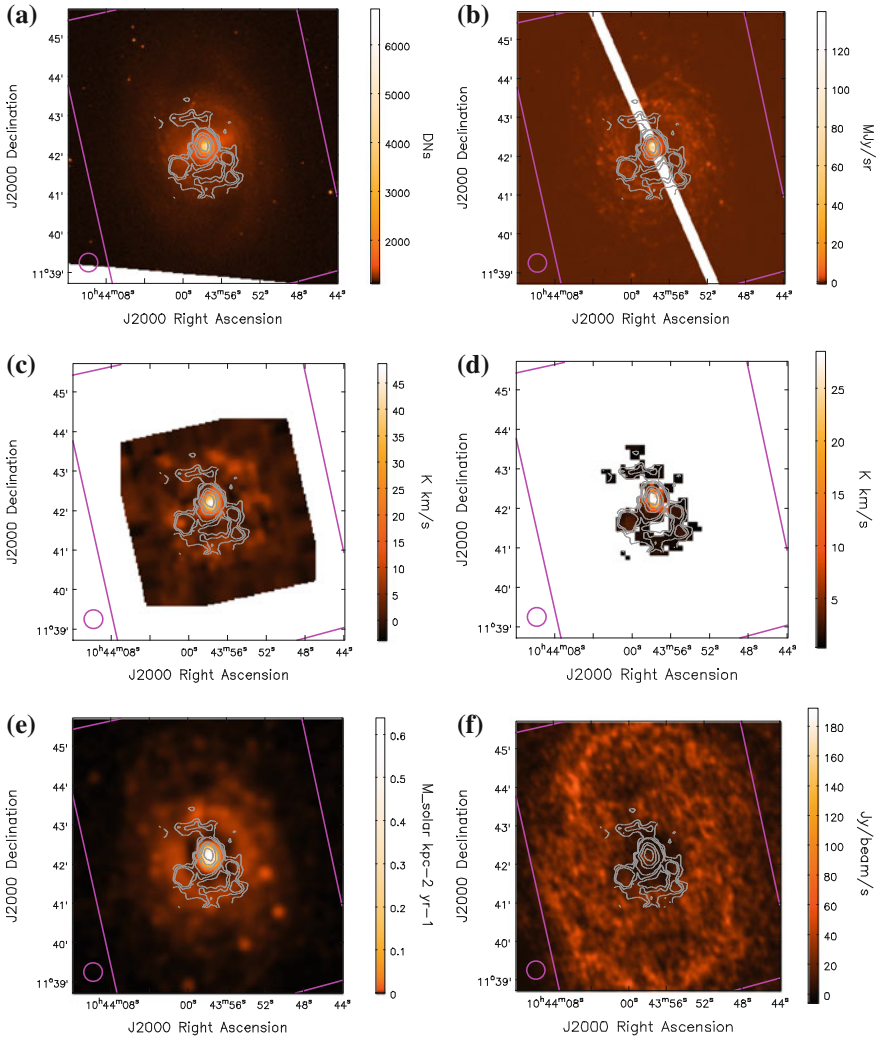

Fig. 10.2 Contours of the ^{12}CO $J = 3\rightarrow2$ data of NGC3351 overlaid on the corresponding ancillary images from the archives. The contour levels are 0.43 (3σ), 0.86, 1.29, 5.0, 10.0, 20.0 and 30.0 K km s^{-1} (temperature in T_{mb}). In all panels, a *magenta box* is drawn to show the region mapped by HARP-B, and a *magenta circle* to indicate the 14.5″ angular resolution of the ^{12}CO $J = 3\rightarrow2$ data. All images are oriented North up and East to the *left*. The 8 μm image is affected by Muxbleed, hence the affected area is blanked out. The image representing Σ_{SFR} had been convolved to the HARP-B beam size. **a** Optical (SDSS). **b** 8 μm (*Spitzer* IRAC). **c** ^{12}CO $J = 1\rightarrow0$ (BIMA). **d** ^{12}CO $J = 3\rightarrow2$ (JCMT NGLS). **e** Σ_{SFR} (*Spitzer* MIPS 24 μm and *GALEX* FUV). **f** H_1 (THINGS)

The NGC 2976 ^{12}CO $J = 3 \rightarrow 2$ map traces an inverse-S-like feature with a small extension along the minor axis at R.A. 09:47:07 and Dec. +67:54:30. This inverse-S-like structure is not seen in the other wavebands compared here, but does exist in the ^{12}CO $J = 2 \rightarrow 1$ image from the HERA CO-Line Extragalactic Survey (HERACLES, Leroy et al. 2009). This is possibly caused by the coarse resolution of the CO maps compared to the other wavebands, smoothing out the embedded small scale structure, thus making the large structure easier to identify. In both ^{12}CO $J = 2 \rightarrow 1$ and our ^{12}CO $J = 3 \rightarrow 2$ maps, the emission near the two ends of the major axis is stronger than the emission in the central region. IRAC 8 μm, MIPS 24 μm and THINGS H_1 observation detect similar strong emission here, but the same is not seen in the optical images.

A weak detection near the central region of our ^{12}CO $J = 3 \rightarrow 2$ map is only evident in the SFRD image (produced with combination of 24 μm and FUV maps), indicating the existence of hot dust in this region. This shows up as a faint blob near the centre of the SFR surface density map, but appears to be slightly shifted compared to the ^{12}CO $J = 3 \rightarrow 2$ detection. This central region of the emission is detected in ^{12}CO $J = 1 \rightarrow 0$ from the BIMA SONG observations, and the position is closer to the MIPS 24 μm central detection location. However, due to the small area covered by of the BIMA footprint, the two bright end regions were partly missed.

This offset in the detection near the central region of NGC 2976 between ^{12}CO $J = 3 \rightarrow 2$ and other maps hints at the possible existence of different star formation phases between this central region and the two bright end regions. The bright end regions are currently undergoing intense star formation, while the star formation activity in the central region might be slowed down by the disruption of the H_1 or H_2 fuel. This could be caused by the recent interaction of NGC 2976 with the M81 group, disturbing the gas and dust distribution within the galaxy, and igniting a new phase of star formation near the two bright ends.

Another possible explanation of this offset is that ^{12}CO $J = 3 \rightarrow 2$ is in fact coming from a different sub-kpc location compared to the ^{12}CO $J = 1 \rightarrow 0$ and 24 μm emission, though the separation between these two regions might be too small to be resolved here. But the evidence that this location separation exists can be inferred from the fact that the offsets only occur in the weaker emission area but not in the bright end regions. At high brightness areas, the strong emission from the sub-kpc region will dominate the entire telescope beam, hence smearing out the different individual location. However, if the emission is weaker and due to the nature of the Gaussian-like beam profile, the spill-over effect to the adjacent beam is less prominent, hence one can start to distinguish the difference in location where different emission originated.

NGC 3351 has a dominant circumnuclear region that is detected in all wavebands shown here. The distribution of the ^{12}CO $J = 3 \rightarrow 2$ integrated intensity across the galactic disk has a huge contrast between the dominant central detection and the surrounding area. Only a certain area around the southern part of the 2′ ring is detected in our ^{12}CO $J = 3 \rightarrow 2$ map. The signal from the northern part of the ring is weak and does not trace the entire ring structure as seen in the ^{12}CO $J = 1 \rightarrow 0$ map. The bar structure visible in the optical image is not traced in our ^{12}CO $J = 3 \rightarrow 2$ map.

The offset in the position of detection from the weaker emitting regions seen in NGC 2976 is also evident in the NGC 3351 maps. The complex near the southwest extent of the nucleus, between the centre of the galaxy and the 2′ ring, only shows up in our ^{12}CO $J = 3\rightarrow 2$, but not in other maps. The complex extending from the nucleus towards the southern ring on the east also seems to be offset from the detection region in the NRO ^{12}CO $J = 1\rightarrow 0$ map. However, this southeast complex and the branch extending slightly towards the northwest, are in fact tracing the dust lane (Swartz et al. 2006) surrounding the nuclear region. These dust lanes are visible in the single filter optical image,[11] and they extend along the leading edge of a bar that is oriented at an angle of 110° east of north. From the IRAC 3.6 μm and the optical image, this bar terminates at the 2′ ring, with faint spiral arms extending beyond the ring. As well as the double ring structure (see Sect. 10.2), NGC 3351 has an interesting double bar feature too. An inner bar terminating at the 15″ ring is detected in the BIMA ^{12}CO $J = 1\rightarrow 0$ observation (Helfer et al. 2003). This 15″ bar is almost perpendicular to the outer 2′ bar, but is too small to be resolved at the resolution of HARP-B.

The detected ^{12}CO $J = 3\rightarrow 2$ spectra of NGC 2976 are generally narrower at the southeast bright end with half power line width of around 15 km s^{-1}, compared to the wider width at the northwest bright end of around 30 km s^{-1}. The spectra of these two bright end regions are shown in Fig. 10.3a, b. The peak intensity T_{MB} is 0.14 K. The emission line can be traced along the inverse-S-like structure from the southeast end towards the northwest end, with the central velocity of the line shifting from −53 towards 68 km s^{-1}.

The ^{12}CO $J = 3\rightarrow 2$ emission line near the central region of NGC 3351 exhibits a prominent twin peak feature, as depicted in Fig. 10.3c. This feature points to the rotation of the 15″ ring and the inflow/outflow of gas within the inner bar. Each peak has a rather broad, ∼70–90 km s^{-1} half power line width, with a peak intensity of 0.13 K.

10.4.1 R_{31} Line Ratio

To estimate the molecular gas mass using the CO-to-H_2 conversion factor (X_{CO}), one often uses the ^{12}CO $J = 1\rightarrow 0$ transition. However, as Greve et al. (2005) point out, the ^{12}CO $J = 1\rightarrow 0$ line, which includes emission from more diffuse molecular gas, does not trace star formation on a one-to-one basis. ^{12}CO $J = 3\rightarrow 2$ on the other hand correlates almost linearly with the global star formation rate over five orders of magnitude (e.g., Iono et al. 2009). Hence, to derive H_2 gas mass from the warmer and denser gas region, where ^{12}CO $J = 3\rightarrow 2$ is thermalised, the ratio between ^{12}CO $J = 3\rightarrow 2$ and ^{12}CO $J = 1\rightarrow 0$ is important. We thus construct ratio maps using the present ^{12}CO $J = 3\rightarrow 2$ map in combination with interferometric ^{12}CO $J = 1\rightarrow 0$ map from BIMA SONG for NGC 2976 and the NRO raster map for NGC 3351, as described in Sect. 10.3.1.1.

[11] Refer to Fig. 1 in Swartz et al. (2006).

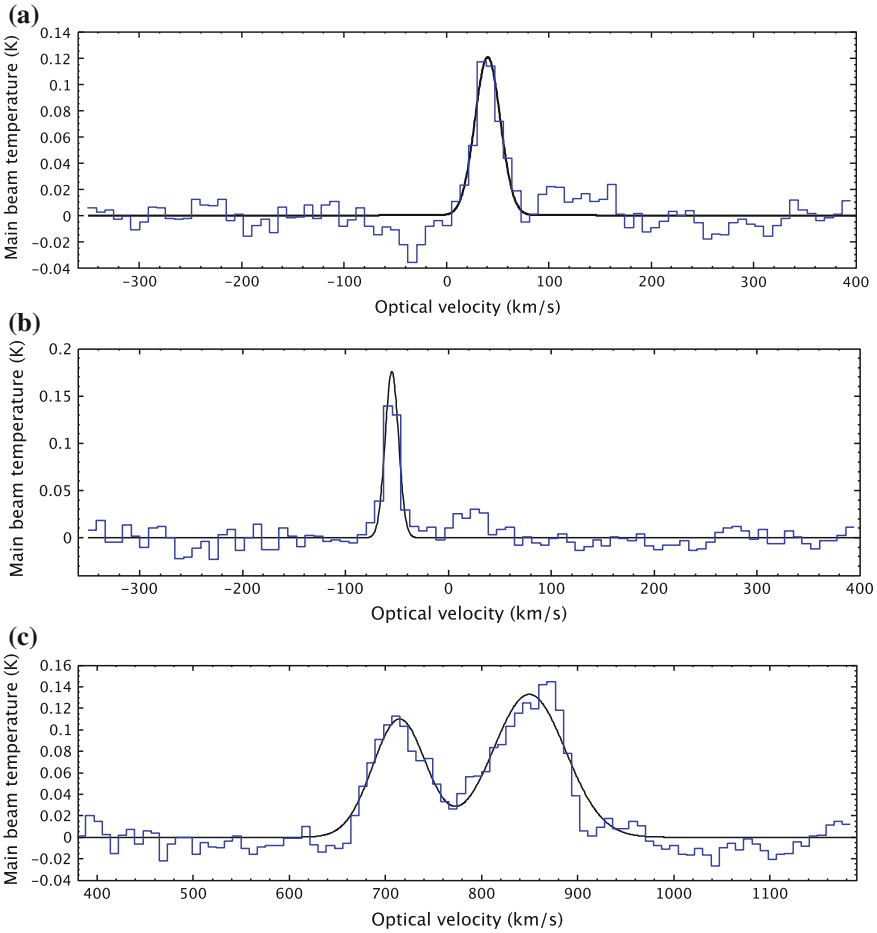

Fig. 10.3 ^{12}CO $J = 3 \rightarrow 2$ spectra, on the main-beam antenna temperature (T_{mb}) scale, of the brightest pixel in NGC 2976 and NGC 3351, smoothed to 10 km s^{-1}. All spectra are overlaid with a Gaussian fits. The central velocity of spectrum **a** is fitted at 40.3 km s^{-1}, with a peak temperature of 0.12 K and FWHM of 30.0 km s^{-1}. Spectrum **b** has a central velocity of -51.8 km s^{-1}, with the peak temperature of 0.14 K and FWHM of 15.0 km s^{-1}. Spectrum **c** has peak temperatures of 0.12 and 0.14 K, with the lower peak velocity at 715 km s^{-1} and higher peak velocity at 850 km s^{-1}. The FWHM is 72.4 km s^{-1} for the lower peak and 94.6 km s^{-1} for the higher peak. **a** Northwest bright end region of NGC 2976 at RA 9:47:08.1 Dec +67:55:50.2 with $\alpha = 0.012$ K. **b** Southeast bright end of NGC 2976 at RA 9:47:23.6 Dec +67:54:01.2 with $\alpha = 0.013$ K. **c** Central bright region of NGC 3351 at RA 10:43:57.6 Dec +11:42:13.9 with $\alpha = 0.012$ K

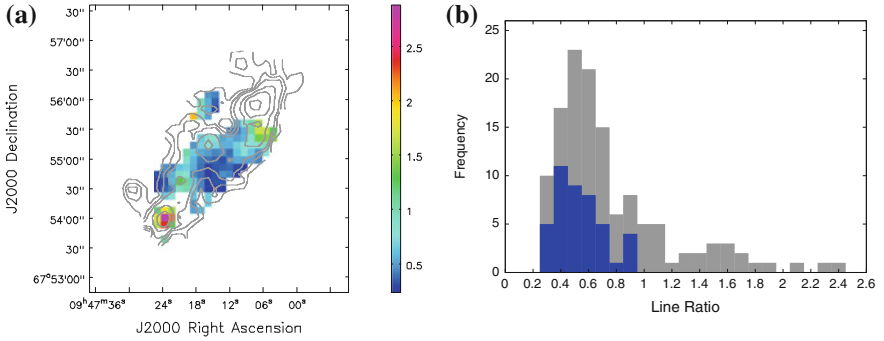

Fig. 10.4 **a** The R_{31} ratio map for NGC 2976 constructed using the ^{12}CO $J = 1\rightarrow0$ map from BIMA SONG. The *grey* contour line is the ^{12}CO $J = 3\rightarrow2$ contour map to show the position of the ratio map relative to the galaxy. **b** The distribution of the value of R_{31} across the galaxy. The *grey* histogram shows the pixel count when including all the pixels within the ratio map, whereas in the *blue* histogram we discard pixels within the ratio map with SNR less than 2.

In Figs. 10.4 and 10.5, we show the distribution of R_{31} across the disks of NGC 2976 and NGC 3351 respectively. One notes that completeness of the NGC 2976 R_{31} map is limited due the restricted sky coverage of the NGC 2976 BIMA ^{12}CO $J = 1\rightarrow0$ map and that accuracy of the intensity values may be affected by the reduction in BIMA map sensitivities away from the map centre (Helfer et al. 2003; Warren et al. 2010). This later calibration effect gives rise to the higher R_{31} values occurs towards the south-eastern end of NGC 2976. Similar higher R_{31} is seen towards the complex that extends towards the southwest of the centre of NGC 3351, but this is the direct consequence of the offset in the detection of ^{12}CO $J = 3\rightarrow2$ and ^{12}CO $J = 1\rightarrow0$ as explained in Sect. 10.4.

Averaging R_{31} across the entire galaxy disc, we obtain a global mean ratio of 0.51 $\pm$ 0.13 for NGC 2976 and 0.49 $\pm$ 0.03 for NGC 3351. These values generally agree within $\sim$20 % with the R_{31} value obtained by comparing our map with the single-beam ^{12}CO $J = 1\rightarrow0$ observations, which are obtained from a central pointing on the galaxy. For example, using the ^{12}CO $J = 1\rightarrow0$ data from Sage (1993), we arrive at a ratio of 0.42 $\pm$ 0.04 for NGC 2976 and 0.48 $\pm$ 0.03 for NGC 3351. The larger difference here for NGC 2976 is simply because the single-beam ^{12}CO $J = 1\rightarrow0$ data does not cover the south-eastern bright end region.

Figures 10.4b and 10.5b show the variation of the R_{31} ratio within each galaxy. The observed range of R_{31} values, mostly between 0.2–0.7, is similar to the range of global values obtained for the 28 nearby galaxies studied by Mauersberger et al. (1999), and also similar to the range (0.4–0.8) observed in individual giant molecular clouds in M33 (Thornley and Wilson 1994; Wilson et al. 1997). We note that similar variations in R_{31} have been seen in other galaxies reported so far from the NGLS survey (Wilson et al. 2009; Warren et al. 2010; Bendo et al. 2010; Irwin et al. 2011; Sánchez-Gallego et al. 2011).

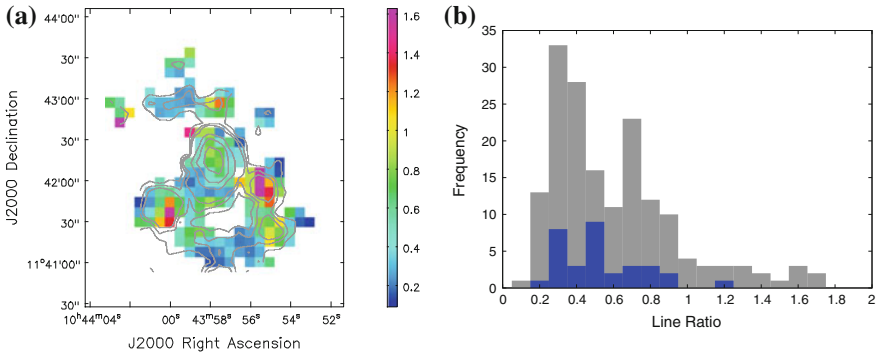

Fig. 10.5 Same as Fig. 10.4 but for NGC 3351. Ratio map and R_{31} distribution histogram constructed using the ^{12}CO $J = 1 \rightarrow 0$ map from the NRO Atlas. **a** Ratio map. **b** R_{31} distribution

In Fig. 10.6, we plot the relation of $\log_{10} R_{31}$ with $\log_{10} I_{CO(1-0)}$, $\log_{10} I_{CO(3-2)}$ and the surface density of SFR. We see no obvious correlation between the $\log_{10} I_{CO(1-0)}$ line brightness and the R_{31} line ratio for either galaxy, indicating no correlation in the spatial distribution of the total molecular gas mass, as traced by $\log_{10} I_{CO(1-0)}$ and the areas of dense, warm gas with enhanced R_{31} line ratio. We do, however, see a correlation between $\log_{10} R_{31}$ and $\log_{10} I_{CO(3-2)}$, indicating that the $I_{CO(3-2)}$ line is bright where the line ratio is largest i.e., that the ^{12}CO $J = 1 \rightarrow 0$ emission is more diffuse compared to the more strongly clumped ^{12}CO $J = 3 \rightarrow 2$ emission.

Plotting R_{31} against the SFR surface density maps in the rightmost panel of Fig. 10.6 shows no clear correlation for NGC 2976 and a weak correlation for NGC 3351 (Pearson correlation index $n = 0.19 \pm 0.05$). It appears that for NGC 3351, the galaxy with more ongoing star formation, the warmer denser gas traced by high R_{31} ratios is reasonably well correlated with the star formation activity, on the spatial

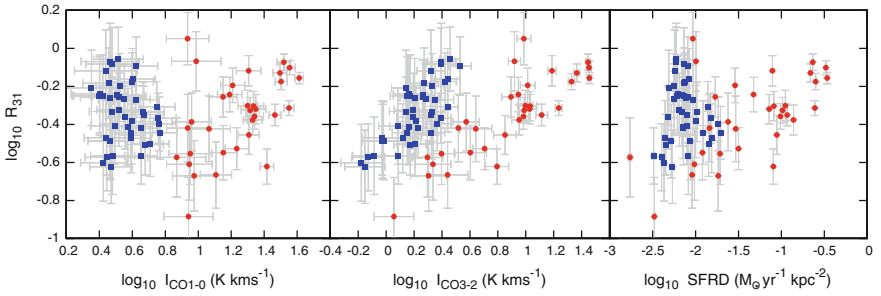

Fig. 10.6 Correlation of R_{31} with ^{12}CO $J = 1 \rightarrow 0$, ^{12}CO $J = 3 \rightarrow 2$ and SFR surface density respectively. The *blue square* represent pixel points from NGC 2976, whereas the *red dots* represent pixel points from NGC 3351

scales set by the pixel size of the map (108.9×10^3 pc^2). This correlation is not seen for the more nearby NGC 2976 which has less star formation activity and is mapped with a smaller pixel size (15.6×10^3 pc^2).

10.4.2 Molecular Gas Mass Estimation

In this section, we derive molecular hydrogen gas masses (M_{H_2}) using the ^{12}CO $J = 3\rightarrow2$ and the ^{12}CO $J = 1\rightarrow0$ data. For this purpose we make use of the R_{31} ratio discussed in Sect. 10.4.1, and investigate the influence of the various R_{31} values adopted on the derived molecular hydrogen mass estimates. We smooth the ^{12}CO $J = 1\rightarrow0$ map to the HARP-B resolution and compare only the common area covered in both maps. We compute ^{12}CO luminosity (for both ^{12}CO $J = 1\rightarrow0$ and ^{12}CO $J = 3\rightarrow2$ data) following:

$$L_{CO} = I_{avg} \times N_{pix} \times 23.5 \times (D \times \Delta_{pix})^2, \tag{10.3}$$

where L_{CO} is the ^{12}CO luminosity in K km s^{-1} pc^2, I_{avg} is the average ^{12}CO intensity (K km s^{-1}) obtained from the integrated intensity map on main beam temperature scale, N_{pix} is the number of pixels included, D is the distance to the galaxy in Mpc and Δ_{pix} is the pixel size in arc-seconds. The molecular gas masses are derived using

$$M_{H_2} = 1.6 \times 10^{-20} \times L_{CO} \times X_{CO} \quad (M_\odot), \tag{10.4}$$

where $L_{CO} = L_{CO(1\rightarrow0)}$ and $L_{CO} = L_{CO(3\rightarrow2)}/R_{31}$ for M_{H_2} based on ^{12}CO $J = 1\rightarrow0$ and ^{12}CO $J = 3\rightarrow2$ observations, respectively. Here, we use $X_{CO} = 2 \times 10^{20}$ (K km s^{-1})$^{-1}$ (Strong et al. 1988), consistent with the other papers published from the NGLS series, and assume that this conversion factor does not vary across the galactic disc. We do not take into account the effect of metallicity on the conversion factor, but we note that using the equation reported in Israel (2000) to calibrate X_{CO} for metallicity, the H_2 gas mass estimates for NGC 3351 would remain almost unchanged while the result for NGC 2976 would be lower by $\leq$5 %, which is far less than the uncertainty caused likely by systematic calibration errors ($\sim\pm$20 %).

We now investigate the effect of various R_{31} values on M_{H_2} estimates. First, we assume a generic line ratio of 0.6, which is a typical ratio appropriate for the molecular gas in Galactic and extragalactic GMCs (Wilson et al. 2009). Israel (2008) also found similar line ratios (0.6 ± 0.13) from observations of 15 nearby galaxies with modest starbursts . Second, we used the global mean ratio of 0.51 for NGC 2976 and 0.49 for NGC 3351, calculated directly from the present observations. Finally, we use a theoretically predicted (direct) CO(3→2)-to-H_2 conversion factor ($X_{CO(3\rightarrow2)}$) taken from Bell et al. (2007). We chose the value of $X_{CO(3\rightarrow2)} = 2.9 \times 10^{20}$ for NGC 2976 and $X_{CO(3\rightarrow2)} = 3.5 \times 10^{20}$ for NGC 3351, corresponding to types of galaxies similar to the ones studied here as outlined in Bell et al. (2007).

Table 10.3 Molecular gas mass M_{H_2} derived from our ^{12}CO $J = 3 \rightarrow 2$ data, compared to the literature

	J	NGC 2976	NGC 3351
L_{CO} (K km s$^{\otimes 1}$ pc^2)	$3 \rightarrow 2$	$(0.5 \circ\ 0.08) \times 10^7$	$(5.1 \circ\ 0.6) \times 10^7$
Line ratio	Derived M_{H_2} (10^8 $M_\odot$)		
$R \Im\ 0.6$	$3 \rightarrow 2$	$0.27 \circ\ 0.04$	$2.72 \circ\ 0.32$
$R \Im\ 0.51 \circ\ 0.13$[a]	$3 \rightarrow 2$	$0.31 \circ\ 0.09$	–
$R \Im\ 0.49 \circ\ 0.03$[b]	$3 \rightarrow 2$	–	$3.33 \circ\ 0.44$
$X_{CO(3 \rightarrow 2)}$	$3 \rightarrow 2$	$0.23 \circ\ 0.04$	$2.86 \circ\ 0.34$
Survey	M_{H_2} (10^8 $M_\odot$) from literature		
BIMA SONG[c]	$1 \rightarrow 0$	–	$10.3 \circ\ 1.53$
NRO[d]	$1 \rightarrow 0$	–	7.50
HERACLES[e]	$2 \rightarrow 1$	0.61	8.14

Notes
[a]Global ratio derived for NGC 2976
[b]Global ratio derived for NGC 3351
[c]Helfer et al. (2003)
[d]Kuno et al. (2007). The value was corrected for the same distance and X_{CO} used here and not corrected for heavy elements
[e]Leroy et al. (2009). The value was corrected for the same distance used here and does not includes any correction for heavy elements

Table 10.3 summarises the molecular hydrogen gas mass estimates using different R_{31} values. For comparison, we also include M_{H_2} estimates based on ^{12}CO $J = 1 \rightarrow 0$ and ^{12}CO $J = 2 \rightarrow 1$ data from the literature (Kuno et al. 2007; Helfer et al. 2003; Leroy et al. 2009) with appropriate corrections for the same distance and X_{CO} used in the present work.

Overall, the molecular gas mass M_{H_2} estimates derived using different values of R_{31} are consistent within each galaxy. These estimates for the warmer gas (based on ^{12}CO $J = 3 \rightarrow 2$ data) are typically lower than the M_{H_2} based on ^{12}CO $J = 1 \rightarrow 0$ which traces more diffuse and cooler gas. H_2 gas masses calculated using the global mean R_{31} value averaged across the disk of the galaxy (0.51 for NGC 2976 and 0.49 for NGC 3351) appear to be slightly higher compared with those obtained using other values of R_{31}. We conclude that our estimates of the warm and denser gas (based on ^{12}CO $J = 3 \rightarrow 2$ data) are fairly robust against various R_{31} values and also X_{CO} factors.

10.4.2.1 Molecular Gas Mass and SFRD

In this section we investigate how the ratio H_2-to-H_1 (which we denote as R_{mol}) varies as a function of the SFRD in two different environments, an H_1 rich dwarf

(NGC 2976) and an H_2 dominated galaxy (NGC 3351). We use the present ^{12}CO $J = 3\rightarrow2$ data to derive the molecular gas mass using a generic line ratio of $R_{31} = 0.6$. We include the same analysis, but with the molecular gas mass derived directly from the ^{12}CO $J = 1\rightarrow0$, corrected to the same beam size and distance. This allows us to systematically compare the difference between gas mass derived from ^{12}CO $J = 3\rightarrow2$, which traces denser and warmer molecular gas, and the gas traced by ^{12}CO $J = 1\rightarrow0$ which is thermalised at lower critical densities. We excluded the use of $X_{CO(3\rightarrow2)}$ for this analysis because the M_{H_2} distribution derived is very similar to the one calculated using the generic $R_{31} = 0.6$ value.

In Fig. 10.7, we show the relation of the surface density of H_2, surface density of total gas mass ($H_1 + H_2$), and the ratio of H_2-to-H_1 with SFRD. The upper panels show the relation with M_{H_2} derived from ^{12}CO $J = 3\rightarrow2$ data, while the lower panels plot the same quantities calculated from ^{12}CO $J = 1\rightarrow0$ data. Each point in these diagrams represents the corresponding quantity calculated within an area of 15.6×10^3 pc^2 for NGC 2976 and 108.9×10^3 pc^2 for NGC 3351, which corresponds to the pixel size of our ^{12}CO $J = 3\rightarrow2$ map. The surface densities of both molecular and atomic gas were calculated directly by dividing the gas mass estimated within that single pixel by the corresponding pixel area, taking into account the inclination of the respective galaxy. We found no correlation between the H_1 surface density and SFRD, hence we have not plotted it here, although we note that most pixels have Σ_{H_1} surface densities below $10\,M_\odot$ pc^{-2}, as seen in Schruba et al. (2011) and Leroy et al. (2008).

As is evident from the plots in Fig. 10.7a–d, the pixel points from each galaxy (blue for NGC 2976 and red for NGC 3351) follow different slopes when ^{12}CO $J =$

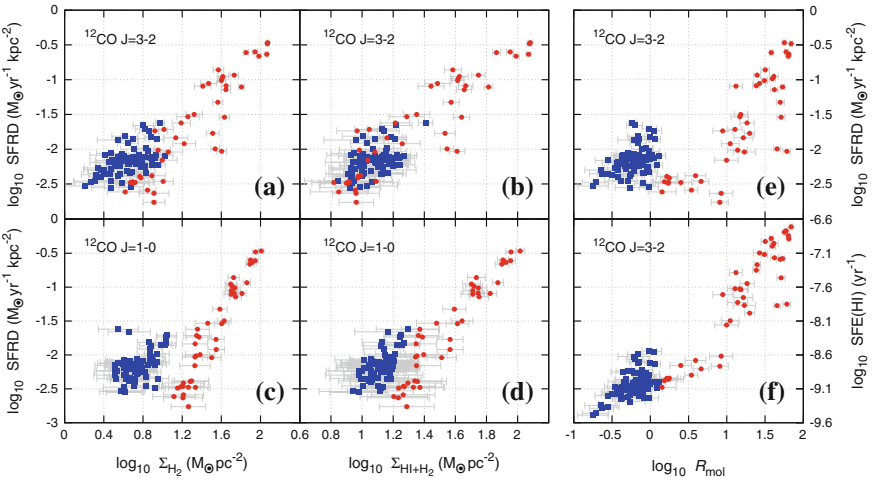

Fig. 10.7 Σ_{SFR} as a function of different gas phase: (*left*) H_2 only, (*centre*) $H_1 + H_2$ and (*right*) H_2-to-H_1 ratio. Each point in these diagrams represents a single pixel corresponding to the pixel size of our ^{12}CO $J = 3\rightarrow2$ map. Pixels from NGC 2976 are plotted with *blue square*, while regions from NGC 3351 in *red circle*

1→0 data are used, but have similar slopes if ^{12}CO *J = 3→2* data are used. Focusing on Fig. 10.7a, c, one sees that at higher H_2 mass surface densities, both upper and lower plots seem to point to the same rate of star formation, but at areas of lower surface density, the diffuse ^{12}CO *J = 1→0* emission appears to show lower rates of star formation compared to that from ^{12}CO *J = 3→2*. This is especially clear in the case of NGC 3351. This can be explained by the fact that this lower gas mass region of the diffuse ISM (traced by ^{12}CO *J = 1→0* line) might not be directly related to active star formation.

Figure 10.7e shows the relation between R_{mol} and SFRD. This plot clearly shows that NGC 2976 is mainly H_1 dominated, whereas NGC 3351 is dominated by H_2. Both galaxies appear to have a similar behaviour, where higher R_{mol} seems to be indicative of more active star formation activity, but this relation is less clearly defined in NGC 2976. This power law relation between R_{mol} and SFRD is not a surprising result given the Schmidt-Kennicutt relation that correlates the high concentration of H_2 with higher rate of star formation (this relation is also reflected in Fig. 10.7a, c). Nevertheless, one would naively expect that the higher the H_2-to-H_1 ratio, the higher the rate of star formation (i.e. a tight power law relation), but this is not the case. This potentially shows that the role of H_1 in star formation can not be completely ignored. In fact, as shown in Fig. 10.7f, higher values of R_{mol} do indeed correlate with higher star formation efficiency SFE(H_1) (SFR surface density per unit H_1 gas surface density), especially for NGC 3351. This seems to indicate that higher molecular gas fraction is due to the accretion of H_1 towards the local centre of gravity and thus increases the consumption of H_1. This assists the conversion of H_1 into molecular hydrogen with a faster rate, hence producing more H_2 gas to increase the rate of star formation.

However, this linear relationship between SFE(H_1) and R_{mol} is not seen with the SFE(H_2) (SFR surface density per unit H_2 gas surface density), nor with SFE(H_1 + H_2) (the SFR surface density per unit neutral gas surface density). It would thus be very informative if we could plot the relation of H_1, H_2 and SFRD concurrently to understand how the different species of gas affecting SFRD.

Another common feature one can see here is that both galaxies appear to follow two different power law slopes when Σ_{H_2} is plotted against SFRD ($n = 0.74 \pm 0.14$ for NGC 2976 and $n = 2.5 \pm 0.11$ for NGC 3351), compared to their relation of $\Sigma_{H_1+H_2}$ with SFRD ($n = 1.77 \pm 0.23$ for NGC 2976 and $n = 2.5 \pm 0.12$ for NGC 3351), which appears to have a similar power law index. This is especially distinct if Σ_{H_2} was derived from ^{12}CO *J = 1→0* data. The fact that the differences in the power law slopes between the two galaxies in the Σ_{H_2} and SFRD plot disappear when Σ_{H_1} is added, shows that, given the R_{mol} ratio alone we cannot predict the star formation rate. This implies that different surface densities are likely to have different star formation efficiencies and that other environmental effects may affect the way H_1 and H_2 relates to SFRD. As pointed out by Schruba et al. (2011), the Schmidt-Kennicutt relation was mostly plotted with the mean surface density averaging throughout the entire galaxy, hence smearing out the scale variance effect. The intriguing fact here is that even though the same kind of difference in the power law of Schmidt-Kennicutt relation is

seen in Schruba et al. (2011), it seems that in their plot,[12] the H_1 dominated galaxies have steeper correlation instead of the opposite seen here. However, we should note that Schruba et al. (2011) use a stacked average of a tilted ring of 15″ wide for the surface density calculation, whereas here we concentrate on pixel-by-pixel treatment. In addition, these authors estimate their Σ_{H_2} using ^{12}CO $J = 2\rightarrow1$ data combined with a certain aspect ratio, and hence comparison with our plots is not completely straightforward.

10.4.3 Correlation with PAH Emission

In both Figs. 10.1 and 10.2, the large structures traced by ^{12}CO $J = 3\rightarrow2$ appear to match those seen in the PAH 8 μm image. The two bright end regions of NGC 2976 can be seen in both wavebands. The ratio between the surface brightness of these bright end regions to the centre of the galaxy is larger in the PAH 8 μm image, and the weak inverse-S shape structure that was visible in the ^{12}CO $J = 3\rightarrow2$ map appears to show regions of stronger emission in the PAH 8 μm map as well. There is, however, a difference in the small scale structures among these images. One example is the small structure directly to the south of the northern bright end region in the ^{12}CO $J = 3\rightarrow2$ map which does not have a comparable counterpart in the PAH 8 μm image.

The emission from the central circumnuclear ring region of NGC 3351 dominates the brightness map in all three wavebands. The 2′ ring structure is clearly seen in the PAH 8 μm image. This ring structure is only partially detected in ^{12}CO $J = 3\rightarrow2$ map. We note that the areas that were detected here do not seem any brighter in the PAH 8 μm image. Also, the coverage of the PAH 8 μm emission is more extended than ^{12}CO $J = 3\rightarrow2$ in this galaxy, but the opposite is true for NGC 2976.

One might expect that ^{12}CO $J = 3\rightarrow2$, which is excited in the warm and dense molecular gas regions nearer to the star formation sites, would have a high spatial correlation with PAH emission, if the PAH emission is connected to star formation activity. Regan et al. (2006) studied the radial distribution of the 8 μm emission and the ^{12}CO $J = 1\rightarrow0$ emission for 11 disk galaxies and found a high spatial correlation between them. Bendo et al. (2010) compared the radial profiles of PAH 8 μm surface brightness to the ^{12}CO $J = 3\rightarrow2$ in NGC 2403 and found that the scale lengths in both cases are statistically identical. But their examination in sub-kpc scale regions within the galaxy reveals that ^{12}CO $J = 3\rightarrow2$ and PAH 8 μm surface brightness seemed to be uncorrelated. Here we investigate this correlation for NGC 2976 and NGC 3351 by comparing the radial profile of the ^{12}CO $J = 3\rightarrow2$ emission to the PAH 8 μm surface brightness.

Figure 10.8 shows the radial profile of both the PAH 8 μm and the ^{12}CO $J = 3\rightarrow2$ surface brightness for both NGC 2976 and NGC 3351. The general shapes appear to match in both galaxies, however on smaller spatial scales the profiles match less well. The scale lengths, defined as the radial distances where the intensity drops by

[12] Figures 8 and 9 in Schruba et al. (2011).

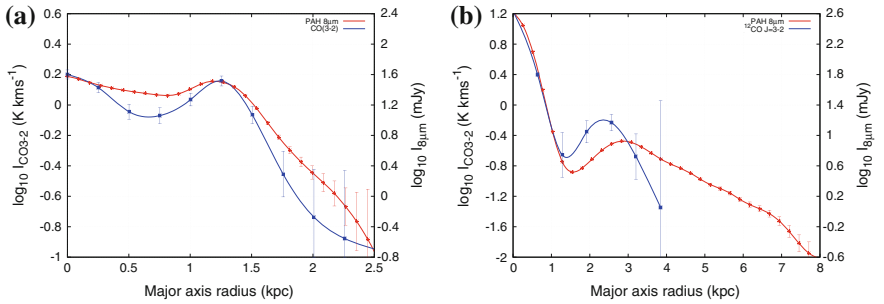

Fig. 10.8 Comparison of ^{12}CO $J = 3\rightarrow 2$ radial profile with that of *Spitzer* IRAC 8μm for both NGC 2976 and NGC 3351. ^{12}CO $J = 3\rightarrow 2$ intensity is in K km s^{-1} (*blue*, *left* axis) and PAH 8 μm is in mJy (*red*, *right* axis). All data were convolved with kernels that match the PSF of ^{12}CO $J = 3\rightarrow 2$ data. **a** NGC 2976. **b** NGC 3351

$1/e$ from the peak intensity, for NGC 2976 are 1.65 and 1.85 kpc for the ^{12}CO $J = 3\rightarrow 2$ and PAH 8 μm emission, respectively. These scale lengths are larger than the two bright end regions which correspond to the local maxima at ∼1.3 kpc away from the centre of the galaxy. Beyond ∼1.3 kpc, both emissions decay rapidly with almost the same rate. The ratio between the peak brightness of the two bright end regions with the galaxy centre, and the position of these bright end regions, are similar in both radial profiles. This might suggest that within high surface brightness regions, both components correlate better compared to lower brightness regions. Bendo et al. (2010) examined this relation in NGC 2403 at the sub-kpc scale, and found a similar trend. In their plot,[13] it appears that both indicators only overlapped in the area where ^{12}CO $J = 3\rightarrow 2$ intensity is higher than 1.0 K km s^{-1} and PAH 8 μm surface brightness is higher than 2.0 MJy sr^{-1}.

Within the central ∼1 kpc of NGC 3351, the two radial profiles follow each other closely. This is likely to be due to the resolution limit imposed by the HARP-B beam size (FWHM of ∼660 pc at a distance of 9.33 Mpc). The PSF for both data have been convolved to the same resolution and the galaxy centre contains a bright source that is unresolved at the resolution of 14.5″. Away from the central region, the two profiles do not trace each other well. Note that the ratio of the 2′ ring-to-nucleus intensity of the ^{12}CO $J = 3\rightarrow 2$ is higher than the PAH 8 μm profile. Outside the 2′ ring, the ^{12}CO $J = 3\rightarrow 2$ emission decays much faster than the PAH 8 μm,the latter extending almost twice as far as the ^{12}CO $J = 3\rightarrow 2$ profile. As we saw in NGC 2976, this might indicate that the correlation of the two components is better at higher brightness region in the galaxy. But again, the detection of ^{12}CO $J = 3\rightarrow 2$ at this region is too faint to reach a definite conclusion.

To further examine this relation, we compare both detections pixel by pixel and plot their correlation in Fig. 10.9, using only the pixels detected within our ^{12}CO $J = 3\rightarrow 2$ map. Again, the PAH 8 μm map is convolved and re-gridded to match the

[13] Figure 14 in Bendo et al. (2010).

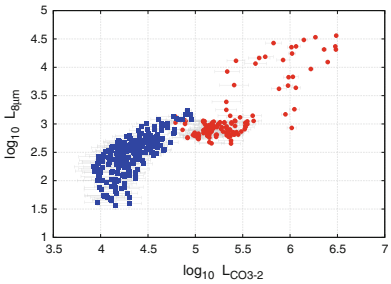

Fig. 10.9 Pixel-by-pixel comparison of the ^{12}CO $J = 3\rightarrow2$ luminosity with PAH 8 μm luminosity. Each *red circle* represent a pixel from NGC 3351, while each *blue square* corresponds to a single pixel in NGC 2976 map

resolution of our ^{12}CO $J = 3\rightarrow2$ map. Note that due to the difference in distance, each point within this plot corresponds to an area of 15.6×10^3 pc^2 for NGC 2976 and 108.9×10^3 pc^2 for NGC 3351. As with the radial profile comparison, this pixel-by-pixel approach seems to show that both kinds of emission are quite well correlated. However, there seems to be a larger scatter at higher surface brightness end of the plot, and the correlation seems to break down at $\log L_{CO3\rightarrow2} < 4.5$. This seems to agree with the argument from Bendo et al. (2010) that this correlation would break down at lower intensity or smaller spatial scales. It would be interesting to further examine this relation with a larger sample of galaxies to determine where this correlation begins to fail.

In order to determine whether this relationship only holds for these two galaxies, we examined all the SINGS galaxies within NGLS to see if NGC 2976 and NGC 3351 are typical of the entire sample. In Fig. 10.10, we plot the *total* ^{12}CO $J = 3\rightarrow2$ luminosity against the *total* PAH 8 μm luminosity for NGC 2976 and NGC 3351, together with 23 SINGS galaxies that have ^{12}CO $J = 3\rightarrow2$ detected. The luminosity values are tabulated in Table 10.4. The ^{12}CO $J = 3\rightarrow2$ maps of these 23 galaxies were obtained from the early release of the NGLS data set (Wilson et al. 2012). The PAH 8 μm maps were obtained from the same source as described in Sect. 10.2.1.

Clearly, the correlation of the two indicators is tight. There seems to be an approximately linear relation between the two, with $\log L_{8\,\mu m} \approx 0.74 \log I_{CO(3-2)} - 0.32$. The Pearson correlation coefficient is as high as 0.97, with both NGC 2976 and NGC 3351 lying close to the best fit line. To investigate whether this tight relation is not

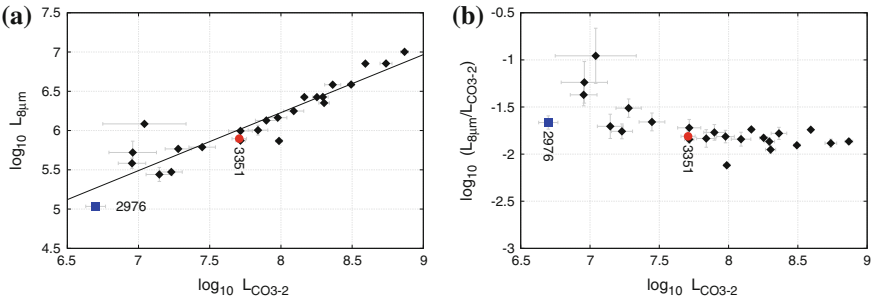

Fig. 10.10 Correlation of total integrated PAH 8μm luminosity and the total integrated ^{12}CO $J = 3\rightarrow2$ luminosity of the 25 SINGS galaxies in the NGLS samples

entirely dominated by the strong nuclear emission regions, we made a similar plot of the median luminosity instead of total luminosity, and found that the high correlation still holds.

Even though both ^{12}CO $J = 3 \rightarrow 2$ and PAH 8 μm are believed to be linked to star formation, their origins within the ISM and their fundamental excitation mechanisms are different. The 8 μm emission originates from PAHs found near the stars, in particular in the photospheres of AGB stars (Tielens 2008), while molecular CO is formed on the surface of interstellar dust grains. The surface brightness of PAH 8 μm emission is mostly proportional to the number of FUV photons and the number density of PAH molecules. The ^{12}CO $J = 3 \rightarrow 2$ intensity, on the other hand, is controlled mainly by the collision rate with the molecular hydrogen, the temperature of the gas and the density of molecular CO. It is thus important to understand why they correlate so well in a global environment.

One possible explanation is that there is a spatial co-existence of the PAH molecules and molecular CO in photo-dissociat.0ion regions (PDR), although not at specific sub-kpc locations within individual clouds. At the front of a PDR, the UV flux from hot stars or the interstellar radiation field excite the PAH molecules and heat the small grains in the ISM. This is responsible for the generation of intense irradiation from PAHs and the continuum dust emission in the mid-infrared. CO rotational transitions are generally believed to be generated from regions that reside deeper in the photo-dissociation regions (Hollenbach and Tielens 1999). In this region, the UV source is still strongly photo-dissociating species like OH and H_2O, but is weaker compared to the ionisation front, and thus molecular hydrogen and CO start to form in this region. Given a certain amount of UV photons, a higher density of PAHs would absorb a larger portion of these stellar fluxes, and reduce the photo-dissociation of CO molecules, hence resulting in a positive correlation of the two constituents. Also, both PAHs and molecular CO would not exist in high UV radiation region, as both species would be dissociated.

The same scenario can be applied to the star forming regions within the molecular clouds. If the ^{12}CO $J = 3 \rightarrow 2$ intensity indicates the amount of gas fuelling star formation in the core, it could be approximately proportional to the number of UV photons radiated by these newly born O and B stars. If a linear fraction of these photons is absorbed by the PAHs, their surface brightness will then be approximately proportional to the ^{12}CO $J = 3 \rightarrow 2$ intensity.

There are other alternative explanations in the literature, for example due to the molecular cloud formation triggered in regions with stellar potential wells (Leroy et al. 2008; Bendo et al. 2010), or due to the effects of cosmic rays from star formation (Bendo et al. 2008). Haas et al. (2002) and Bendo et al. (2008) also found an association between the PAH emission and the cold dust. If molecular gas is associated with cold dust, then the PAH and ^{12}CO $J = 3 \rightarrow 2$ would be expected to be associated with each other as well. In general, we believe that the ^{12}CO $J = 3 \rightarrow 2$ luminosity does correlate well with PAH 8 μm luminosity at larger scale, but this correlation might not hold for smaller sub-kpc scale.

Table 10.4 *Total* luminosity of PAH 8 μm and ^{12}CO $J = 3\rightarrow2$ of 25 SINGS galaxies within NGLS samples

Galaxy	Distance (Mpc)	$L_{PAH8\,\mu m}$ (MJy pc^2)	$L_{CO(3-2)}$ ($\times10^7$ K km s^{-1} pc^2)
NGC 0628	7.3	0.99 ± 0.07	5.2 ± 1.0
NGC 0925	9.1	0.38 ± 0.15	0.9 ± 0.2
NGC 2403	3.2	0.30 ± 0.04	1.7 ± 0.3
NGC 2841	14.1	1.22 ± 0.04	<1.1
NGC 2976	3.6	0.11 ± 0.03	0.50 ± 0.08
NGC 3031	3.6	0.53 ± 0.33	0.91 ± 0.35
NGC 3034	3.6	7.12 ± 0.01	39.2 ± 0.4
NGC 3049	22.7	0.26 ± 0.21	1.4 ± 0.3
NGC 3184	11.1	1.46 ± 0.04	9.5 ± 1.4
NGC 3198	13.7	1.01 ± 0.14	6.9 ± 1.1
NGC 3351	9.3	0.79 ± 0.06	5.1 ± 0.6
NGC 3521	7.9	2.53 ± 0.01	17.9 ± 1.2
NGC 3627	9.4	3.86 ± 0.01	31.1 ± 1.7
NGC 3938	14.7	1.65 ± 0.05	12.3 ± 2.0
NGC 4254	16.7	10.06 ± 0.02	73.8 ± 4.8
NGC 4321	16.7	7.14 ± 0.02	54.7 ± 5.3
NGC 4559	9.3	0.58 ± 0.08	1.9 ± 0.4
NGC 4569	16.7	2.25 ± 0.04	20.1 ± 1.7
NGC 4579	16.7	1.34 ± 0.07	7.9 ± 1.4
NGC 4631	7.7	2.67 ± 0.02	14.6 ± 0.7
NGC 4736	5.2	0.75 ± 0.05	5.2 ± 0.4
NGC 4826	7.5	0.74 ± 0.02	9.7 ± 0.5
NGC 5033	16.2	3.60 ± 0.07	23.1 ± 3.0
NGC 5055	7.9	2.75 ± 0.02	19.7 ± 1.7
UGC 05720	25.0	0.58 ± 0.04	2.8 ± 0.6

10.5 Summary

We have presented ^{12}CO $J = 3\rightarrow2$ maps of NGC 2976 and NGC 3351, observed using HARP-B on the JCMT. We compared our observations to the optical, ^{12}CO $J = 1\rightarrow0$, PAH 8 μm, H_1 and SFRD maps constructed using a combination of 24 μm and FUV data. ^{12}CO $J = 3\rightarrow2$ emission from NGC 2976 is strong at both ends of the galaxy major axis, whereas NGC 3351 is very bright in the nuclear region. NGC 2976 shows a large scale structure that is seen only in the ^{12}CO $J = 2\rightarrow1$ image, but not in other wavebands included in this chapter, due to the coarse resolution of the ^{12}CO $J = 3\rightarrow2$ and ^{12}CO $J = 1\rightarrow0$ maps. In contrast, the dominant circumnuclear region in NGC 3351 was visible in all waveband maps presented here. However, the prominent 2′ ring structure is only weakly detected in our ^{12}CO $J = 3\rightarrow2$ map.

We combined our ^{12}CO $J = 3\rightarrow2$ data with ^{12}CO $J = 1\rightarrow0$ data from various sources to probe the molecular gas mass using the ^{12}CO $J = 3\rightarrow2$ to ^{12}CO $J = 1\rightarrow0$ line ratio. The ratio values we obtained are within the range derived for various nearby galaxy surveys, but we find that the line ratios vary moderately within the galactic disk. We use the disc-averaged line ratio and a typical line ratio similar to the value derived for the Galactic and extragalactic GMCs to estimate the molecular gas masses using the standard CO(1→0)-to-H_2 conversion factor. Our results are about a factor of 2 smaller than the gas masses derived using direct ^{12}CO $J = 1\rightarrow0$ data. We argue that this is because we were tracing the molecular gas regions that are warmer, denser and closer to the sites of star formation, and this should give a better estimate of the actual gas masses that fuel star formation.

We have plotted the SFRD against surface density of H_2 mass and neutral hydrogen gas mass to compare the difference between the star formation law based on the more diffuse ISM region traced by the ^{12}CO $J = 1\rightarrow0$ emission and the denser and warmer region traced by the ^{12}CO $J = 3\rightarrow2$ data. The SFRD correlates better with the ^{12}CO $J = 3\rightarrow2$ emission, while the power law relation of Σ_{H_2} calculated from ^{12}CO $J = 1\rightarrow0$ with SFRD appears to be different between the two galaxies. We use the H_1 data from THINGS to derive the H_2-to-H_1 ratio and compare it with the SFE(H_1) and notice a power law relation between the two quantities.

We have also studied the correlation of the ^{12}CO $J = 3\rightarrow2$ surface brightness with the PAH 8 μm as both are prominent indicators linked to star formation activity. We first investigate their relation within NGC 2976 and NGC 3351 using both the radial distribution of the surface brightness and a pixel-per-pixel comparison. We find that they correlate well in the higher surface brightness regions. We further study the global correlation of the *total* luminosity of the two physical parameters using the data from all 25 SINGS galaxies within the NGLS and reached a similar conclusion. We suggest that this could be the result of the coexistence of both ^{12}CO and PAH molecules in the PDR regions, provided that the lifetime of both species are matched. In conclusion, we suggest that this correlation is high at large spatial scales, but at smaller sub-kpc scales, the correlation may break down.

References

Abazajian, K. N., Adelman-McCarthy, J. K., Agüeros, M. A., Allam, S. S., Allende Prieto, C., An, D., et al. (2009). The seventh data release of the sloan digital sky survey. *ApJS*, *182*, 543–558.

Albrecht, M., Chini, R., Krügel, E., Müller, S. A. H., & Lemke, R. (2004). Cold dust and molecular gas towards the centers of magellanic type galaxies and irregulars. I. The data. *A&A*, *414*, 141–153.

Alloin, D., & Nieto, J.-L. (1982). On the inner ring of HII regions in NGC 3351. *A&AS*, *50*, 491–504.

Appleton, P. N., Davies, R. D., & Stephenson, R. J. (1981). The neutral hydrogen content of the M81/M82 group of galaxies. I—The observations. *MNRAS*, *195*, 327–352.

Bell, T. A., Viti, S., & Williams, D. A. (2007). Molecular line intensities as measures of cloud masses—II. Conversion factors for specific galaxy types. *MNRAS*, *378*, 983–994.

Bendo, G. J., Dale, D. A., Draine, B. T., Engelbracht, C. W., et al. (2006). The spectral energy distribution of dust emission in the edge-on spiral galaxy NGC 4631 as seen with spitzer and the James Clerk Maxwell telescope. *ApJ*, *652*, 283–305.

Bendo, G. J., Draine, B. T., Engelbracht, C. W., et al. (2008). The relations among 8, 24 and 160 μm dust emission within nearby spiral galaxies. *MNRAS*, *389*, 629–650.

Bendo, G. J., Wilson, C. D., Warren, B. E., Brinks, E., et al. (2010). The JCMT nearby galaxies legacy survey—III. Comparisons of cold dust, polycyclic aromatic hydrocarbons, molecular gas and atomic gas in NGC 2403. *MNRAS*, *402*, 1409–1425.

Braine, J., Combes, F., Casoli, F., Dupraz, C., Gerin, M., Klein, U., et al. (1993). A CO(1–0) and CO(2–1) survey of nearby spiral galaxies. I—Data and observations. *A&AS*, *97*, 887–936.

Buckle, J. V., Hills, R. E., Smith, H., Dent, W. R. F., Bell, G., Curtis, E. I., et al. (2009). HARP/ACSIS: A submillimetre spectral imaging system on the James Clerk Maxwell telescope. *MNRAS*, *399*, 1026–1043.

Buta, R. J. (2013). Galaxy morphology. In *Planets, Stars and Stellar Systems* (pp. 1–89). New York: Springer.

Buta, R. J., Corwin, H. G., & Odewahn, S. C. (2007). *The de Vaucouleurs Altlas of Galaxies*. Cambridge: Cambridge University Press.

Buta, R., & Crocker, D. A. (1993). Metric characteristics of nuclear rings and related features in spiral galaxies. *AJ*, *105*, 1344–1357.

Calzetti, D., Kennicutt, R. C, Jr, Bianchi, L., Thilker, D. A., Dale, D. A., Engelbracht, C. W., et al. (2005). Star formation in NGC 5194 (M51a): The panchromatic view from GALEX to spitzer. *ApJ*, *633*, 871–893.

Calzetti, D., Kennicutt, R. C., Engelbracht, C. W., Leitherer, C., Draine, B. T., Kewley, L., et al. (2007). The calibration of mid-infrared star formation rate indicators. *ApJ*, *666*, 870–895.

Colina, L., Garcia Vargas, M. L., Mas-Hesse, J. M., Alberdi, A., & Krabbe, A. (1997). Nuclear spiral and ring star-forming structures and the starburst–active galactic nucleus connection in barred spirals NGC 3351 and NGC 4303. *ApJ*, *484*, L41+.

de Blok, W. J. G., Walter, F., Brinks, E., Trachternach, C., Oh, S., & Kennicutt, R. C. (2008). High-resolution rotation curves and galaxy mass models from THINGS. *AJ*, *136*, 2648–2719.

de Vaucouleurs, G., de Vaucouleurs, A., Corwin, H. G., Buta, R. J., Paturel, G., & Fouque, P. (1995). Third reference cat. of bright galaxies (RC3) (de Vaucouleurs + 1991). *VizieR Online Data Catalog*, *7155*, 0–+.

Elfhag, T., Booth, R. S., Hoeglund, B., Johansson, L. E. B., & Sandqvist, A. (1996). A CO survey of galaxies with the SEST and the 20-m Onsala telescope. *A&AS*, *115*, 439–468.

Elmegreen, D. M., Chromey, F. R., Santos, M., & Marshall, D. (1997). Near-infrared observations of circumnuclear star formation in NGC 3351, NGC 3504, and NGC 5248. *AJ*, *114*, 1850–+.

Foyle, K., Wilson, C. D., Mentuch, E., Bendo, G., Dariush, A., et al. (2012). The dust and gas properties of M83. ArXiv e-prints.

Freedman, W. L., Madore, B. F., Gibson, B. K., et al. (2001). Final results from the hubble space telescope key project to measure the hubble constant. *ApJ*, *553*, 47–72.

Frei, Z., Guhathakurta, P., Gunn, J. E., & Tyson, J. A. (1996). A catalog of digital images of 113 nearby galaxies. *AJ*, *111*, 174–+.

Gordon, K. D., Engelbracht, C. W., Rieke, G. H., Misselt, K. A., Smith, J.-D. T., & Kennicutt, R. C, Jr. (2008). The behavior of the aromatic features in M101 H II regions: Evidence for dust processing. *ApJ*, *682*, 336–354.

Greve, T. R., Bertoldi, F., Smail, I., Neri, R., Chapman, S. C., Blain, A. W., et al. (2005). An interferometric CO survey of luminous submillimetre galaxies. *MNRAS*, *359*, 1165–1183.

Haas, M., Klaas, U., & Bianchi, S. (2002). The relation of PAH strength with cold dust in galaxies. *A&A*, *385*, L23–L26.

Hägele, G. F., Díaz, Á. I., Cardaci, M. V., Terlevich, E., & Terlevich, R. (2007). Kinematics of gas and stars in the circumnuclear star-forming ring of NGC3351. *MNRAS*, *378*, 163–178.

Helfer, T. T., Thornley, M. D., Regan, M. W., Wong, T., Sheth, K., Vogel, S. N., et al. (2003). The BIMA Survey of Nearby Galaxies (BIMA SONG). II. The CO data. *ApJS*, *145*, 259–327.

Helou, G., Roussel, H., Appleton, P., Frayer, D., Stolovy, S., Storrie-Lombardi, L., et al. (2004). The anatomy of star formation in NGC 300. *ApJS*, *154*, 253–258.

Hollenbach, D. J., & Tielens, A. G. G. M. (1999). Photodissociation regions in the interstellar medium of galaxies. *Reviews of Modern Physics*, *71*, 173–230.

Iono, D., Wilson, C. D., Yun, M. S., Baker, A. J., Petitpas, G. R., Peck, A. B., et al. (2009). Luminous infrared galaxies with the submillimeter array. II. Comparing the CO (3–2) sizes and luminosities of local and high-redshift luminous infrared galaxies. *ApJ*, *695*, 1537–1549.

Irwin, J. A., Wilson, C. D., Wiegert, T., Bendo, G. J., Warren, B. E., Wang, Q. D., et al. (2011). The JCMT nearby galaxies legacy survey—V. The CO(J = 3–2) distribution and molecular outflow in NGC 4631. *MNRAS*, *410*, 1423–1440.

Israel, F. (2000). Extragalactic H_2 and its variable relation to CO. In F. Combes & G. Pineau Des Forets (Eds.) *Molecular Hydrogen in Space* (p. 293).

Israel, F. P. (2008). Molecular gas in spiral galaxy centers. In C. Kramer, S. Aalto & R. Simon (Eds.), *EAS Publications Series* (Vol. 31, pp. 89–92).

Israel, F. P. (2005). Molecular gas in compact galaxies. *A&A*, *438*, 855–866.

Jenness, T., Berry, D. S., Cavanagh, B., Currie, M. J., Draper, P. W., & Economou, F. (2009). Developments in the starlink software collection. In *Astronomical Society of the Pacific Conference Series* (Vol. 411, pp. 418–+).

Karachentsev, I. D., Dolphin, A. E., Geisler, D., Grebel, E. K., Guhathakurta, P., Hodge, P. W., et al. (2002). The M 81 group of galaxies: New distances, kinematics and structure. *A&A*, *383*, 125–136.

Kennicutt, R. C, Jr, Armus, L., Bendo, G., Calzetti, D., Dale, D. A., Draine, B. T., et al. (2003). SINGS: The SIRTF nearby galaxies survey. *PASP*, *115*, 928–952.

Kennicutt, R. C., Hao, C., Calzetti, D., Moustakas, J., Dale, D. A., Bendo, G., et al. (2009). Dust-corrected star formation rates of galaxies. I. Combinations of Hα and infrared tracers. *ApJ*, *703*, 1672–1695.

Krist, J. (2002). *Tiny Tim*. SSC, Pasadena: SIRTF User's Guide.

Kuno, N., Sato, N., Nakanishi, H., Hirota, A., Tosaki, T., Shioya, Y., et al. (2007). Nobeyama CO Atlas of nearby spiral galaxies: Distribution of molecular gas in barred and nonbarred spiral galaxies. *Publications of the Astronomical Society of Japan*, *59*, 117–166.

Laine, S. (2011). IRAC instrument handbook. http://irsa.ipac.caltech.edu/data/SPITZER/docs/irac/iracinstrumenthandbook/.

Leroy, A. K., Walter, F., Bigiel, F., Usero, A., Weiss, A., Brinks, E., et al. (2009). Heracles: The HERA CO line extragalactic survey. *AJ*, *137*, 4670–4696.

Leroy, A. K., Walter, F., Brinks, E., Bigiel, F., de Blok, W. J. G., Madore, B., et al. (2008). The star formation efficiency in nearby galaxies: Measuring where gas forms stars effectively. *Astronomical Journal*, *136*, 2782–2845.

Mauersberger, R., Henkel, C., Walsh, W., & Schulz, A. (1999). Dense gas in nearby galaxies. XII. A survey for CO J = 3–2 emission. *A&A*, *341*, 256–263.

Meier, D. S., Turner, J. L., Crosthwaite, L. P., & Beck, S. C. (2001). Warm molecular gas in Dwarf starburst galaxies: CO(3–2) observations. *AJ*, *121*, 740–752.

Prescott, M. K. M., Kennicutt, R. C, Jr, Bendo, G. J., et al. (2007). The incidence of highly obscured star-forming regions in SINGS galaxies. *ApJ*, *668*, 182–202.

Reach, W. T., Megeath, S. T., Cohen, M., Hora, J., Carey, S., Surace, J., et al. (2005). Absolute calibration of the infrared array camera on the spitzer space telescope. *PASP*, *117*, 978–990.

Regan, M. W., Thornley, M. D., Helfer, T. T., Sheth, K., Wong, T., Vogel, S. N., et al. (2001). The BIMA survey of nearby galaxies. I. The radial distribution of CO emission in spiral galaxies. *ApJ*, *561*, 218–237.

Regan, M. W., Thornley, M. D., Vogel, S. N., Sheth, K., Draine, B. T., Hollenbach, D. J., et al. (2006). The radial distribution of the interstellar medium in disk galaxies: Evidence for secular evolution. *ApJ*, *652*, 1112–1121.

Robson, I. & Holland, W. (2007). SCUBA-2: The submillimeter mapping machine. In *From Z-Machines to ALMA: (Sub)Millimeter Spectroscopy of Galaxies, Astronomical Society of the Pacific Conference Series* (Vol. 375, pp. 275–+).

Sage, L. J. (1993). Molecular gas in nearby galaxies. II—The data. *A&AS*, *100*, 537–569.

Sakamoto, K., Okumura, S. K., Ishizuki, S., & Scoville, N. Z. (1999). CO images of the central regions of 20 nearby spiral galaxies. *ApJS*, *124*, 403–437.

Sánchez-Gallego, J. R., Knapen, J. H., Heiner, J. S., et al. (2011). The JCMT nearby galaxies legacy survey. VI. The distribution of gas and star formation in M 81. *A&A*, *527*, A16.

Schruba, A., Leroy, A. K., Walter, F., Bigiel, F., Brinks, E., et al. (2011). A molecular star formation law in the atomic-gas-dominated regime in nearby galaxies. *AJ*, *142*, 37–+.

Simon, J. D., Bolatto, A. D., Leroy, A., & Blitz, L. (2003). High-resolution measurements of the dark matter halo of NGC 2976: Evidence for a shallow density profile. *ApJ*, *596*, 957–981.

Smith, H., Hills, R. E., Withington, S., Richer, J., Leech, J., Williamson, R., et al. (2003). HARP-B: A 350-GHz 16-element focal plane array for the James Clerk Maxwell telescope. In *Society of Photo-Optical Instrumentation Engineers (SPIE) Conference Series* (Vol. 4855, pp. 338–348).

Smith, J. D. T., Draine, B. T., Dale, D. A., Moustakas, J., Kennicutt, R. C, Jr, Helou, G., et al. (2007). The mid-infrared spectrum of star-forming galaxies: Global properties of polycyclic aromatic hydrocarbon emission. *ApJ*, *656*, 770–791.

Strong, A. W., Bloemen, J. B. G. M., Dame, T. M., Grenier, I. A., Hermsen, W., Lebrun, F., et al. (1988). The radial distribution of galactic gamma rays. IV—The whole galaxy. *A&A*, *207*, 1–15.

Swartz, D. A., Yukita, M., Tennant, A. F., Soria, R., & Ghosh, K. K. (2006). Chandra observations of circumnuclear star formation in NGC 3351. *Astrophysical Journal*, *647*, 1030–1039.

Thornley, M. D., & Wilson, C. D. (1994). Constraining the influence of star formation on the lowest (12)CO line ratios in M33. *ApJ*, *421*, 458–474.

Tielens, A. G. G. M. (2008). Interstellar polycyclic aromatic hydrocarbon molecules. ARA&A *46*, 289–337.

Walter, F., Brinks, E., de Blok, W. J. G., Bigiel, F., Kennicutt, R. C., Thornley, M. D., et al. (2008). Things: The H I nearby galaxy survey. *Astronomical Journal*, *136*, 2563–2647.

Warren, B. E., Wilson, C. D., Israel, F. P., Serjeant, S., Bendo, G. J., Brinks, E., et al. (2010). The James Clerk Maxwell telescope nearby galaxies legacy survey. II. Warm molecular gas and star formation in three field spiral galaxies. *ApJ*, *714*, 571–588.

Williams, B. F., Dalcanton, J. J., Stilp, A., Gilbert, K. M., Roškar, R., Seth, A. C., et al. (2010). The advanced camera for surveys nearby galaxy survey treasury. IV. The star formation history of NGC 2976. *ApJ*, *709*, 135–148.

Wilson, C. D., Walker, C. E., & Thornley, M. D. (1997). The density and temperature of molecular clouds in M33. *ApJ*, *483*, 210–+.

Wilson, C. D., Warren, B. E., Israel, F. P., Serjeant, S., Attewell, D., Bendo, G. J., et al. (2012). The JCMT nearby galaxies legacy survey—VIII. CO data and the $L_{CO(3-2)}$ correlation in the SINGS sample. *Monthly Notices of the Royal Astronomical Society*, *424*, 3050–3080.

Wilson, C. D., Warren, B. E., Israel, F. P., Serjeant, S., Bendo, G., Brinks, E., et al. (2009). The James Clerk Maxwell telescope nearby galaxies legacy survey. I. Star-forming molecular gas in virgo cluster spiral galaxies. *ApJ*, *693*, 1736–1748.

Young, J. S., Xie, S., Tacconi, L., Knezek, P., Viscuso, P., et al. (1995). The FCRAO extragalactic CO survey. I. The data. *ApJS*, *98*, 219–+.

Yun, M. S. (1999). Tidal interactions in M81 group. In J. E. Barnes & D. B. Sanders (Eds.), *Galaxy interactions at low and high redshift*, *IAU Symposium* (Vol. 186, pp. 81–+).

Zhu, Y.-N., Wu, H., Cao, C., & Li, H.-N. (2008). Correlations between mid-infrared, far-infrared, Hα, and FUV luminosities for spitzer SWIRE field galaxies. *ApJ*, *686*, 155–171.

Chapter 11
Concluding Remarks

The work described in this thesis has covered several areas of heterodyne receiver developments based on the SIS mixer technology, near the niobium superconducting gap frequency. Even though SIS technologies have now matured and used routinely at low frequencies, applications at high frequencies are still challenging due to the rapid increase in losses and the small size of mechanical components. Nevertheless, as shown in this thesis, high performance SIS receivers with advanced capabilities are feasible with careful design and the rapid improvement of device fabrication and machining technologies. Here, I will briefly describe some of the key contributions achieved in this thesis.

A high performance smooth-walled horn that has similar performance to the conventional corrugated horn, and yet is easy to fabricate, has been successfully designed and experimentally tested from 600–740 GHz range. We have fabricated several prototypes via direct milling using a standard CNC milling machine, and the beam patterns measured for these prototypes agree well with the predicted good performance despite the stringent machining requirements for high frequency operation at 700 GHz.

The efficient coupling of the output signal from the feed horn, travelling in a rectangular waveguide, to an SIS tunnel junction is essential for a high performance SIS mixer. Instead of the commonly used waveguide probes, in our new designs we utilised a unilateral finline taper to transform the waveguide mode to microstrip mode, with transition through slotline or CPWs. These designs yield broadband operation, an easy-to-fabricate mixer block and a large substrate area for integrating advanced mixer circuits. For a tuning circuit, we employed two inductive microstrip stubs fabricated alongside the SIS junction to tune out the junction capacitance over a relatively broad bandwidth. The entire structure has been simulated rigorously using HFSS and SuperMix, and since the mixer chip does not need any mechanical tuners, only a straight waveguide mixer block is required. We have fabricated and tested these new mixer designs on both a 60 μm quartz and a novel 15 μm SOI substrates. The extensive experimental investigations have show encouraging wide band performance with a best noise temperature of 143 K. The overall performance

B.-K. Tan, *Development of Coherent Detector Technologies for Sub-Millimetre Wave Astronomy Observations*, Springer Theses, DOI 10.1007/978-3-319-19363-2_11

was compromised though, due to an error in junction size and offsets in junction position during fabrication.

An upgrade from the single junction SIS mixer to a balanced SIS mixer that is capable of rejecting additional noise from the LO is also presented. The devices were fabricated using the same planar circuit technology as the single ended design, on a 15 μm SOI substrate. The unique feature of this new design is the back-to-back finline structure that allows the RF and the LO to be coupled separately into the mixer chip, hence eliminating the need for a beam combiner. Preliminary test results show performance inferior to current state-of-the-art balanced SIS mixer, but from rigorous analysis, we demonstrated that the performance would improve substantially if the junctions are well aligned and identical. Nonetheless, we managed to measure acceptable performance with the best DSB noise temperature around 700 K and have demonstrated that the additional planar RF hybrid and the DC/IF block work well.

We have also designed single sideband SIS mixers using the same planar circuit technology. All the required circuit components were fully integrated on a 15 μm SOI substrate chip to ensure only a simple mixer block would be required. By exporting the S-parameters of these individual circuit components simulated by HFSS into SuperMix to form a complete mixer model, we have shown that they exhibit good performance in sensitivity and noise rejection ratio.

An essential component of the SIS receiver assembly is the local oscillator source. As an alternative to conventional multiplied sources, we worked on the generation of sub-mm signal by beating of two commercially available infrared lasers. We have successfully demonstrated that the method is feasible, especially around 100–200 GHz, and have successfully used it to pump a 230 GHz SIS mixer. Using a PID controller, we have also managed to frequency-lock the lasers to ensure stable operation of the photonic LO system.

In Chap. 8, we have investigated the heating effect of tunnel junction by the LO power and have presented a method to retrieve the electron-phonon interaction time by extending the impedance recovery procedure. The recovered value of the electron-phonon interaction time from our Nb-based SIS device was found to be consistent within the range measured by other groups for different thickness of niobium.

The final chapter of this thesis presents observations of ^{12}CO $J = 3 \rightarrow 2$ from NGC 2976 and NGC 3351 using HARP-B, the 16-pixel SIS array receiver on the JCMT. The obtained 350 GHz data was combined with the ^{12}CO $J = 1 \rightarrow 0$ data from the literature to derive ^{12}CO line ratios, and we have found that the line ratios lie between 0.3–0.8, a similar range to that seen in other field galaxies from the NGLS survey. Using a generic line ratio of 0.6, a typical line ratio for Galactic and extra-galactic GMC, we estimated a total dense molecular gas mass of $2.7 \times 10^7\,M_\odot$ and $2.72 \times 10^8\,M_\odot$ for NGC 2976 and NGC 3351, respectively. Using these data, we also investigated the correlation between H_1 and H_2 with star formation rate density (SFRD), and we found that the correlation between the total gas mass ($H_1 + H_2$) is better with SFRD compared to H_2 gas mass alone. The most interesting result generated from this project is the discovery of a very tight correlation between the ^{12}CO $J = 3 \rightarrow 2$ intensity with the PAH 8 μm surface brightness, in particular in the high surface brightness regions. We extended this study to include another

23 galaxies within the NGLS sample, and found that the same tight relation held even at large spatial scales. We believe that this is most likely due to both PAH 8 μm and ^{12}CO $J = 3 \rightarrow 2$ emission are originating from the proximate site of active star formation.

These observations at 350 GHz are important as they probe the denser and warmer regions of the molecular clouds within the galactic disks that are more directly involved in star formation activity. Combining this with higher-J data e.g., ^{12}CO $J = 6 \rightarrow 5$ near 650 GHz, would therefore allow further constraints to be placed on star formation models, in particular the chemistries and dynamics of their formation.

11.1 Toward Multi-pixel Focal Plane Array Receivers

Heterodyne detectors are already approaching quantum-limited sensitivity in the sub-mm regime. Further improvement in single dish telescope's mapping speed must therefore come from the deployment of multi-pixel focal plane arrays, integrating a large number of SIS mixers into a single receiver unit. Such a closely packed instrument like HARP-B, not only helps to reduce integration time for a specific sensitivity, but allows sensible observation for objects significantly larger than the telescope beam size e.g., spectroscopic mapping of the Galactic plane with high spatial and spectral resolution.

All the developments reported in this thesis regarding the sub-mm heterodyne instrumentation will enable the construction of compact and yet high performance focal plane SIS mixer arrays at high frequency. The development and rigorous tests of the 700 GHz smooth-walled horn and the good performance of the 230 GHz smooth-walled horn array demonstrated by Leech et al. (2010) hold a very strong promise for deployment of tens or even hundreds of feed horns at a reasonable cost and manufacturing time. The SOI and planar circuit technology used in this thesis reduce the complexity of mixer blocks extensively, in particular if a more sophisticated SIS mixer design is to be used, since all the required circuit components are integrated on-chip.

The unique feature of finline SIS mixers i.e., that the mixer chip is oriented along the axis of wave propagation, allows great flexibility in the design of the array assembly, especially the elegant back-to-back architecture for LO injection. This particular arrangement allows the elimination of the need for beam splitters and helps to reduce the LO power requirements by a factor of ten or more. In conjunction with developments such as compact and flexible photonic LO sources, this could help make heterodyne focal plane arrays at sub-mm interferometers a reality. The laser unit for photonic LO could be placed centrally remote from the individual receivers, while only the miniature photomixer and biasing electronics are integrated into the receiver. Distribution of optical power from lasers can be easily done using low-loss fibre optic technology.

High frequency heterodyne arrays are becoming increasingly attractive and are being actively pursued by many leaders in this field. There are already technology demonstrators being built such as SuperCam (Groppi et al. 2010) or planned KAPPa (the Kilopixel Array Pathfinder Project, Groppi et al. 2011), aiming to develop technologies suitable for constructing a thousand pixel heterodyne array. KAPPa, which operate in the 650 GHz band has already adopted a variant of the high performance smooth-walled horn presented in this thesis. We are thus very optimistic that the technology development presented in this thesis will be useful for future sub-mm instrumentation and will enable us to further probe into the largely unexplored regions of the sub-mm universe.

References

Groppi, C. E., Walker, C., Kulesa, C., Golish, D., et al. (2010). Supercam: A 64-pixel array receiver for the 870 micron atmospheric window. *Bulletin of the American Astronomical Society*, *36*, 604.

Groppi, C., Wheeler, C., Mani, H., Weinreb, S., Russell, D., Kooi, J., et al. (2011). The Kilopixel Array Pathfinder Project (KAPPa): A 16 pixel 660 GHz pathfinder instrument with an integrated heterodyne focal plane detector. In *Twenty-Second International Symposium on Space Terahertz Technology*.

Leech, J., Tan, B. K., Yassin, G., Kittara, P., Jiralucksanawong, A., & Wangsuya, S. (2010). Measured performance of a 230 GHz prototype focal-plane feedhorn array made by direct drilling of smooth-walled horns. In *Twenty-First International Symposium on Space Terahertz Technology* (pp. 114–119).

Appendix A
Ancillary Data of Individual Tested Device

A.1 Influence of Various Experimental Parameters on the Mixer Test Results

It is well known that the noise temperature measured at a certain bias point depends on several environment factors e.g., the physical temperature of the mixer chip, the LO pumping level, the strength of the magnetic field, and the influence of the first-stage cryogenic amplifier noise performance. We thus performed an experimental test to measure the effects of these parameters on the Y-factor measurement, as shown in Fig. A.1. The relation between the mixer noise temperature with the physical temperature appears to follow a quartic power law trend. Cooling the device from 4.5 to 3 K can easily halve the noise temperature measured, and this cooling effect has the most profound influence in scale compared to the LO pumping level and the effect of the amplifier. For the amplifier, we measured the optimum operating current to be around 25 mA at 4.2 K, agreeing well with the test data from the manufacturer, which was tested at 11 K physical temperature. The LO pumping level at the first photon step gave the best noise temperature was found to be around a fifth to a quarter of the critical current level. All these measurements, and those presented in the main text, were done with the magnetic current applied around the second Josephson minima.

A.2 Supporting Data from Single-Ended Mixer Tests

See Figs. A.2, A.3, A.4 and A.5; Tables A.1, A.2, A.3, A.4, A.5, A.6, A.7 and A.8.

B.-K. Tan, *Development of Coherent Detector Technologies for Sub-Millimetre Wave Astronomy Observations*, Springer Theses, DOI 10.1007/978-3-319-19363-2

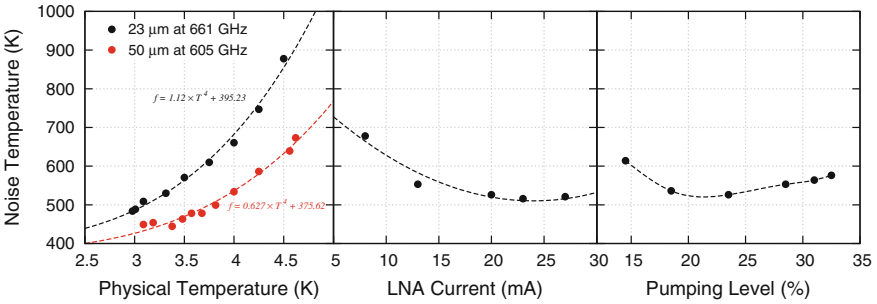

Fig. A.1 All the data were taken using the quartz device F74 A-D4N1. **a** The effect of temperature influencing the measured noise temperature at a constant LO pumping level. **b** The effect of current drawn by the cryogenic amplifier influencing the noise temperature performance, at 661 GHz with a 23 μm beam splitter at a constant LO pumping level. **c** The effect of LO pumping level, at 661 GHz with 23 μm beam splitter

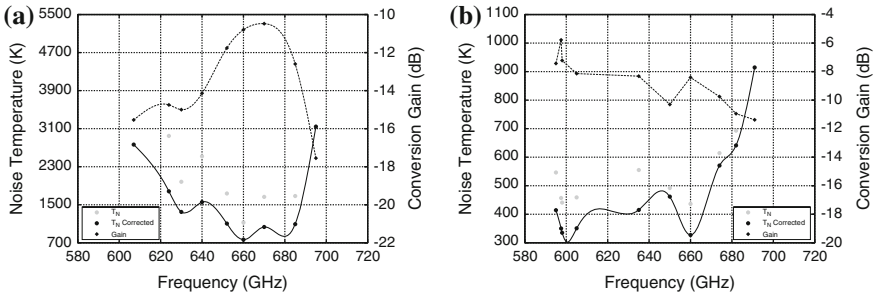

Fig. A.2 Measured noise temperature and DSB conversion gain of F74 A-D7N1 and F74 A-D4N1 across the operating RF bandwidth. The *grey points* corresponding to the uncorrected noise measurement. **a** F74 A-D7N1. **b** F74 A-D4N1

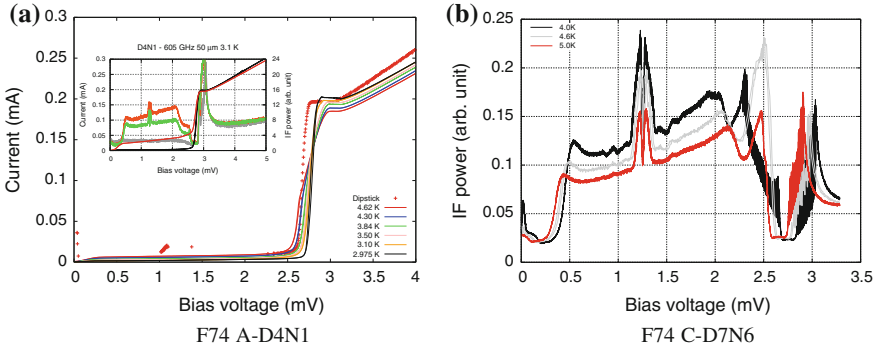

Fig. A.3 **a** Slope change near the gap of the IV curve of F74 A-D4N1, which become less prominent when the device was colder. **b** The effect of the instability was only observed when the device was colder

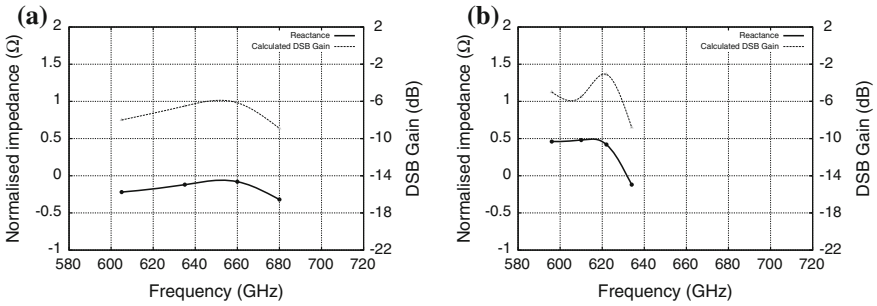

Fig. A.4 Impedance recovered for FSOI C-D2N1 and FSOI C-C2N8. **a** FSOI C-C2N8. **b** FSOI C-D2N2

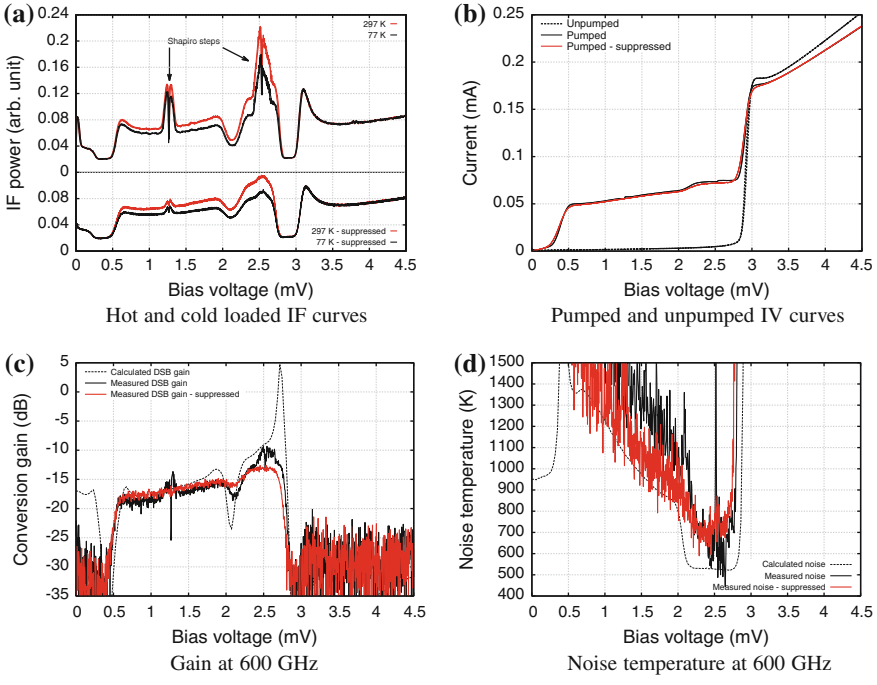

Fig. A.5 **a**, **b** IV and IF response of FSOI C-D2N1 at 600 GHz showing the effect of higher magnetic field strength to suppress the Josephson features. The mixer was pumped at $\alpha_1 = 0.548$. **c**, **d** Comparison with SuperMix model computed from the recovered impedance

Table A.1 Results of mixer tests carried out on 2011-01-17 for F74 A-D7N1

$T = 3.5\,\text{K}$, $R_N = 17.90\,\Omega$, $f_{Fiske} = 532\,\text{GHz}$

f_{LO} (GHz)	T_N (K)	G_R (dB)	d_{bs} (μm)	$T_{N(c)}$ (K)	$G_{R(c)}$ (dB)
607	5588	−25.3	57	2765	−15.5
624	2948	−22.3	57	1783	−14.7
630	1983	−20.9	57	1349	−15.0
640	2519	−21.3	57	1556	−14.1
652	1738	−18.3	57	1103	−11.7
660	1126	−16.0	57	765	−10.8
670	1666	−17.2	57	1032	−10.4
685	1683	−18.8	57	1091	−12.6
695	6083	−26.5	57	3143	−17.5

Table A.2 Results of mixer tests carried out on 2011-02-18 for F74 A-D4N1

$T = 3.0\,\text{K}$, $R_N = 17.90\,\Omega$, $f_{Fiske} = 556\,\text{GHz}$

f_{LO} (GHz)	T_N (K)	G_R (dB)	d_{bs} (μm)	$T_{N(c)}$ (K)	$G_{R(c)}$ (dB)
595	546	−11.0	50	414	−7.4
597	456	−9.1	50	350	−5.8
598	440	−10.2	50	335	−7.2
605	459	−11.1	50	350	−8.1
635	555	−11.8	50	415	−8.3
650	491	−13.1	19	461	−10.3
660	436	−11.2	50	327	−8.4
674	614	−13.2	19	570	−9.7
682	693	−14.5	19	641	−10.9
691	1395	−17.2	57	914	−11.3

Table A.3 Results of mixer tests carried out on 2011-04-18 for mixer F74 C-D7N6

$T = 3.0\,\text{K}$, $R_N = 18.18\,\Omega$, $f_{Fiske} = 551\,\text{GHz}$

f_{LO} (GHz)	T_N (K)	G_R (dB)	d_{bs} (μm)	$T_{N(c)}$ (K)	$G_{R(c)}$ (dB)
594	400	−12.1	50	313	−9.7
605	356	−11.2	50	275	−9.0
610	350	−12.7	19	332	−10.9
615	430	−12.7	23	397	−10.3
623	443	−13.3	23	409	−10.9
625	432	−12.7	19	408	−10.2
635	390	−13.3	19	369	−11.3
642	383	−13.2	19	362	−11.3

(continued)

Table A.3 (continued)

$T = 3.0\,\text{K}$, $R_N = 18.18\,\Omega$, $f_{Fiske} = 551\,\text{GHz}$					
650	365	−12.8	19	345	−11.0
661	369	−12.8	19	348	−10.9
670	426	−13.9	19	401	−11.9
673	473	−13.7	19	444	−11.3
682	562	−15.1	19	528	−12.5
691	685	−15.8	19	641	−12.8
702	1070	−18.5	19	996	−14.7
Measured on actual first step					
595	311	−4	75	216	−5.8
596	281	−5.9	75	193	−4.0
599	221	−6.7	75	150	−5.1
600	210	−6.5	75	143	−4.9

Table A.4 Results of mixer tests carried out on 2011-04-14 for FSOI C-D2N8

$T = 3.65\,\text{K}$, $R_N = 19.22\,\Omega$					
f_{LO} (GHz)	T_N (K)	G_R (dB)	d_{bs} (μm)	$T_{N(c)}$ (K)	$G_{R(c)}$ (dB)
600	729	−15.0	50	559	−11.3
605	609	−14.1	50	471	−10.8
610	520	−13.1	50	402	−10.1
615	621	−13.6	50	473	−10.1
620	588	−14.0	50	452	−10.8
630	528	−13.9	50	409	−11.1
640	515	−13.9	50	399	−11.2
650	515	−14.1	50	399	−11.5
660	470	−13.7	50	363	−11.2
670	469	−13.8	50	363	−11.4
680	539	−14.6	50	416	−12.0
691	645	−15.4	50	494	−12.3
702	741	−15.7	50	557	−12.2
724	1809	−21.1	50	1308	−16.1
642	749	−17.3	19	711	−14.6
650	484	−14.4	19	457	−12.0
660	399	−13.4	19	376	−11.4
673	455	−14.5	19	429	−12.5
680	670	−16.2	19	631	−13.4

Table A.5 Results of mixer tests carried out on 2011-05-26 for FSOI C-C2N7

$T = 3.77\,\text{K}$, $R_N = 16.70\,\Omega$

f_{LO} (GHz)	T_N (K)	G_R (dB)	d_{bs} (μm)	$T_{N(c)}$ (K)	$G_{R(c)}$ (dB)
595	464	−13.4	75	342	−10.9
600	517	−13.1	75	375	−10.1
630	685	−14.8	75	496	−11.2
660	799	−16.3	75	588	−12.6
690	1132	−17.3	75	800	−12.6
710	1766	−19.4	75	1177	−13.3

Table A.6 Results of mixer tests carried out on 2011-06-02 for FSOI C-C2N8

$T = 3.3\,\text{K}$, $R_N = 20.49\,\Omega$

f_{LO} (GHz)	T_N (K)	G_R (dB)	d_{bs} (μm)	$T_{N(c)}$ (K)	$G_{R(c)}$ (dB)
605	4226	−24.8	75	2413	−16.9
635	2456	−21.4	75	1511	−14.5
660	1999	−20.1	75	1272	−13.6
680	3097	−22.4	75	1808	−14.7

Table A.7 Results of mixer tests carried out on 2011-06-14 for FSOI C-D2N1

$T = 3.6\,\text{K}$, $R_N = 20.67\,\Omega$

f_{LO} (GHz)	T_N (K)	G_R (dB)	d_{bs} (μm)	$T_{N(c)}$ (K)	$G_{R(c)}$ (dB)
596	789	−14.6	75	602	−10.4
600	750	−15.3	75	557	−11.6
605	738	−14.5	75	567	−10.6
620	640	−14.1	75	493	−10.6
633	611	−14.4	36	531	−11.3
642	638	−15.0	36	556	−11.8
650	585	−14.6	19	557	−11.7
660	544	−14.5	19	518	−11.8
670	547	−14.4	19	520	−11.7
680	626	−15.3	19	594	−12.4
690	741	−15.7	19	703	−12.2
700	958	−16.7	19	907	−12.5
Measured on actual first step					
596	642	−13.0	75	451	−9.2
600	575	−11.0	75	399	−7.2
605	563	−12.3	75	398	−8.8

Table A.8 Results of mixer tests carried out on 2011-06-21 for FSOI F-D2N2

$T = 3.5\,\mathrm{K}$, $R_N = 22.37\,\Omega$

f_{LO} (GHz)	T_N (K)	G_R (dB)	d_{bs} (μm)	$T_{N(c)}$ (K)	$G_{R(c)}$ (dB)
602	1076	−15.4	75	714	−10.2
605	1059	−15.7	75	712	−10.7
610	833	−15.5	75	590	−11.4
622	634	−13.6	75	453	−10.0
634	455	−12.5	36	381	−9.8
660	432	−13.5	19	407	−11.3

Appendix B
Ancillary Data of Individual Tested Balanced Device

B.1 Supporting Data from Balanced Mixer Tests

See Fig. B.1; Tables B.1, B.2, B.3, B.4 and B.5.

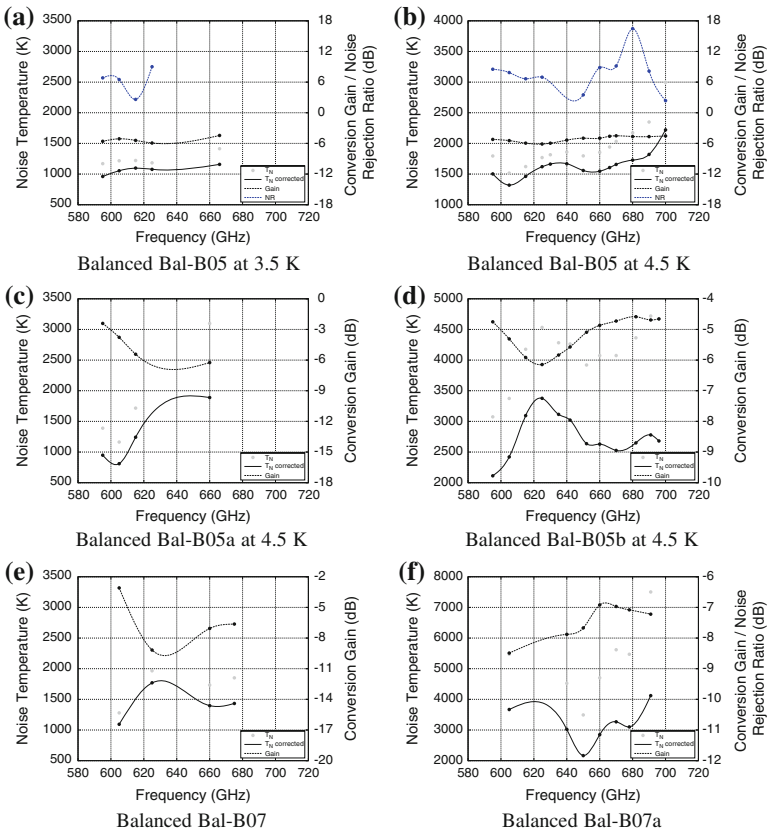

Fig. B.1 Measured noise temperature and DSB conversion gain of Balanced Bal-B05 and Bal-B07 across the operating RF bandwidth. The *grey points* corresponding to the uncorrected values

B.-K. Tan, *Development of Coherent Detector Technologies for Sub-Millimetre Wave Astronomy Observations*, Springer Theses, DOI 10.1007/978-3-319-19363-2

Table B.1 Results of balanced mixer tests for FSOI Bal-B05

$T = 3.5\,\text{K}$, $R_N = 19.21\,\Omega$ and $20.75\,\Omega$							
f_{LO} (GHz)	T_N (K)	G_R (dB)	NR (dB)	$G_{R(c)}$ (dB)	$T_{N(c)}$ (K)		
					HDPE 460 μm	Zitex	WG groove
595	1169	−12.7	6.8	−5.5	1045	1028	961
605	1217	−12.2	6.5	−5.1	1120	1103	1053
615	1221	−12.3	2.6	−5.4	1157	1139	1097
625	1183	−12.8	9.0	−5.9	1147	1129	1076
666	1413	−13.5	–	−4.4	1401	1377	1158
$T = 4.5\,\text{K}$							
595	1794	−13.9	8.5	−5.2	1616	1592	1502
605	1516	−13.3	7.8	−5.4	1401	1380	1319
615	1622	−13.8	6.6	−5.9	1540	1517	1462
625	1769	−14.4	6.9	−6.1	1719	1694	1620
630	1815	−14.5	–	−5.9	1781	1755	1662
640	1859	−14.5	–	−5.3	1848	1820	1668
650	1797	−14.5	3.5	−4.9	1797	1769	1557
660	1854	−14.9	8.8	−4.9	1848	1818	1546
666	1941	−14.8	–	−4.6	1925	1894	1605
670	2033	−15.0	9.1	−4.5	2006	1974	1657
680	2172	−15.5	16.4	−4.6	2106	2072	1727
690	2348	−15.8	8.1	−4.6	2227	2191	1820
700	2995	−16.8	2.3	−4.5	2775	2730	2221

Table B.2 Results of balanced mixer tests for FSOI Bal-B05, biased for testing it as a single junction (B05b) device

$T = 4.3\,\text{K}$, $R_N = 20.75\,\Omega$							
f_{LO} (GHz)	T_N (K)	G_R (dB)	$G_{R(c)}$ (dB)	$T_{N(c)}$ (K)			
				HDPE 460 μm	Zitex	WG groove	RF Hybrid
595	3074	−17.8	−4.7	2788	2741	2502	2113
605	3374	−18.4	−5.3	3138	3086	2883	2420
615	4176	−19.7	−5.9	3987	3921	3708	3094
625	4532	−20.2	−6.1	4413	4339	4059	3376
635	4283	−20.0	−5.8	4232	4159	3734	3114
642	4263	−20.0	−5.5	4245	4170	3613	3020

(continued)

Table B.2 (continued)

$T = 4.3\,\text{K}$, $R_N = 20.75\,\Omega$

652	3919	−19.7	−5.0	3919	3847	3143	2637
660	4074	−19.9	−4.8	4062	3986	3128	2629
670	4074	−19.9	−4.7	4013	3936	3005	2526
682	4363	−20.0	−4.5	4226	4146	3148	2649
691	4719	−20.5	−4.6	4472	4386	3306	2778
696	4675	−20.5	−4.6	4385	4300	3192	2680

Note that the other junction is simply terminated with a 50 Ω load without changing in the optical arrangement, hence the 300 K noise from the LO will be directly injected into the mixer

Table B.3 Same as Table B.2, but for FSOI Bal-B05a

$T = 4.3\,\text{K}$, $R_N = 19.21\,\Omega$

f_{LO} (GHz)	T_N (K)	G_R (dB)	$G_{R(c)}$ (dB)	$T_{N(c)}$ (K)			
				HDPE 460 μm	Zitex	WG groove	RF Hybrid
595	1389	−12.7	−2.4	1246	1223	1119	948
605	1163	−13.1	−3.7	1070	1051	977	810
615	1716	−15.8	−5.4	1630	1601	1508	1242
660	3097	−19.9	−6.2	3089	3027	2307	1888

Table B.4 Results of balanced mixer tests for FSOI Bal-B07

$T = 4.5\,\text{K}$, $R_N = 21.03\,\Omega$ & $19.00\,\Omega$

f_{LO} (GHz)	T_N (K)	G_R (dB)	NR (dB)	$G_{R(c)}$ (dB)	$T_{N(c)}$ (K)		
					HDPE 460 μm	Zitex	WG groove
605	1279	−10.1	–	−3.0	1178	1159	1093
625	1965	−17.4	–	−9.1	1911	1879	1769
660	1733	−16.5	–	−7.0	1728	1697	1396
675	1851	−16.6	–	−6.6	1811	1779	1433

Table B.5 RSame as Table B.2, but for FSOI Bal-B07a

$T = 4.5\,\text{K}$, $R_N = 21.03\,\Omega$

f_{LO} (GHz)	T_N (K)	G_R (dB)	$G_{R(c)}$ (dB)	$T_{N(c)}$ (K)			
				HDPE 460 μm	Zitex	WG groove	RF Hybrid
605	5471	−22.9	−8.4	5110	5016	4597	3668
640	4523	−22.0	−7.8	4503	4417	3763	3023
650	3491	−21.2	−7.6	3491	3422	2704	2165
660	4703	−22.0	−6.9	4688	4595	3490	2849
670	5618	−22.9	−6.9	5541	5430	4003	3268
678	5471	−22.9	−7.0	5341	5232	3811	3101
691	7504	−24.3	−7.2	7128	6984	5062	4120

Appendix C
List of All Beam Patterns Measured Up to Date

C.1 Beam Patterns of the First Generation 700 GHz Horn

See Fig. C.1.

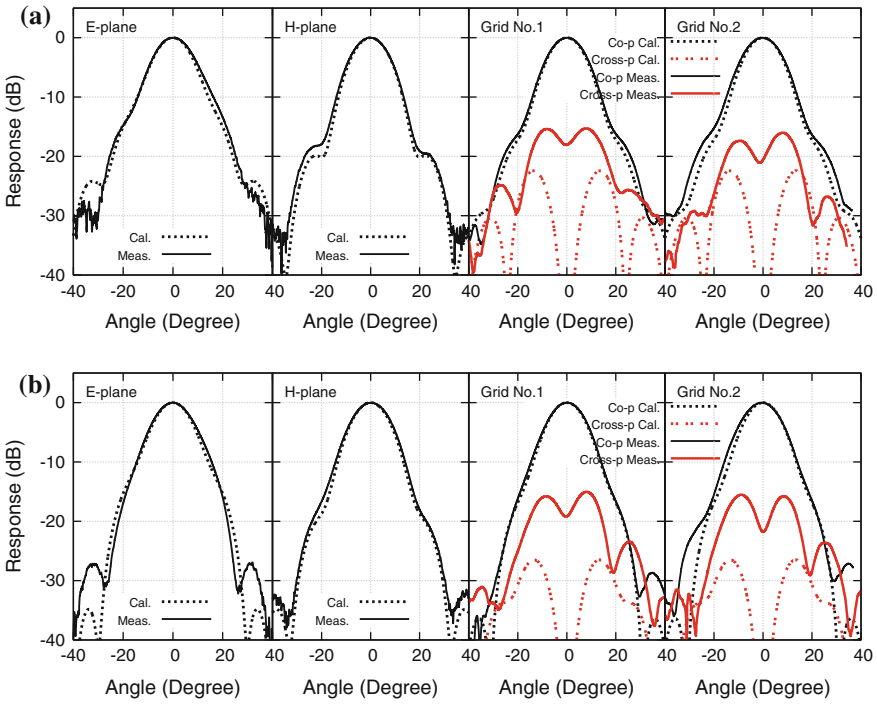

Fig. C.1 Continued from Fig. 2.7. **a** 600 GHz. **b** 630 GHz. **c** 650 GHz. **d** 660 GHz. **e** 690 GHz. **f** 720 GHz

B.-K. Tan, *Development of Coherent Detector Technologies for Sub-Millimetre Wave Astronomy Observations*, Springer Theses, DOI 10.1007/978-3-319-19363-2

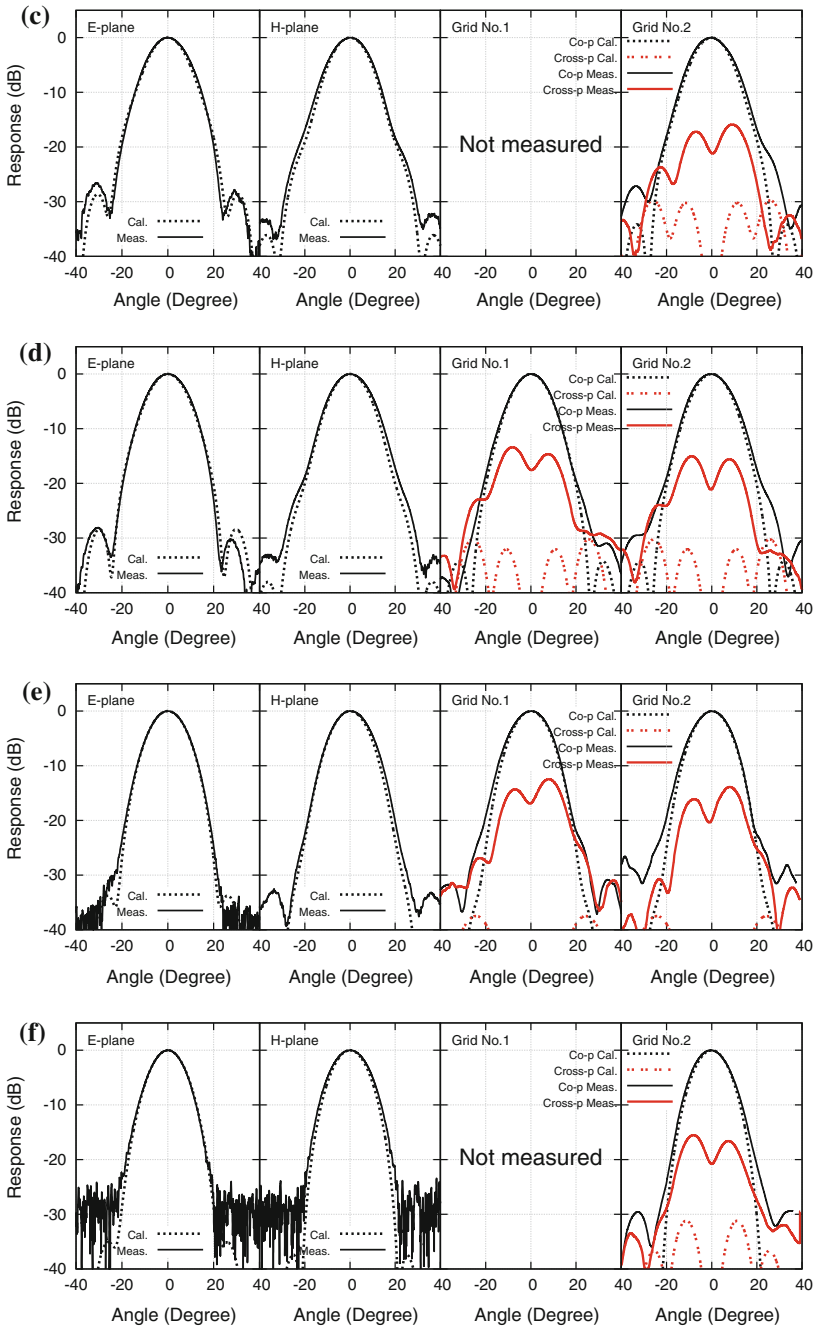

Fig. C.1 (continued)

C.2 Beam Patterns of the Second Generation 700 GHz Horn

See Fig. C.2.

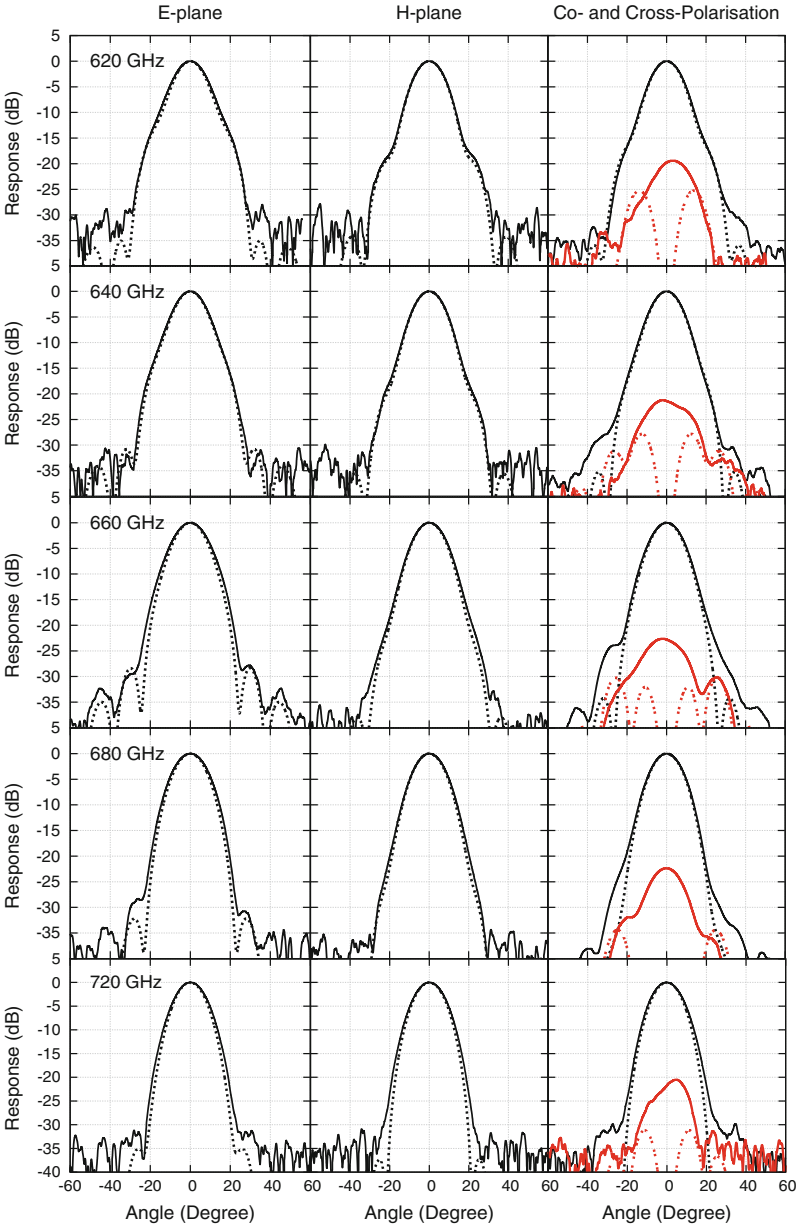

Fig. C.2 Continued from Fig. 2.12

Appendix D
230 GHz Scalable Design

This appendix presents the designs of various unilateral finline SIS mixers centred at 230 GHz. The purpose here is to demonstrate that planar-circuit-based SIS mixer designs are easily scalable. Hence, these 230 GHz designs are mostly simply scaled-up versions of those described in Chaps. 4, 6 and 7. The dimensions of most of the RF circuit components, especially the widths, remain similar to the 700 GHz design, except the lengths are often longer by a factor of 700/230. Note that these designs have not been fully optimised for highest performance and broadest operational bandwidth, but were simply scaled from the 700 GHz design with minimum adjustments. Therefore, there are scope for improvements. Nevertheless, the simulated performances were reasonable, as good as conventional 230 GHz designs.

There are four different designs presented here: a single-ended, a balanced, a sideband-separating, and a balanced-2SB mixer design. All these designs utilised a 15 μm SOI substrate, with the same stacking topology as the 700 GHz counterpart, and were designed to cover a frequency range from 180–260 GHz.

D.1 Performances of RF Circuit Component

Since the design procedure had been discussed extensively in the main text, only the HFSS simulated results for each of the passive circuit components are presented here. For simplicity, only one notch was used to match the impedance of the waveguide to the finline, and only the slotline-to-microstrip transition via CPW sections design was used. The IF transformer was designed using a 9-stage transformer, giving an 8 GHz wide IF bandwidth from 4 to 12 GHz, for the single-ended SIS mixer (Fig. D.1).

B.-K. Tan, *Development of Coherent Detector Technologies for Sub-Millimetre Wave Astronomy Observations*, Springer Theses, DOI 10.1007/978-3-319-19363-2

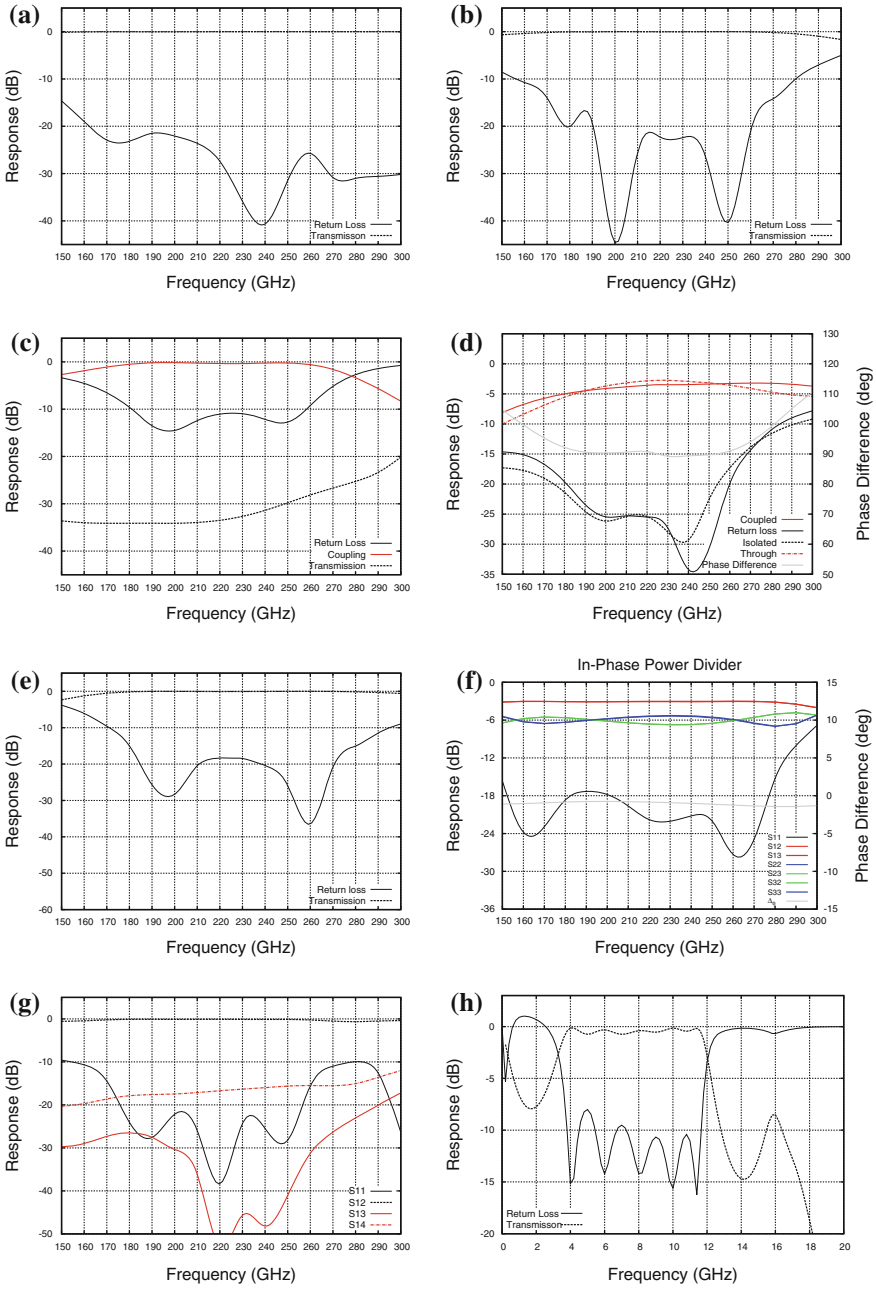

Fig. D.1 Scattering parameters describing the performance of each circuit component simulated using HFSS. In general, all components show good performance from 180 to 260 GHz. **a** Unilateral finline. **b** Slotline-to-microstrip transition. **c** Tuner circuit. **d** RF quadrature hybrid. **e** DC/IF block. **f** In-phase power divider. **g** LO directional coupler. **h** IF transformer

D.2 Full Mixer Chip Simulation

The following sections summarise the heterodyne performance for each mixer design, simulated using SuperMix and HFSS, as described in Chap. 4. A simply layout is attached alongside each section (except the balanced 2-SB design) to show the physical layout of the final mixer chip.

D.2.1 Single-Ended Mixer Design

See Figs. D.2, D.3, D.4, D.5, D.6, D.7 and D.8.

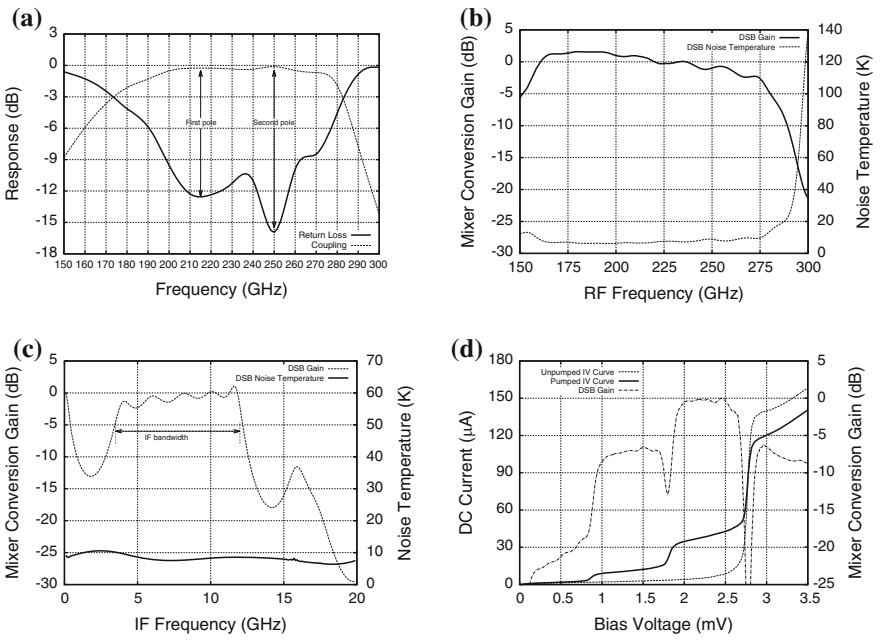

Fig. D.2 HFSS and SuperMix simulations showing the predicted behaviour of the complete single-ended mixer chip design, with the following settings: bias voltage at 2.2 mV, IF frequency at 8 GHz, and RF frequency at 230 GHz. **a** HFSS simulation. **b** RF gain and noise temperature. **c** IF response. **d** IV curves and DSB gain

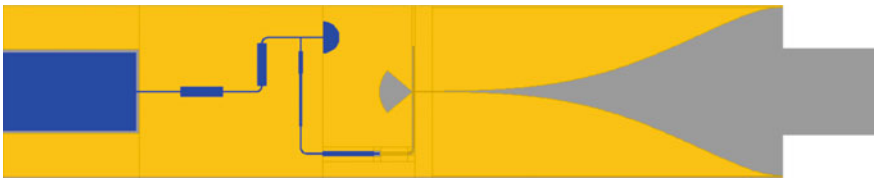

Fig. D.3 The layout of the single-port SIS mixer chip

D.2.2 Balanced Mixer Design

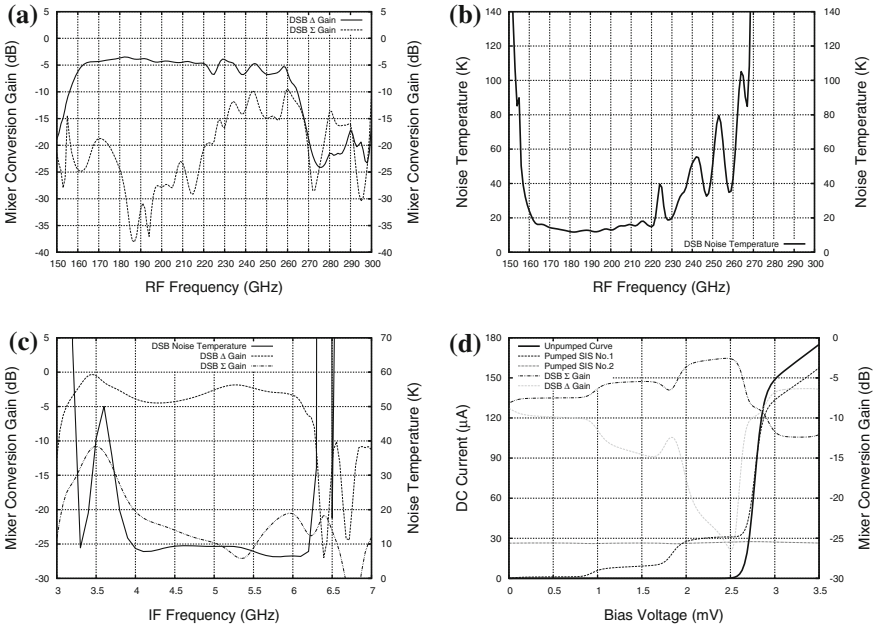

Fig. D.4 SuperMix simulations showing the predicted behaviour of the complete balanced SIS mixer chip design. The simulation was carried out with the following settings: bias voltage at 2.4 mV, IF frequency at 5 GHz, and RF frequency at 220 GHz. **a** DSB gain at RF frequencies. **b** Noise temperature at RF frequencies. **c** IF response. **d** IV curves and DSB gain

Fig. D.5 The layout of the balanced SIS mixer chip

D.2.3 Sideband Separation Mixer

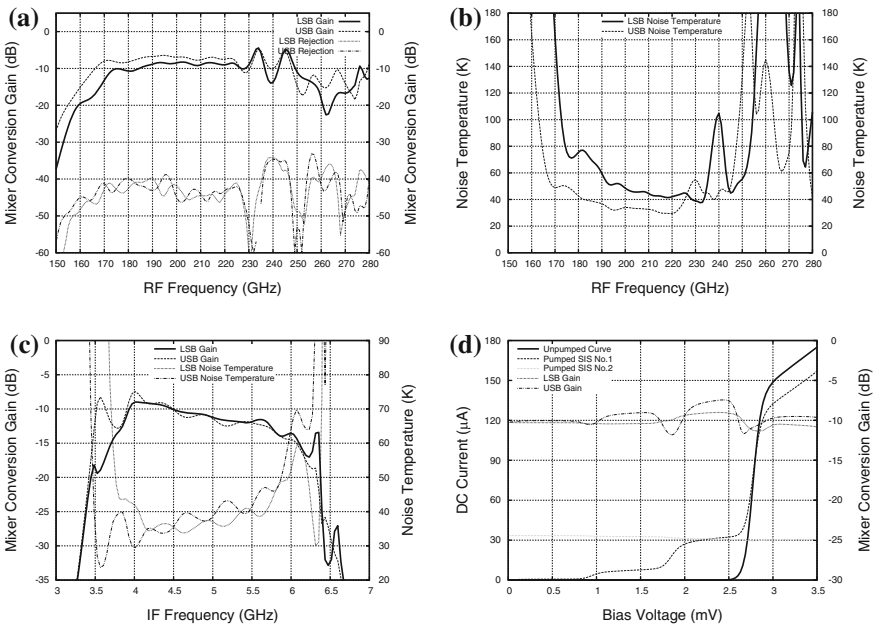

Fig. D.6 SuperMix simulations showing the predicted behaviour of the complete sideband separating SIS mixer chip design. The simulation was carried out with the following settings: bias voltage at 2.4 mV, IF frequency at 4 GHz, and RF frequency at 220 GHz. **a** DSB gain at RF frequencies. **b** Noise temperature at RF frequencies. **c** IF response. **d** IV curves and DSB gain

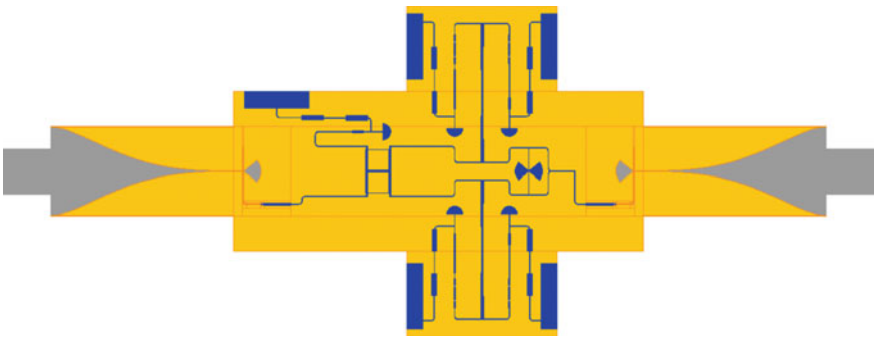

Fig. D.7 The layout of the sideband separating SIS mixer chip

D.2.4 Balanced with Sideband Separation Mixer

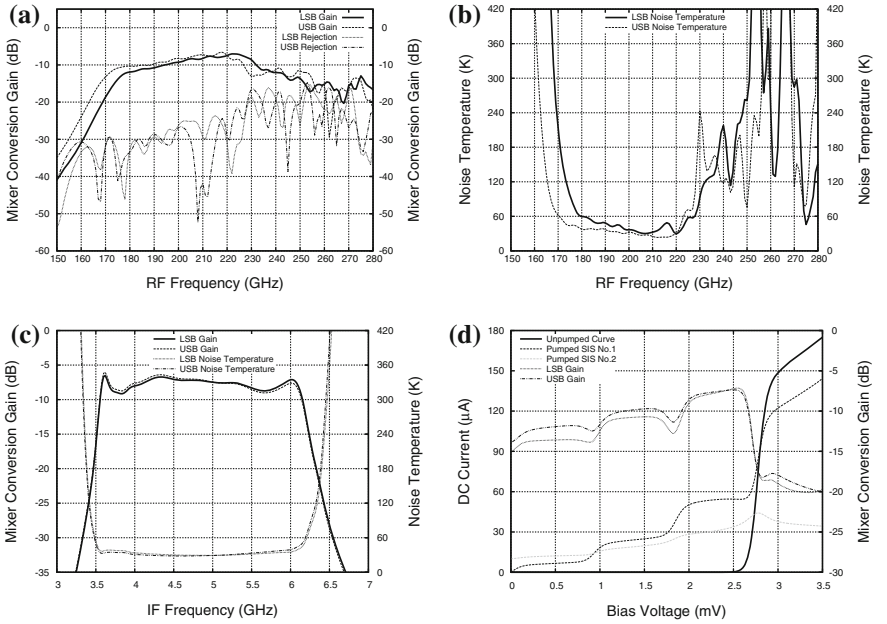

Fig. D.8 SuperMix simulations showing the predicted behaviour of the complete balanced with sideband separating mixer chip design. The simulation was carried out with the following settings: bias voltage at 2.4 mV, IF frequency at 5 GHz, and RF frequency at 220 GHz. **a** DSB gain at RF frequencies. **b** Noise temperature at RF frequencies. **c** IF response. **d** IV curves and DSB gain

Index

B.-K. Tan, *Development of Coherent Detector Technologies for Sub-Millimetre Wave Astronomy Observations*, Springer Theses, DOI 10.1007/978-3-319-19363-2

C

D

T